Dissertation

# The Dual-Polarization Radar Signature of a Wind Turbine: Characterization and Suppression

Submitted by

Robert M. Beauchamp

Department of Electrical and Computer Engineering

In partial fulfillment of the requirements

For the Degree of Doctor of Philosophy

Colorado State University

Fort Collins, Colorado

Fall 2016

Doctoral Committee:

Advisor: V. Chandrasekar

Margaret Cheney
Anura P. Jayasumana
Paul Mielke

## Abstract

### The Dual-Polarization Radar Signature of a Wind Turbine: Characterization and Suppression

Wind turbines can represent large, dynamic targets for radar systems. Their echoes can inhibit normal radar operations for observation volumes in and beyond the ranges occupied by the turbines. As a result of this interference, also referred to as "wind turbine clutter," the construction and location of wind turbines is restricted, and radar operations are limited to suboptimal performance in the contaminated areas.

With the exponential growth of wind energy production, reducing the interference caused by wind turbines is critical to maintaining the performance of radar systems. In this work, characterizations of precipitation, ground clutter, and wind turbines are presented using dual-polarization weather radar observations. Without direct knowledge of a wind turbine's operating state, the physical characteristics of the turbine—specifically, its cyclostationarity—are exploited to implement a temporal suppression method to mitigate wind turbine clutter. Using the cyclostationary characteristics, 15-20 dB of suppression of the turbine blades' signature is demonstrated.

A field experiment that simultaneously collected radar observations of a wind turbine and turbine state telemetry is also discussed in this work. Characteristics of the wind turbine's signature are evaluated according to the turbine's state. With this, it is demonstrated that the radar signature of the turbine is deterministic for a given turbine's state and can be modeled. With the observation-based model and state telemetry, the wind turbine blades' signature can be significantly suppressed (by more than 25 dB) in radar observations.

## Acknowledgments

My wife Catherine's patience and encouragement cannot be overstated. I am grateful to Dr. Chandrasekar for his mentorship, support, and direction during my time at CSU. I also must thank all of my group members and colleagues at CSU for their collaboration and help, especially Haonan Chen, Joseph Hardin, and Manuel Vega for helping to ensure that my time here was a success.

Regular discussions with Margaret Cheney, Louis Scharf, and V. Chandrasekar have been instrumental to the development of the work presented here. I also want to acknowledge my committee, Pooria Pakrooh, Matthew Ferrara, Andrew Homan, and Douglas Cochran for their contributions in helping me gain a deeper understanding of a wind turbine's radar signature.

The CSU-CHILL data was provided by the National Science Foundation's CSU-CHILL radar facility. The data collected for this work was recorded over multiple years and only possible due to the patience and effort of Patrick Kennedy.

The field experiment at NREL would not have been possible without support from Francesc Junyent, Andrew Clifton, and the rest of the staff at NREL. The deployment of the CSU X-band radar at NREL was facilitated through the efforts of Andrew Clifton, and its success is a direct result of assistance from David Jager, Jason Roadman, Jeroen van Dam, Andrew Scholbrock, and Dana Scholbrock.

The work presented in Chapters 4 and 5 was supported by the Air Force Office of Scientific Research under contract number FA9550-14-C-0053. Consequently, the U.S. government is authorized to reproduce and distribute reprints of these chapters for governmental purposes, notwithstanding any copyright notation thereon. The views and conclusions contained herein are those of the authors and should not be interpreted as necessarily representing the official policies or endorsements, either expressed or implied, of the Air Force Research Laboratory or the U.S. government.

# Table of Contents



[1] ©2016 IEEE [1]
[2] ©2016 IEEE [1]
[3] ©2016 IEEE [1]
[4] ©2016 IEEE [1]

CHAPTER 1

# Introduction

Wind turbine interference has been a persistent and growing concern for radar system operations. Wind turbine interference is also referred to as "wind turbine clutter" (WTC), with "clutter" describing unwanted echoes in observations. The exponential growth of renewable wind energy production in the United States and around the world is exacerbating the technical challenges of providing accurate results from radar system algorithms in the presence of wind turbine radar interference. Due to the adverse impact of wind turbines on radar operations, the installation of new wind turbine farms in areas where wind turbines may interfere with the proper operation of radars needs to be scrutinized [2, 3].

In the United States, all wind farm plans must be reviewed and approved by a range of government agencies prior to starting construction [2]. These agencies may include the Federal Aviation Administration (FAA), Department of Defense (DOD), Department of Homeland Security (DHS), National Oceanic and Atmospheric Administration (NOAA), the U.S. Fish and Wildlife Service (due to the negative impact to raptor populations because of wind turbine bird strikes), and possibly state and local agencies. The goal is to assess the potential impact of a new wind farm on the status quo. The outcome of this review and approval process can result in delays or modifications to plans if any radar interference, real or perceived, is deemed problematic.

With the exponential growth in wind turbine power production [4], as well as the increasing size of the turbines installed [5], radar interference and the restrictions placed on wind farm locations present conflicting requirements for common resources. To alleviate the pressures imposed, radar characterization activities continue to be used to investigate the

nature of this interference, with goals of implementing signal processing algorithms to mitigate concerns. Numerous field studies, scale model observations, and numerical simulations have been carried out to characterize, in detail, wind turbine radar signatures [6–12]. From this, a number of suppression techniques have been introduced with varying levels of performance and restrictions [13, 14, 3, 15, 16]. However, no single solution has yet provided an adequate means of mitigating WTC in radar systems or alleviating the problems associated with placing wind farms near radar facilities [3].

Wind turbine clutter presents concerns for a variety of radar applications such as air surveillance radar (ASR), marine radar, and weather radar systems. The non-zero Doppler signature and large radar cross-section (RCS) of a wind turbine can confuse aircraft tracking algorithms when aircraft occupy the same range cell as wind turbines. For weather radar, conventional ground clutter filters are unable to suppress the dynamic wind turbine signature and, subsequently, may include wind turbines as precipitation. Short-time statistical moments of a radar's received power are used to describe a radar-observed volume [17]. These moments are used to derive other radar products such as rainfall rate, total accumulated rainfall, severe weather identification, etc. The effects of not removing the WTC can include incorrect rainfall estimation for an area and may adversely impact a radar's velocity estimates, which are used to detect tornado signatures and relative storm motion [18]. Beam blockage (or shadowing) from wind turbines presents another issue with radar systems, but, in general, such blockage is only partial and does not completely obscure targets of interest.

Examples of wind farms and resulting interference with radar systems can be found in operational radar data from around the world. A map for U.S.-based wind farms can be found in [19]. Examples of radar interference in the United States can be identified in a careful review of the National Weather Service's NEXRAD radar products [20], including the following:

- southeast of Fairfield, California
- east-northeast of Livermore, California
- between Ames, Iowa, and Marshalltown, Iowa
- east-northeast of Utica, New York

These wind farms can be identified in the absence of weather events by their stationary location and relatively large reflectivities. When a wind farm is generating power, the radar reflectivities vary with time, and the velocity signatures can appear to exhibit a random behavior, changing from negative to positive velocities. U.S. land-based wind farms, such as the Roscoe Wind Farm in Roscoe, Texas, cover an area of nearly 400 square kilometers [21]. As of 2013, the world's largest wind farm (in terms of energy production), Alta Wind Energy Center, has a capacity of 1,550 megawatts and is located in Tehachapi Pass in Kern County, California [22].

The wind farms southeast of Fairfield, California, located in Montezuma Hills, are in close proximity to Travis Air Force Base. The wind turbines there are as close as 9.3 km to the air traffic control (ATC) tower and cover an area that extends beyond 25 km in range from the ATC tower. The Montezuma Hills area is home to more than 800 wind turbines from a multitude of vendors and operators. Wind turbine interference from the area observed by the KDAX NEXRAD weather radar is shown in Figure 1.1. The figure shows the locations of individual wind turbines as black markers with the observed reflectivities (greater than 20 dBZ) overlaid as a colormap. For reference, the location of the Travis Air Force Base ATC tower is shown as a pink marker.

## 1.1. Problem Statement

Wind turbines are a rapidly growing sector of energy production around the world. Radar systems are critical for air traffic control, defense systems, water management, and natural

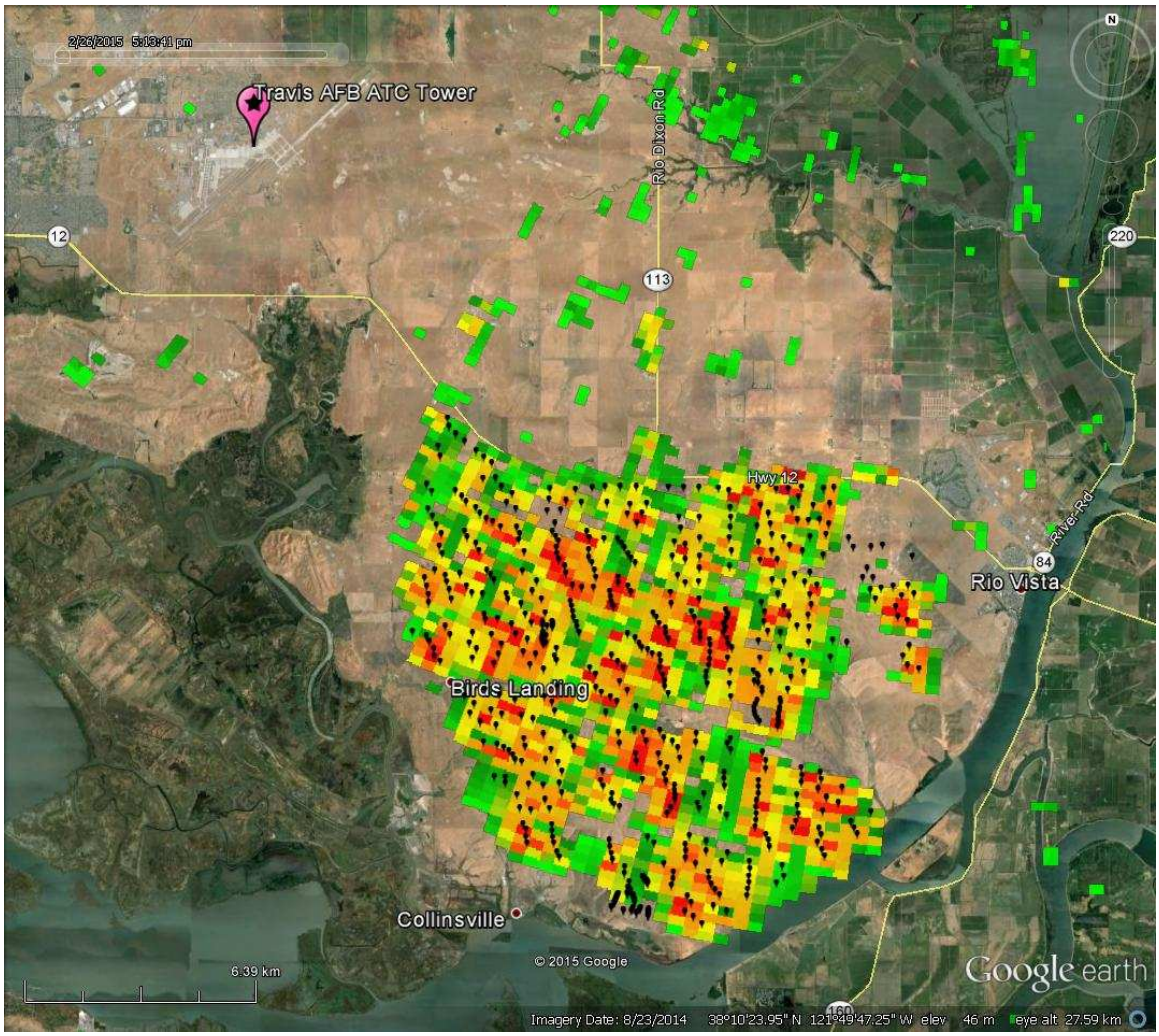


FIGURE 1.1. The Montezuma Hills region southeast of Fairfield, California. Black markers represent individual wind turbines. The image shows the reflectivity field, for reflectivities greater than 20 dBZ, of a clear-air, 0.49-degree elevation scan from KDAX NEXRAD WSR-88D in Sacramento, California, on February 27, 2015, at 00:13 UTC.

disaster warnings. With the proliferation of wind farms, there is an increasing need for radars to operate unimpeded by wind turbines. Currently, interference concerns are being addressed in three major ways: wind farm location planning, wind turbine design, and radar algorithms. In this work, the focus is on the characterization of WTC and subsequent development of radar signal processing algorithms to mitigate a wind turbine's radar signature in observations. The characterization and algorithm evaluation will utilize weather radar systems, although the results may be applicable to other radar applications.

The RCS of a wind turbine observed by a stationary radar can be diverse. Even for a single turbine make and model, this diversity comes from the range of operating states and results from changes in the wind turbine's yaw, rotation, pitch, rate, or deflection. The variety of parameters presents a complex estimation problem for determining the RCS of the wind turbine and is further complicated in the presence of other dynamic scattering bodies, such as precipitation or aircraft.

For weather radar processing, a sampling volume with wide-sense stationary statistical characteristics is assumed over short time periods. For a well-designed radar, the sampled voltage at the receiver is a mean-zero process with variance (power) proportional to the RCS of the scatterer (or the coherent integration of multiple scatterers). Pulse radar systems only sample a single realization at one instant in time. For a wide-sense stationary process, ergodicity is used to replace multiple realizations with samples in time to estimate power. For a statistically non-stationary scatterer (such as a wind turbine), the variance of the process changes with time, and the process is not ergodic. For non-stationary processes, sampling in time cannot accurately characterize the variance of the process. This is neglected in many cases, and short instances in time are used, assuming the process is approximately stationary to make some estimate of the variance (with varying levels of accuracy).

A multitude of field experiments and scale model tests aimed at characterizing wind turbine radar signatures have been undertaken. However, the data sets and results of these experiments are not readily available to the public for further independent analysis. Also, wind turbine designs are as diverse as the radar systems that may be considered. Further characterization of real wind turbines is needed, both to validate the findings presented in other data sets, as well as to expand the characterization to consider dual-polarization in greater detail.

Wind turbine interference mitigation techniques in radar signal processing can be subdivided. Statistical models of WTC have been characterized but require long-duration sampling and do not provide fine temporal resolution. The statistical models are more easily applied to the detection of targets. Spatial filtering techniques have been investigated and demonstrate good performance for widespread volume targets. For fine resolution spatial features, these techniques can remove the dynamic signatures that may represent a target of interest. A temporal filtering method is desirable for the suppression of wind turbine interference when mixed with the signature of a desired target. The target of interest may vary according to radar application and may include aircraft or meteorological phenomena. Synthetic and model wind turbine observations have shown promise, but demonstrations of temporal filtering techniques for real-world wind turbine observations have not been forthcoming.

## 1.2. Research Objectives

This dissertation aims to characterize and suppress wind turbine clutter in weather radar systems. The characterization is focused on two separate aspects: 1) the cyclic dual-polarization signature of wind turbines in the presence of precipitation and ground clutter and 2) characterizing the Doppler spectral signature of a wind turbine using wind turbine state telemetry. Suppression of WTC considers a temporal—not spatial—filter. A temporal filter is of primary interest to retain fine spatial features and localized targets within the radar's domain.

Characterization of a wind turbine signature in the Doppler velocity domain, with comparison to the signatures of ground clutter and precipitation, is necessary to identify signal features that can be used to aid in separating the wind turbine's contribution from the total observed radar return power. A fixed-pointing mode is used to collect data from targets

of interest over an extended time period. The dual-polarization radar signature of a wind turbine provides additional indicators and features to aid in the detection and estimation of its signature when simultaneously observed with precipitation or ground clutter.

Although radar systems with a mechanically scanning, parabolic antenna cannot dwell on wind farm-contaminated areas for multiple seconds, the characterization technique is critical to understanding the wind turbine radar cross-section features that can be exploited for suppression. Phased-array radar systems utilizing electronic beamforming techniques have the ability to dwell on wind turbine-contaminated areas for durations long enough to use techniques developed for fixed-pointing.

A wind turbine rotates on an axis that is mounted to a fixed tower. When the wind turbine's blades are rotated about a fixed axis with a fixed rotation rate, the observed behavior is cyclic in nature. A statistically stationary process is a subset of a wider class of cyclostationary processes. To this end, the physical properties of a wind turbine can be exploited to provide a-priori information to estimate the turbine's state from previous observations. The non-stationary, cyclic behavior of the wind turbine requires new techniques relying on the wider class of cyclostationary processes.

The key points that are addressed by this research are:

- A description of a wind turbine's operational characteristics as they impact the turbine's radar signatures
- A characterization of WTC using dual-polarization radar in a fixed-pointing mode
- Identification of characteristics unique to wind turbines in the context of weather applications (i.e., compared to ground clutter and precipitation), which can aid in the suppression of WTC
- The development a wind turbine suppression technique applicable to weather radar applications and an evaluation of its performance

- A demonstration of a deterministic relationship between the wind turbine state (via telemetry) and the wind turbine's signature.
- A demonstration of how a wind turbine's telemetry enables the suppression of its signature.

## 1.3. Dissertation Overview

Chapter 2 presents a brief (and necessarily partial) review of the relevant work characterizing, describing, and in some cases suppressing wind turbine clutter in the presence of precipitation or moving targets. Following the literature review, scattering phenomena which determine the observed RCSs, are explained from theory as well as the estimation of Doppler velocity, with considerations applicable to observations of wind turbines. In this Chapter, typical radar systems used for weather and air surveillance are briefly discussed, with the meteorological parameter estimates derived from dual-polarization observations. The two Colorado State University (CSU) radar systems used for the experimental observations of wind turbines are also introduced.

In Chapter 3, the ubiquitous three-blade wind turbine structure is described, and the physical attributes are considered in detail for two wind turbine models present in the Ponnequin Wind Farm located in northern Colorado. The CSU-CHILL radar was used to observe the Ponnequin Wind Farm, which consists of 44 wind turbines. With this wind farm used as an example, the characteristics of it and its wind turbines are discussed. The Department of Energy's (DOE) National Renewable Energy Lab's (NREL) National Wind Technology Center (NWTC) and two of its wind turbines with state telemetry are also introduced here. Additionally, considerations for interpreting the radar observations of wind turbines are mentioned to highlight sources of variation and the complexity of interpreting real-world observations.

A new characterization method is presented in Chapter 4. The dual-polarization observations of ground clutter, precipitation, and wind turbines are considered. To supplement the analysis of real wind turbine observations, a numerical simulation of a simple wind turbine model is evaluated. The cyclostationary behavior of the wind turbine's signature is demonstrated in observations. The characterization of all scatterers is presented within a consistent framework, enabling direct comparison. From this analysis, features unique to these scatterers are discussed, which enables the development of suppression techniques.

In Chapter 5, using the differentiating features of the scatterer types, wind turbine parameter estimation and WTC suppression techniques are introduced. The suppression techniques leverage the cyclostationary characteristics of the turbine, and an effective mitigation algorithm is developed that relies on prior observations of the same wind turbine. The performance of the wind turbine signature mitigation is considered in this Chapter for varying cases and mixtures of wind turbines and precipitation.

Radar observations of the DOE three-blade controls adaptive research turbine (CART3), located at NREL, are presented and discussed in Chapter 6. The characteristics of the spectral radar signature are directly related to the wind turbine's state telemetry. A model for the wind turbine signature is presented in this chapter, and suppression techniques to mitigate the turbine signature, which relying on the state telemetry, are also presented and evaluated.

Finally, Chapter 7 summarizes the key findings contained within this dissertation.

CHAPTER 2

# Background

Radar interference from wind turbines reduces radar effectiveness for a variety of applications, including marine radar systems, weather radar, and air traffic control radar. Varying degrees of radar characterization and the development of radar interference mitigation techniques have been an active area of research for decades. The breadth of work available is vast; however, mitigation techniques have not yet substantially addressed the radar interference issue presented by wind turbines. As wind turbine technology evolves, the number of wind farm installations grows, and the corpus of available research increases, the research community's knowledge regarding the characteristics of WTC has, as one would expect, led to a deeper understanding of the nature of the problem as well as its technical challenges. The extent of the impact wind turbines have on radar system operations continues to redefine requirements for the installation of new wind farms as well as improve our understanding of how to enhance a radar system's immunity to WTC.

A brief survey of publicly available research and technology is introduced in this chapter as both a reference and a context for the research presented in this dissertation. The methods used to characterize wind turbine clutter are briefly reviewed, as the concepts will be used throughout the remainder of this work. Following the literature review, the background theory used for the characterization and suppression of a wind turbine signature is considered. The observation used in this work are from dual-polarization weather radar systems. In this context, wind turbine interference is explained using terminology and parameters widely available in dual-polarization weather radar systems.

## 2.1. Prior Work

Radar interference posed by wind turbines has been a widely researched topic. A broad range of radar applications are impacted by the proliferation of wind energy, and this is exacerbated by the increasing size of wind turbines installed for power generation both on land and offshore. For marine and air-surveillance radar systems, the large RCS of wind turbines and the large scale of wind farms can mask aircraft or ships in their vicinity. The reduced detection capability and degraded performance of detection and tracking algorithms present safety and security concerns. In some cases, gap-filling radars have been installed as a mitigation technique for air-surveillance systems [3].

The NOAA National Weather Service Milwaukee/Sullivan field office discussed interference from a local wind farm in [18]. The interference and blockage result in operational concerns for forecasters and emergency management officials. In extreme cases, the wind turbines can make the detection of mesoscale cyclones (tornadoes) more difficult. Specifically, WTC hampers automated detection algorithms looking for velocity couplets indicative of tornadoes. Neighboring wind turbines can create opposite Doppler velocity signatures. The wind turbine areas may have such detection algorithms disabled due to the increased false-alarm rate. Additionally, a more persistent source of contamination from wind farms in meteorological applications is rainfall estimation, which, in some algorithms, estimates rainfall as a function of reflectivity. The wind farm is a constant, potentially significant source of return echo power. If WTC-contaminated ranges are ignored, rainfall contribution in the area is not captured. Conversely, if WTC-contaminated ranges are included in estimates, the resulting rainfall for the area may be significantly overestimated.

Air traffic control [3] and national defense organizations (e.g., the U.S. DOD or the U.K. Ministry of Defense) [2] are concerned with radar interference from wind turbines because

of potential impacts on public safety and security. Trials performed by the U.K.'s Ministry of Defense and the U.S. DOD have demonstrated that wind turbines present radar cross-sections consistent with military and commercial passenger aircraft at Doppler velocities similar to aircraft. When aircraft are in the vicinity of wind farms, the radar's detection performance degrades significantly.

Careful site selection and the locating of new wind farms—and the wind turbines within the wind farms—with regard to radar installations is one means of mitigating radar interference from wind farms [3]. The landscape can be used to block the line of sight between the wind turbines and the radar system, effectively hiding the problem behind other clutter sources like hills or mountains. At a sufficient range, the Earth's curvature can also place wind turbines below a radar's beam height, significantly reducing interference. Depending on the directions of prevailing winds, the appropriate sizing of wind turbines and tower heights can also reduce the potential impact of a wind farm installation. Simulations and analysis of the interference potential during the planning phase are a low-cost means that, in some cases, may significantly address interference concerns [11].

For all radar applications, whether air surveillance or weather, characterization and analysis of wind turbine interference have been considered both through experimental observations and simulations of wind turbines. A field experiment conducted to characterize a wind turbine's radar signature was sponsored by the U.S. DOD using the Air Force Research Laboratory's Mobile Diagnostic Laboratory (MDL), a mobile, multifrequency (L,S,C,X bands) radar system certified for RCS measurements [7, 8]. The results indicate that the characterization of wind turbines in the field was an extremely difficult task due to the lack of experimental control [2]. In part, such limitations have led many researchers to use scale and numerical models to better understand a wind turbine's radar signature.

A rigorous numerical simulation of a wind turbine based on a 1.5-megawatt General Electric commercial turbine was considered in [6]. In their results, using a supercomputing cluster with simplifications in the physics, it was shown that the simulation of a full-scale wind turbine over its full range of operating states (yaw and rotation) could take months (or longer) due to the electrical size of wind turbines. The turbine simulations in [6] are of the same wind turbine model observed in the MDL field campaign to facilitate model validation. Comparisons between the simulated and observed RCS from the wind turbine show that good agreement and accurate RCS calculations are possible. The authors, though, are careful to note that measurement uncertainties include variable blade pitch and blade flexing as sources of inconsistencies.

Scale model wind turbines can provide a link between real-world observations and numerical simulations. In [12], a scale model was characterized over its entire range of operating parameters (yaw and rotation). The results presented provide insight into the underlying phenomenon observed in full-scale wind turbines. The authors are careful to note that the scale model is not representative of the electrical size observed by operational radars of commercial wind turbines. Similarly, the scale model results in [9] exhibit the basic behavior of wind turbines but lack the scattering features observed in full-scale wind turbines. This is important for fully and accurately characterizing the dual-polarization wind turbine signature. The cross-pol scattering is heavily influenced by wavelength-scale features.

Comparisons among simulation, scale model, and full-scale wind turbine observations show good agreement in their first-order characteristics [6, 12]. With enough computational power and detailed modeling, simulations of wind turbines can accurately capture radar observations. The difficulty in directly applying simulations or scale models to radar observations comes from the continuous state change from the dynamic control systems of the

wind turbine tasked with maximizing power output and maintaining safe operating conditions. Similarly, the non-linear, dynamic forces due to wind-forcing and wake interactions are not represented in such models [6].

The mitigation of wind turbine interference is being considered from different points of view within the research community [3]. Considering radar interference during the location planning of new wind farm sites is necessary. Manufacturing and design modifications can be evaluated to reduce a wind turbine's RCS as a means of reducing radar interference. The radar system can also be modified or augmented with signal processing algorithms to reduce sensitivity to WTC. The signal processing algorithms vary drastically in technique and performance. The success of a particular method also depends, in part, on the application. These techniques can be split broadly into two categories: spatial and temporal. Spatial filters have demonstrated good performance for spatially widespread volume targets but do not perform well in the presence of scatterers that only occupy a single range-volume cell during the observation. Temporal filters can operate on a single range-volume cell but require extended acquisition times to provide sufficient data to filter the wind turbine signature. Temporal filters present challenges to operational radar systems where integration times for targets are generally on the order of milliseconds when observations on the order of seconds may be required.

Physical modifications to new turbine designs are a means of reducing the overall RCS of the wind turbines. Stealth design methodology and material selection can reduce the radar cross-section of wind turbines and therefore the overall dynamic component of WTC. One simulation result [23] shows only a 10 dB reduction in a wind turbine's RCS by applying radar-absorbing materials. Another investigation [24] suggests that an RCS reduction of more than 30 dB is possible with radar absorption materials. The first commercially available wind turbine implementing stealth technology was introduced by Vestas, and units were

planned for installation in France during 2015 [25]. However, Vestas acknowledges that the stealth turbine was developed for a specific application and is not a cost-effective solution for addressing radar interference [26].

Due to the dynamic, time-varying velocity observations of operational wind turbines, current ground clutter filtering techniques have limited effects on the overall suppression of WTC. That being said, the RCS contribution of the stationary tower and nacelle is significant, and ground clutter filtering can improve radar volume parameter estimation. From simulation, the tower's and nacelle's combined RCS can be an order of magnitude greater than the dynamic blade RCS for certain wind turbine states [11, 24]. Ground clutter filters assume a constant clutter velocity (usually zero) with a narrow spectrum width and effectively implement a band-stop filter. Adaptive clutter filter algorithms such as GMAP [27] or GMAP-TD [28] go a step further and interpolate the precipitation power spectra across the band-stop region. These algorithms assume a Gaussian precipitation spectrum model and interpolate over the band-stop Doppler velocities using the observed Doppler spectrum in the band-pass region. Given a wind turbine's time-varying spectrum in the pass-band region, the Gaussian model may be ill-suited, and the interpolation process may adversely affect results.

For volume targets, adaptive WTC detection [29] and spatial filtering methods [14, 3] have demonstrated improved radar moment estimates in the presence of WTC for scanning weather radar where meteorological length scales exceed that of the wind farm area of contamination. For large, dense wind farms, the length scales of meteorological phenomena of interest (such as mesoscale convective systems) may be within the wind turbine contamination area and therefore could be missed using such a spatial filter.

The other broadly grouped class of signal processing algorithms focuses on the temporal features of a wind turbine's RCS. For these algorithms to work, assumptions about the targets of interest (other than wind turbines) must be made. The general assumption is that the target of interest is either transient, such as an aircraft flying through the range-volume cell, or slow-varying, such as weather. An image processing technique proposed by [10] used the Radon transform to filter wind turbine blade flashes. Preliminary qualitative results show good suppression of wind turbine clutter, but the technique has not been developed further. For wind turbine observations without impulsive blade flashes, the Radon transform technique's effectiveness is significantly reduced, limiting the effectiveness to a subset of WTC-operating states. Generally, temporal filter techniques require a carefully considered set of basis functions to filter WTC. One method using basis functions represents a wind turbine's full rotation and applies a matched-filtering approach [30]. Other techniques leverage sparse-filtering methods to separate the observations into periodic and transient components [31]. In [16], separation of weather and wind turbines was considered, leveraging the group-sparsity of weather and the sparsity of the wind turbine's time-derivative. With parameter-tuning, good results were shown on coherently added precipitation and wind turbine observations. The majority of the mitigation techniques mentioned here have been demonstrated on scale models, simulation data, or synthesized weather and wind turbine observations. None of these techniques, however, can be found yet in operational environments due to the diversity and complexity of wind turbine signatures.

## 2.2. Scattering Background

Received radar echo power is from emitted or scattered electromagnetic power. In the case of radar, emitted power (not scattered echo power) is generally not wanted and considered noise. The scattered electromagnetic power of interest is from a known and well-characterized

transmitter source operating in concert with the receiver. In this section, a monostatic radar system is considered, in which the transmitter and receiver use the same antenna. Bi-static cases also exist, with the transmitter and receiver in physically separate locations.

The degree to which an object scatters an incident field is characterized by its RCS,

$$\sigma = 4\pi R^2 \frac{|E_s|^2}{|E_i|^2} \tag{1}$$

is the ratio of scattered electric field intensity $E_s$ to incident electric field intensity $E_i$, under the assumption that the backscattered power is isotropic (hence, the $4\pi R^2$), where $R$ is the range. A complex object's RCS can vary with the angle of incidence and angle of scattering (which, for a monostatic radar, are equal). The radar equation for a point scatterer [32] is

$$P_r = P_t \frac{\lambda^2 G_r^{(ant)} G_t^{(ant)}}{(4\pi)^3 R^4} \sigma, \tag{2}$$

where $\lambda$ is the radar wavelength, $R$ is the range, $\sigma$ is the RCS of the target, and $G_r^{(ant)}$ and $G_t^{(ant)}$ are the receiver and transmitter antenna gains.

For a dual-polarized radar system, the description of a scatterer requires four elements. The Sinclair matrix, $\mathbf{S}$ [33], is used to characterize a scatterer with a linear polarization basis as

$$\mathbf{S} = \begin{bmatrix} s_{hh} & s_{hv} \\ s_{vh} & s_{vv}, \end{bmatrix} \tag{3}$$

which adopts the backscatter alignment convention for monostatic radar systems. The scattering matrix elements "$s$," are denoted with appropriate subscripts to denote the received

and transmitted polarization states. The first subscript is the received, or scattered, polarization. The second subscript is the transmitted, or incident, polarization. The four-element Sinclair scattering matrix contains co-polar scattering coefficients ($s_{hh}$ and $s_{vv}$) and cross-polar scattering coefficients ($s_{hv}$ and $s_{vh}$). The cross-polar scattering coefficients are complex-conjugate pairs for a reciprocal scattering medium (which is typically the case).

A scattering volume can be represented using the same Sinclair scattering matrix [17]. Each element within the volume contributes to the overall response observed by a radar. As a first-order approximation, the volume's scattering matrix is a coherent integration of the scatterers within the volume. However, this approximation may vary from actual observations due to multiple-scattering (i.e., the signal is scattered more than once on its path from the transmitter to the receiver) within the volume. This effect may be pronounced.

The antenna pattern spatially integrates the volume, and the electric field is proportional to a voltage that is amplified, filtered, mixed, and digitized. The received power at the antenna port for uniformly distributed volume targets can be expressed as [34, 17]

$$P_r = P_t \frac{\lambda^2 G_r^{(ant)} G_t^{(ant)}}{(4\pi)^3 R^4} \left( \frac{cT_0}{2} \frac{\pi\theta_1\phi_1}{8\ln 2} R^2 \right) \bar{\eta}, \tag{4}$$

where $c$ is the speed of light, $T_0$ is the transmit duration, and $G_t^{(ant)}$ and $G_r^{(ant)}$ are the peak transmit and receiver antenna gains. Additionally, $\bar{\eta}$ is the average radar cross-section per unit of volume $V$, expressed as

$$\bar{\eta} = \frac{\sum_n \sigma_n}{V}. \tag{5}$$

An approximation to account for the antenna main-lobe integration area of narrow-beam antennas [34] is represented as $\frac{\pi\theta_1\phi_1}{8\ln 2}$, where $\theta_1$ is the antenna's one-way, elevation, -3 dB beamwidth and $\phi_1$ is the antenna's one-way, azimuth, -3 dB beamwidth.

The average RCS of water hydrometeors (i.e., rain) per unit volume is

$$\bar{\eta} = \frac{\pi^5 |K_w|^2}{\lambda^4} \frac{\sum_n D_n^6}{V}, \tag{6}$$

with $D$ being the raindrop diameter and $K_w$ the dielectric factor for water defined as $K_w = \frac{\epsilon_r - 1}{\epsilon_r + 2}$, with permittivity $\epsilon = \epsilon_r \epsilon_0$. The permittivity of water is temperature- and frequency-dependent. Because the composition and temperature of the observed volume is not known, in weather radar it is typically fixed to a constant value $|K_w|^2 = 0.934$, which corresponds to water at 10°C at 10 cm wavelength. The Sinclair scattering matrix coefficients are representative of the mean volume RCSs.

The radar equivalent reflectivity can be calculated from the average RCS as

$$Z_e = \frac{\sum_n D_n^6}{V} = \frac{\lambda^4}{\pi^5 |K_w|^2} \bar{\eta}. \tag{7}$$

The weather radar constant in Equation 4 is given with respect to the power at the antenna ports and does not account for receiver gain (or filter finite bandwidth loss). The receiver's effect can be included as

$$P_o = P_r \left( \frac{G_r}{l_r} \right), \tag{8}$$

where $G_r$ is the receiver gain and $l_r$ the finite bandwidth loss factor. For a monostatic radar system receiving and transmitting the same polarization, $G_t^{(ant)} = G_r^{(ant)} = G_0$. The received power is related to the volume's reflectivity by

$$P_o = \left( \frac{cT_0}{2} \right) \left( \frac{G_r}{l_r} \right) \left( \frac{\lambda^2 P_t G_0^2}{(4\pi)^3} \right) \left( \frac{\pi \theta_1 \phi_1}{8 \ln 2} \right) \left( \frac{\pi^5 |K_w|^2}{\lambda^4 R^2} \right) Z_e, \tag{9a}$$

which simplifies to

$$P_o = \frac{CZ_e}{R^2}, \tag{9b}$$

where the weather radar constant is

$$C = \frac{G_r P_t G_0^2 \pi^3 |K_w|^2 c T_0 \theta_1 \phi_1}{l_r \lambda^2 1024 \ln 2}. \tag{10}$$

This relationship provides a means for calculating reflectivity from received power. In addition, $Z_e$ is in units of $mm^6/m^3$, which requires a scale factor to be applied $(10^{-3})^6$ to calculated reflectivity in its appropriate units.

2.2.1. Specular Reflections. For objects with electrically large dimensions ($L >> \lambda$), specular reflection results in large magnitude radar cross-sections compared to observations at oblique angles of incidence/scattering. Consider an object with a size much greater than a radar's wavelength. The object can be thought of as a collection of distributed scattering phase centers. The coherent integration of all the scattering phase centers is less than or equal to the incoherent integration of all phase centers by the Cauchy-Shwarz inequality. A specular reflection occurs when the coherent and incoherent integrated powers are equal and, when all scatterers have equal phases, results in the maximum backscattered power.

To further illustrate the specular scattering effect, consider a simple model of a wind turbine blade. The wind turbine blade can be modeled as a thin wire that is rotated about an axis perpendicular to the direction of observation. Assume each point on the wire is an isotropic scatterer (with unity amplitude) with the same (constant) phase at $t = 0$. This gives $A(\theta, r) = 1$, where $\theta$ is the rotation angle of the wire and $r$ is the radial distance to the scattering point. The wave number is $k = \omega_c \sqrt{\epsilon \mu}$. For free space, the wave number is $k_0 = 2\pi f_c / c = 2\pi / \lambda_0$. Following the method in [12], assuming far-field observations (the

incident and scattered fields are plane waves), the scattered field of the wire wind turbine blade can be modeled as

$$e_s(\theta) = \int_0^L A(\theta, r) e^{jk_0 2r\sin(\theta)} dr. \tag{11}$$

Equation 11 assumes a uniform incident plane wave and a constant isotropic coupling factor for each element of the wire. For an impinging plane wave that is then scattered, the wave has to travel twice the distance, which is accounted for by the $2r\sin(\theta)$ term. The scattered field from Equation 11 simplifies to

$$e_s(\theta) = \frac{e^{j\beta L} - 1}{j\beta}, \tag{12}$$

where $\beta = \frac{2\pi}{\lambda_0} 2\sin\theta$. The amplitude of the scattered field is

$$|e_s(\theta)| = \sqrt{\frac{\cos(\beta L) + j\sin(\beta L) - 1}{j\beta} \frac{\cos(\beta L) - j\sin(\beta L) - 1}{-j\beta}} \tag{13a}$$

$$= \sqrt{\frac{2 - 2\cos(\beta L)}{\beta^2}} \tag{13b}$$

$$= \left| \frac{2\sin(\frac{\beta L}{2})}{\beta} \right|. \tag{13c}$$

Equation 13 is undefined for $\theta$ equal to integer multiples of $\pi$. In the limit at $\theta = n\pi$, where $n$ is an integer, $|e_s(\theta)|$ is equal to the integration length $L$. To normalize the response to a maximum amplitude for specular angles (i.e., multiples of $\pi$), Equation 13 can be divided by the length $L$, giving

$$|e_s(\theta)| \propto \left| \frac{2\sin(\frac{\beta L}{2})}{L\beta} \right|. \tag{14}$$

The coherently integrated observation of all scatterer phase centers of the wire model has a mean phase center located at $L/2$ with amplitude $|e_s(\theta)|$. If the reflectivity weighting function, $A(\theta, r)$, changes with angle $\theta$, this results in a moving phase center that also varies with angle $\theta$ and manifests as additional velocity variation. The rotation angle can be calculated by $\theta = \dot{\theta}t$, where the rotation rate, $\dot{\theta}$, is in radians per second. To convert from rotation rate in revolutions per minute (RPM) to $\dot{\theta}$,

$$\dot{\theta} = RPM \cdot \frac{2\pi}{60}. \tag{15}$$

2.2.2. Doppler Velocity. Doppler shift is a well-understood phenomenon readily observed in acoustics. It affects electromagnetic radiation, including that used in radar. In pulsed Doppler radar systems, estimation of a scatterer's radial velocity is possible; however, it does not rely directly on the Doppler frequency shift. Instead, the Doppler velocity is estimated by comparing the object's position at two instances in time. The difference in the object's position is measured by the phase shift between the two observations, which is related to physical distance by the radar's wavelength. The Doppler velocity is simply the ratio of distance over time and is unambiguous for phase shifts from 0 to $2\pi$, corresponding to a physical distance equal to one wavelength for a phase shift of $2\pi$.

The electromagnetic radiation Doppler frequency shift, $f_d$, for a stationary observer in free space [35] is

$$f_d = f_c \left( \frac{c - v}{c + v} - 1 \right) \tag{16a}$$

and

$$f_d \approx f_c \frac{2v}{c} \approx \frac{2v}{\lambda_c}, \tag{16b}$$

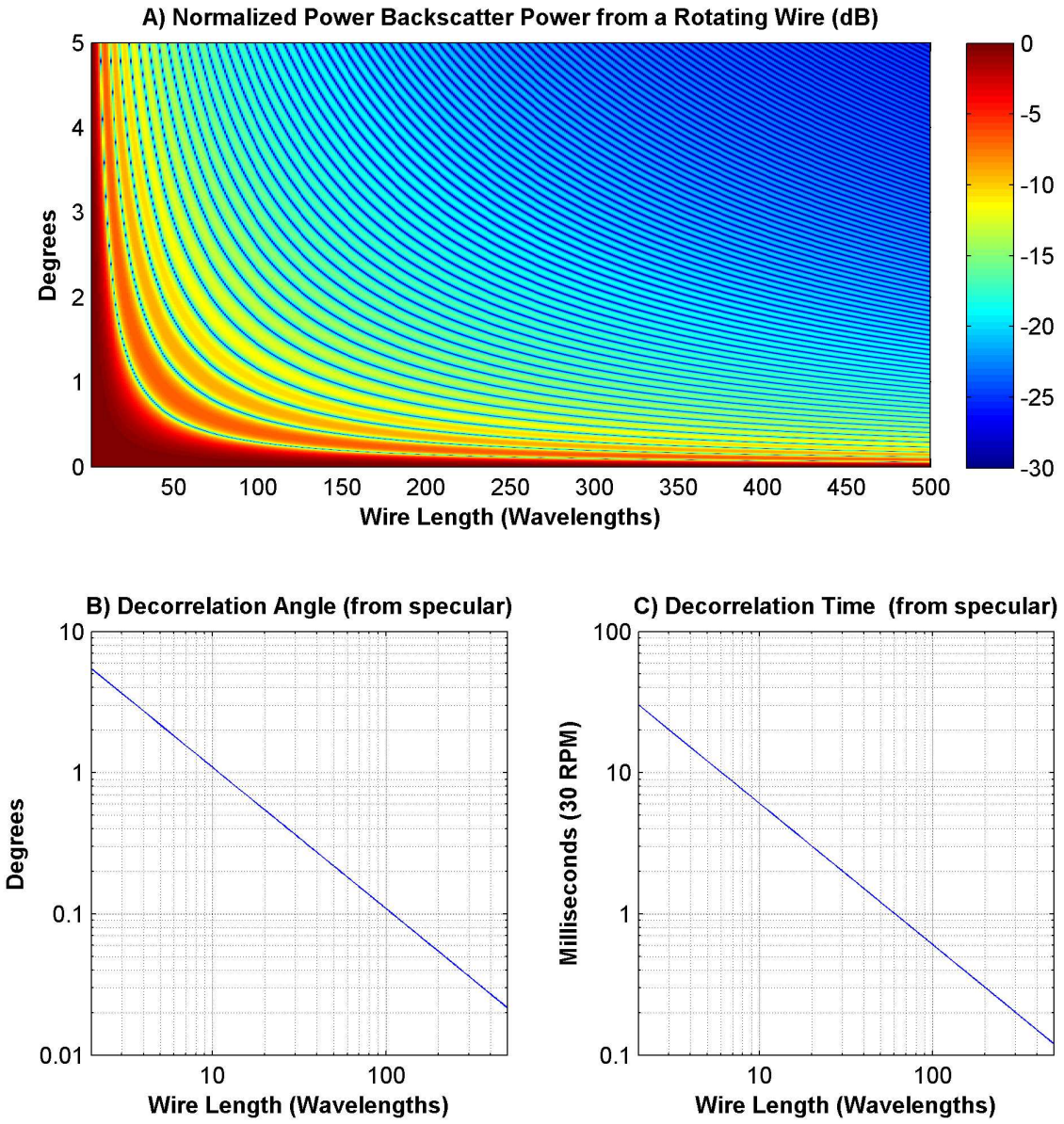


FIGURE 2.1. Normalized RCS for a rotating wire without accounting for projection. The decorrelation angle, referenced to the specular angle, is shown in degrees (Graph B) and decorrelation time (Graph C). A 30 RPM rotation rate is selected for the estimation of decorrelation time. The decorrelation angles and times are the points where the RCS decreases to $e^{-0.5} = 60.7\%$.

where $c$ is the speed of light and $v$ is the target velocity (positive toward the observer).

Radar observations of a point-scatterer target can be modeled as

$$e_{rf} = ae^{j2\pi f_c t} e^{j2\pi f_d t} e^{j\phi}, \tag{17}$$

where $a$ is an amplitude scale factor, $f_c$ is the carrier frequency, and $\phi$ is the scatterer's phase. The radio frequency is demodulated to the base-band frequency to give the base-band signal representation as

$$e_{bb} = e_{rf} e^{-j2\pi f_c t} = a e^{j2\pi f_d t} e^{j\phi}. \tag{18}$$

In Doppler radar systems, Doppler velocity is estimated using successive pulses separated in time by a pulse repetition period ($T_s$). Consider two such pulses, one at $t_0$ and one at $T_s$ time later, given by

$$e_0 = a_0 e^{j2\pi f_{d_0} t_0} e^{j\phi_0} \tag{19a}$$

and

$$e_1 = a_1 e^{j2\pi f_{d_1}(t_0+T_s)} e^{j\phi_1}, \tag{19b}$$

where $a_0$ and $a_1$ are real-valued, positive amplitudes. The Doppler velocity is estimated from the lag-$T_s$ covariance, $r[T_s]$, of the observations. For the two pulses, the lag-$T_s$ covariance is

$$r[T_s] = e_1 e_0^* = a_1 e^{j2\pi f_{d_1}(t_0+T_s)} e^{j\phi_1} a_0 e^{-j2\pi f_{d_0} t_0} e^{-j\phi_0}, \tag{20a}$$

which simplifies to

$$r[T_s] = a_1 a_0 e^{j2\pi\left(f_{d_1}(t_0+T_s) - f_{d_0} t_0\right)} e^{j(\phi_1-\phi_0)}. \tag{20b}$$

If the scattering object is not accelerating, then the Doppler velocity for both samples is equal, $f_d = f_{d_0} = f_{d_1}$, and, if the backscatter phase is constant ($\phi = \phi_0 = \phi_1$), Equation 20

reduces to

$$r[T_s] = a_1 a_0 e^{j2\pi f_d T_s}. \tag{21}$$

To convert the covariance to a velocity, use

$$v = \arg\left(r[T_s]\right) \frac{-\lambda}{4\pi T_s} = \frac{f_d \lambda}{2}, \tag{22}$$

which is a standard method of estimating Doppler velocity in radar systems. The convention here is that a positive velocity is away from the radar, hence the minus sign. Modulation of the amplitude is also impressed on the observed Doppler velocity. If the amplitude is time-varying, it can be represented as a complex-valued, time-varying function, $A = |A_0|e^{j\omega_a t}$, where $\omega_a$ can be a function of $t$.

For small velocities, the Doppler shift is also small and generally neglected, giving

$$\frac{f_d}{f_0} \approx \frac{2v}{c} \approx 0. \tag{23}$$

The implication is that the instantaneous Doppler shift can be assumed to be zero without a loss of accuracy. Estimation of the Doppler velocity can be made using time-separated pulses, where the velocity is derived from a change in distance represented as a phase shift. This also highlights other potential sources of perceived Doppler velocity, including changes in acceleration or changes in observed scatterer phases (or the transmit phase). The observed scatterer phase can change due to RCS-weighted projection, which amounts to a change in the phase center of the scattering body.

## 2.3. Radar Systems

Pulsed Doppler radar systems are commonly used for weather surveillance and air traffic control. A typical dual-polarization radar system block diagram is shown in Figure 2.2. At the highest functional level, a radar system is composed of transmitter and receiver subsystems. Weather and air surveillance pulsed radar systems are typically used in a monostatic configuration to reduce complexity, cost, and space. The radar electronics for weather radar and ASR are fundamentally similar, but the operational requirements and mission of the two radar applications are different. ASR systems are operated in the vicinity of airports for air traffic control.

The ASR-9 [36] and ASR-11 systems allow for the transmission of vertical, linear polarization or right-hand, circular polarization. For receiving, the ASR-9 and ASR-11 can observe either the co-polar signals (the same polarization that was transmitted) or cross-polar signals (horizontal for linear polarization or left-hand for circular polarization). The ASR-9 and ASR-11 antennas also have two antenna patterns available for receiving (low beam and high beam) that weight echoes differently from the lowest elevations [37]. The ASR system's antenna has a "fan beam" that is parabolic (in dB), with a 1.4-degree beamwidth in azimuth and an approximately cosecant-squared shape (in dB), with a 5-degree half-power beamwidth in elevation [37]. The antenna rotation rate is 12.5 RPM [37] for the ASR systems. Operationally, the circular polarization mode is used when weather is present because it is affected less by precipitation than linear polarization [17].

The pulse-repetition frequency (PRF) used for S-band ASR-9 and ASR-11 systems is approximately 1 kHz (average PRF). A 9/7 ratio multi-PRF scheme is used for ASR systems with 10 pulses for the shorter pulse repetition period (PRT) and 8 pulses for the longer PRT, resulting in an integration time of approximately 18 milliseconds. A full 1.4-degree

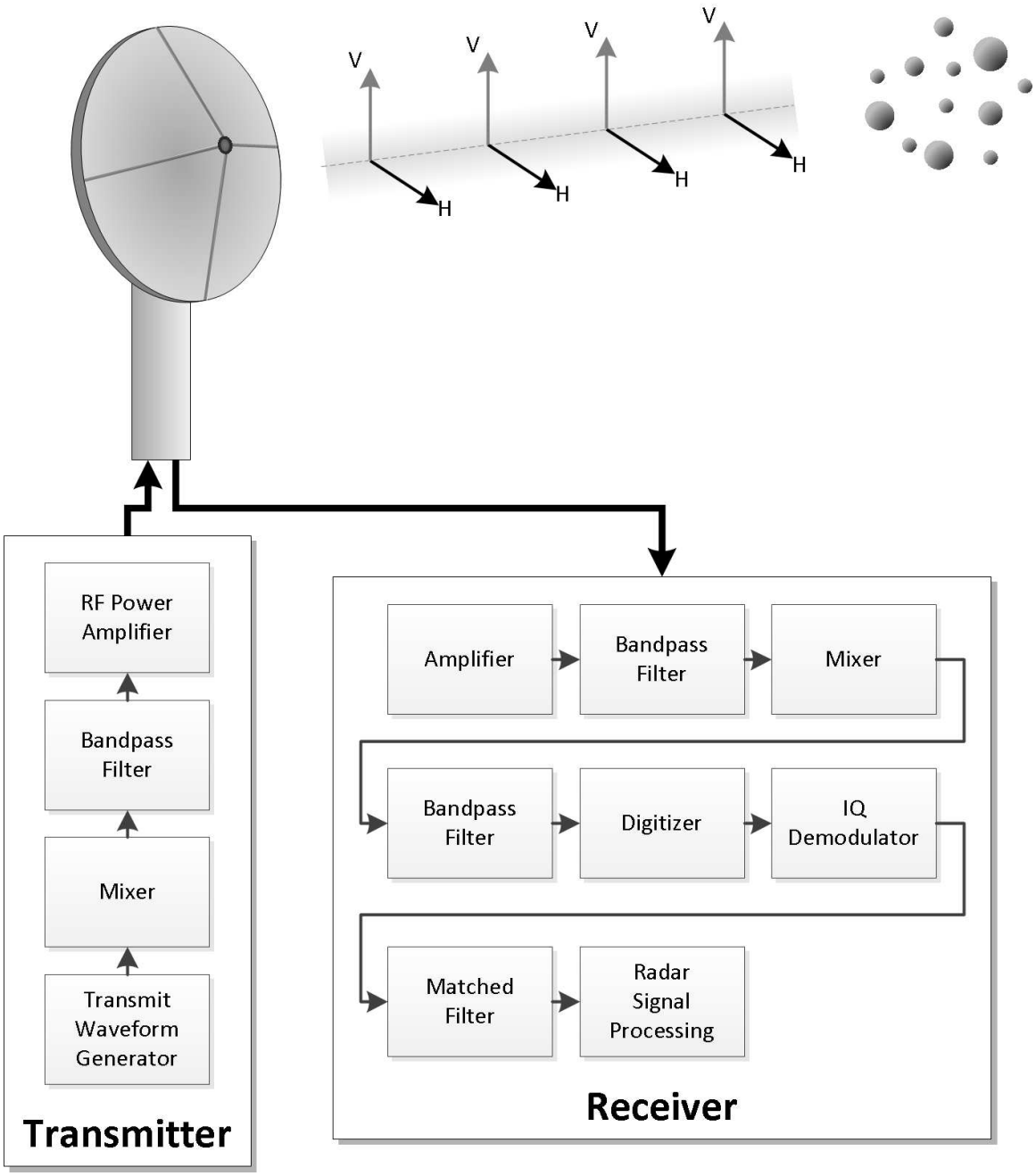


FIGURE 2.2. A block diagram of a typical dual-polarization monostatic radar system. The basic components of the transmitter and receiver are included.

beamwidth has approximately 21 pulses, of which only 18 are processed [36]. The ASR-9 and ASR-11 observe ranges up to 111 km, with a 230-meter range resolution.

The U.S. national weather radar system, the NEXRAD WSR-88D, completed the upgrade to dual-polarization in the summer of 2013. Other weather radar systems are available

within the U.S. and are operating at a range of frequencies, but all follow similar operating and design principles. Weather radar antennas are designed for a "pencil beam" with a parabolic pattern (in dB) and equal azimuth and elevation beamwidths, typically between 0.5 and 3 degrees. The NEXRAD WSR-88D radars have a 0.95-degree beamwidth [37]. Scanning weather radar integration times are typically on the order of 30-100 milliseconds, and rotation rates are generally less than 4 RPM. The NEXRAD system's rotation rate is 18 degrees per second (or 3 RPM), and it completes a typical volume scan in 4.5, 5, 6, or 10 minutes, depending on the volume coverage pattern selected [20]. The NEXRAD "Super Resolution" data resolves range-volume cells of 0.5 degrees in azimuth and 250 meters in range. Scanning rates and integration periods can deviate from the typical ranges for specific weather radar applications, such as those requiring high spatial update rates for severe weather characterization.

Consider two different time-scales: fast-time (or range-time) and slow-time (or pulse-time). The fast-time sampling is the sampling of the radar echo in range. For weather radar, a typical value is an $f_s = 1$ MHz sample rate, corresponding to a 150-meter range resolution. For a given time delay, $\tau$, after the radar pulse transmission time $t_0$, the radar will sample at a range of $\tau/c$, where $c$ is the speed of light. The bandwidth of the transmitted pulse and receiver filter dictates the range bin's "size," which is determined by $\Delta r = \frac{c}{2f_s}$.

For a given PRT, the radar's unambiguous range and unambiguous velocity can be calculated. The maximum possible unambiguous range is calculated as

$$r_{max} \leq \frac{c}{2T_s}, \tag{24}$$

and the maximum unambiguous velocity (for a uniform pulse scheme) is

$$v_{max} = \pm \frac{\lambda}{4T_s}. \tag{25}$$

For multi-PRF observations, the effective PRT can be substantially reduced, enabling unambiguous velocity estimation at higher velocities than is possible for a uniform PRT at the same average PRT. For example, a staggered PRT (alternating the PRT on each pulse) using 1 and 1.5 milliseconds gives an average PRT of 1.25 milliseconds and provides an effective PRT for velocity estimation of 0.5 milliseconds using Equation 25.

The observation range-volume cells are determined by a "range window" and "antenna window." The range window function is determined by the transmit pulse and the receiver filter's impulse response. The center of the range window is determined by the receiver's sampling delay. The transmit pulse, receiver filter, and receiver's sampling frequency are designed as a complete system for optimal performance. The range window size and sample delay are of interest. If the sample delay is varied, the observed volume moves in range. A 1-microsecond rectangular pulse with matched receiver filter represents a 150-meter range integration volume. If the received signal is sampled at 1-microsecond intervals, each range volume is independent (neglecting multi-path reflections and assuming propagation in free space). The transmit pulse and receiver filter implement a range window. The receiver sampling delay, relative to the transmit pulse's start time, determines the range volume that is sampled.

The radar's antenna pattern has an angle-dependent gain and phase that determines the antenna's windowing effect. The antenna's -3 dB beamwidth characterizes the angular extent of the half-power antenna pattern mainlobe. It is generally assumed that the gain and phase of the antenna is approximately constant and neglected. The mainlobe antenna

gain pattern for a parabolic antenna is approximated by a parabola in the decibel scale. For a 1-degree, -3 dB, two-way beamwidth, the width of the range-volume cell is approximately 175 meters at 10 km and 873 meters at 50 km. It is apparent that even with short range-window lengths, the beamwidth can be an order of magnitude larger (or more). It should also be considered that large-magnitude RCS targets outside of the antenna's mainlobe can still make a non-trivial echo contribution to the observed echo power.

The scan rate, antenna beamwidth, and observation accuracy effectively determine the radar signal integration time. For meaningful results, the integration time should be set so that observations within the integration volume fulfill the wide-sense stationary assumption. When scanning, the observation volume changes from pulse to pulse. For neighboring pulses, the volume is almost identical, but as time increases, there is less and less overlap of the observed volume. As with changes in range, for non-overlapping volumes, the samples are independent. The radar integration time is limited by the coherency of the observed volume and can be approximated by

$$N = \frac{B}{\dot{\theta}_a \cdot T_s}, \tag{26}$$

where $B$ is the radar's antenna beamwidth in degrees, $\dot{\theta}_a$ is the antenna scan rate in degrees per second, and $T_s$ is the average pulse repetition period in seconds. If the observed volume changes substantially during the integration time, the underlying observed processes may be unrelated (i.e., independent), and the resulting coherent integration will yield noise-like results.

In weather radar systems, the integration times also take into account a desired standard deviation of the measurement. Typically, the goal is for reflectivity estimates to be accurate

TABLE 2.1. Dual-polarization radar operating modes and the measured Sinclair scattering matrix components.

| Mode | $s_{hh}$ | $s_{vv}$ | $s_{vh}$ | $s_{hv}$ |
|---|---|---|---|---|
| **Simultaneous** | √ | √ | | |
| **Alternate** | √ | √ | √ | √ |
| **H-Only** | √ | | √ | |
| **V-Only** | | √ | | √ |

to within 1 dB and differential reflectivity to be accurate to within 0.2 dB. Assuming perfect system calibration, these standard deviations can be determined for expected spectrum widths and integration times [17].

The scanning effect acts to window the observed volume with the complex antenna pattern. The convolution of the antenna pattern effect due to scanning a radar target effectively adds a spectral broadening effect and possible velocity bias. Additional spectral broadening is introduced from scanning by microphysical differences in the sampled volume between successive pulses.

2.3.1. DUAL-POLARIZED DOPPLER WEATHER RADAR. In realizing a linearly dual-polarized radar system, at most four modes of operation are available. The modes, which are summarized in Table 2.1, are simultaneous-transmit and simultaneous-receive (sim mode, simultaneous mode, or STAR mode for short), alternate-transmit and simultaneous-receive (alt mode, alternate mode, or ATSR for short), H-pol-transmit and simultaneous-receive (H-only or HTSR for short), and V-pol-transmit and simultaneous-receive (V-only or VTSR). A diagram of the transmit waveforms is shown in Figure 2.3. In the case of a linearly polarized weather radar, these are denoted with the subscripts "h" and "v" to distinguish H-polarization and V-polarization, respectively.

A complete linear polarization characterization provides a more detailed representation of the volume being sampled by a radar. The NEXRAD dual-polarization upgrade implements simultaneous mode operation, ideally with a 45-degree linear polarization wave (i.e., equal

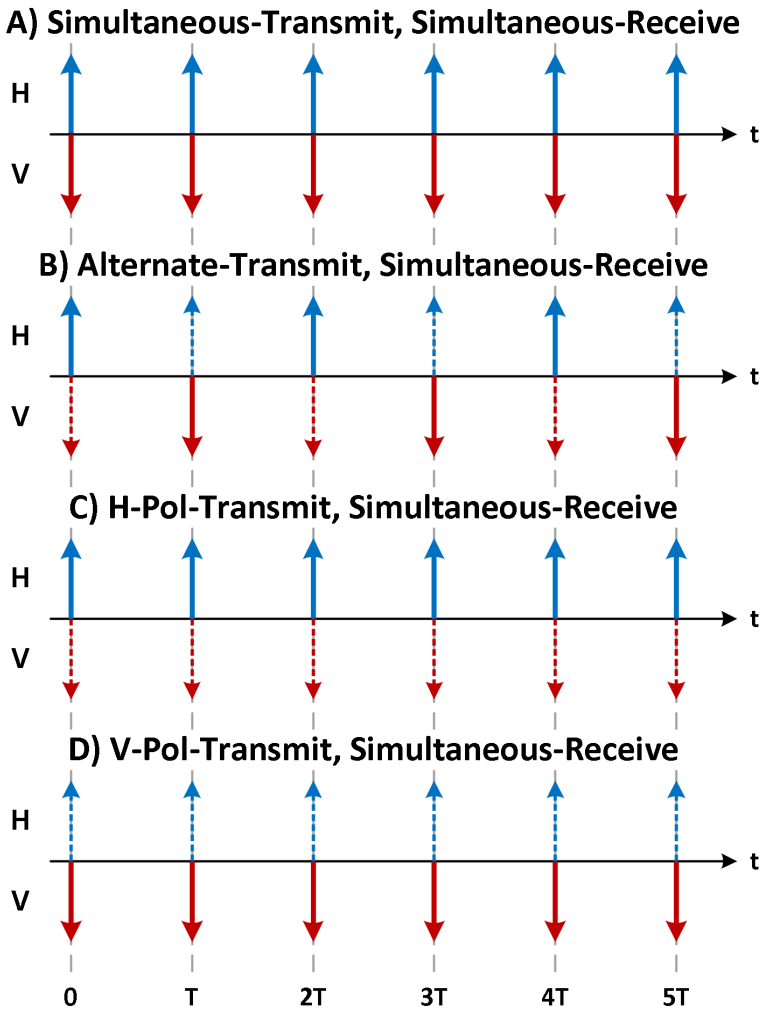


FIGURE 2.3. A graphical representation of the four dual-polarization radar operation modes with a uniform pulse repetition period ($T_s$). Solid colored lines represent the transmitted polarization state, which is also received (the co-polar observation). The dashed lines represent the polarization state that is in receive-only mode (the cross-pol observation).

magnitude and phase for both H- and V-polarizations). This implementation is typical of most dual-polarization radar systems to reduce costs and complexity. A single transmitter can be used with a power splitter, enabling the simultaneous transmission of both polarizations. In simultaneous mode, the cross-polar signal is generally orders of magnitude less than the copolar signal power. As such, the cross-pol signal is neglected for simultaneous mode operations.

TABLE 2.2. Characteristics of the CSU-CHILL S-band radar [38] (with S-band-only feed horn) located in Greeley, Colorado.

| | |
|---|---|
| **Antenna** | |
| Diameter | 8.5 m |
| Gain | 43 dBi |
| Beamwidth | 1.0 degree |
| LDR Limit | -42 dB |
| Max Scan Rate | 18 degrees/sec |
| **Transmitter** | |
| Type | Dual Klystron |
| Wavelength | 11.01 cm (2.725 GHz) |
| Peak Power | 1 MW (each polarization) |
| Pulse Repetition Period | 800 - 12000 $\mu$s |
| Pulse Width | 0.2 - 1.6 $\mu$s |
| Max Duty Cycle | 0.16% |
| **Receiver** | |
| Digitizer | 14 bits @ 40 MHz |
| Sensitivity | -38 dBZ @ 1 km |
| Noise Power | -113 dBm @ 1 MHz bandwidth |
| Range Resolution | 150 m (30 m minimum) |
| Max Range Gates | 6000 |

2.3.2. CSU RADAR SYSTEMS. The wind turbine observations presented throughout this dissertation were collected using two Colorado State University (CSU) radar systems. The first radar system considered is the CSU-CHILL, radar located in Greeley, Colorado [38]. This radar is a state-of-the-art, dual-polarized, Doppler weather radar with S-band and X-band capability. Its dual-offset Gregorian antenna reduces antenna cross-pol contamination and antenna sidelobes compared to more traditional center-fed, parabolic antenna. The relevant performance characteristics of the S-band system are included in Table 2.2. The CSU-CHILL S-band radar system can operate in all dual-polarization configurations.

In addition to the CSU-CHILL S-band radar, CSU has a portable X-band dual-polarization weather radar system. The relevant technical details of this simultaneous-transmit and simultaneous-receive radar are shown in Table 2.3. This portable radar facilitates targeted radar observations in different locations as science and operational conditions require. The

TABLE 2.3. Characteristics of the CSU portable X-band research radar.

| | |
|---|---|
| **Antenna** | |
| Diameter | 1.8 m |
| Gain | 42 dBi |
| Beamwidth | 1.4 degree |
| Max Scan Rate | 60 degrees/sec |
| **Transmitter** | |
| Type | Magnetron |
| Wavelength | 3.2 cm (9.40 GHz) |
| Peak Power | 18 kW (total) |
| Pulse Repetition Frequency | 3.0 kHz (max.) |
| Max Duty Cycle | 0.12% |
| **Receiver** | |
| Digitizer | 14 bits @ 200 MHz |
| Range Sampling | 1.5 - 192 m |

X-band radar was deployed at the NREL's NWTC in Louisville, Colorado during November and December of 2015 for intensive observation of research wind turbines.

2.3.3. RADAR TIME SERIES ANALYSIS. After the received echo power is suitably demodulated to base-band and filtered, the echo power is sampled. Any observed frequency at base-band is due to a Doppler frequency shift or target variation. The resulting in-phase and quadrature (IQ) base-band echo signals are ready for further processing. The complex-valued echo signal's variance is the signal's power. This IQ signal is used in all radar parameter estimations. For a dual-polarized radar, two time series of IQ data are available, one for each polarization state. Weather radar signal processing as it relates to radar IQ observations will be discussed in more detail in Section 2.3.4.

A strict-sense stationary process is a stochastic process whose statistical moments do not change with time. The random process can be completely represented, without loss, by these statistical moments. Wide-sense stationary is a weaker form of strict-sense stationary, and only the first- and second-order statistical moments are required to be constant with time. Stationary processes enable the estimation of the statistical moments of a sampled

process by averaging in time. A process is ergodic when samples in time can be used in place of different realizations of the same process. This is fundamental to the theory of radar moment estimation (although the sampled volume may not truly meet the requirements to be wide-sense stationary).

To analysis a wide-sense stationary process, only the mean ($\mu$) and variance ($\sigma^2$) are required (up to second-order moments). The IQ signal is a zero-mean process; therefore, only the variance needs to be estimated. For discrete random processes $\mathbf{x}$ and $\mathbf{y}$, the cross-covariance of the processes is

$$r_{xy}[t, T] = cov(\mathbf{x}(t+T), \mathbf{y}(t)) = \mathbb{E}\left[\mathbf{x}(t+T)\mathbf{y}^*(t)\right], \tag{27}$$

where $\mathbb{E}$ is the expectation and $^*$ denotes complex conjugation. The autocorrelation of $\mathbf{x}$ can be calculated with $\mathbf{y} = \mathbf{x}$. The radar observation volume is characterized by the autocovariance and cross-covariance of the two polarizations. The autocovariance function is estimated from radar observation $\mathbf{x}$ with an integration period of $N$ samples, assuming it is wide-sense stationary, as

$$\hat{r}_{xx}[h] = \frac{1}{N} \sum_{t=0}^{N-h-1} \mathbf{x}[t+h]\mathbf{x}^*[t]; \quad 0 \leq h < N. \tag{28}$$

This definition of autocovariance is biased for a finite number of samples but is defined to ensure the sample function is a valid autocovariance [17]. It is equivalent to applying a triangle window to the autocovariance estimated using the mean of the number of samples at the time-lag considered.

From radar observations, estimates of the intrinsic scattering matrix parameters can be made. Time averages over a short duration are considered where the physical process being observed is wide-sense stationary. For an estimate of the four parameters of the scattering

matrix, $\mathbf{S}$, the radar operates in an alternating transmission mode. In this mode, for even-numbered pulses, one polarization is transmitted, and for odd-numbered pulses, the other polarization is transmitted. For all pulses, both polarizations are received. A uniform PRT, $T_s$, is considered. Using an alternating transmission mode, the complex-valued received voltage vector is represented as

$$\mathbf{x}_{alt} = \begin{bmatrix} e_{hh}[t] & e_{vh}[t] & e_{hv}[t+T_s] & e_{vv}[t+T_s] \end{bmatrix}^T, \tag{29}$$

which contains observations of the four scattering matrix parameters. From the received voltages, complex powers can be estimated by coherently averaging over the integration period with $N$ samples. For a uniform sampling period, assuming that $e_{hh}$ and $e_{vh}$ are observed at even time periods, $n = 2mT_s$, where $n$ is the pulse number and $m$ is the pulse pair number. Parameters $e_{vh}$ and $e_{vv}$ are observed at odd time periods, with $n = (2m+1)T_s$. The complex power matrix for the observations is given by

$$\mathbf{P}_{xx}^{(alt)} = \langle \mathbf{x}_{alt} \mathbf{x}_{alt}^H \rangle = \begin{bmatrix} P_{hh,hh}[0] & P_{hh,vh}[0] & P_{hh,hv}[T_s] & P_{hh,vv}[T_s] \\ P_{hh,vh}^*[0] & P_{vh,vh}[0] & P_{vh,hv}[T_s] & P_{vh,vv}[T_s] \\ P_{hh,hv}^*[T_s] & P_{vh,hv}^*[T_s] & P_{hv,hv}[0] & P_{hv,vv}[0] \\ P_{hh,vv}^*[T_s] & P_{vh,vv}^*[T_s] & P_{hv,vv}^*[0] & P_{vv,vv}[0] \end{bmatrix}, \tag{30}$$

where $^H$ represents the complex-transpose operation. The covariances, $P$, are observed at two different time-lags (0 and $T_s$), and not all covariance estimates are observed at both time-lags. For a wide-sense stationary process, the matrix is conjugate-symmetric, and $P^*[T_s] = P[-T_s]$. These considerations are used in the construction of Equation 30. The resulting covariance matrix $\mathbf{P}_{xx}^{(alt)}$ yields 10 unique elements. For $N$ finite samples, the

estimates can be averaged over an integration period, with $M = N/2$ sets available to estimate $\widehat{\mathbf{P}_{xx}^{(alt)}}$.

Similarly, for simultaneous mode, the observed polarimetric parameters are

$$\mathbf{x}_{sim} = \begin{bmatrix} e_{hh}[t] & e_{vv}[t] \end{bmatrix}^T, \tag{31a}$$

and the resulting covariance matrix for simultaneous mode observations is

$$\mathbf{P}_{xx}^{(sim)} = \langle \mathbf{x}_{sim} \mathbf{x}_{sim}^H \rangle = \begin{bmatrix} P_{hh,hh}[0] & P_{hh,vv}[0] \\ P_{hh,vv}^*[0] & P_{vv,vv}[0] \end{bmatrix}. \tag{31b}$$

For H-only observation mode, the observed polarimetric parameters are

$$\mathbf{x}_{Honly} = \begin{bmatrix} e_{hh}[t] & e_{vh}[t] \end{bmatrix}^T, \tag{32a}$$

and the H-only observation covariance matrix is

$$\mathbf{P}_{xx}^{(Honly)} = \langle \mathbf{x}_{Honly} \mathbf{x}_{Honly}^H \rangle = \begin{bmatrix} P_{hh,hh}[0] & P_{hh,vh}[0] \\ P_{hh,vh}^*[0] & P_{vh,vh}[0] \end{bmatrix}. \tag{32b}$$

The observation matrices give insight into the possible polarimetric information available for the various modes of operation. Without compensating for system gains (or losses), the measurements are relative to system-specific gains. This relative value can be converted to an absolute measurement (such as watts) by multiplying by the system-specific gain factor. In practice, the estimation of scattering parameters from radar observations requires replacing the ensemble average with a suitable time average (assuming an ergodic process) and multiplying by the appropriate radar constant.

In some cases, it is desirable to use spectral representations of radar parameters for parameter estimation and observation analysis [17, 39]. The short-time Fourier transform (STFT) of the signal $x$, with window function $w$, is defined as

$$\mathrm{STFT}\{\mathrm{x(t)}\}(\tau,\omega) \equiv \mathrm{X}(\tau,\omega) = \int_{-\infty}^{\infty} \mathrm{x(t)w(t-\tau)e^{-j\omega t}dt}, \tag{33a}$$

where $\tau$ and $\omega$ are the time delay and Doppler frequency, respectively. The magnitude-squared of the STFT yields an estimate of the spectrogram:

$$\mathrm{spectrogram}\{\mathrm{x(t)}\}(\tau,\omega) \equiv \mathrm{S}(\tau,\omega) = \left|\mathrm{X}(\tau,\omega)\right|^2, \tag{33b}$$

where for any $\tau$, the "instantaneous" spectra is termed an energy spectral density (ESD). The term ESD is used instead of power spectral density (PSD) to emphasize that the underlying process may be non-stationary and the PSD may not be constant during the observation period. The spectrogram is an intuitive basis on which to characterize a wind turbine, given that the time-varying Doppler velocity signatures are of interest.

The ESD for a $N$-length, windowed observation of $x$ can be estimated with the discrete Fourier transform (DFT) as

$$S[t,k] = \left|\frac{1}{\sqrt{N}} \sum_{n=0}^{N-1} x[t+n]w[n]e^{-j2\pi kn/N}\right|^2, \tag{34}$$

where $w$ is an appropriate taper function [40]. The frequency resolution of the Doppler spectrum, $\Delta f$, is inversely proportional to the number or samples used, $N$, by

$$\Delta f = \frac{f_s}{N}, \tag{35}$$

where $f_s$ is the sample frequency.

2.3.4. Meteorological Radar Parameters. For weather radar, radar parameters are calculated directly from the covariance estimates. Using combinations of magnitudes and phases of the covariance estimates at different time-lags, a radar volume can be characterized. The radar parameters of interest correspond to microphysical properties of the observed volume. For an incoherent radar system (i.e., no Doppler capability), with no polarization diversity or only a single polarization, reflectivity ($Z$) and spectrum width ($w$) can be estimated. Reflectivity is proportional to the mean radar cross-section in a volume with units $mm^6/m^3$ and assumes water hydrometeors in the Rayleigh scattering regime. For a dual-polarization radar, the horizontal reflectivity is

$$Z_h = 10\log_{10}\left(|r_{hh}[0]|^2\right) - C_h + 20\log_{10}(R), \tag{36}$$

and similarly, the vertical reflectivity is

$$Z_v = 10\log_{10}\left(|r_{vv}[0]|^2\right) - C_v + 20\log_{10}(R), \tag{37}$$

where $C$ is the radar constant from Equation 10, with subscripts denoting the appropriate polarization, and $R$ is the range in meters.

The spectrum width, in meters per second, provides insight into the range of velocities within a volume. For large spectrum widths, the decorrelation time within a volume is lower, implying that shear, vorticity, or turbulence may be significant within the volume. It should be noted that spectrum width may be estimated without coherency between the transmitter and receiver (i.e., without Doppler capability):

$$w = \sigma_v = \frac{\lambda}{2\pi T_s\sqrt{2}}\left(\ln\left|\frac{r_{hh}[0]}{r_{hh}[T_s]}\right|\right)^{\frac{1}{2}}. \tag{38}$$

If Doppler capability is available, the radial Doppler velocity, $\bar{v}$, of the volume can be estimated by comparing the phase of successive samples as

$$\bar{v} = \frac{-\lambda}{4\pi} \arg\left(r_{hh}[T_s]\right), \tag{39}$$

where the unambiguous Doppler velocity limits are determined by the radar wavelength and PRT $T_s$ as

$$v_{amb} = \pm \frac{\lambda}{4\pi T_s}. \tag{40}$$

For dual-polarized weather radar, a number of meteorologically significant parameters are used to describe the observed volume [17]. The dual-polarization parameters include differential reflectivity ($Z_{dr}$), differential phase ($\phi_{dp}$), and copolar correlation ($\rho_{hv}$ or $\rho_{co}$). For alternate mode and H-only mode, an additional dual-polarization parameter, the linear depolarization ratio (LDR), can be estimated. Additional variables have been proposed beyond those noted here, but these are the basic radar parameters found in most dual-polarization weather radars (with LDR not available to a radar operating in simultaneous mode). Dual-polarization radar observations are a significant advance over single polarization observations, providing further insight into the microphysical structure of the scatterers.

Differential reflectivity is the ratio of the H-pol to V-pol reflectivity:

$$Z_{dr} = \frac{Z_h}{Z_v}. \tag{41}$$

The differential reflectivity provides an estimate of the aspect ratio of the particles. If the radar constants for both polarizations are equivalent, the magnitudes of H-pol-received power

and V-pol-received power can be used:

$$Z_{dr} = 10 \log_{10} \left( \frac{|r_{hh,hh}[0]|^2}{|r_{vv,vv}[0]|^2} \right). \tag{42}$$

Differential phase, $\phi_{dp}$, is the phase difference between H-pol and V-pol observations and is calculated as

$$\phi_{dp} = \frac{180}{\pi} \arg \left( r_{hh,vv}[0] \right). \tag{43}$$

The propagation of one polarization can be slower than another due to the physical structure of precipitation. Larger raindrops are bigger on the horizontal axis than the vertical axis, which results in a slight increase in the effective permittivity of the horizontal-propagating wave and, therefore, a slower effective speed of light. This results in a differential phase shift due to propagation in precipitation. A backscattering phase shift is also included in the observation of $\phi_{dp}$.

The copolar correlation coefficient, $\rho_{hv}$, is the cross-correlation of H-pol and V-pol observations and is represented as

$$\rho_{hv} = \frac{|r_{hh,vv}[0]|^2}{\left|r_{hh,hh}[0]\right| \left|r_{vv,vv}[0]\right|}. \tag{44}$$

The copolar correlation coefficient provides insight into the similiarity in scattering mechanisms for both H- and V-polarizations. For rain, the correlation is very high, near unity. For objects with length scales into the Mie scattering regime, the correlation can drop significantly due to highly non-linear behavior because of slight variations in the scattering volume's complex-valued RCS.

The last dual-polarization parameter that will be considered here is the LDR. Assuming that the radar constants are equal between the polarization states, the LDR is the ratio of

cross-polar received power to copolar received power. In alternate mode or H-only transmit mode, $LDR_{vh}$ is

$$LDR_{vh} = \frac{|r_{vh,vh}[0]|^2}{|r_{hh,hh}[0]|^2}. \tag{45}$$

Similarly, $LDR_{hv}$ can be calculated in alternate mode and V-only mode.

Radar moments may also be estimated from the Doppler spectra. Given an ESD $S$ for a single polarization, the total echo power, mean velocity, and spectrum width can be directly estimated [17]. The total echo power (the zeroth moment) is

$$P = \sum_{k}^{K} S[k], \tag{46}$$

where $K$ is the length of $S$. Reflectivity, with units in dBZ, is then

$$Z = 10\log_{10}(P) - 10\log_{10}(C) + 20\log_{10} R, \tag{47}$$

where $C$ is the radar constant and $R$ is the range in kilometers. The mean velocity (the first moment), in meters per second, is

$$\bar{v} = \frac{\sum_{k}^{K} S[k]v[k]}{P}, \tag{48}$$

where $v$ represents the velocity of the ESD bin. Following the same pattern, the spectrum width, in meters per second, is estimated as

$$w = \sigma_v = \sqrt{\frac{\sum_{k}^{K} S[k](v[k] - \bar{v})^2}{P}}. \tag{49}$$

CHAPTER 3

# Wind Turbines for Power Generation

Windmill power turbine designs vary drastically in configuration, shape, and size, resulting from a diverse range of available technology, manufacturers, and requirements. The most ubiquitous design for commercial power generation is the three-blade, tower-mounted, horizontal-axis wind turbine (HAWT). For commercial power generation, the power output of a HAWT can range from tens of kilowatts to ten megawatts, with blade diameters of up to 190 meters [5, 41]. The demand for wind energy has resulted in exponential growth in the number of operational wind turbines in many countries, with wind farms both on land and offshore.

The radar characterization presented here focuses on three-blade wind turbines. Specifically, wind turbines from two different locations are considered within this dissertation. For CSU-CHILL S-band radar observations, two turbine models from two different vendors operating in the Ponnequin Wind Farm were observed. And, while the CSU portable X-band radar was deployed at the DOE NREL NTWC, a research turbine of similar size and power to those in the Ponnequin Wind Farm was also considered. The following sections describe a HAWT's basic structure and behavior and include a brief discussion of wind farms as they impact radar observations, as well as considerations for characterizing observations of a wind turbine's RCS.

## 3.1. Three-Blade Wind Turbine Structure

Tower-mounted, three-blade HAWTs are composed of three main structures: the blades, the nacelle, and the tower. A diagram of a representative three-blade turbine is shown in Figure 3.1. The blade rotation angle ($\theta$) is the angle from the leading edge of a reference

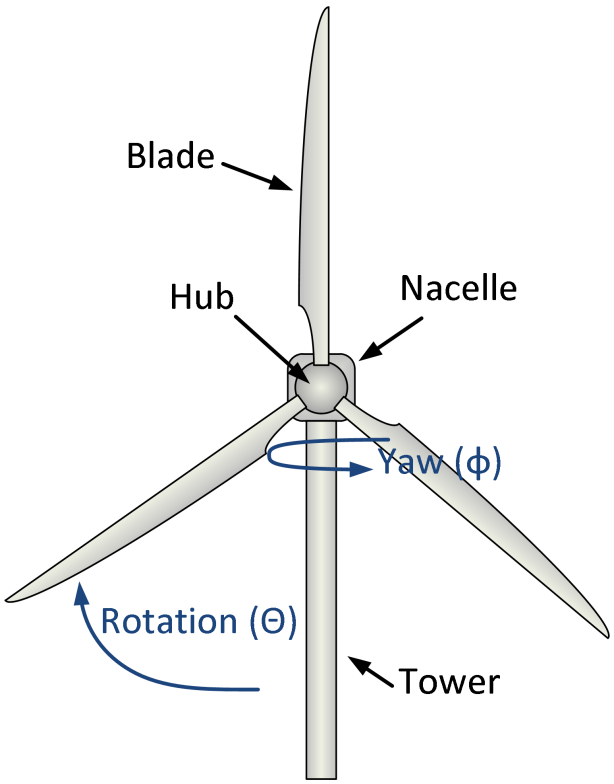


FIGURE 3.1. Basic three-blade HAWT components and directions of motion ©2016 IEEE [1].

blade when it is parallel to the tower and upright. The hub provides the rotation axis for the three blades. The yaw angle ($\phi$) (in a plane that is perpendicular to the tower) is the angle at which the hub is facing relative to the radar, with $\phi = 0$ degrees directly facing the radar. The three-blade wind turbine is designed with 120° of symmetry in rotation when all blades are equally pitched.

The wind turbine's rotation rate is primarily determined by the target wind speed, the airfoil's tip-speed ratio (TSR), and the blade length. The TSR is the ratio of tip-speed to wind speed, expressed as

$$\lambda_{tsr} = \frac{\dot{\theta} R_b}{v_w}, \tag{50}$$

where $\dot{\theta}$ is the rotation rate, $R_b$ is the blade radius, and $v_w$ is the wind speed. For fixed-speed wind turbines, the target operating wind speed is typically in the neighborhood of

15 m/s. For the blade-tip section to be aerodynamically advantageous (i.e., not inhibiting power extraction), the TSR must be less than the blade's target TSR. For three-blade wind turbines, the optimal TSR is generally between 6 and 8 [42]. With a rated wind speed of 15 m/s and TSR of 6, the tip-speed is 90 m/s. For wind speeds that exceed the TSR, the overall efficiency of the wind turbine decreases. Blade tip-speeds are typically kept below the compressible flow regime of 0.3x the speed of sound ($< 100$ m/s). For tip-speeds above 80 m/s, special consideration is needed for the leading edge of the blades because of erosion from particles [42]. For wind turbines implementing variable speed operations, the rotation period is proportional to the impinging wind speed up to a specified maximum rotation rate.

The hub axis is not parallel to the ground but instead is at some tilt angle. The tilt angle is the angle at which the hub's rotation axis is off-perpendicular from the tower. This tilt angle provides clearance between the blade and the tower and considers blade flexing plus a safety margin [43]. A five-degree tilt angle has been noticed in the documentation of multiple turbine vendors (e.g., NEG Micon and GE). Furthermore, wind turbine geometry is also determined by the cone angle, which is the angle from the blade's rotation plane to the blade's leading edge, with positive angles toward the expected wind's direction. Wind turbine blades have a pitch angle that defines their angle of attack. The blade's geometry and angle of attack determine its lift and drag. Some wind turbine designs provide variable blade pitch as an operationally controlled parameter, and the pitch control may be independent between blades. Blade pitch control varies among wind turbine designs and may be fixed for all blades, independently variable (where the pitch of each blade is independent), or collectively variable (where all blades are pitched together). Additionally, a turbine's blade is designed with a "twist," which varies the angle of attack at a position on the blade as a function of distance from the hub. In fact, for a given blade rotation rate and wind velocity, the angle of attack should be constant along the blade's length for a given twist. This blade

twist is designed to optimize the blade's efficiency for a set of operating conditions. Further details and descriptions of wind turbines can be found in [44, 5].

The sole purpose of a windmill power turbine is to generate electricity. To this end, the wind turbine's control system is designed to maximize power generation while maintaining safe operating conditions [5]. A wind turbine control system tunes the turbine's operating parameters to maximize power output and, above all, prevent damage to the wind turbine itself. The operating parameters are, for all practical purposes, a function of the wind's speed and direction. Given that a dynamic control system is constantly adjusting the operating state of a wind turbine and wind can present a stochastic forcing-function, the characterization of a wind turbine is problematic in field operations because conditions are not well controlled and the wind turbine's state information is generally not available.

Aerodynamic forces are sources of oscillatory torsion and deflection modes that occur in wind turbine blades and towers [45, 46]. Non-steady, wind-forced oscillations contribute to variations in the observed radar cross-section of the rotating assembly. The wind's force is not necessarily constant over a turbine's swept area. In fact, a wind turbine is well within the atmospheric boundary layer, and a natural velocity gradient (as a function of height) exists in this boundary layer. In wind farms, the wake caused by upwind turbines can sufficiently perturb the flow around the downwind turbines, creating turbulence and adversely impacting the turbine's power generation. These sources of variation act as forcing functions for wind turbine blade oscillation, in addition to the affects of gravity as the blade rotates and deflects due to its own mass. Inertial forces from control state changes can also induce oscillatory modes in the blades and towers.

The three main components of a wind turbine each contribute to a wind turbine's total RCS. The nacelle and tower are similar to stationary ground clutter. The tower's and nacelle's RCSs can be suppressed using standard ground clutter filter techniques. The rotating

turbine blades present a time-varying RCS with a non-zero radial velocity component. The resulting Doppler spectrum changes with time, and in many cases, the radial velocity can exceed the ambiguous Doppler velocity limits of the radar (i.e., spectral aliasing occurs). This time-varying velocity component due to rotating wind turbine blades is the primary source of complexity in the mitigation of wind turbine interference. Using the 120-degree symmetry of a three-blade wind turbine, the RCS of a turbine with a full rotation period of 3 seconds ideally looks like a single blade turbine with a period of 1 second.

Given non-zero tilt and cone angles, even when the hub yaw angle is parallel to the radar radial (the radar is looking directly at the hub or the back of the nacelle), there is still a measurable velocity due to the procession of the blades toward and away from the radar as the wind turbine rotates. The minimum-observed velocity signature for a rotating turbine may be small, but it is not zero. For a 5-degree tilt and 0-degree cone angles, and a 48 meter diameter blade area rotating at 30 RPM, the blade tip's peak velocity with respect to the radar is 6.6 m/s when the yaw angle is parallel to the radar's observation radial, not accounting for blade flex. Given that the angular separation of the blades is fixed, the negative velocity and positive velocity excursions of the blades are ideally equal in magnitude, and any deviation must be due to blade deflection or oscillation.

Structural oscillations, or "vibration," can result in multi-wavelength position deviations at the nacelle and hub and along the tower and blades. The total RCS is the integration of all the scattering centers, which adds up coherently. The coherent integration may be constructive or destructive in magnitude. When the scattering surface is near the angle of specular reflection with respect to the radar, the variation in RCS may be more pronounced for small changes in angles, resulting in large variations in the total RCS and a rapid decorrelation of observations.

## 3.2. Ponnequin Wind Farm

A wind turbine generally presents a large RCS at a fixed position in space but with a non-zero velocity component. Wind turbines that are a concern to radar system operations typically do not exist alone; these turbines are usually part of a larger wind farm that can consist of tens or hundreds of wind turbines, sometimes installed in high-density configurations. The separation distance for wind turbine operation is generally greater than 7 times the turbine diameter [47]. Depending on the relative position of a radar compared to a wind farm, as well as the radar's specification, one or multiple turbines may exist in a range-volume cell.

The Ponnequin Wind Farm contains 44 wind turbines and has a total electrical generation capacity of 25.3 megawatts [48]. It is located in Weld County, Colorado, on the border of Wyoming close to Cheyenne, Wyoming. Ponnequin was commissioned in 1999 with 29 NEG Micon NM48/750 wind turbines. A 2001 expansion (as part of "Ponnequin III") added 15 Vestas V47/660 turbines. The characteristics of both wind turbine models are presented in Table 3.1. Both models operate nominally at discrete rotation rates, with the Vestas allowing for some variability in optimizing power output. The Vestas model also provides variable blade pitch as a method to optimize power generation [49]. The NEG Micon turbine has a fixed blade pitch but allows for two discrete operating frequencies [50].

The Ponnequin Wind Farm's physical layout and position with respect to the CSU-CHILL radar are illustrated in Figure 3.2. The two western lines of turbines represent the 29 NEG Micon turbines. The two easternmost lines contain the 15 Vestas turbines. The CSU-CHILL radial lines (with 0.1-degree spacing) and range rings (with 150-meter spacing) are shown using a spherical Earth model. The range cell locations are provided to give a sense of the observation volume size, but the actual observation volumes may be different

TABLE 3.1. Characteristics of the wind turbines in the Ponnequin Wind Farm [51, 48–50], located on the Wyoming/Colorado border approximately 63 km northwest of the CSU-CHILL radar ©2016 IEEE [1].

| | Vestas V47/660 | NEG Micon NM48/750 |
|---|---|---|
| Rotation Rate | 28.5±10% RPM | 15 or 22 RPM |
| Rotor Diameter | 47 m | 48.2 m |
| Nominal Hub Height | 65 m | 55 m |
| Blade Tip Speed | 70.1 m/s | 55.5 m/s |
| Nominal Power | 660 kW | 750 kW |
| Swept Area | 1,735 $m^2$ | 1,824 $m^2$ |
| Cut-In Wind Speed | 4 m/s | 4 m/s |
| Rated Wind Speed | 15 m/s | 16 m/s |
| Cut-Out Wind Speed | 25 m/s | 25 m/s |

due to variations in the propagation path length, sample phase of the return echo, circular Earth model errors, etc. Close inspection of the map data reveals an approximately 9.4x spacing between rows and approximately 2.9x spacing between neighboring turbines of a row. The rows are aligned to ensure that the maximum separation between upwind/downwind turbines occurs in the direction of the prevailing (highest probability) wind. This separation is necessary to maximize the potential for stable laminar flow for the wind turbine to extract power from the wind. If a turbine is in the wake or turbulent area behind another turbine, this will induce additional mechanical stress on the leeward turbine, as well as reduce its energy-producing potential.

The layout of wind turbines is arranged to maximize energy production for the given terrain and location. The wind farm layout is tightly coupled to the probability of a wind turbine operating in a certain orientation. For the Ponnequin Wind Farm, the optimal wind direction is presumably between ±60-degrees off-perpendicular to the rows, with some margin allowed for a conical wake pattern behind the turbines. The rows of wind turbines run along an approximately 52-degree heading. Using the ±60-degree window, this allows for best performance (longest wake path length) when the wind direction is between 262 degrees clockwise to 22 degrees and 82 degrees clockwise to 202 degrees. A study of wind velocity at

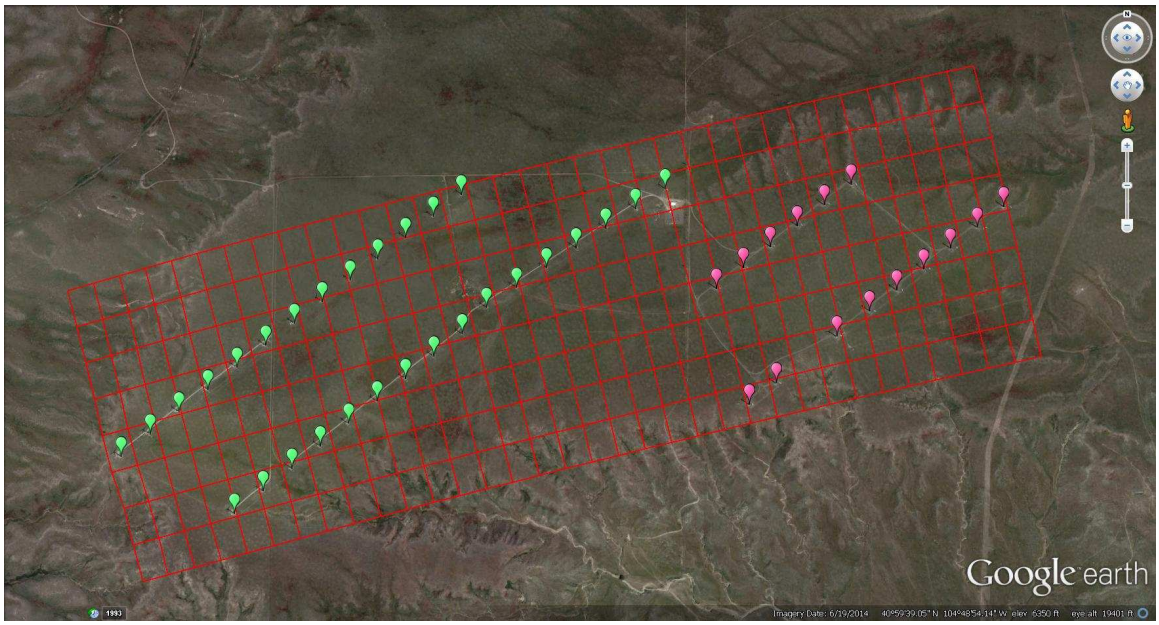


FIGURE 3.2. Arrangement of the Ponnequin Wind Farm. The green points mark the locations of NEG Micon NM48/750 wind turbines, and the pink points mark Vestas V47/660 wind turbines. The red lines represent radials from CSU-CHILL in 0.1-degree azimuth increments and radius rings in 150-meter increments using a spherical Earth model. These illustrate the approximate range-volume cell locations observed by the radar. Note that CSU-CHILL has a 1-degree beamwidth and 150-meter range resolution ©2016 IEEE [1].

30-meters-above-ground-level, at a point 20 miles east of Ponnequin (from December 30, 2009 to April 28, 2011), showed the highest-frequency wind direction at 300 degrees (±5 degrees) [52]. The wind direction was between 140 degrees clockwise to 10 degrees the majority of the time during the experiment (87+% of the time). Of this, the majority of wind energy was from directions between 260 degrees clockwise to 10 degrees.

## 3.3. DOE NREL National Wind Technology Center

The U.S. Department of Energy, National Renewable Energy Lab's National Wind Technology Center is located in Louisville, Colorado. The site's wind characteristics are well characterized and provide an ideal location for renewable wind energy research and development. Among the wind turbines located at the NWTC are the DOE-owned 1.5 MW General

TABLE 3.2. Characteristics of the NWTC wind turbines [53] relevant to the CSU X-band radar observations. The range to each turbine's nacelle is estimated using Google Earth. The azimuth is the radar's azimuth angle where the antenna's boresight is pointing at the wind turbine's tower. The when the turbine is pointed at the yaw angle in this table, the wind turbine's hub is pointed at the radar system.

| | CART3 | GE 1.5 MW |
|---|---|---|
| Tower Height | 36.6 m | 80 m |
| Rotor Diameter | 40 m | 77 m |
| Rated Output Power | 600 kW | 1.5 MW |
| Installed | 1997 | 2009 |
| Range to Nacelle | 935 m | 1250 m |
| Beamwidth at Nacelle | 22.8 m | 30.5 m |
| Radar Azimuth | 83° | 68° |
| Turbine Yaw | 263° | 248° |

Electric (GE) wind turbine and the controls advanced research turbine 3 (CART3), both of which are three-blade HAWTs. Relevant details about these two turbines are presented in Table 3.2.

Images of NREL's CART3 and GE turbines are shown in Figure 3.3. Figure 3.3A shows the CART3 with its blades pitched 90 degrees to shed wind load. The wind turbine's blades are oriented in this direction until wind speeds are within the turbine's operational range. Figures 3.3B and 3.3C show the CART3 and GE turbines during operation.

CSU's portable X-band radar was deployed at NREL for a two-month intensive observation of two wind turbines during November and December of 2015. Figure 3.4 shows the radar's view, taken at approximately the antenna's boresight, of the wind turbines and meteorological towers at the NWTC. Figure 3.5 shows the reflectivities greater than 35 dBZ of a clear-air scan of the NWTC at 2.0 degrees elevation. The locations of the wind turbines, meteorological towers, and buildings align well with areas of high reflectivity.

These two wind turbines were selected for observation due to the availability of turbine state information. (The GE wind turbine's high-rate telemetry system was under development during deployment and therefore will not be discussed.) The CART3 acquisition

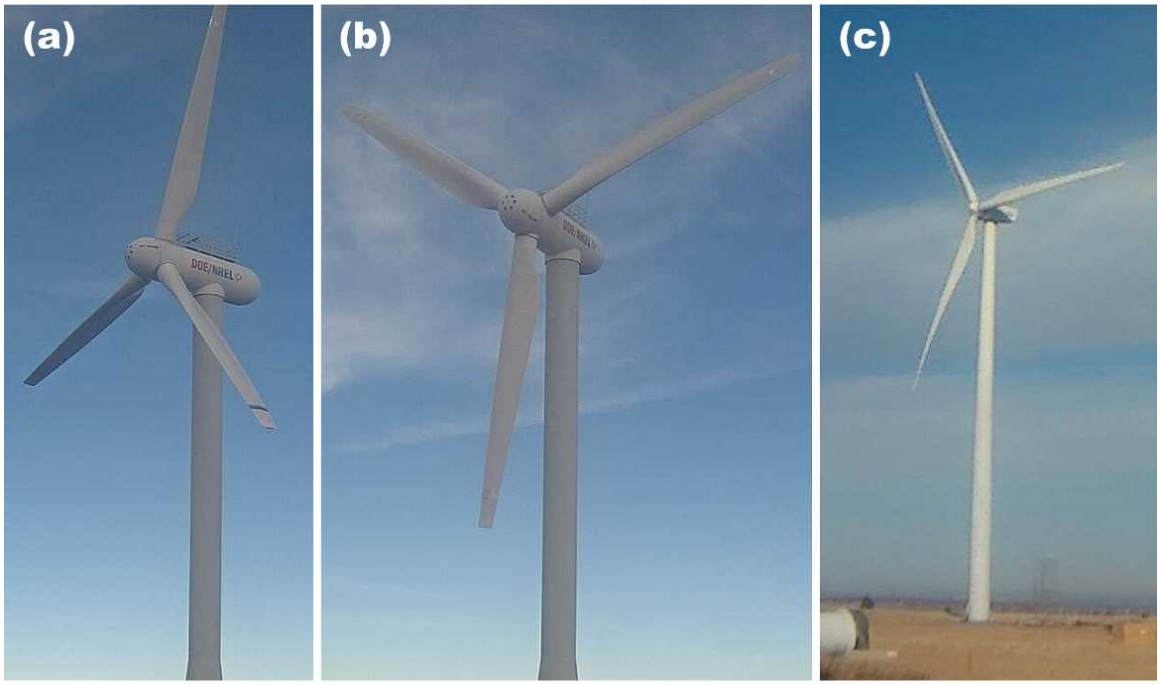


FIGURE 3.3. Images A and B show the CART3 wind turbine at NREL's NWTC in standby and operation, respectively. Image C shows the GE wind turbine during operation. Images courtesy of NREL.

system operates at 400 Hz and is time-synchronized to the GPS system. In addition to the GPS-synchronized UTC time-stamp, a subset of the available telemetry was recorded for use in characterizing the wind turbine's RCS. The additional state parameters of interest are blade pitch for all three blades, absolute rotation angle, instantaneous rotation rate, yaw angle, controller state, and meteorological tower wind speed and direction at 36.6 meters high.

3.3.1. VARIABILITY OF THE CART3'S STATE. Using the available telemetry from nine days of CART3 operations in November and December of 2015, Figure 3.6 shows the relationship between meteorological tower observations (at the hub height of 36.6 meters) of the wind's velocity and the CART3's operating state. In the absence of any state telemetry from the wind turbine, the meteorological tower can provide some degree of state information. The relationship between the wind direction and CART3's yaw angle is presented in

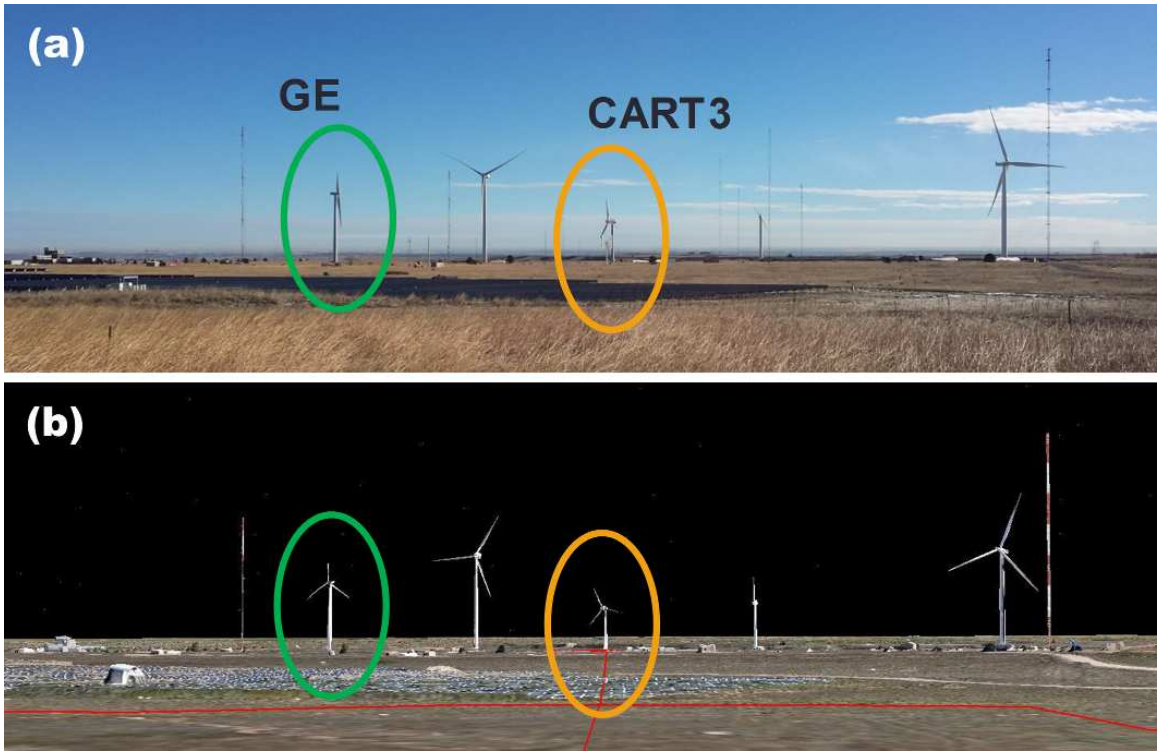


FIGURE 3.4. Image A is a photo from the position of the antenna's boresight looking over the wind turbines at the NWTC. Image B shows the same perspective using Google Earth. The positions and alignment of the structures in both images agree very well. The CART3 and GE wind turbines are highlighted by orange and green circles, respectively.

Figure 3.6A, and Figure 3.6B relates the wind's velocity to the CART3's rotation rate. The CART3's "optimal" tip-speed ratio was reported to be 7.0 [5]. The relationship between the CART3's rotation rate and the wind speed for the optimal TSR is shown as a solid black line in Figure 3.6B.

For the CART3, consider the minimum and maximum excursions in yaw and RPM as a function of time delay. This provides a statistical limit for the change in the turbine's state during a period of time. These bounds yield some insight into the suitability of applying prior state estimates to current observations in the event that low update rates for the state are used (whether the state is updated from radar-based estimators or actual turbine telemetry). Consider the results in Figure 3.7, where the state telemetry is used to evaluate the observed minimum and maximum yaw and RPM, up to each graph's respective time-lag in the future.

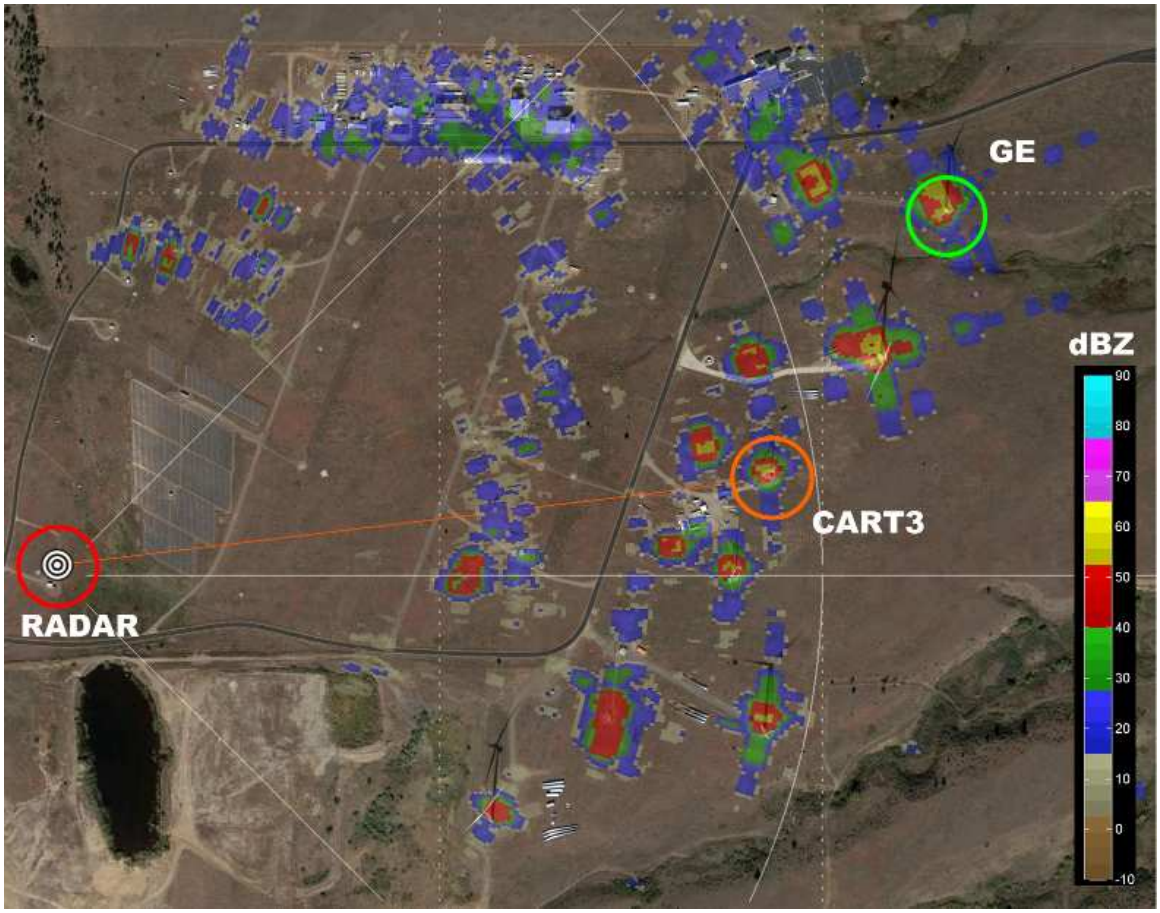


FIGURE 3.5. A top-down view, with the top of the image oriented to be north, of the NWTC is shown. Clear-air reflectivity observations from a 2.0-degree PPI scan are superimposed over the image and aligned with the reflectivity signatures of the wind turbines and other ground clutter. Reflectivities less than 35 dBZ are omitted. The CART3 and GE wind turbines are highlighted by orange and green 50-meter radius circles, respectively. The radar's location is denoted by a red 50-meter radius circle. The base image comes from Google Earth.

The minimum and maximum results are sub-sampled at a 1 Hz rate to generate the presented histograms. Observations (i.e., occurrences) of data outside of the x-axis' limits may exist but have been omitted for clarity. The time-lags selected approximate refresh rates typical of radar systems and wind turbines. A wind turbine's full rotation period can be on the order of 1-6 seconds (i.e., 10-60 RPM). 3-10 seconds represent the order-of-magnitude refresh period for short-range surveillance radar. 300 seconds (5 minutes) represents the shorter end of current NEXRAD volume coverage pattern scan repetition periods. The operating yaw angle

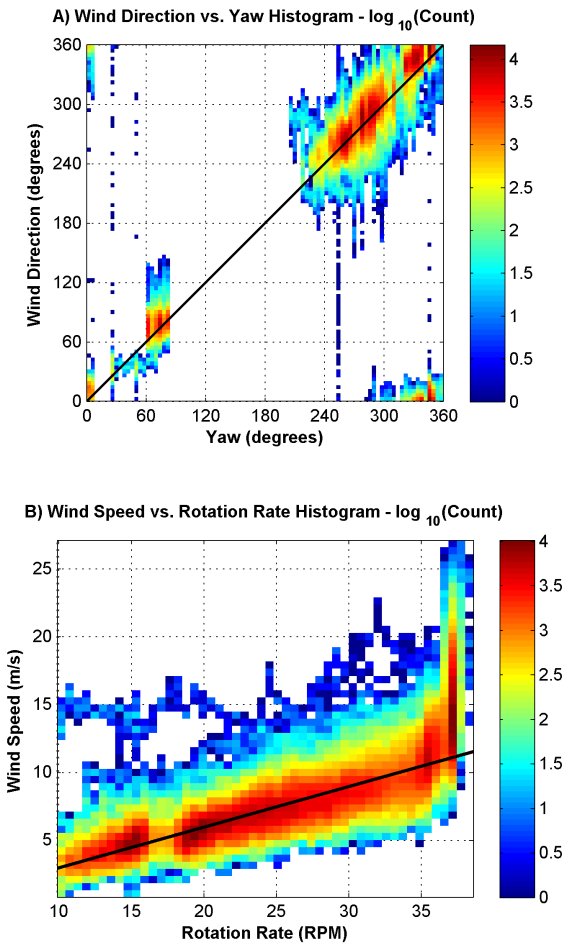


FIGURE 3.6. Relationship between meteorological tower observations (at hub height) and turbine state (operating mode only). The black line in Graph A shows the 1:1 line, and in Graph B, the black line represents the relationship between RPM and wind velocity for a CART3 tip-speed ratio of 7.0.

appears to stay constant until the operational state decides to change to another point. This explains the "peaks" on the tails of the minimum/maximum yaw change histograms (the right column of Figure 3.7). The narrow peaks of the yaw histograms at zero also suggest that once a yaw angle is selected, the CART3 controller (in the configuration selected for the days considered) tended to operate at a discrete yaw angle, and the RPM was modulated as the priority. For observation periods up to 10 seconds, the yaw changes were typically within 5 degrees, and for 30 seconds, the changes were typically within 15 degrees. This

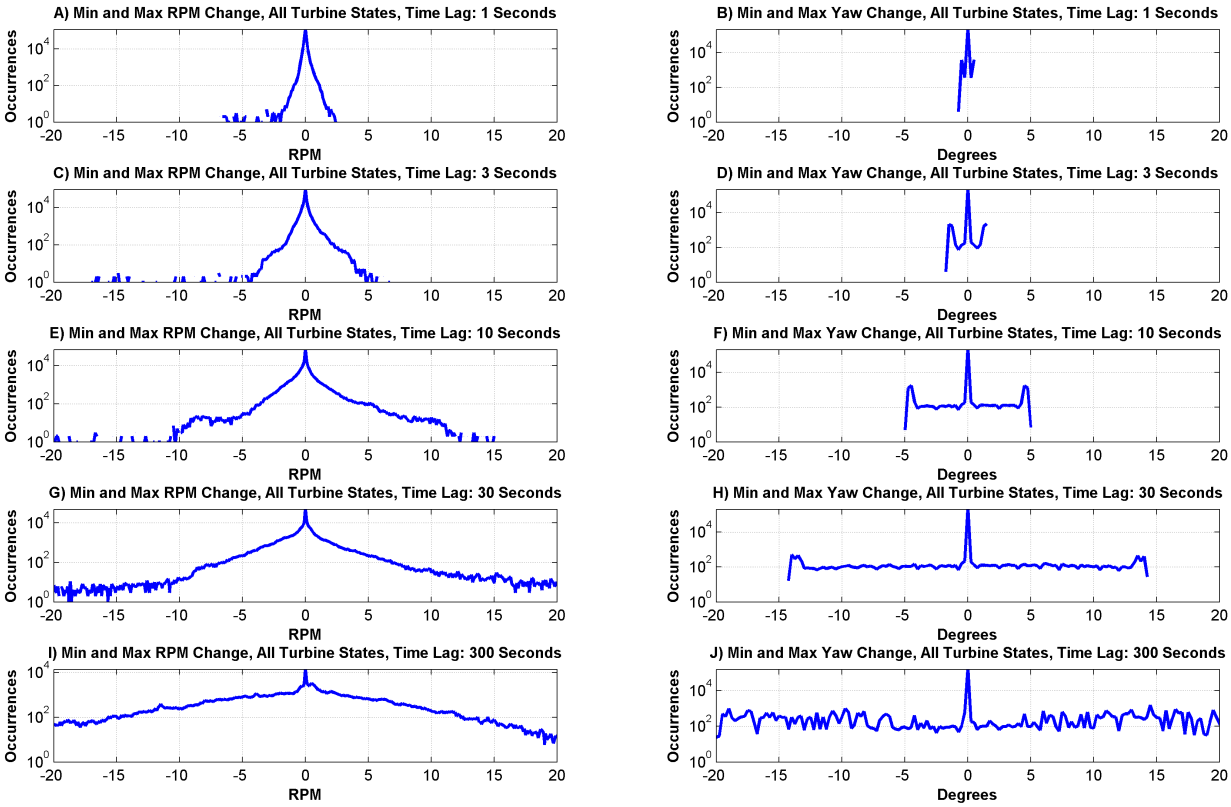


FIGURE 3.7. Histograms of the minimum and maximum change for rotation rate (left column) and yaw angle (right column) for different observation time periods. The minimum and maximum observed values within the given time periods are both included in the histograms.

yields a yaw slew rate of 0.5 degrees per second if the yaw changes state. A review of the left column of Figure 3.7 shows the RPM to be much more variable with time. The distribution of minimum and maximum rotation rate changes has an exponential-like distribution for short time periods (represented as a linear slope on a logorithmic axis). The rotation rate's acceleration can be as much as 2 RPM/second but is usually much less.

The meteorological tower observations from Figure 3.6, as well as the minimum and maximum state excursions from Figure 3.7, demonstrate that a-priori information is available to enable or improve the estimation of a wind turbine's state, even in the absence of high-rate wind turbine telemetry.

## 3.4. Wind Turbine Scattering Model

Numerical models with varying degrees of complexity and scattering assumptions have been demonstrated for wind turbine RCS calculations [6, 8, 9, 11]. The computational complexity of electrically full-scale turbines without simplifying assumptions has been shown to be unfeasible for typical commercial wind turbine electrical sizes at radar frequencies regularly used for weather and air-surveillance radars [6]. This, however, does not mean that numerical models cannot provide insight into the radar observations of real wind turbines.

A wind turbine's RCS can be approximated by dividing the wind turbine into subsections and coherently integrating the contribution of each section's RCS as

$$e_s = \sum_N |A_n(\lambda, \phi, \theta)| e^{-j(k2r + \varphi(\lambda,\phi,\theta))}, \tag{51}$$

where $r = ||\vec{o} - \vec{p_n}||$ and $k = 2\pi f_c/c$. The scattering phase, $\varphi$, accounts for the shifting phase centers as a function of the turbine's position, and $A_n$ is a real-valued amplitude. The wind turbine section's amplitude and phase are described by the radar's wavelength ($\lambda$) and observation angles ($\phi$ and $\theta$) for the radar's transmitted wave. The scatterer's shift in phase is equivalent to shifting the distance of the scattering object. A dynamic wind turbine can be simulated by appropriately varying $\phi$ and $\theta$. This technique has been used by [11] to simulate radar cross-sections and Doppler spectra for a wind farm. Each element is assumed to be isolated from one another, and no mutual coupling or multiple scattering is considered.

Following this method, a model of a wind turbine using a first-order approximation of the geometry is presented here and will be discussed in detail later. The model includes only the three wind turbine blades and omits the tower, nacelle, and hub. Each blade is modeled after a tapered NACA 3317 airfoil without a twist. There is nothing special about the NACA 3317 airfoil other than the model was available and is convex (i.e., convexity simplifies the

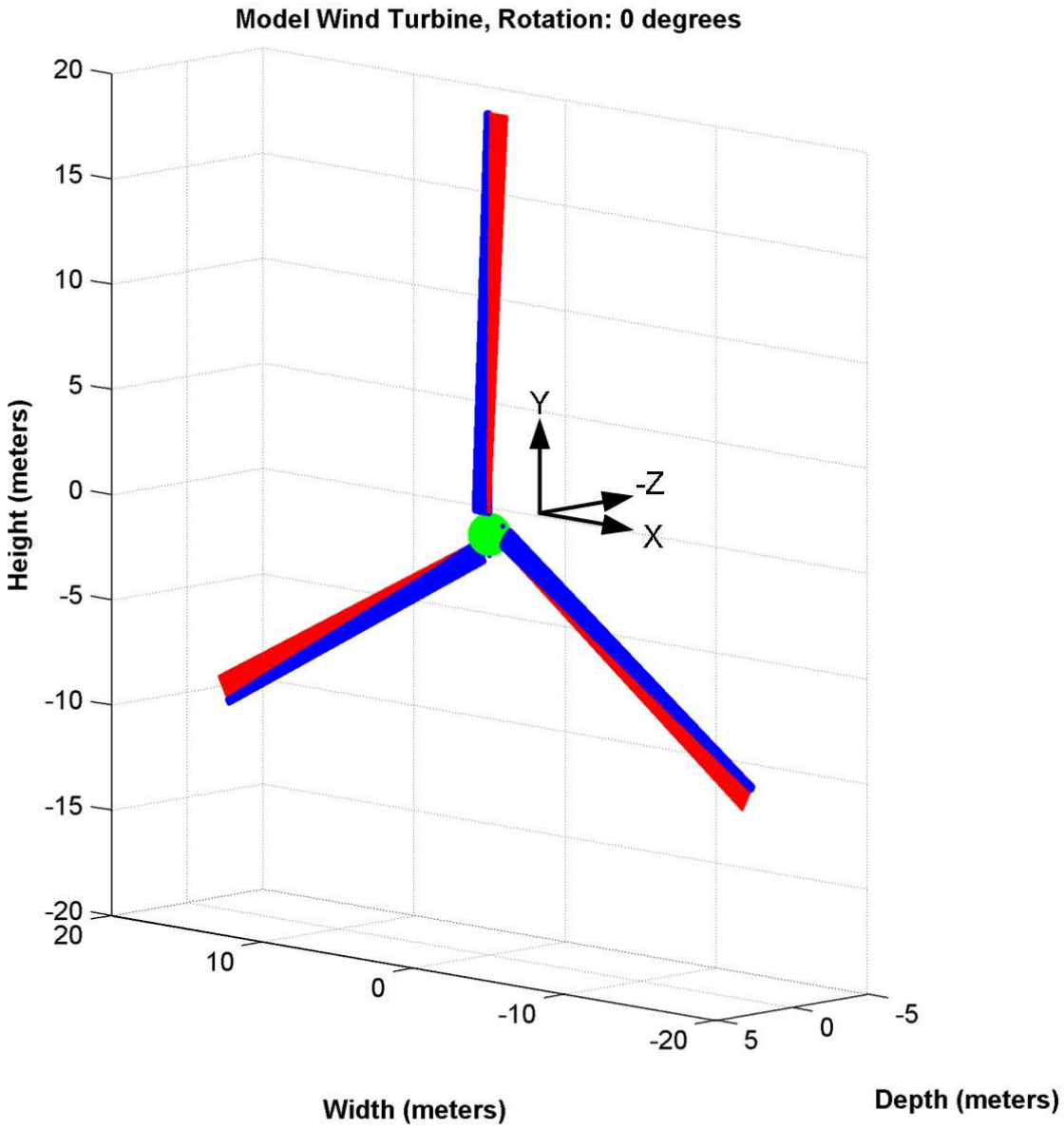


FIGURE 3.8. This wind turbine numerical model is based on the NACA 3317 airfoil and is linearly scaled from the blade start near the rotation center to the tip. The blue points represent the scattering centers that are coherently integrated, the red lines represent the velocity vectors of each point, and the green circle is the center of rotation for the simulated wind turbine. The radar's incident wave propagates in the direction of the negative z-axis (the "Depth" axis).

shadowing algorithm). The blade root is omitted. Self-shadowing and the projection area for the incident and scattered wave are accounted for. The scattered wave is assumed to be isotropic for each individual element. The numerical turbine model is shown in Figure 3.8.

This model provides only basic insight into the wind turbine's rotating contribution; as noted, no stationary components are included. Even with the simplifications and inaccurate geometries, though, the model provides a key understanding of real wind turbine observations. Controlled investigation and evaluation of signal processing techniques are possible with such a model. A controlled examination may not be feasible with radar observations of full-scale, operational wind turbines due to safety concerns and mechanical limitations.

## 3.5. Radar Observations of Wind Turbines

Weather radar observations that are provided for operators, forecasters, and algorithms are discussed here for a clear-air observation of a wind turbine. The meteorological radar parameter estimates are shown in Figure 3.9 for the simultaneous-mode observation of a Vestas wind turbine in the Ponnequin Wind Farm. The parameters are "raw," meaning there has been no filtering or modification of the receiver observations (no noise subtraction, no clutter filtering). The integration period is 64 non-overlapping samples used in the estimation of each parameter. The wind turbine is sampled with a PRT of 0.962 milliseconds, for a total integration time of 61.568 milliseconds.

The wind turbine's tower and nacelle present stationary targets with relatively large RCSs. The contribution of the stationary components is easily noticed in the H-pol power spectrum in Figure 3.9A. At observations around 3.1 seconds, the contribution of the ground clutter is reduced (as seen in the reflectivity parameter), and the velocity excursion due to the blade flash increases because of the reduced reflectivity-weighting of the stationary scatterers. The blade "flashes," which have a broad Doppler spectrum, are aliased because the turbine blades tips' velocity exceeds the maximum unambiguous velocity ($v_{max}$) of for the radar configuration. The blade flash effect is seen in all radar parameters with periodic behavior. The peaks in reflectivity do not coincide with the peaks in velocity, indicating that

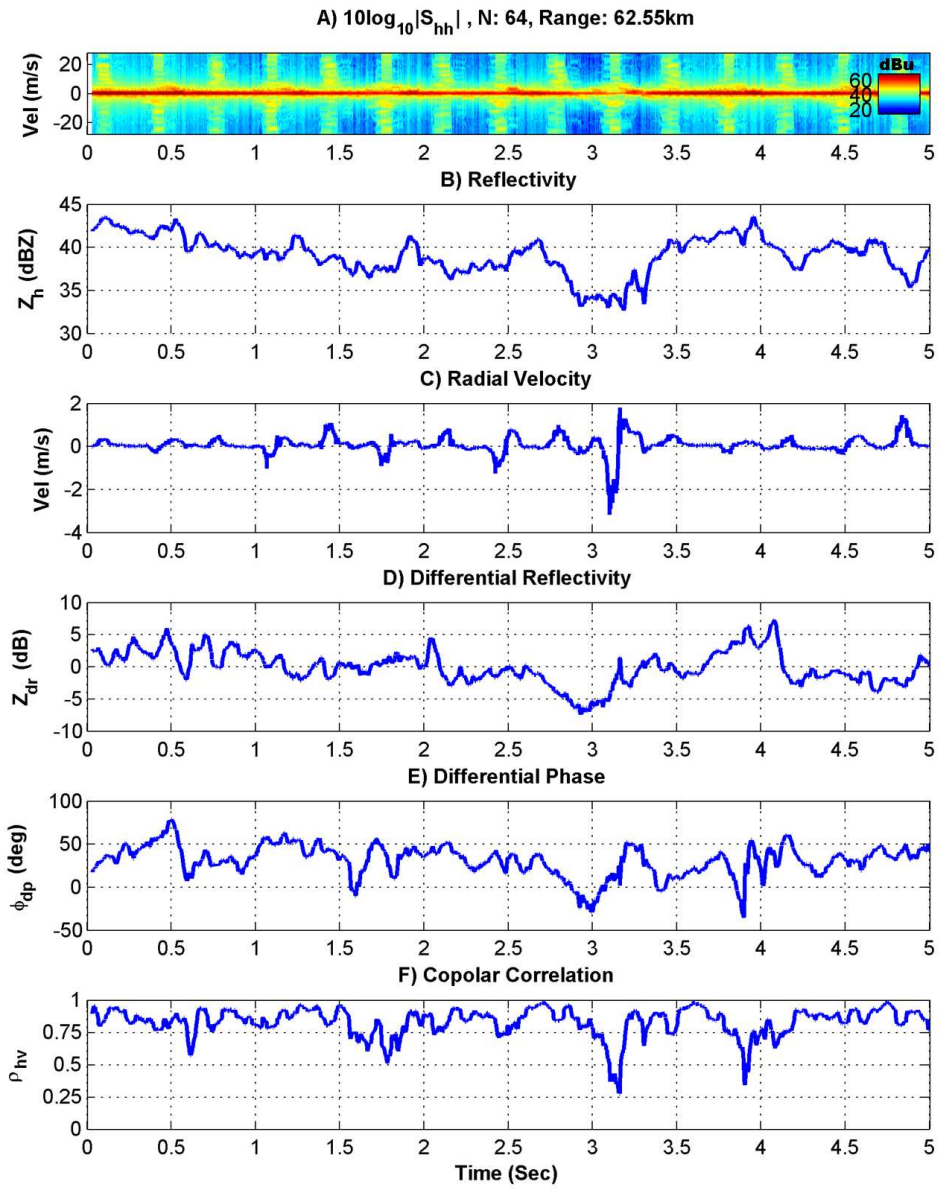


FIGURE 3.9. Observations of a Vestas V47 wind turbine in the Ponnequin Wind Farm using CSU-CHILL operating in simultaneous-mode without precipitation present on December 2, 2013, 21:10 UTC, at a range of 62.55 km. The radar antenna is pointed at 346.60 degrees azimuth and 0.50 degrees elevation.

the turbine blades may be masking the tower and/or nacelle. During the observation periods with reduced stationary clutter contributions, the correlation coefficient also decreases along with differential reflectivity. For observation times between 3.8 and 4.1 seconds, differential reflectivity increases, which coincides with an increase in the stationary clutter components

of the power spectra, as shown in Figure 3.9A. The wind turbine blade's contribution to overall reflectivity is low compared to that of the stationary RCS sources.

A few practical considerations for analyzing radar data should mentioned. The degree to which these may or may not affect the interpretation of observations is varied (perhaps nonexistent), but nevertheless, they are briefly considered here. The magnitude of the effects each of these has will vary on a case-by-case basis and can be highly nonlinear due to external conditions. It is important to understand the underlying causes of these effects to be able to identify them in observations to determine if a feature is significant to the overall data-processing objective.

3.5.1. Antenna and Range Windowing. The antenna pattern windowing effect and the range windowing effect due to the transmit pulse length, receiver filters, and sampling delay were introduced in Section 2.3. Given the physical size of wind turbines, range and antenna windowing are readily observed in radar observations. The location of a wind turbine within a sampled range-volume cell, particularly if the entire turbine is not within the range-volume cell, determines the observed response. Given the diameters of commercial wind turbines, it is probable that a wind turbine may not be completely contained within a single range-volume cell. Further, the degree of inclusion can vary as a function of the wind turbine's yaw and rotation angles.

A radar antenna with a 1-degree beamwidth at short ranges can be on the order of the size of wind turbines. If a wind turbine is not contained completely within the antenna's mainlobe, the variation in gain can introduce significant weighting effects to the RCS. The effect of this is to convolve the radar's observations and introduce spectral broadening and possible velocity bias.

3.5.2. Near-Field and Far-Field. The RCS observed from a scattering body is generally grouped into three regions, depending on length scales and the observation range. These regions are the reactive near-field, radiating near-field, and far-field [32]. The far-field distance starts at

$$r_{ff} = \frac{2D^2}{\lambda}. \tag{52}$$

The far-field assumption of a scattering body is valid when the following conditions are met: $r > r_{ff}$, $r >> D$, and $r >> \lambda$.

For moderate-size wind turbines, such as those in the Ponnequin Wind Farm observed by the CSU-CHILL S-band (10 cm wavelength) radar, the far-field distance of the rotating wind turbine assembly is approximately 45 km. The radar cross-section of an object can be considered constant in range (only varying by angle) when observed in the far-field. For observations in the near-field, a range dependency is introduced to the observed RCS.

The implication is that the distance between the radar and the wind turbine can have an impact on observations. The range dependency is negligible when far-field conditions hold. For observation-driven modeling of wind turbines for the purposes of filtering, this means that a homogeneous wind farm may exhibit different turbine signatures as a function of range, with all other conditions being equivalent. If the far-field approximation holds, the homogeneous wind farm should show the same statistics regardless of range. In [54, 11], the authors considered the implications of near-field and far-field radar observations of wind turbines.

3.5.3. Multiple Scattering. Multi-path is a well known and problematic issue for communication systems. The effects can be observed in cities when a GPS system fails to accurately locate a receiver's position. In radar, multiple scattering (or multi-path) is the

process of the transmitted radar signal being scattered from one body to another and then back to the radar. The incident radar power is scattered in all directions by a scattering body (although not necessarily isotropically). The power from the first scatterer will impinge on another scattering body and subsequently be scattered in all directions. The scattered power from a point scatterer decays (one way) by $R^2$, where $R$ is the range. Multiple scattering echoes are typically at a far lower power level than backscattered power. For strong scattering sources in close proximity to other large RCS objects, such as multiple metal wind turbine towers in a wind farm or a metal wind turbine tower and the wind turbine blade, multiple scattering can be observed.

In [9] the forward-scattering and multiple-scattering effects of wind turbines are considered. From the field experiment observations in [2], the frequency-doubling effects in L-band observations were shown to be due to wind turbine tower-to-blade multiple scattering. Multipath reflections in a wind farm can also present artifacts of wind turbines in range cells where no turbine physically exists. The perceived range is determined by the total path length of the multiple scattering. For example, if two targets exist at a range of 1.000 km but are separated in azimuth by 100 meters, the second reflection (due to scattering from one object and then the second) will be observed at a range of 1.050 km. The single reflection has to travel 2.0 km round-trip to the radar, while the second reflection has to travel 2.1 km.

3.5.4. Shadowing. As noted, wind turbine is composed of stationary and rotating components. Each component contributes to the overall RCS. At some wind turbine yaw angles, the blades may pass between the wind turbine tower or nacelle. At other yaw angles, the turbine's blades may pass behind the stationary components. In both cases, some fraction of the wind turbine that contributes to the overall RCS effectively "disappears" and is shadowed. Shadowing occurs when a scatterer is blocked or obscured by another scattering body

(which could be itself). The shadowing effect can cause a sudden change in the position and magnitude of the coherently integrated phase center from pulse to pulse. During Doppler velocity estimation, this phase shift manifests as a large velocity. In addition to the overall phase center's location change, the magnitude of the RCS may appear to impulsively change. Both of these effects lead to wide-band (in terms of Doppler frequency) perturbations. For an observation window in which such an event occurs, the Doppler spectra will appear to have an increased noise power, which subsequently reduces the dynamic range available for the detection or estimation of Doppler features.

CHAPTER 4

# Characterization

Operational wind turbines do not exist in ideal environments for isolated and controlled characterization using a radar system. Observations of wind turbines can include echoes from stationary statterers such as buildings, the ground, or volume scatterers like insects or precipitation. Characterization of these stationary "ground clutter" scatterers and moving volume scatterers is important for two reasons: 1) maximum isolation of the wind turbine's scattering contribution and 2) suppression of the turbine's echo in the presence of the desired target (such as precipitation). To analyze the radar signature of wind turbines, precipitation, and ground clutter, CSU-CHILL's S-band radar was used in two modes of operation: simultaneous mode and H-only mode. During observations, the antenna position was fixed to ensure that target illumination and observation remained constant during the measurement intervals.

As previously noted, the wind turbines observed are located in the Ponnequin Wind Farm and include two turbine models: the Vestas V47-660 and the NEG Micon NM48/750. The precipitation and ground clutter observations were made along the same radial as the wind turbine observations. To investigate precipitation and ground clutter, range-volume cells before the wind turbines were selected to ensure that no multi-path contamination from the turbines would be present in the observations. Doppler spectra observations from December 2, 2013, at 21:10 UTC from the Ponnequin Wind Farm are shown in Figure 4.1. The spectra presented highlight a wide variation of Doppler features such as ground clutter, radiometric noise, homogeneous and heterogeneous mixes of turbines, and a variety of turbine operating states. The observations are representative of typical WTC without echoes from precipitation or biological scatterers.

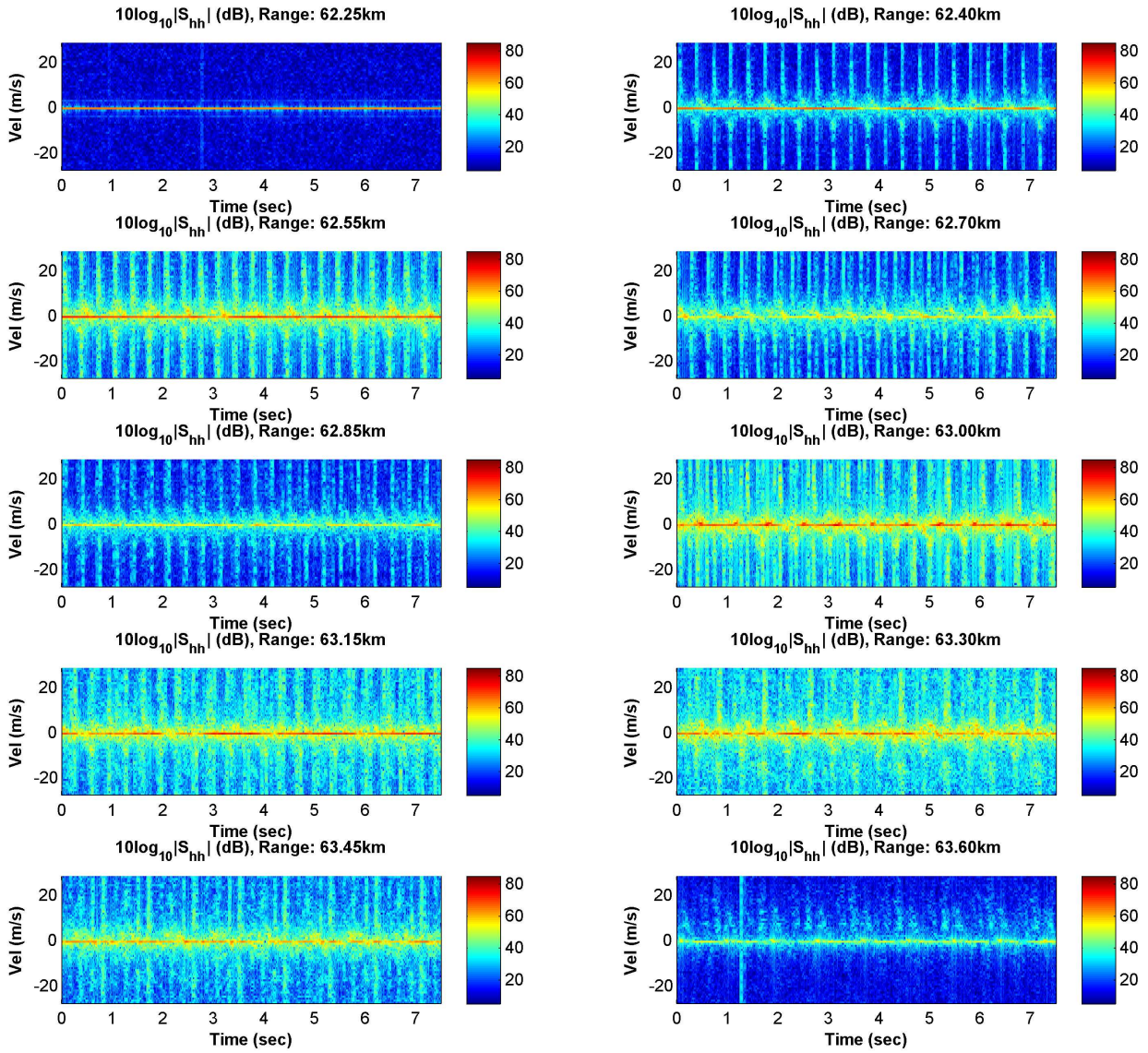


FIGURE 4.1. CSU-CHILL S-band simultaneous-mode observations from December 2, 2013, at 21:10 UTC. The fixed pointing angles are 346.60 degrees azimuth and 0.50 degrees elevation. No precipitation was present in the range-volume cells observed.

Considering the physical behavior of the scatterers of interest and understanding the radar's representation of a scattering volume, the time-varying radar cross-section for targets of interest can be characterized. The goal of this characterization effort is to understand the dual-polarization radar signature of a wind turbine with sufficient fidelity to suppress it in the presence of precipitation or other targets of interest. The first step is to focus on radar

observations of real wind turbine measurements. From the radar observations, features expected in the physical behavior of a wind turbine may be identified. The wind turbine signature is considered along with radar observations of ground clutter and precipitation. The analysis of the signatures of these scatterers follows a consistent technique, enabling direct comparison of the results.

The wind turbine analysis presented here does not contain a full examination of all turbine states. Telemetry, for instance, is not available from the wind turbines under observation. Therefore, any wind turbine state information must be inferred directly from the observations. In addition to evaluating real wind turbine observations made with the CSU-CHILL radar, a numerical simulation of a simple turbine model is examined in this chapter. The simulated radar observations provide additional insight into real wind turbine observations. The numerical model of the turbine allows for the exact state to be known. Even though the model is an oversimplification of a real wind turbine, its first-order characteristics and the real observations are similar.

## 4.1. Analysis Method for Dual-Polarization Radar Observations[1]

The observed radar signal, $\mathbf{x}$, is available as a time series of in-phase and quadrature (IQ) voltages. Each sample in time is a coherent integration of the scatterers within the radar's observation volume. For the sources of interest here, the radar signal is modeled as

$$x(t) = x_p(t) + x_{gc}(t) + x_t(t) + n(t), \tag{53}$$

which accounts for precipitation volume scatterers ($x_p$), stationary ground clutter scatterers ($x_{gc}$), "dynamic" wind turbine clutter (such as the rotating blade scatterers) ($x_t$), and noise

[1] ©2016 IEEE [1]

$(n)$. It is assumed that all constituent echo contributions are zero-mean processes and are independent from each other.

The short-time Fourier transform (STFT) of the signal $x$, with window function $w$, is defined as

$$\text{STFT}\{\text{x(t)}\}(\tau,\omega) \equiv \text{X}(\tau,\omega) = \int_{-\infty}^{\infty} \text{x(t)w(t}-\tau)\text{e}^{-\text{j}\omega\text{t}}\text{dt}, \tag{54a}$$

where $\tau$ and $\omega$ are the time delay and Doppler frequency, respectively. The magnitude-squared of the STFT yields an estimate of the spectrogram:

$$\text{spectrogram}\{\text{x(t)}\}(\tau,\omega) \equiv \text{S}(\tau,\omega) = \left|\text{X}(\tau,\omega)\right|^2, \tag{54b}$$

where for any $\tau$, the "instantaneous" spectra is termed an energy spectral density (ESD). The term ESD is used instead of power spectral density to emphasize that the underlying process may be non-stationary and the spectral power density may not be constant during the observation period. The spectrogram is an intuitive basis on which to characterize a wind turbine, given that the time-varying Doppler velocity signatures are of interest.

To characterize the received signal, the correlation of the individual IQ observations is evaluated. The covariance of the IQ observation is calculated as

$$r_{xy}^{(IQ)}[i] = \begin{cases} \frac{1}{M-i} \sum_{j=0}^{M-i-1} x[j]y^*[i+j] & i \geq 0 \\ \frac{1}{M-|i|} \sum_{j=|i|}^{M-1} x[j]y^*[i+j] & i < 0 \end{cases}, \tag{55a}$$

where $^*$ indicates complex-conjugation and $M$ is the number of observation samples. In Equation 55a, signals $x$ and $y$ may be two different time series (i.e., the horizontal and vertical polarization signals) or the same signal. The IQ correlation is calculated from the

IQ covariance estimates as

$$\rho_{xy}^{(IQ)}[i] = \frac{r_{xy}^{(IQ)}[i]}{\sqrt{r_{xx}^{(IQ)}[0] r_{yy}^{(IQ)}[0]}}. \tag{55b}$$

For a completely stationary observer and scatterer, without time-varying dispersion or noise, the correlation will be unity. Slight variations in position or incident angle can result in a reduction of correlation as the time-lag increases. A complex scattering enviroment is composed of a collection of scattering centers, each with its own reflectivity factor and phase. The phase is determined by the component's position and backscatter phase shift. As the scatterers move, the reflectivity weighting factor or phase will change.

The correlation of the spectrogram can also be estimated. The "ESD correlation" implemented here is not strictly the correlation of the ESD; rather, it is the correlation of the STFT magnitude (or square root of the ESD). It is defined in this way so that the correlation is linearly proportional to the ESD (rather than linearly proportional to the square of the ESD). The ESD covariance, with the time-varying mean removed, is calculated for two ESD vectors as

$$r_{xy}^{(ESD)}[i] = \begin{cases} \frac{1}{M-i} \sum_{j=0}^{M-i-1} \left(\mathbf{X}_j - \overline{X_j}\right)^T \left(\mathbf{Y}_{i+j} - \overline{Y_{i+j}}\right) & i \geq 0 \\ \frac{1}{M-|i|} \sum_{j=|i|}^{M-1} \left(\mathbf{X}_j - \overline{X_j}\right)^T \left(\mathbf{Y}_{i+j} - \overline{Y_{i+j}}\right) & i < 0 \end{cases}, \tag{56a}$$

where the bar denotes the respective vector's mean. Similar to the IQ correlation, the ESD correlation is estimated as

$$\rho_{xy}^{(ESD)}[i] = \frac{r_{xy}^{(ESD)}[i]}{\sqrt{r_{xx}^{(ESD)}[0] r_{yy}^{(ESD)}[0]}}. \tag{56b}$$

Consider the implications of the ESD correlation. The ESD is derived from a windowed sample of IQ observations. The window duration should be small with respect to the inertial time-constants of the structure, which dampen vibration and oscillations. With an appropriate window, the mean position of the structure is nearly stationary, and changes in the phase center location are dominated by the blade motion. As the window shifts in time, the mean position is nearly constant (remaining within the zero-Doppler bin). For sufficiently short window lengths, the tower oscillation Doppler features cannot be resolved. The ESD then represents the relative motion about some mean position. Therefore, high correlation of the ESD will correspond to similar dynamic blade RCSs. If the position of the turbine changes over a rotation period, the IQ correlation (which resolves position changes as signal phase differences) at a full period may be uncorrelated, but the ESD can be identical.

The sequential IQ and ESD estimates considered in this work are separated by one pulse repetition period ($T$), which is 0.962 milliseconds. Similarly, the autocorrelation of the ESD and IQ time series is estimated at time-lags of integer multiples of $T$. To visualize the spectrograms, the Doppler frequency, $f_D$ (in Hertz), is converted to Doppler velocity, $v_D$ (in meters per second), by

$$v_D = -\frac{\lambda}{4T} f_D, \tag{57}$$

where $\lambda$ is the radar's wavelength. The minus sign is used so that objects with a closing distance (and positive Doppler frequency) have a negative Doppler velocity. For the ESD and IQ correlation estimate and analysis, 30,000 samples have been considered for each case (giving an observation period of 28.8 seconds). The correlation is plotted for time-lags up to 8 seconds as a balance between highlighting the correlation behavior over multiple wind

turbine rotation periods and retaining temporal fidelity of the correlation features in the figures.

Appropriate selection of the data window is important to spectral processing performance. For the purposes of investigation and characterization of a wind turbine's dual-polarized radar signature, a general purpose window providing good spectral and temporal localization is desirable. The temporal resolution of the data window is a function of the window's length and main-lobe width. The shape of the window influences the spectral side-lobe performance and frequency localization of the window function. For the spectral analysis presented here, a 64-sample sliding rectangular window is used (a total observation of approximately 61.6 milliseconds). The rectangular window was selected as a general window function with minimal manipulation of the selected samples. Refinement of this window function may enhance the results. The wind turbine ESD correlation indicates that the optimal window length is on the order of 64 samples. With the sliding window, the sequential ESD samples presented differ by a single IQ sample (i.e., 63 of 64 samples are common between sequential ESD estimates) and, therefore, will be artificially correlated.

## 4.2. Data Window

Data window selection is critical to spectral processing performance. The data windows can be tailored to specific applications. For the purposes of investigating and characterizating a wind turbine's dual-polarized radar signature, a general purpose window providing good spectral and temporal localization is desirable. Additionally, the spectral leakage (the contribution of power to spectral components outside the frequency bin, where the true frequency component is located) and spectral sidelobe performance of the window is important due to the large power contributions from some targets (specifically, ground clutter). Ground

clutter RCS, such as the wind turbine mast, may be 40 dB or more than the RCS of targets of interest. It is desired that the spectral sidelobe not obscure these targets of interest.

Both window length and window shape are explored here with regard to the characterization of the wind turbine signature. The temporal resolution of the data window is a function of the window's length and mainlobe width. The shape of the window influences the spectral sidelobe performance and frequency localization of the window function. An exhaustive evaluation of window functions for spectral characterization is not considered here. Instead, a comparison of window lengths of a rectangular window and the shape parameter for a Gaussian window is presented to highlight the non-trivial impact that window functions can have on spectral analysis. To examine the effects of window length, radar observations of a wind turbine are studied in this section. Using a rectangular window for the selection of IQ data, the length of the window is varied. The correlation behavior of the spectrogram is evaluated for the selection of the appropriate window length for the remainder of the investigation presented. The window lengths examined are integer powers of two.

A sample plot of the spectrogram correlation using different window lengths is shown in Figure 4.2. A sliding window with a shift of one pulse is used to generate each ESD. This is done to ensure that transient events (e.g., blade flash) are captured and so that the peak correlation can be identified, as it may not align with the turbine period when sub-sampled. The overlapping window introduces an artificial correlation in the data because of windowing effects. This artificial correlation is observed with an increase in window size. The optimal window provides a balance between frequency resolution and the temporal localization of correlation, as well as the high correlation between blade passes and between full rotations and the low correlation for intervals outside the blade-pass period. The $N = 64$ window length was selected to provide this balance.

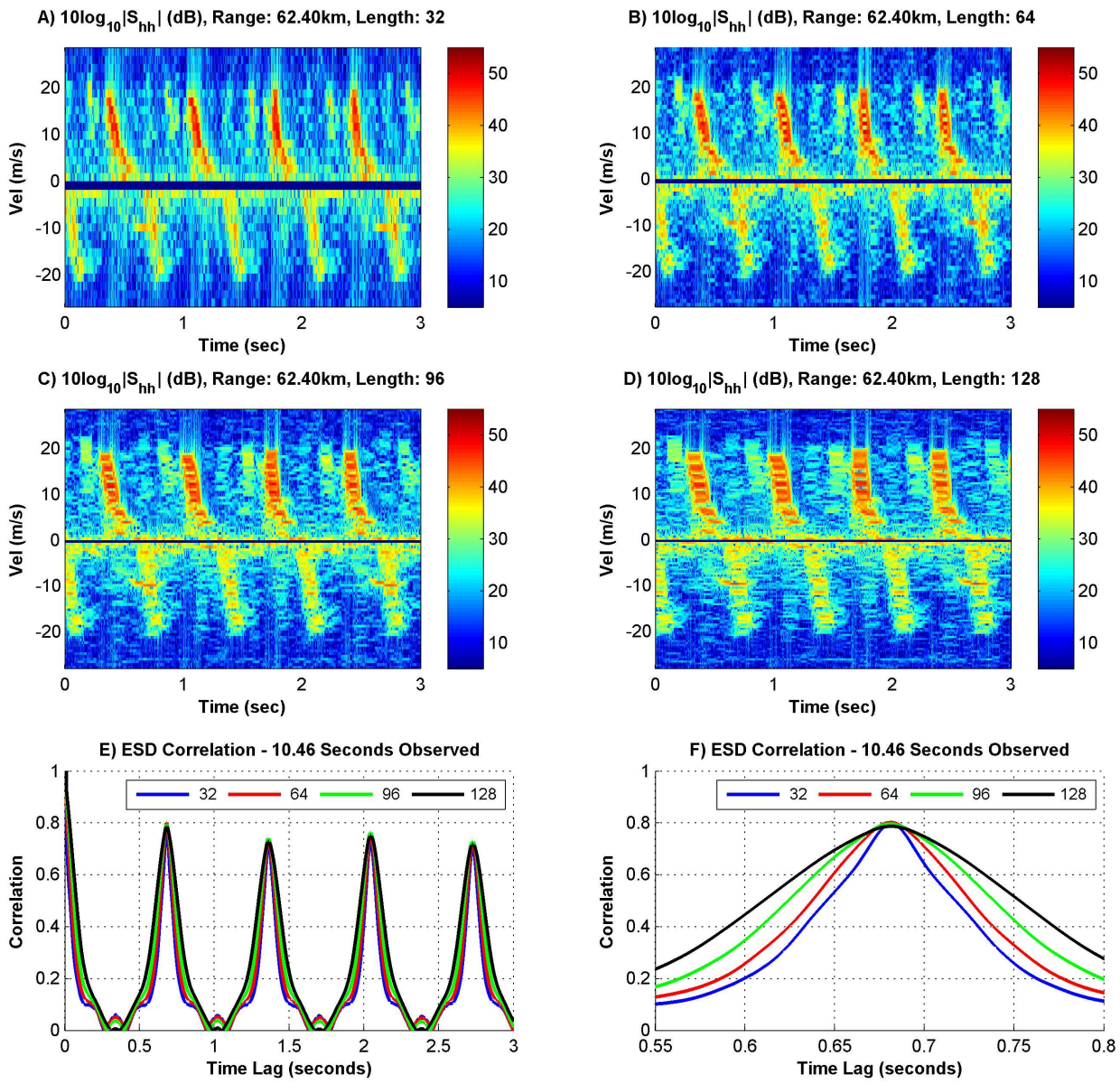


FIGURE 4.2. March 11, 2014, 14:33 UTC, at a range of 62.4 km. These figures show the spectrograms and their autocorrelations using different window lengths (in samples used). The window is shifted one sample at a time. The window size effect on the correlation between ESD vectors is apparent.

A number of window function shapes are available with differing spectral properties suiting them to particular applications. To evaluate the effect of window length, a rectangular window was considered. Take a Gaussian window function, described as

$$w[n] = e^{\frac{1}{2}\left(\alpha \frac{n}{N/2}\right)^2}, \tag{58}$$

where $-\frac{1}{2}(N-1) \leq n \leq \frac{1}{2}(N-1)$ and there is a shape factor, $\alpha$. The standard deviation, $\sigma$, is related to the shape factor by $\sigma = N/(2\alpha)$. The Gaussian window function has a Gaussian shape in both the temporal and frequency domains. As the temporal width narrows, the spectral width increases. In Figure 4.3, the same wind turbine case used to examine window length is used to evaluate the effect of window shape using overlapping windows with $N = 64$ samples. A direct comparison between the rectangular window in Figure 4.3A and the Gaussian window with shape factor $\alpha = 4.0$ in Figure 4.3B can be made. The temporal resolution of the observations increases with the narrower Gaussian window at the expense of reduced Doppler frequency resolution. The impulsive spectral noise observed in the rectangular window is significantly reduced by the tapered Gaussian window. For reference, the window shapes applied to the IQ vectors prior to the discrete Fourier transform are shown in Figure 4.3C. The correlations for the various window functions (for time-lags including the first blade-pass period) are shown in Figure 4.3D. The Gaussian windows up to and including a scale factor of $\alpha = 2.5$ show approximately the same peak correlation for the blade-pass period. For $\alpha = 2.5$, the ESD correlation, frequency localization, and temporal localization show good performance. As the shape factor continues to increase, a slight reduction of the peak correlation is noticed, and the correlation with time-lags between blade passes increases.

Now, consider observations of precipitation with the stationary power (i.e, the IQ vector's mean) removed as shown in Figure 4.4. The steady-state correlation of precipitation increases with the spectral broadening effects induced by the window function increase. The decorrelation time of the precipitation observations decreases as the window function's width decreases (and as the shape factor $\alpha$ increases).

The Gaussian window parameter controls the shape of the window, which equates to a spectral broadening factor. A Gaussian window function is also representative of the antenna

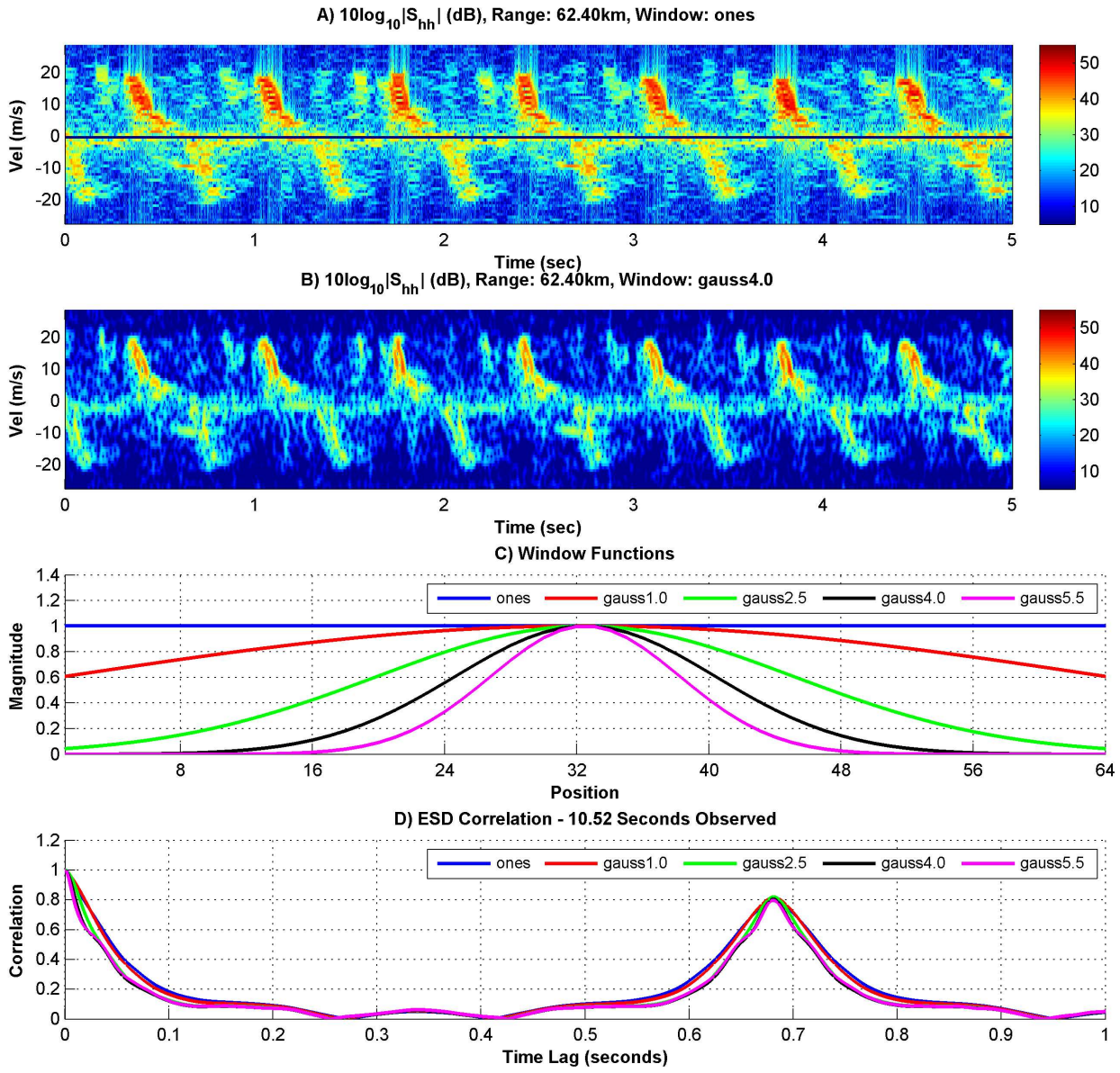


FIGURE 4.3. Wind turbine observations from March 11, 2014, 14:33 UTC, at a range of 62.4 km, with ground clutter suppressed. The graphs show the spectrograms and their autocorrelation using different Gaussian window shapes for a 64-sample window. The window is shifted one sample at a time.

pattern's gain-weighting effect during scanning (but neglects the antenna's phase). Scanning of the antenna acts to spectrally broaden observations of wide-sense stationary scatterers.

For the purposes of developing a generalized wind turbine signature suppression technique, highly detailed temporal and spectral features may not be desirable. If the object being observed does not meet the Nyquist sampling criteria (i.e., Doppler aliasing occurs),

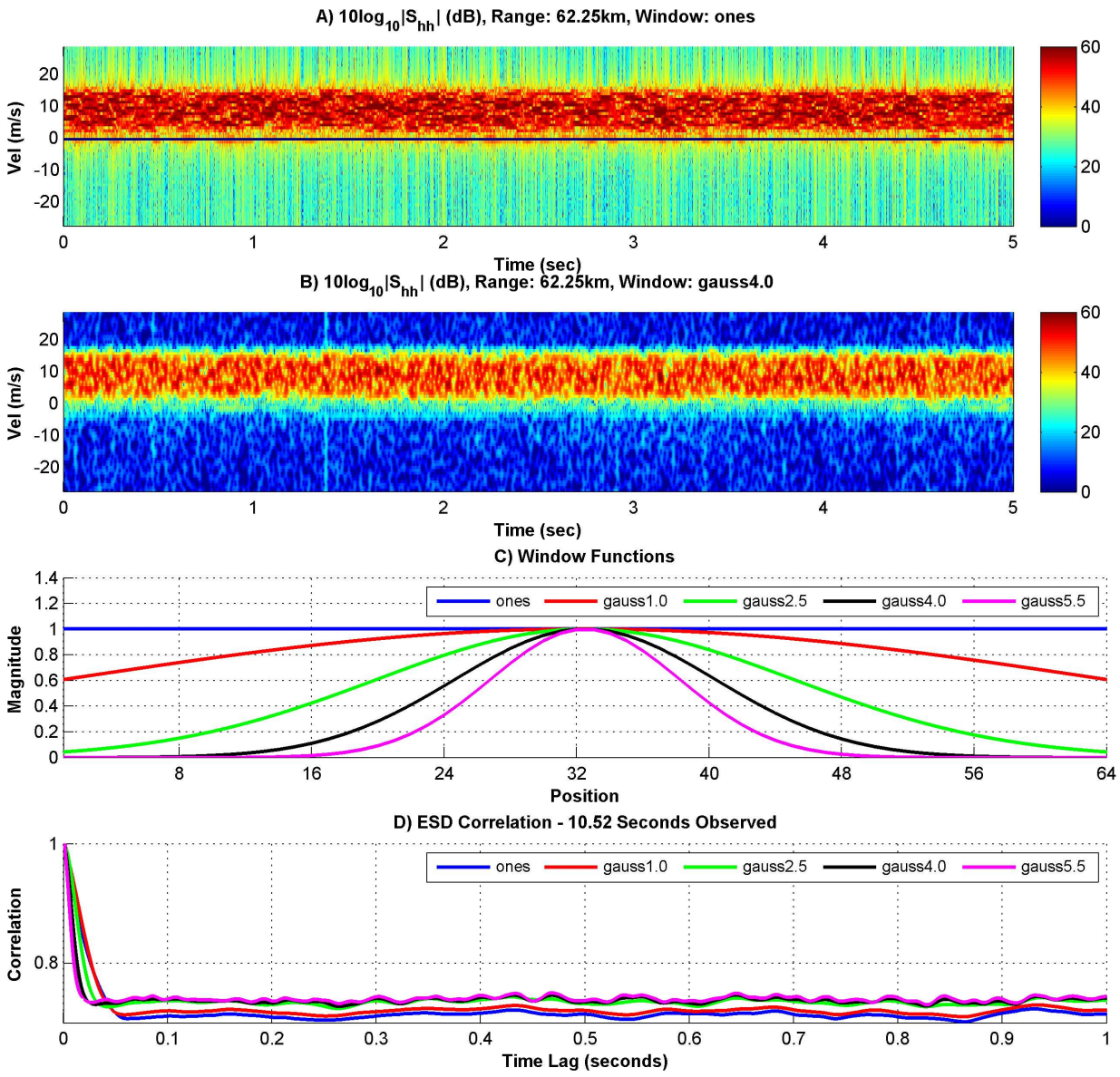


FIGURE 4.4. Precipitation observations from June 26, 2014, 23:07 UTC, at a range of 62.25 km, with ground clutter suppressed. The spectrograms and their autocorrelations are shown for precipitation using different window shapes for a 64-sample window length. The window is shifted one sample at a time.

these fine temporal and spectral features can result in a reduced correlation if the object is not sampled precisely at the instance where correlation (or decorrelation) is desired. Some flexibility in the sampling may be necessary to preserve a suppression algorithm's performance when sub-sampling the physical process within the observation volume. For observations

of a wind turbine with induced random oscillations, spectral and temporal broadening can reduce the effects of such "noise" by acting as spectra-averaging filters.

In the spectral analysis presented next, an $N = 64$ sliding rectangular window is used, unless noted otherwise. The rectangular window was selected as a general window function that has minimal manipulation of the available samples. There is room for future refinement of this window function to enhance performance and suppression depending on observation conditions. Sequential ESD samples differ by a single IQ sample. The unbiased ESD magnitudes are considered in the correlation of ESD spectra. All necessary phase information is included in the Doppler velocity. For IQ correlation, the complex-valued samples are used for determining it. The mean of the IQ samples is zero.

## 4.3. Ground Clutter, Precipitation, and Noise Observations[2]

Before characterizing a wind turbine's radar signature, noise, precipitation, and ground clutter are considered to more effectively understand and isolate the turbine's characteristics. Other sources of signal power can exist but will not be investigated here. This discussion of ground clutter and precipitation is not exhaustive but demonstrates their fundamental characteristics in the context of differentiating a wind turbine's dual-polarization radar signature. Thus, to consider precipitation and ground clutter, range-volume cells at ranges prior to any wind turbines were selected to ensure that no multi-path contamination from the turbines was present in the observations.

Radar system noise is typically modeled as additive Gaussian white noise [17]. For white noise sources, the IQ auto-correlation is zero for time-lags greater than zero. For a wide-sense stationary noise source, the mean spectrum magnitude is constant for all frequencies. If the correlation between two independent, noise-only ESDs is taken without the mean removed

[2]©2016 IEEE [1]

(i.e., biased correlation), the correlation tends to unity for all time-lags as the window length extends to infinity. If the mean is removed, any variation is noise-like, and the correlation between the unbiased, independent spectra for non-zero time-lags will tend toward zero (again, as the window length extends to infinity).

Ground clutter filters work by selectively removing a narrow band of Doppler spectra under the assumption that the ground clutter is not moving with respect to the radar. For weather applications, more sophisticated ground clutter filter (GCF) algorithms estimate the precipitation spectra and then interpolate to add back the precipitation power (that was erroneously removed as ground clutter) in the GCF's Doppler range [27, 28]. Given that fixed-pointing observations are used exclusively, and for simplicity, the stationary clutter filtering was performed by subtracting the mean from the IQ data vector, which effectively removes all power in the zero-Doppler velocity bin. This method of filtering ground clutter demonstrates good results, with minimal impact on the overall Doppler spectra, by only modifying a single spectral bin.

Figure 4.5 presents observations of ground clutter. Figures 4.5A through 4.5D do not use GCF. Figures 4.5E through 4.5H have GCF enabled. A representative example of the IQ time series magnitude is shown in Figures 4.5A and 4.5E, and the corresponding ESD time series is shown in Figures 4.5C and 4.5G. The IQ and ESD correlations, estimated from 28.8 seconds of observations, are presented in Figures 4.5B/F and 4.5D/H, respectively. The correlation behavior of the IQ observations and ESD observations are similar for ground clutter. In this example, the H-polarization auto-correlation is slightly lower than that of the V-polarization auto-correlation, but this is not necessarily representative of all ground clutter targets. The H-V cross-correlation remains near unity for the observation period. Physically, the correlation of a stationary target should approach unity if no variation in aspect angle or position occurs, regardless of polarization, because the same aspect of the target is observed.

For the ESD correlation, because overlapping samples are used, an artificial correlation was observed for time-lags up the window length. For Figures 4.5D through 4.5H, if all ground clutter is sufficiently suppressed, ideally the only remaining observation is radiometric noise. Comparing the IQ correlation of Figure 4.5B to Figure 4.5F, suppression of the ground clutter results in the IQ observations being nearly uncorrelated. Similarly, the ESD correlation in Figure 4.5D can be compared to Figure 4.5H, showing a substantial reduction in the auto-correlation of the individual polarizations. Residual correlation in the IQ and ESD is likely due to a residual signal, possibly from spectral leakage (due to the window), Bragg scatter, or biological scatterers.

In Figure 4.6, the time series containing a mixture of ground clutter and precipitation (rain) is presented. As with the ground clutter-only examination, the IQ time series magnitude and the ESD time series are presented with their respective polarization correlations. With ground clutter included, both the IQ and ESD time series are well correlated for extended time periods due to significant reflectivity weighting of the ground clutter component. With the ground clutter suppressed, the observed spectra are now dominated by precipitation, with little residual bias due to stationary clutter or noise. Compare the IQ and ESD correlations of Figures 4.6B/D, with ground clutter included, to those of Figures 4.6F/H, with ground clutter suppressed. The IQ correlation behavior is similar to that of noise only, with limited correlation between successive samples. The intensity of the precipitation and microphysical behavior can vary the IQ decorrelation time and may be on the order of tens of milliseconds [17]. After sufficient time-lags, the IQ correlation will decay to zero. For the ESD correlation in Figure 4.6D, there is a fast decorrelation, limited by the sliding window function used, and then a steady-state correlation of approximately 0.7 for this example. The ESD correlation is the result of a near-constant spectral shape of precipitation during the observation period. For a wide-sense stationary physical process, this shape will remain

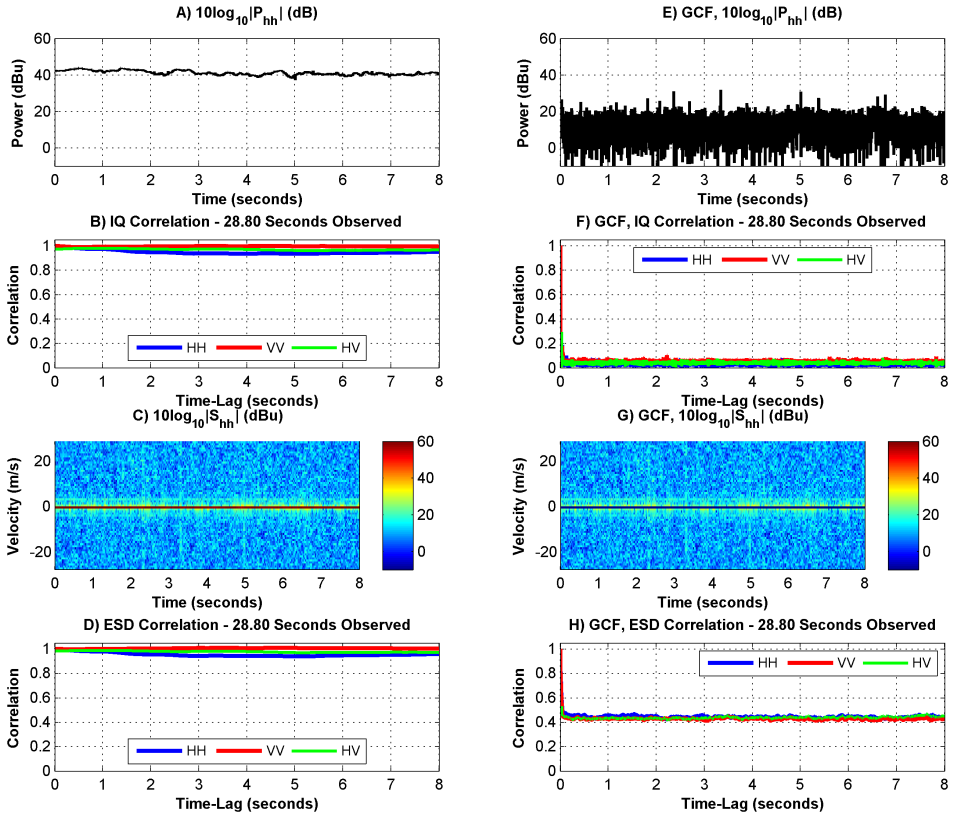


FIGURE 4.5. CSU-CHILL observations of ground clutter only on March 11, 2014, 14:33 UTC. The ground clutter was observed at a distance of 62.25 km for a duration of 28.8 seconds. The sample IQ time series magnitude and ESD magnitudes are presented along with the correlation behavior of both time series with and without zero-Doppler clutter filtering. The $P_{hh}$ IQ observations represent the single-pulse horizontal reflectivity observations. Graph A shows $P_{hh}$ without ground clutter filtering (GCF), and Graph E is the same observations with ground clutter filtering enabled. In Graph B, the auto-correlation function of the horizontal (HH) and vertical (VV) polarization IQ observations is shown for time-lags up to 8 seconds. The cross-correlation between the horizontal and vertical polarizations (HV) is included. The auto-correlations and cross-correlation for the IQ observations with GCF enabled is shown in Graph F. The ground clutter results in a high degree of correlation in Graph B, which is not observed in Graph F with GCF. The ESD ($S_{hh}$) for the horizontal-polarization observations is shown in Graph C without GCF and in Graph G with GCF. Similar to the IQ correlations, the ESD vector auto-correlation and cross-correlation is calculated using Equation 56b. As with the IQ correlation, the ground clutter exhibits a high degree of sustained correlation. With the GCF enabled, the ESD correlation is substantially reduced, and the residual correlation is a result of a non-zero mean noise power and a slight residual signal at non-zero Doppler velocities between -5 and 5 m/s.

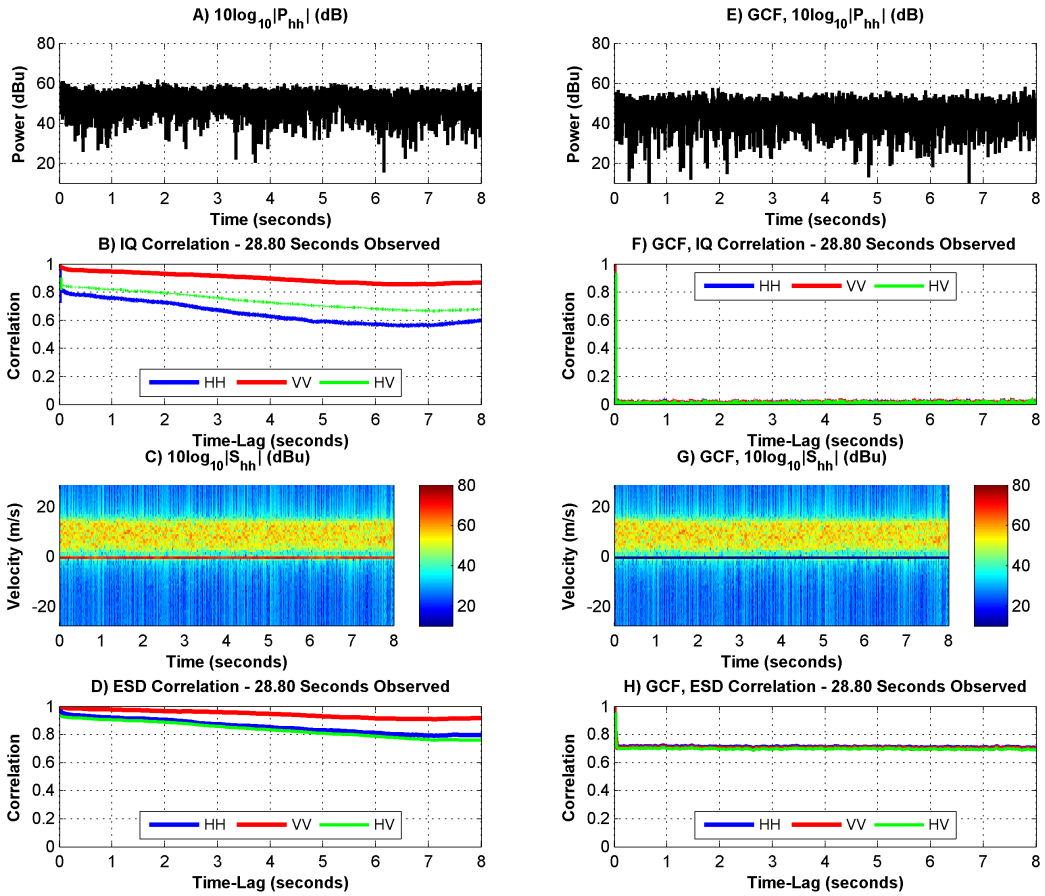


FIGURE 4.6. CSU-CHILL observations of precipitation with and without ground clutter suppression. The observations are from June 26, 2014, 23:07 UTC, at a range of 62.25 km for a duration of 28.8 seconds. The sample IQ time series magnitude and ESD magnitudes are presented along with the correlation behavior of both time series. Graphs A through D are without GCF, and Graphs E through H have GCF enabled. The ground clutter's biasing effects are observed in the IQ and ESD correlations. The precipitation's mean ESD shows a high degree of sustained correlation once ground clutter is suppressed (Graph H). This correlation behavior is not observed in the IQ correlation with GCF (Graph F). The IQ correlation of precipitation has a decorrelation time on the order of tens to hundreds of milliseconds at S-band [17].

constant. The movement and reshuffling of hydrometeors within the observation volume can result in coherency noise in the estimated Doppler spectra. This coherency noise, for short time observations, is observed in the ESD correlation behavior as the noise-like decorrelation over short time-lags but with a higher steady-state correlation. The wide-sense stationary underlying spectral shape results in the near-constant, sustained correlation of precipitation.

## 4.4. Wind Turbine Observations[3]

The three main wind turbine components each contribute to a wind turbine's total RCS. The turbine's nacelle and tower are stationary ground clutter and can be suppressed using ground clutter filter techniques. The rotating turbine blades present a time-varying RCS with a non-zero radial velocity component. The resulting Doppler spectrum is time-varying, and in some cases, the radial velocity can exceed the ambiguous Doppler velocity limits of the radar (i.e., velocity-aliasing occurs). This time-varying velocity component due to a wind turbine's blades is the primary source of complexity in the characterization of a wind turbine's RCS.

CSU-CHILL radar observations of the Ponnequin Wind Farm at an azimuth angle of 346.63 degrees and an elevation of 0.51 degrees are considered at a 62.4 km range. The range cells considered here are 150 meters long and, with the antenna's 1.0-degree beamwidth, approximately 1.09 km in diameter. This range-volume cell is of interest due to scattering dominated by a single wind turbine. There may be contributions from other wind turbines in this range-volume cell from antenna side-lobes or possibly wind turbines partially included in the range-volume cell, but these contributions are significantly lower than that of the primary wind turbine of interest. Similar to prior examinations of ground clutter and precipitation (Figures 4.5 and 4.6, respectively), the correlation behavior 28.8-second observation period is presented in Figure 4.7. A representative length of the IQ and ESD time series (with/without GCF) is shown in Figures 4.7A/E and 4.7C/G, respectively. The correlation of the IQ and ESD observations is considered in Figures 4.7B/F and 4.7D/H. The rotation period of this three-blade wind turbine is approximately 2 seconds, suggesting a Vestas V47 wind turbine, which is consistent with the wind farm's layout and the radar's observation angles.

[3]

Without GCF, the IQ correlation fails to highlight the periodicity of the wind turbine signature. From the high steady-state IQ correlation, it appears to be significantly weighted by stationary ground clutter. The ESD correlation, on the other hand, effectively highlights the periodicity of the wind turbine's blade. This periodic behavior has a distinct influence on the ESD correlation (Figure 4.7D) but remains small due to the significant biasing effect of the stationary ground clutter. When the ground clutter is suppressed, the IQ correlation (Figure 4.7F) exhibits a periodic structure but with very low correlation. Compare this to the ESD correlation with the GCF (Figure 4.7H), which shows a substantial correlation between the individual wind turbine blades. It also appears that correlation with the same blade (at multiples of a full rotation period) is slightly higher than the correlation of different blades. This may indicate a slight asymmetry between the three blades.

Inspection of the ESD correlation also reveals an exponentially decaying correlation with time. The decorrelation of the ESD as the time-lag increases can result from state variation due to a wind turbine's control system and/or stochastic motion due to wind-forcing. Fitting the wind turbine peak correlations with an exponential function may not predict a lag-zero correlation of one. This underestimation is likely a result of the wind turbine's "state noise" due to stochastic, wind-forced motion and time-varying control system variation. Consider the observed peak Doppler velocity for each blade-pass period (a third of a rotation period) in the ESD time series in Figures 4.7C/G. The peak velocities vary from blade-pass to blade-pass, with deviations of 2 m/s or more ($> 10\%$ of the velocity). This slow time variation is consistent with the time-constants of wind turbine control systems for yaw angle variation [5].

In Figure 4.8, the correlation structure within the individual Doppler velocity bins of the spectrogram is examined. This evaluation considers the same spectrogram used in Figure 4.7 where the entire Doppler spectra was correlated. Note that the correlation structure is

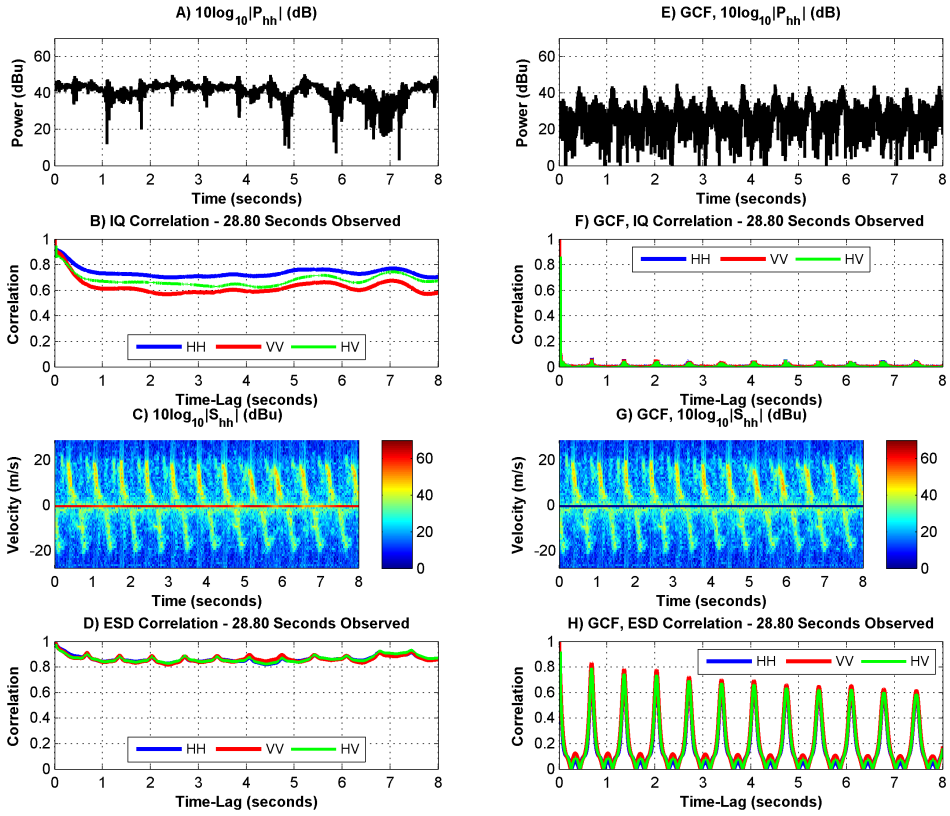


FIGURE 4.7. CSU-CHILL observations primarily consisting of one wind turbine with and without ground clutter suppression. The observations are from March 3, 2014, 14:33 UTC, at a range of 62.4 km. A simultaneous mode observation period of 28.8 seconds is used to estimate the correlation behavior. The sample IQ time series magnitude and ESD magnitudes are presented along with the correlation behavior of both time series, highlighting the biasing effect of strong ground clutter RCS on the correlation. Graphs A through D are with the GCF disabled, and Graphs E though F implement GCF. A periodic structure due to the rotating blades is observed in most graphs. The observations without GCF are biased by the significant RCS of the ground clutter (here, this included the wind turbine's tower and nacelle). The IQ correlations without GCF hint at a periodic structure but with a low frequency of oscillation that may be indicative of a swaying tower. This is also supported by the low IQ correlation at the blade-pass period with GCF enabled. (The blade-pass period is one-third of the rotation period for a symmetric three-blade wind turbine.) The ESD correlation without GCF (Graph D) indicates a substantial bias from the ground clutter. This bias is removed when the GCF is applied (Graph H), and a high degree of correlation is observed, peaking at multiples of the blade-pass period. The decay of the peak correlations at multiples of the blade-pass period indicates that the wind turbine's state is somewhat dynamic and may be a result of non-steady wind loads or a variable yaw angle during the observation period. This dynamic situation is supported by both the ESD and IQ correlations with and without GCF.

similar for all Doppler velocity bins occupied by the wind turbines echo and each exhibit a distinct periodic signature. In general, a faster decorrelation around the blade-pass period is observed for echoes with higher Doppler velocity magnitudes. The zero-Doppler bin contains the sustained high correlation of the echoes from stationary ground clutter. The velocity bins free from echo power (i.e., noise only bins) occupy velocity bins with a magnitude greater than $\pm 22$ m/s. For these noise-only Doppler bins, some residual spectra leakage from the turbine is observed in the correlation structure but, in general, the correlation of the noise power is high for the time lags considered here.

For the CHILL S-band radar configuration used, the radars total unambiguous velocity range is approximately 57.2 m/s (i.e., $\pm 28.6$ m/s). Consider the Vestas V47 turbine operating at its nominal rotation rate; The blade tip speed is $\pm 70.1$ m/s from Table 3.1. As the wind turbine's yaw angle (with respect to the radar's radial) approaches either 90 or 180 degrees, velocity aliasing of the echoes from the turbine's blade will occur. These velocity-aliased echo features will also be periodically correlated.

Up to now, the discussion has focused only on copolar observations in the simultaneous transmit and receive mode. Consider the H-only mode, where only the horizontal-polarization is transmitted, and both polarizations are received. This allows for the characterization of the horizontal copolar and the cross-polar scattering signatures. Figure 4.9 considers H-only observations of a wind turbine with embedded, light precipitation. The GCF is enabled for these results to focus on the characteristics of precipitation and the wind turbine. In Figure 4.9D, the cross-polar observations clearly show the wind turbine's signature, while the cross-polar signal from rain remains negligible. This is expected from rain hydrometeors, which have low cross-polar scattering [17]. From close comparisons of the copolar (Figure 4.9C) and cross-polar spectrograms (Figure 4.9D), a difference in location of the "peak" is noticed (both temporally and in the Doppler velocity). This difference is a

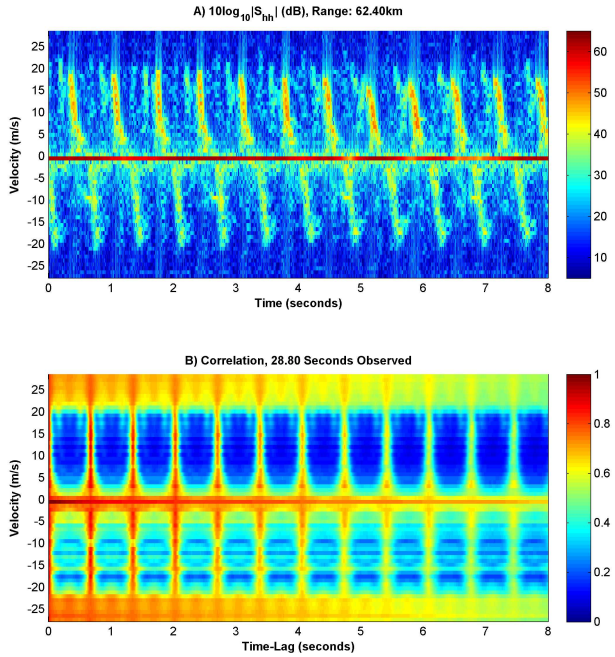


FIGURE 4.8. The correlation structure of the individual Doppler bins is estimated for the same observations as Figure 4.7. A subset of the 28.8 second long H-polarization spectrogram is shown in Graph A. Graph B shows the correlation of each of the 64 Doppler velocity bins for time-lags up to 8 seconds. For all Doppler bins containing echoes from the rotating wind turbine, a periodic correlation is observed with the same periodicity. The zero Doppler bin is dominated by ground clutter and the turbine's tower and nacelle.

result of the variations in scattering characteristics between the leading and trailing edges of the wind turbine blade. The leading edge is a large and slowly varying surface (with respect to the radar's wavelength). Cross-polar scattering is typically attributed to physical features that are on the order of a wavelength. (Edges and sharp transitions are such features.) If the positive Doppler velocities represent the leading edge of the wind turbine blades, then the negative Doppler velocities will contain scattering from the trailing edge of the blades, where physically "sharp" features are more prevalent.

The wind turbine's IQ correlations (Figures 4.9E and 4.9F) show periodic correlations, which indicate that the spatial correlation of the scattering centers is high (i.e., there is little blade vibration or tower motion). Figure 4.9G shows the ESD auto-correlation of the copolar echo (hh,hh) and auto-correlation of the cross-polar echo (vh,vh). Figure 4.9H shows the

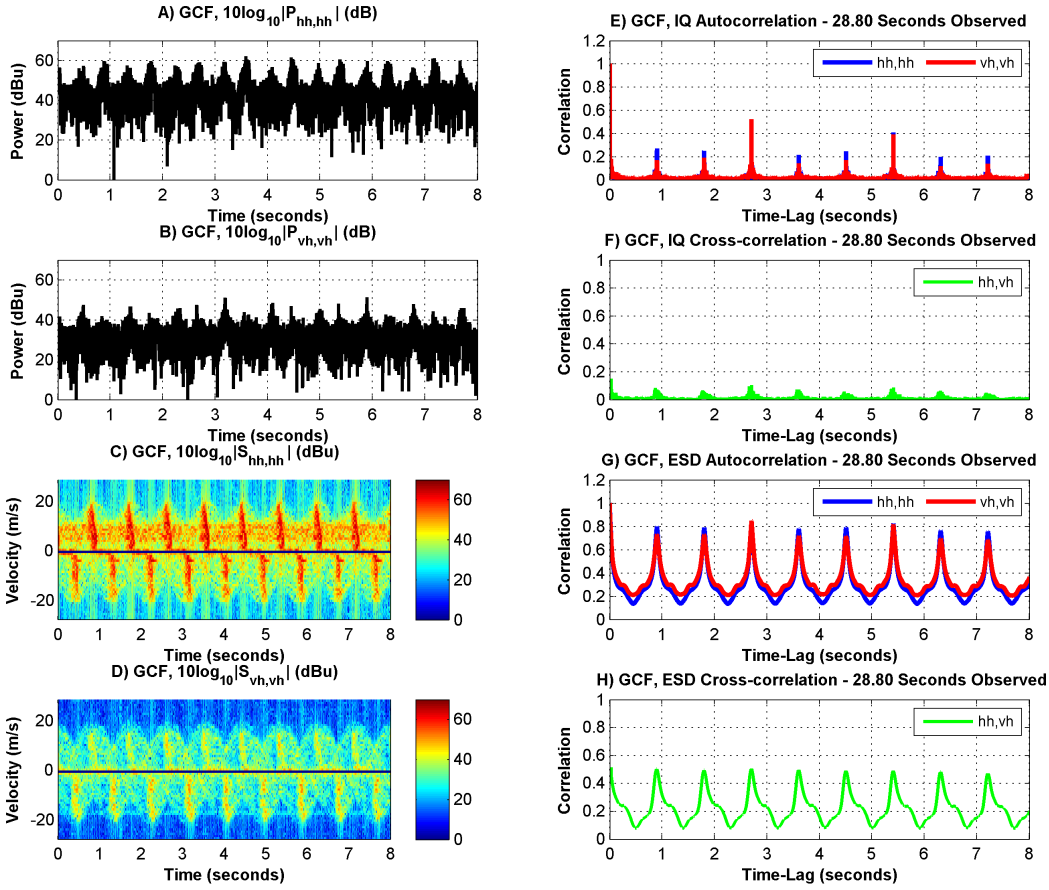


FIGURE 4.9. CSU-CHILL S-band observations on June 26, 2014, 23:10 UTC, in H-only mode. The IQ and ESD copolar (hh) and cross-polar (vh) observations and correlations are presented for a wind turbine with embedded, light precipitation at a range of 62.55 km. The GCF is enabled for all observations. Graph A shows the individual pulse, horizontal copolar power ($P_{hh,hh}$) time series. Graph B shows the individual pulse, horizontal cross-polar power ($P_{vh,vh}$) time series. Similarly, the spectrograms for the copolar observations ($S_{hh,hh}$) and cross-polar observations ($S_{vh,vh}$) are shown in Graphs C and D, respectively. The precipitation is observed in Graph C, primarily in the 5 to 10 m/s spectral bins. The auto-correlation for the IQ observations is shown in Graph E, and the copolar to cross-polar cross-correlation for the IQ observation is shown in Graph F. The ESD time series auto-correlations are presented in Graph G, and the cross-correlation of the copolar and cross-polar spectrograms appears in Graph H. The IQ correlation shows a higher degree of correlation than that observed in Figure 4.7 while the ESD correlation decay rate is significantly lower. This indicates that the wind turbine state is more stable and may imply reduced dynamic wind-loading (which allows for a higher IQ correlation for long time-lags).

ESD cross-correlation between the copolar and cross-polar spectra. For all ESD correlations, the correlation at time-lags that are integer multiples of a full rotation period (i.e., the same blade) is higher than the correlation between different blades of the turbine. Both the cross-polar and copolar ESD auto-correlations show similar behavior in this regard. The cross-correlation shows an asymmetry around the blade-pass period time-lags not readily observed in the auto-correlations.

4.4.1. Cyclostationarity of a Wind Turbine's RCS[4]. A wind turbine's rotating blades result in a periodic ESD correlation with a high degree of correlation at integer multiples of the blade-pass period. A review of Figures 4.7 and 4.9 clearly shows this periodic correlation, which is unique to the wind turbines in the three classes considered here. For short observation windows with steady wind, the yaw angle, blade pitch, and rotation rate are nominally constant. Given these physical characteristics, a high degree of periodic correlation is expected. Ideally, for perfect 120-degree blade symmetry, the peak correlation will be observed at the blade-pass period. Slight irregularities, however, in the blades can result in the peak correlation being observed at the full rotation period.

A wide-sense stationary process is described by time-invariant first- and second-order statistics. A wide-sense cyclostationary process can be described by first- and second-order statistics that are time-varying up to some period and then repeated [55]. Note that stationary processes are a subset of cyclostationary processes. A wind turbine, with rotation angle ($\theta$) as the only time-varying state variable, is an example of a cyclostationary process. The radar's received signal is modeled as a zero-mean stochastic process, with variance proportional to the RCS of the observed scatterers. Assuming that the only variation in the observed wind turbine's RCS is due to rotation, the stochastic process can be assumed to be ergodic at each time-lag. For an ergodic process, realizations in time can be used to estimate

[4]©2016 IEEE [1]

the process' statistics. Because a cyclostationary process is time-varying for some period and then repeats, to be ergodic the temporal samples for estimating the statistics must be observed at the same time-lag with respect to a reference-state. For a wind turbine, the reference state can be fixed at any rotation angle $\theta_0$ (this does not necessarily need to be the reference blade located at top-dead-center). For the wind turbine observations considered in Figure 4.7, the estimated wind turbine rotation period is approximately 2.032 seconds. This estimate is consistent with the Vestas V47 wind turbine's nominal rotation period of 2.105 seconds (which is allowed to vary by $\pm 10\%$ from nominal).

The previous correlation presented for the wind turbine assumes that for all starting rotation angles, the same periodic correlation structure exists. From the scale model results in [12], the decorrelation times have been shown to be shorter for observations near the blade flash. To consider the correlation structure of full-scale wind turbine observations, 22 full rotations are used in Figure 4.10 to estimate the correlation between the starting rotation angle, $\theta_0 = \theta_i$, and all other angles within a full rotation. Figure 4.10A shows a subset of the spectrogram used for estimating the correlation, with the mean of each ESD (in dB) subtracted. Upon close observation, slight variations in the wind turbine's spectral response are noticed from rotation to rotation. It must be noted that this analysis assumes that the wind turbine is wide-sense stationary in all states except rotation, for which it is assumed to be wide-sense cyclostationary. These fluctuations are likely due to variations in yaw angle, and, therefore, the wide-sense cyclostationary assumption is only approximated.

Using the 22 rotation observation period, the correlation of the ESDs, as a function of rotation angles, is presented in Figure 4.10B. The correlation at the blade-pass period is high regardless of starting rotation angle, as expected given the symmetry of the blades. The positive velocity, leading-edge blade flashes are at the rotation reference angles of approximately 80, 200, and 320 degrees. The broad spectral "flash" exhibits some correlation

with the negative velocity, trailing-edge blade flash, which is offset by approximately 60-70 degrees after each of the leading-edge blade flashes. The regions of the wind turbine's spectrogram in between the blade flashes, where the total RCS is lowest, exhibit longer correlation times around the blade-pass intervals but show a lower peak correlation at rotation lags corresponding to the blade-pass interval (consider rotation reference angles of 110, 230, and 350 degrees). When the total RCS is lowest, the ESD has a lower signal-to-noise ratio. The increased noise factor likely contributes to the reduced correlation at these intervals.

Figure 4.11 considers the cyclostationary statistics of the clear-air wind turbine echo power observations from Figure 4.7. The echo power here is the mean power of the ESD with ground clutter suppression. Using the estimated rotation period of 2.032 seconds, Figures 4.11A and 4.11B present 22 individual realizations of the full rotation period for the horizontal received power ($P_h$) and differential reflectivity ($Z_{dr}$), respectively. These 22 realizations are used to calculate the statistics presented in Figures 4.11C through 4.11F. Some variation in the wind turbine's yaw angle is apparent during the observation time, which results in slight translations of the peak power observations in some of the realizations shown in Figure 4.11A. Here, it is assumed that the rotation rate of the wind turbine ($\dot{\theta}$) is constant. Therefore, time ($t$) and the rotation angle ($\theta$) can be interchanged ($\theta = \dot{\theta}t$). The wind turbine's RCS (and thus the echo power) is expected to be cyclostationary with the rotation angle. But for a time-varying rotation rate, the process but will no longer be cyclostationary with respect to time.

The mean H-polarization echo power (the signal variance) and mean $Z_{dr}$ (the ratio of the signal variance) are shown in Figures 4.11B and 4.11E, respectively. The time-varying echo power highlights that the RCS is periodic with the blade-pass period. Although the mean power was considered over a full rotation period, ideally the wind turbine is rotationally 120 degrees symmetric. This rotational symmetry is demonstrated by the three nearly identical

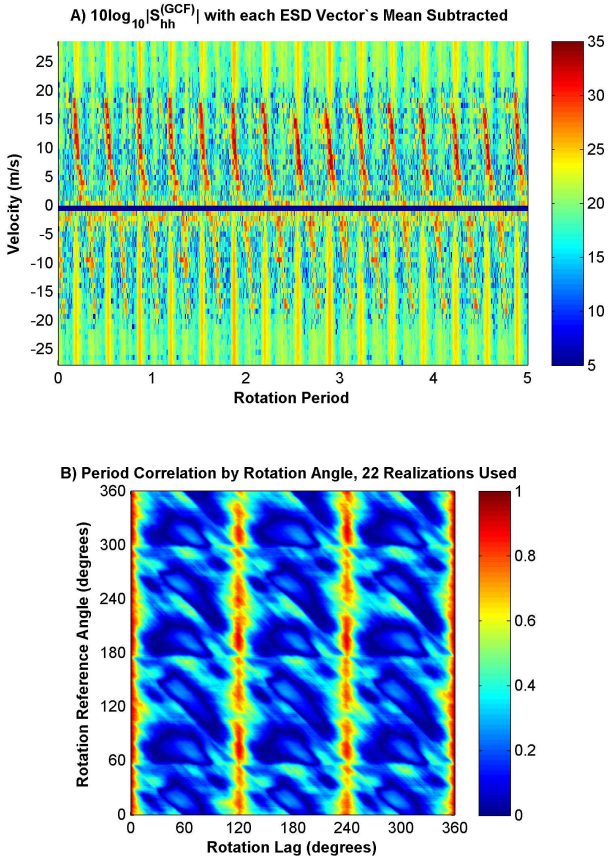


FIGURE 4.10. CSU-CHILL observations of a wind turbine in clear air conditions on March 11, 2014, 14:33 UTC, at a range of 62.4 km. A subset of the observed spectrogram, with the ESD's mean (in dB) subtracted and the zero-Doppler bin set to zero, is shown in Graph A. Graph B shows the ESD correlation (from the data of Graph A) as a function of the absolute rotation angle and rotation-lag. The rotation reference angle is incremented over 360 degrees, so that it starts at all rotation angles. The observations at the reference angle are correlated with all other angles of the rotation (denoted as the "rotation-lag"). Twenty-two realizations of the ESD at each available rotation angle are used for estimating the correlation. Regardless of the rotation reference angle, a periodic correlation is observed with 120 degrees of symmetry.

periods in the results. The standard deviation of the logarithmic echo power in Figures 4.11C and 4.11F highlights that the observations, from period to period, have some variability. The standard deviation of the realizations is highest around the blade-flash, when the fastest decorrelation is observed.

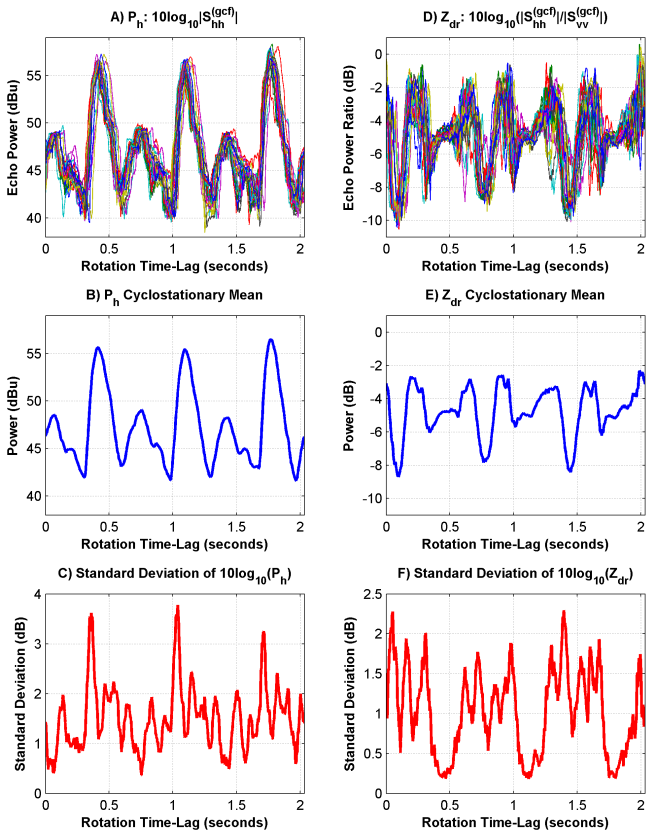


FIGURE 4.11. CSU-CHILL observations of a wind turbine in clear air conditions on March 11, 2014, 14:33 UTC, at a range of 62.4 km. Graph A shows the time series of the mean power of the H-pol ESD (with GCF) divided into 22 full rotation periods. Graph B shows the $Z_{dr}$ estimates and the ratio of the horizontal polarization to the vertical polarization mean ESD power, with the GCF enabled. The cyclostationary mean (Graphs C and D) and standard deviation (Graphs E and F) of the logarithmic powers are shown for both $Z_h$ and $Z_{dr}$. The 120-degree rotation symmetry is observed in all graphs. A review of Graphs A and B shows that the blade "flash" due to the leading edge of the turbine blade has a higher horizontal reflectivity than the trailing edge of the blade. For $Z_{dr}$ observations in Graphs D through F, the trailing edge of the blade exhibits a lower differential reflectivity than the leading edge. The horizontal reflectivity has a high standard deviation in the observations at the onset of the leading-edge blade flash, indicating a fast transition and higher sensitivity to accurate rotation rate estimates. For the $Z_{dr}$ standard deviation in Graph F, the standard deviation is lowest during observations of the leading edge of the blade and has a higher variability through the rest of the rotation.

## 4.5. Discussion[5]

Section 4 introduced dual-polarization spectral features of ground clutter, precipitation, and wind turbines. The features of these three classes of scatterers will be compared and discussed in this section to highlight differentiating features. The dual-polarization scattering properties, cyclostationary characteristics, and physical (or microphysical) structures will also be considered.

Ground clutter is a narrow-band Doppler feature centered at zero-Doppler velocity for a stationary radar system. For weather radar applications, ground clutter is typically suppressed as an unwanted echo source. The echo power from ground clutter can be multiple orders of magnitude greater than other signals of interest. The ground clutter can act to bias estimates of reflectivity-weighted parameters such as velocity or signal correlation. Using existing techniques for ground clutter suppression, the wind turbine's nacelle and tower, which are typically a significant source of wind turbine echo power, may be separated from the rotating structure.

For precipitation, the Doppler spectra is typically assumed to be Gaussian in shape. The mean velocity, spectrum width, and magnitude of precipitation will vary with time and may occupy any part of the Doppler spectrum (and may include velocity-aliasing). Precipitation's echo power can vary drastically in magnitude, in some cases overwhelming that of the wind turbine and ground clutter. The correlation behavior of precipitation has a structure similar to that of noise, with a constant bias for time scales at least on the order of seconds. Varying the ratio of the bias to the variance of the ESD can reproduce the correlation behavior of precipitation for a time interval in which the wide-sense stationary assumptions hold. The correlation duration is determined by the dynamic length scales of the atmospheric process, as well as the extent of the radar's observation volume. The spectral correlation of precipitation

[5]©2016 IEEE [1]

typically will be at least on the order of the wind turbine period, and, in general, the spectral correlation time constants can be much longer due to meteorological length scales. It should also be noted that wind turbines can distort the spectral characteristics of the precipitation (with the wind turbine physically acting on the precipitation). The wake vortex is dynamic and much different than the conditions without a wind turbine present. The wind turbine can induce a periodic signature for the precipitation spectra.

The turbine's tower location is fixed and does not move for the operational life of the wind turbine. Once a wind turbine is identified, neglecting abnormal wave propagation effects, its location and characteristics can be cataloged and monitored. The wind turbine's state parameters such as blade rotation, yaw angle, blade pitch, vibration, tower oscillation, etc., are loosely functions of wind velocity. From symmetry, the peak positive velocity must correlate to the peak negative velocity (although the radar may not observe this due to beam-blockage). With a constant rotation rate, the period of each Doppler velocity component must be the same for a given wind turbine. Once the wind turbine's state has been observed, that observation is representative of the same state for other observation times.

When the wind turbine's blades rotate at a constant rate about a fixed axis with no other state-variable changes, the behavior is cyclical in nature. The cyclic, physical behavior results in radar observations that can be modeled as cyclostationary processes, which also exhibit periodic correlations. The signal considered may be either the IQ or the ESD observations. For IQ observations, the periodic correlation is a more tenuous feature. For higher wind velocities and higher turbulence, the IQ correlation is expected to be very low. The correlation behavior of the IQ and ESD observations is related to the physical behavior of the wind turbine and the representation of both data sets. This will be discussed next.

The correlation of wind turbine echoes from one blade to another (or from one rotation to another) will be zero for non-zero time lags if all phase centers are independent between

observations. Even though a wind turbine has a fixed rest position (i.e., the state with no kinetic energy or elastic potential energy), the scattering phase center can vary through multiple wavelengths due to blade and tower deflection and oscillation in the wind. This motion can result in a near-uniform distribution of the phase center after accounting for phase-aliasing (recall that the position is measured by phase). This large spatial distribution approximates independent observations between samples when considering time-lags on the order of the blade-pass period. A wind turbine hub's position, mounted upon a tall tower, can vary by distances of meters as a result of deflection from wind forces. Even slow-moving (i.e., small velocity) variations due to vibrations or wind-forcing can result in large phase shifts during a full rotation period.

For IQ observations in which the nearly stationary tower and nacelle present a high RCS relative to the moving blades, the IQ observation is dominated by these stationary components' contribution. This can reduce the relative significance of the moving wind turbine blades' RCS in the instantaneously observed power and subsequent correlation. The correlation of the IQ observations is a phase-coherent measurement, meaning the phase relationship between the observations is considered (i.e., the positions are compared). The IQ correlation structure of the moving blades still has significance, which is easily visualized in the ESD. When the time-lags exceed the inertial time-constant of the scatterer (related to the structural oscillation and vibration frequencies), the phase center position due to it's motion is uncorrelated. The coherent integration time of observations is limited by the inertial (coherent) time-constants of the scatterers and limits the utility of the IQ auto-correlation function. Note that the coherent time-constant is also radar wavelength-dependent.

The ESD is directly related to the auto-correlation for the observation window. It characterizes the relationship between all samples within that window. For the ESD correlation, the correlation is between the signal's observed Doppler velocity magnitude, and no absolute

phase information is encoded. All relevant scatterer phase information results in the signal power being localized to a Doppler velocity. The absolute phase is neglected but only contains information about the slowly varying, low-velocity movement of the tower or blades as a result of flexing. Given the Doppler spectra resolution, these low-velocity components are likely resolved to the same Doppler bin (the bin size is determined by the window length and shape).

For the wind turbine observations considered here, the wind turbine's state variables exhibit long time-constants. Using these observations as a guide, the wind turbine's spectrogram remains correlated for time-lags on the order of seconds or tens of seconds. For light, variable winds, the yaw variability may increase as the control system attempts to extract the most energy. For high-speed winds, the wind turbine's structural vibrations increase due to wind-loading, and assuming the wind turbine is operating at the maximum-rated power, variations in the control system are targeted more at operational safety. Radar observations of wind turbines show that the 120-degree symmetry assumption is not perfect, and some asymmetry is observed in the measured RCS. Additionally, the positive-to-negative flash is not necessarily separated by a rotation of 60 degrees as a result of the blade's leading and trailing surfaces having a non-trivial angular separation. The cross-polar scattering of the wind turbine blades shows an increase in cross-polar RCS for the trailing edge of the wind turbine blade, which is consistent for edge-scattering. This trailing edge also exhibits a lower differential reflectivity compared to the leading edge of the blade. The lower horizontal RCS compared to the vertical RCS is consistent with the long, thin, vertically oriented blade for these observations.

A complete spectral representation of the wind turbine signature is difficult to estimate for observation periods less than a blade-pass period. Recall that assuming cyclostationarity (in rotation only), the wind turbine's state must describe a full rotation period, with all other

state variables fixed. A blade-pass period may also be used with little loss of fidelity to reduce the observation time-lags required. The number of possible wind turbine manufacturers and models, wind turbine state variables, and possible contamination from other scatterers make parameterization of a generalized spectral model of a wind turbine challenging. Such a parametric model is beyond the scope of this work.

Broadly speaking, the spectra of noise, precipitation, ground clutter, and wind turbines can be modeled by periodic, constant, and white noise components. For observation periods that include one or more blade-pass periods, the wind turbine observation itself can be used under two assumptions: 1) the wind turbine's state is cyclic in rotation but otherwise constant for an observation window and 2) all other signal sources are either wide-sense stationary or transient, with a duration much less than the wind turbine blade-pass period. The cyclical behavior of the turbine provides a highly correlated representation of the turbine's own signature.

## 4.6. Numerical Wind Turbine Model

In this section, a simple numerical model of a wind turbine will be analyzed using the same radar processing methods applied to real radar data. The model assumes a simplified, unpolarized radar receiver, and a number of scattering simplifications are made. The wind turbine model is discretized into a number of point scatterers that do not interact. Each point scatterer represents an area of the turbine's blades. Self-shadowing is accounted for (where the back of the blade is obscured by the front of the blade). The projection angle of the scattering surface is also accounted for, so a surface 90 degrees to the incident angle will not be illuminated.

A lack of observations of a wind turbine in a controlled manner limits wind turbine feature characterization. Numerical and scale models, however, are representative of first-order

behavior and are useful for comparison. The simulation results considered here provide insight into real wind turbines, which are observed in uncontrolled environments. A numerical simulation is examined to aid in understanding the physical and scattering behaviors of a wind turbine-like object in controlled conditions. It must be said that this mathematical model is very simple, but the qualitative analysis is substantive for interpreting radar observations of real wind turbines. The main purpose of the simulation is to identify features and trends, validate them against the wind turbine's physical characteristics, and extrapolate results of real radar observations.

The spectrograms of the numerical wind turbine model, processed in the same way as real wind turbine observations, are shown in Figure 4.12. Multiple yaw angles are presented from a hub angle parallel to the direction of observation, at a yaw angle of 0 degrees, to nearly perpendicular to the hub, at a yaw angle of 84 degrees. The blade RCS is highest for a yaw angle of zero and decreases as the yaw angle approaches 90 degrees. With a yaw angle of zero degrees, the negative velocity RCS is higher. With the change in yaw angle from zero degrees to 90 degrees, the RCS of the blades decreases, but it is noticed that the RCS for negative Doppler velocities decreases faster, with a difference of more than 10 dB. The leading edge of the blade has a broad, slow-varying geometry compared to the trailing edge when viewed parallel to its chord. For all yaw angles, the blade tip "halo" is observed. For the 36-degree-and-greater yaw angles shown in Figure 4.12, Doppler velocity-aliasing of the blade is observed. The specific angles and RCSs are model-specific, but the qualitative behavior is representative of three-blade wind turbines.

When wind turbines are viewed perpendicular to the axis of rotation, the maximum Doppler velocities are observed (the tip velocity). As the yaw angle approaches this limit, $\phi = \pm 90°$, the turbine interference becomes more impulsive, resulting in blade "flashes."

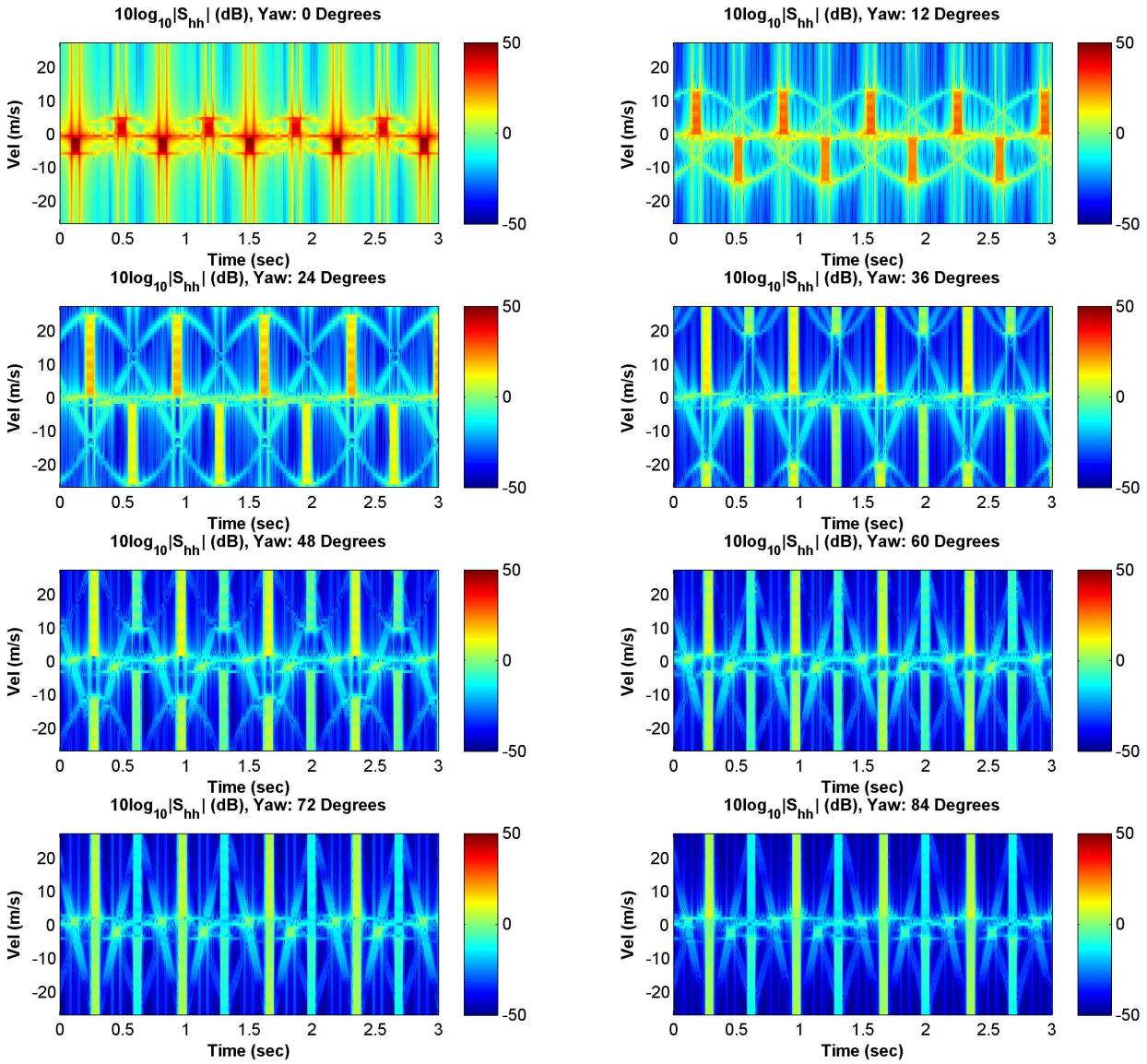


FIGURE 4.12. ESD time-series at multiple yaw angles for a numerical wind turbine model. The model assumes a 2.725 GHz radar at 1 kHz PRF, observing from a range of 60 km. The model turbine blade is 20 meters long, a one-meter chord length is used at the blade root, and the chord length is linearly tapered to 0.2 meters at the blade tip. No twist or pitch is applied to the blade, which is modeled as a NACA 3317 airfoil. The wind turbine rotates at 29 RPM, with a 5-degree tilt, and zero cone angle.

The RCS of the blade flash is relatively low and has a short duration. This results in a time-integrated echo power contamination, which is small. This reduced RCS-time product is the best-case scenario to evaluate whether current noise suppression and bad-data classification can resolve ambiguities due to the dynamic turbine response. As the turbine's yaw angle

approaches a head-on look ($\phi = 0°$ or $\phi = 180°$), the RCS-time product increases, the wind turbine interference is temporally correlated for much longer periods, and the overall energy can dominate targets of interest. For all cases, the interference is cyclic with the blade-pass frequency.

The simulation's IQ correlation is shown in Figure 4.13A. The same model and simulation results as those presented in Figure 4.12 are considered here for the calculation of correlations. The IQ correlation shows a very low correlation, except for samples at the blade-pass period with very short decorrelation times. The correlation at the blade pass-period is not at unity, which suggests that the IQ correlation is especially sensitive to the wind turbine blade's rotation angle. For the given sample rate of 1 kHz, the rotation angle is sampled every 0.174 degrees, and the IQ decorrelation angle is on this order. For observations at yaw angles near parallel to the wind turbine's hub, the IQ decorrelation time increases due to the slower variation in radial distance.

Next, the numerical model's ESD correlation appears in Figure 4.13B. The ESD correlation shows much slower decorrelation times for observations. The 64-sample, overlapping window function acts to correlate neighboring samples. Using the ESD, the correlation is less sensitive to exact sample times. Furthermore, the ESD correlation shows the lowest correlation when viewing the edge of the wind turbine, where observed velocity excursions are highest. Additional correlation features are observed between the blade-pass periods. These stem from correlation with the spectral leakage of the blade flashes as well as correlation of the blade with itself for angles symmetric around the top and bottom of the rotation (i.e., the tip halos).

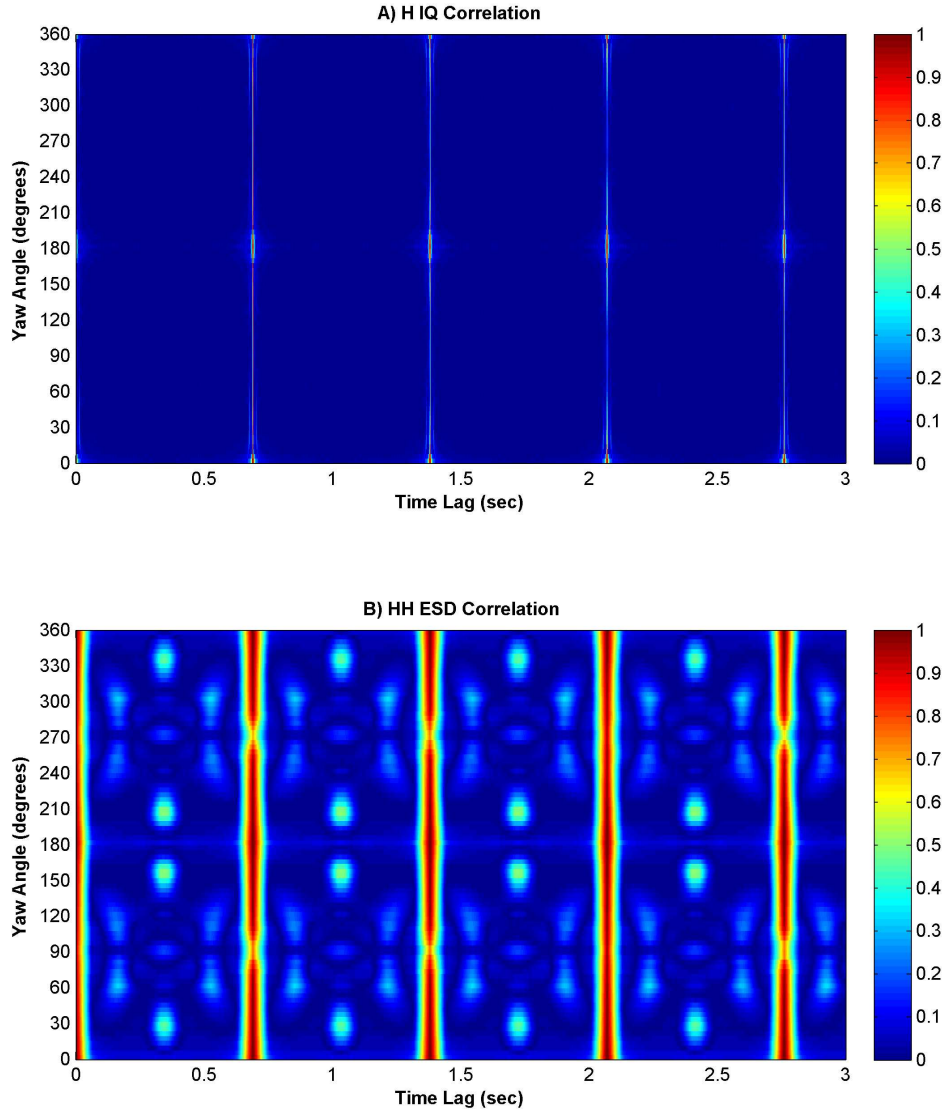


FIGURE 4.13. IQ and ESD correlation characteristics (as a function of yaw angle) of the numerical wind turbine model are shown. The model assumes a 2.725 GHz radar at 1 kHz PRF, observing from a range of 60 km. The model turbine blade is 20 meters long, with a one-meter chord length at the blade root linearly tapered to 0.2 meters at the blade tip. No twist or pitch is applied to the blade, which is modeled as a NACA 3317 airfoil. The turbine is rotated at 29 RPM with a 5-degree tilt and no cone angle.

CHAPTER 5

# Wind Turbine Clutter Suppression

Signal processing methods to suppress wind turbine clutter in the presence of various targets of interest were briefly discussed in Chapter 2. The difficulty in suppressing WTC is largely due to the short-duration and sparse observation periods of scanning radar systems coupled with the time-varying radar cross-section of wind turbines. Spatial filtering techniques are better suited for widespread volume targets, which have consistent statistical properties over a large number of range-volume cells. If the target of interest meets these requirements, spatial filtering techniques have demonstrated good performance for scanning radar systems [14]. For isolated targets of interest that are completely contained in range-volume cells or for volume targets with spatial-length scales less than the dimensions of a wind farm, temporal filter techniques are required to isolate the target of interest and suppress WTC. Here, the focus is on developing temporal filtering methods for wind turbine clutter suppression. As such, WTC suppression is considered for fixed-pointing radar observations of a single range-volume cell. This is a necessary precursor to the investigation and implementation of a temporal filtering method applicable to scanning radar systems.

A fixed-pointing, temporal WTC suppression technique allows for fine spatial resolution and enables the detection of unique targets within a range-volume cell. From the characterization results presented in Chapter 4, dual-polarization spectral features of ground clutter, precipitation, and wind turbines were identified. Using these features, a method for suppressing wind turbine echo power is presented in this chapter.

## 5.1. Radar Signature of a Wind Turbine

The wind turbine's signature is considered here in the context of other scattering sources. For weather radar systems, these targets can typically be categorized as volume targets and stationary targets. Volume targets, such as precipitation (which includes clouds, rain, snow,

or ice), are carried by the wind as they fall toward the ground. Precipitation can have a nonzero velocity relative to the radar, as hydrometers are influenced by local air motion and gravity. Examples of stationary scatterers include buildings, mountains, or vegetation and are typically referred to as "ground clutter". (For ground vegetation, its mean position remains fixed, but it can move in the wind, which results in a mean-zero velocity but a slightly broadened spectra.) For weak echoes, or no echo, the observed signal may be dominated by radiometric noise.

The three-blade HAWT is commonly used for commercial power generation. This design will be considered throughout this discussion. The wind turbine can be divided into three main components: the tower, nacelle, and blades. The wind turbine's variables of primary interest are the rotation angle ($\theta$) of the blades (referenced to blade one's leading edge at top dead center), the blades' rotation rate ($\omega = d\theta/dt$), and the yaw angle $\phi$ (the cardinal direction the blades' rotation axis is pointing) [5]. Some wind turbine designs also have variable pitch blades to control the angle-of-attack and further optimize the turbine's power output. The wind turbine's state variables are a function of the impinging wind field, controlled with the goal of maximizing the generated power within the turbine's safe operating region.

A representation of the wind turbine signature, the target of interest, or both is required for deterministic separation of WTC from the signal of interest. Recall that for weather radar applications, the received radar echo signal can be model as

$$x = x_p + x_{gc} + x_t + w, \tag{59}$$

which includes echo contributions from precipitation ($x_p$), stationary scatterers ($x_{gc}$), turbine statterers ($x_t$), and Gaussian white noise ($w$).

The rotating components of the wind turbine are the source of the difficulty in mitigating the wind turbine's signature without significant impact to the signals of interest. As

mentioned earlier, ground clutter filters have been successfully demonstrated for stationary targets (i.e., targets with near-zero Doppler velocity).

The Doppler spectra is a intuitive basis for characterizing and suppressing a wind turbine's signature. The signal's power spectral density can be estimated using the short-time Fourier transform by

$$\widehat{\mathbf{S}_x}[k] = \left| \frac{1}{\sqrt{N}} \sum_{n=0}^{N-1} x[n] e^{-j2\pi kn/N} \right|^2 \tag{60}$$

for windows of length $N$. For the remainder of the discussion, the term energy spectral density (ESD) is used to highlight that the underlying process is not necessarily wide-sense stationary. For a wide-sense stationary process, the ESD is equivalent to the power spectral density. From the signal model in Equation 59, and with all contributing components independent from each other, the modeled ESD is represented as

$$\mathbf{S}_x = \mathbf{S}_p + \mathbf{S}_{gc} + \mathbf{S}_t + \mathbf{S}_w, \tag{61}$$

where a time-series of ESDs is a spectrogram. For the discussion presented here, the spectrograms are estimated using an approximate confined Gaussian window [56] of length $N = 64$, given by

$$w[n] = G(n) - G\left(-\frac{1}{2}\right) \frac{G(n+N) + G(n-N)}{G(-\frac{1}{2}+N) + G(-\frac{1}{2}-N)} \tag{62a}$$

with

$$G(n) = e^{-\left(\frac{2n-(N-1)}{4\sigma_t}\right)^2} \tag{62b}$$

and, for this application, $\sigma_t = 0.1$.

In Figure 5.1, representative spectrograms are shown for the three scatterer types of interest. Ground clutter (Figure 5.1A), which is not moving, represents a narrow band

around zero but can have a significant magnitude. The wind turbine (Figure 5.1B) shows a ground clutter component (due to the tower and nacelle) with the addition of a time-varying, but cyclic, component from the rotating blades. The spectra of noise has a uniform power but shows variation due to finite window lengths (considered Doppler velocity bins far from zero in Figure 5.1A). Precipitation (Figure 5.1C) is typically much broader in spectrum than ground clutter, and its mean velocity is limited only by wind speed. Over time, precipitation's mean velocity variation is slow, and some coherency noise is observed between ESD samples. Note that in Figure 5.1C, a ground clutter filter (GCF) was enabled to suppress the stationary ground clutter signature. To implement the GCF for the fixed-pointing scans considered here, the signal's mean is subtracted for each windowed observation prior to spectral estimation as

$$\mathbf{x}^{(gcf)} = \mathbf{x} - \bar{x}. \tag{63}$$

5.1.1. Cyclostationarity and Periodic Correlation. A cyclostationary process is a time-varying, nonstationary process whose statistics are repeat with a fixed period [55]. Note that stationary processes are a subset of cyclostationary processes, with an effective period of zero, such that the statistical moments are constant. A strict-sense (cyclo)stationarity process is a process in which all statistical moments are deterministic. For a wide-sense (cyclo)stationarity (WSS or WSCS) process, only the first and second moments must be characterized [57]. For a process that does not change in time, ergodicity can be applied to estimate the process's moments. In the case of a cyclostationary process in time, the observations can be divided by the repetition period, $T$. At each time-lag, $\tau \in [0, T)$, ergodicity may be applied to estimate the process's statistical properties.

For WSS processes, the power spectral density (PSD) remains constant. The variation in the estimated PSD is due to using a finite window length. As such, the power estimate for any Doppler bin in the PSD can be approximated as a nonzero mean, white noise process

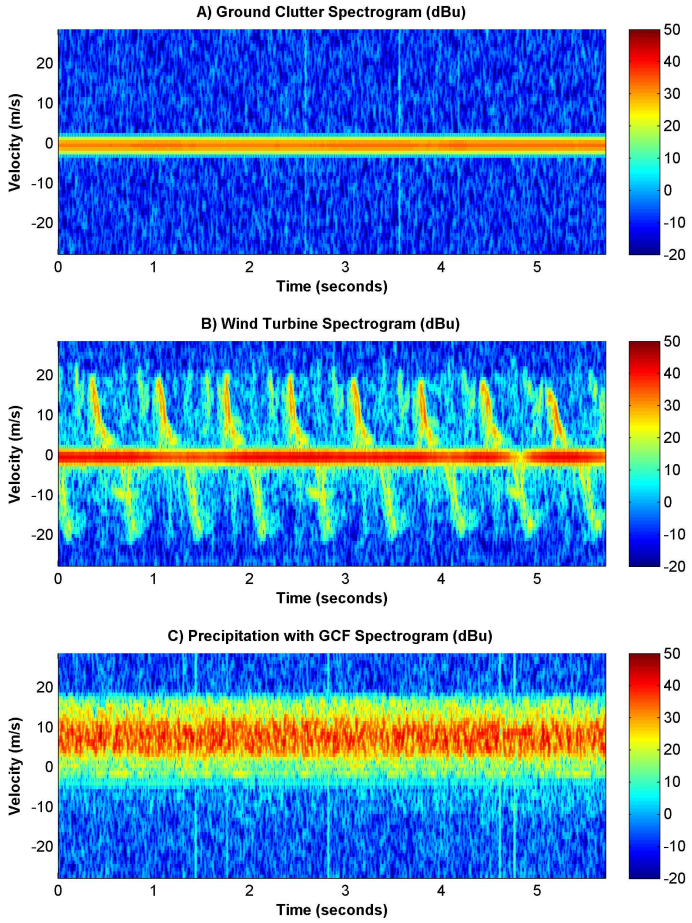


FIGURE 5.1. Representative spectrograms of three classes of scatters are shown. Graph A is ground clutter only. Graph B shows a wind turbine and ground clutter (the stationary tower and nacelle of the wind turbine are included in the ground clutter). Graph C shows a spectrogram of precipitation (rain) with ground clutter filtering enabled.

whose variance is a function of the sample length [17]. Once the mean PSD is removed, the residual PSD is a white noise process. This can be directly applied to statistically stationary precipitation, ground clutter, and radiometric noise. Spectral observations with the mean included are highly correlated. When the mean spectra is removed, the ESD correlation is zero. The degree to which biased noise spectra are correlated is a function of the number of samples used and the time-domain correlation of the scatterers.

For a wind turbine, its location is fixed, and parameters such as blade rotation, yaw angle, blade pitch, vibration, tower oscillation, etc., are loosely functions of wind velocity. A

turbine's rotation leads to a cyclic radar cross section. The turbine signature can be separated into the rotating part, static part, and noise (for at least a short time period). For a wind turbine rotating at a fixed rate with all other state parameters fixed as well, the time-varying radar cross section, as characterized by the Doppler spectra, is a cyclostationary process and periodically correlated to a high level [1]. This periodicity in the turbine's Doppler spectral features can be used to suppress the turbine's signature in the presence of scatterers that are either transient or constant in the Doppler spectra subspace.

5.1.2. Probability Distribution Fits. For precipitation, where the received signal is a coherent integration of a large number of independent scatterers with none dominating the received power, the underlying receiver's in-phase and quadrature (IQ) voltages can be modeled as a complex Gaussian process, where I and Q are independent and the variance of the complex voltage is the signal's power [17]. For an independent and identically distributed random variable, this results in a Rayleigh distribution for the amplitude, a uniform phase distribution, and an exponential power distribution [17].

Consider a single scatterer. If the position of the scatterer varies with a Gaussian distribution due to oscillation, this creates a Gaussian phase distribution. When the position ($\Delta d$) of the scatterer deviates by more than half a wavelength ($\lambda/2$), the phase excursion exceeds the unambiguous limits, resulting in an aliasing effect. As the position oscillation becomes large with respect to the radar's wavelength, aliasing of the phase results in a phase distribution that tends toward being uniform. For precipitation and a rotating wind turbine, the phase distribution is well approximated by a uniform distribution. For the wind turbine, the rotation and wind-forced oscillations result in a displacement of the turbine (and flexing of the blades) that can move through tens of centimeters or more.

For ground clutter, the observations are not necessarily uniformly distributed in phase. Therefore, the amplitude and power distributions do not conform to Rayleigh and exponential distributions, respectively. For observations with truly stationary ground clutter and a

fixed radar, the IQ amplitude and phase tends toward a constant. In this case, the ground clutter is represented by a complex Gaussian distribution with a nonzero mean.

Consider the Doppler spectra representation of the wind turbine and precipitation in the presence of ground clutter. Each spectral bin is uncorrelated (assuming a rectangular window, no zero padding, and negligible window sidelobe contamination) [17, 57]. Within a given spectral bin, the wind turbine makes a periodic, additive contribution to the echo power from other scatterers (given the independence of the scatterers). Between the turbine blade's periodic echoes, the observed spectral power is assumed to be weighted more significantly by other scattering sources (or is noise). (In the zero-velocity Doppler bin, the echo's signature may still exhibit periodicity but tends to be dominated by the physically stationary scatterers.)

If the spectral bin contains a WSS, complex-Gaussian random process (such as noise or precipitation), the estimated WSS power distribution should be well modeled by an exponential distribution. Given that the wind turbine's signature is periodic and typically of a low-duty cycle, the low-probability "tail" of the distribution can be fit to estimate the mean power, which tends to discriminate against the wind turbine's contribution. This provides a lower bias estimator for the precipitation echo power contribution in the presence of the wind turbine. This also supports the claim that the precipitation process is well approximated as a WSS process, whereas the wind turbine is not (although it is WSCS).

The cumulative distribution function (CDF) for an exponential distribution of the random variable $\mathbf{y}$ is given by

$$F(y;\lambda) = P(\mathbf{y} \leq y) = 1 - e^{-\lambda y}, \tag{64}$$

where $\lambda$ is the scale factor with an arithmetic mean, $\lambda^{-1}$ [57]. If $\mathbf{y} = |\mathbf{x}|^2$ and $\mathbf{x}$ is a complex Gaussian process, then the mean of the process $\mathbf{y}$, $\mu_y$, is the variance of $\mathbf{x}$, or more concisely,

$$\lambda = \frac{1}{\mu_y} = \left(\mathbb{E}\left[\mathbf{x}\mathbf{x}^*\right]\right)^{-1}, \tag{65}$$

where $\mathbb{E}$ is the expectation operator and $^*$ denotes the complex-conjugate. Assuming an exponential distribution, the mean signal power can be estimated from the observations using

$$\mu_y = \frac{-y}{\ln\left(1 - P(\mathbf{y} \leq y)\right)}. \tag{66}$$

Here, the mean power of the process is estimated using the exponential distribution model. The arithmetic mean of the model's estimated power, following Equation 66, is taken over $P(\mathbf{y} \leq y) \in [5\%, 10\%, 15\%, 20\%, 25\%, 30\%]$. In Figure 5.2, the exponential model's mean power estimates for ground clutter, precipitation, and a wind turbine are presented. The model is also evaluated at a number of different probabilities and compared to the arithmetic mean power.

The effect of the nonzero mean complex Gaussian process is observed in Figures 5.2A-5.2B, where ground clutter exhibits a biased estimate using the exponential power model. As the probability of occurrence increases (i.e., moves from left to right along the CDF), the exponential model's estimated mean power decreases. This indicates that the distribution of power is not exponential, and therefore, the zero-mean complex Gaussian distributed IQ assumption does not hold. The exponential model (bold black line) overestimates the ground clutter power by 8 dB or more. Once the IQ mean of the velocity bin is subtracted, the power of the residual is again exponentially distributed.

Using the precipitation with GCF spectrogram from Figure 5.2C, the exponential model's estimate of the mean power is shown in Figure 5.2D. For all of the probabilities considered,

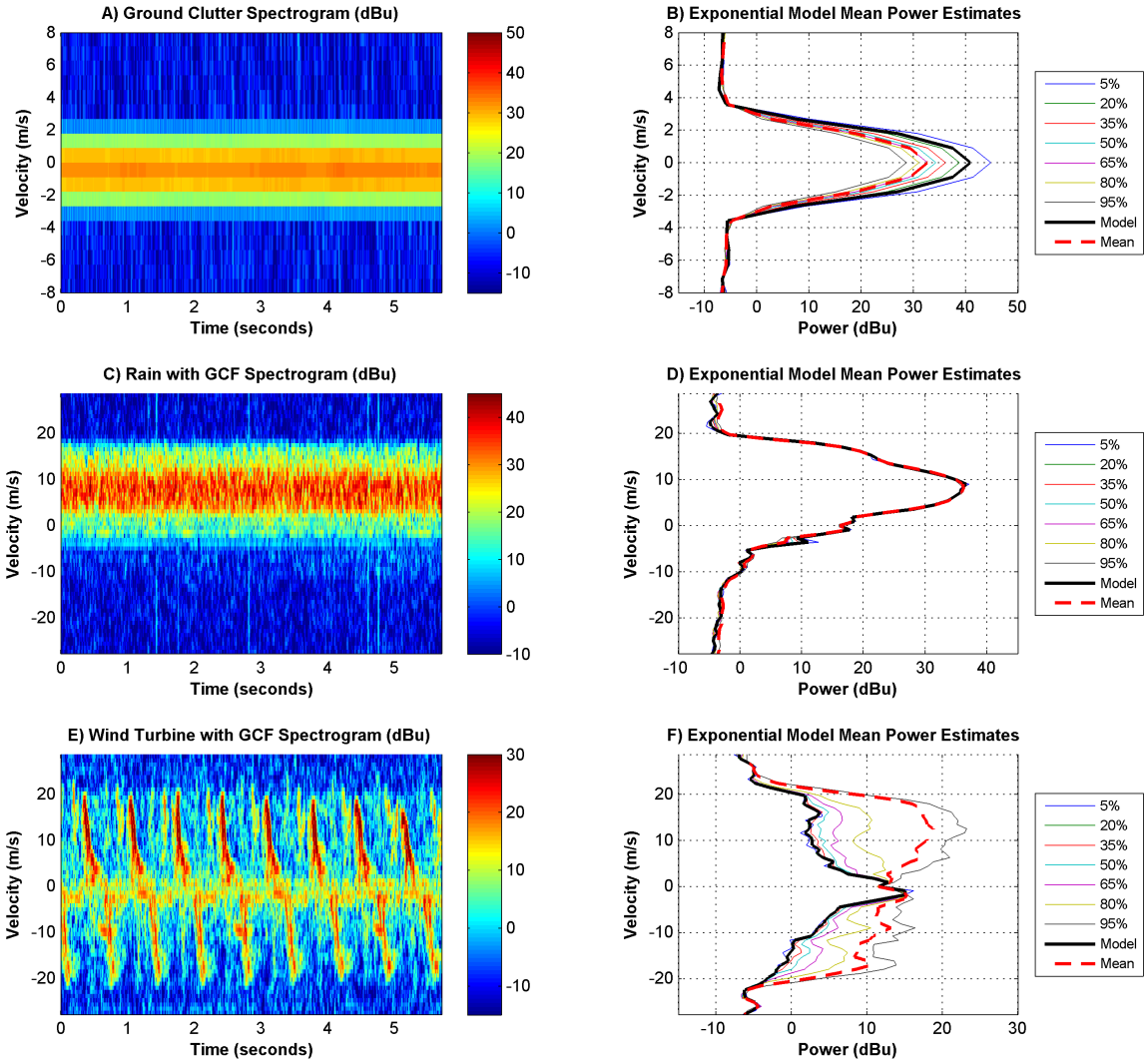


FIGURE 5.2. Exponential model fits to distributions. Graph A shows ground clutter (the scales have been adjusted to focus on the near zero Doppler bins). Precipitation with GCF is shown in Graph B. Graph C shows the wind turbine with GCF. The bold black line shows the model estimates for precipitation power. The dashed red lines are the arithmetic mean of all power samples (a typical power estimator). All other lines are the exponential models' estimate of the mean values using the associated percentiles of CDF.

the exponential model closely matches the arithmetic mean precipitation power. This highlights that the precipitation is wide-sense stationary during the observation period and that the zero-mean complex Gaussian IQ distribution is appropriate for characterizing precipitation in individual Doppler velocity bins.

The wind turbine with GCF observations in Figure 5.2E is considered next. Following the same method, the exponential model is applied to the observations to estimate the mean power. The results are shown in Figure 5.2F. For low probabilities, the exponential model significantly underestimates the arithmetic mean power of the wind turbine for all but the near-zero Doppler bins. This is expected due to the periodic and impulsive signature from the wind turbine blades. For the highest probability considered (95%), the power exceeds the arithmetic mean by as much as 5 dB. Using the exponential model with the lower probability observations, a more appropriate estimate of the constant power in the Doppler velocity bin can be made and is significantly more tolerant of the biasing effects of the wind turbine than the arithmetic mean. Using the exponential model, up to a 20 dB or more suppression of the wind turbine signature in a single Doppler bin can be obtained. This technique will be used here to estimate the underlying stationary process.

5.1.3. Estimating the Wind Turbine's Rotation Period. To utilize the cyclostationarity of the wind turbine for suppression, the wind turbine's state must remain nearly constant (with the exception of the rotation angle), and prior observations of that state are needed. Because of this, the turbine's rotation period must be known. If the turbine's state is slow-varying, it will be nearly cyclostationary in time, and as such, observations of the turbine may be used to estimate its rotation rate.

The mean variance of the observations, assuming a cyclostationary process with rotation period $T_r$, is calculated as

$$\sigma_S^2[T_r] = \frac{1}{NMK} \sum_{m=0}^{M-1} \sum_{n=0}^{N-1} \sum_{k=0}^{K-1} \left( S[k, m + nT_r] - \overline{S}[k, m, T_r] \right)^2, \tag{67a}$$

with

$$\overline{S}[k, m, T_r] = \frac{1}{N} \sum_{n=0}^{N-1} S[k, m + nT_r], \tag{67b}$$

where $S$ is the spectrogram, $N$ is the number of realizations of a full rotation period, $M$ is the number of samples within a full rotation period, and $K$ is the number of Doppler spectra bins. With this method, the full rotation period can be resolved to integer multiples of the sample period, $T_s$, giving $T_r = MT_s$.

Assuming a wind turbine has a fixed rotation period, the period $T_r$ with the minimum variance represents the turbine's blade-pass period or one of its harmonics. This estimated period with minimum variance is denoted as $\widehat{T}_r$. The period $\widehat{T}_r$ may be any of the wind turbine's blade-pass harmonics. Self-consistency checks are required for accurate estimation of the blade-pass period. Consider this: When $\widehat{T}_r$ is the full rotation period, division by the number of wind turbine blades is the blade-pass period, which has a local minimum in the variance. If $\widehat{T}_r$ is the blade-pass period, division by the number of blades will not have a local minimum, but multiplication by the number of blades will be the rotation period and, therefore, will also have a local minimum. For a constant wind turbine state, the highest correlation typically occurs with the same blade configuration (i.e., a full rotation period).

With the wind turbine spectrogram in Figure 5.3A, the minimum variance technique (i.e., Equation 67) is used to estimate the turbine's rotation rate which is shown in Figure 5.3B. The wind turbine's rotation rate is estimated using a sliding window spanning approximately two seconds of observations. Each subsequent estimate of the turbine period is spaced approximately 0.1 seconds apart. Note that during periods where the turbine's yaw angle appears to change, such as times around five seconds, the estimated RPM is also impacted. This is a result of the relation between the relative yaw angle and the blade's rotation angle, at which the scattering surface is aligned such that a specular reflection occurs. (When the yaw angle changes during a full rotation, the turbine's rotation between two sequential specular reflections from the same turbine blade will be greater that or less than 360 degrees due to the turbine's geometry.)

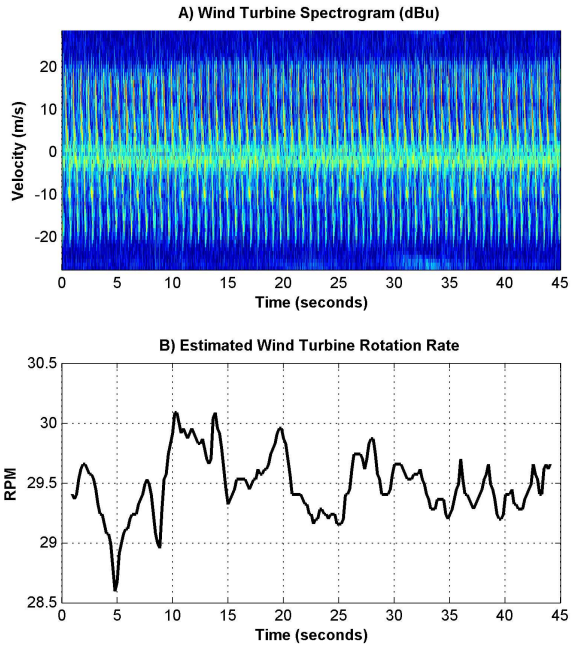


FIGURE 5.3. Graph A presents a spectrogram of CSU-CHILL observations of a wind turbine in clear-air conditions on March 11, 2014, 14:33 UTC, at a range of 62.4 km. Graph B shows the estimate of the turbine's rotation rate using the spectrogram from Graph A and Equation 67.

Using the full spectrogram from Figure 5.3A, the average rotation period and the cyclostationary power can be estimated. In Figure 5.4A, the estimated wind turbine rotation period is 2.032 seconds, which closely matches the Vestas V47 wind turbine, which has a nominal rotation period of $2.105 \pm 10\%$ seconds. Figure 5.4B shows the 21 different realizations of the echo power over a full rotation period, as well as the mean echo power. Some variation in the realizations is noticed due to changes in the wind turbine's state. Figure 5.4C is the mean spectrogram using all 21 realizations.

Consider the cyclostationary period estimation of a different case. In Figure 5.5A, the estimated wind turbine rotation period is 4.070 seconds and closely matches the NEG Micon NM48 wind turbine, which has nominal rotation periods of either 2.727 or 4.000 seconds. (The slower rotation rate is for low wind speed operation.) Figure 5.5B shows 14 different realizations of the echo power over a full rotation period, as well as the mean echo power.

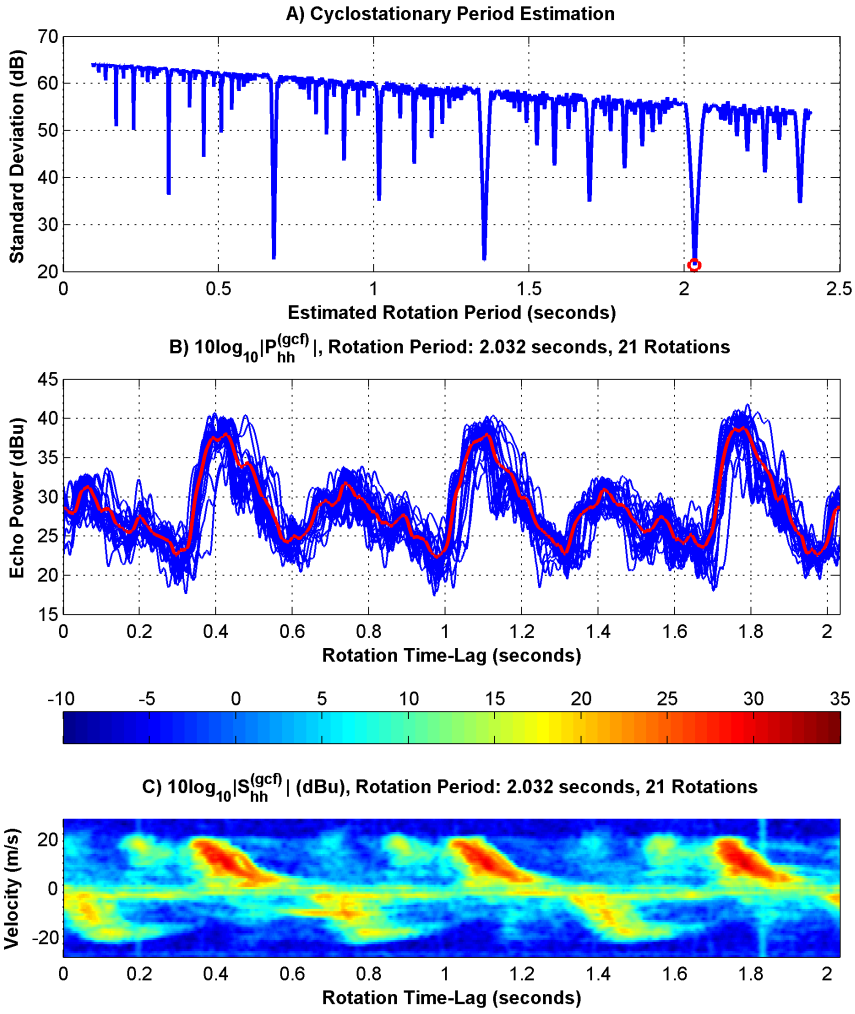


FIGURE 5.4. CSU-CHILL observations of a wind turbine in clear-air conditions on March 11, 2014, 14:33 UTC, at a range of 62.4 km. Graph A shows the wind turbine echo's mean variance (using Equation 67), considering a range of possible rotation periods. The lowest variance was 2.032 seconds. In Graph B, the echo power for 21 realizations of a full rotation period is shown as blue lines, and the mean is shown as a red line. The mean spectrogram of the same 21 realizations is shown in Graph C.

Little variation in the realizations is noticed, which suggests steady wind velocity and a constant wind turbine state. Figure 5.5C shows the mean spectrogram using all 14 realizations. Precipitation can be noticed in the spectrogram at around 7 m/s Doppler velocity. The sinusoidal tip "halos" that are observed in the spectrogram are likely enhanced due to the modulation of the precipitation by the wind turbine.

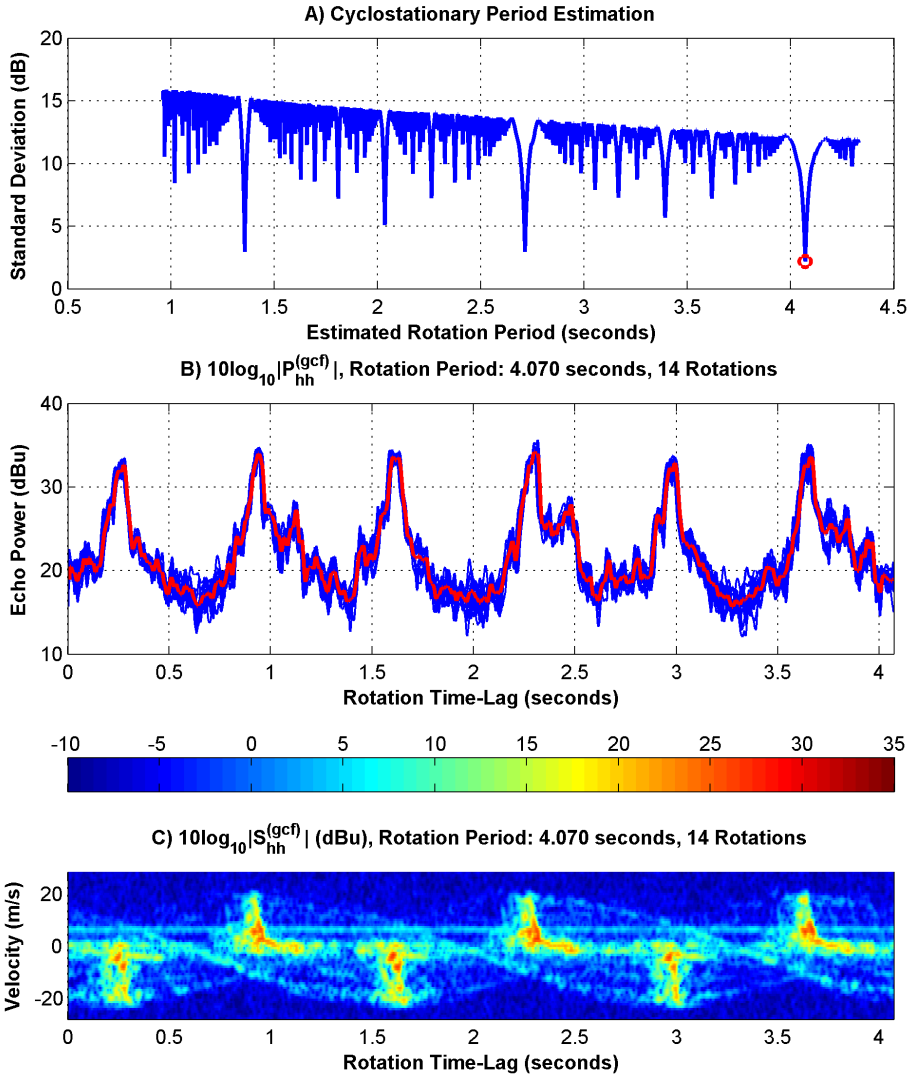


FIGURE 5.5. CSU-CHILL observations of a wind turbine in light precipitation conditions on March 7, 2014, 23:37 UTC, at a range of 62.55 km. Graph A shows the wind turbine echo's mean variance, assuming a range of possible rotation periods. The lowest variance rotation period is 4.070 seconds. In Graph B, the echo power for 14 realizations of a full rotation period is shown as blue lines, and the mean is shown as a red line. The mean spectrogram of the same 14 realizations is shown in Graph C.

## 5.2. SUPPRESSING THE WIND TURBINE SIGNATURE

From the wind turbine observations presented thus far, it can easily be seen that the rotating blade's signature is not stationary but does exhibit cyclostationarity (or is almost cyclostationary, with slight variations in the turbine's state). In weather applications, wind

turbine clutter can bias observations and estimates of precipitation's microphysical properties. By suppressing WTC, these estimates can be improved to better represent precipitation's intrinsic values.

A wind turbine's physically stationary (or nearly stationary) components (such as the nacelle and tower) are easily suppressed by available ground clutter filtering techniques, such as those presented in [27, 28]. Suppression of greater than 40 dB has been demonstrated with these ground clutter filters for near-zero Doppler velocities. Therefore, the rotating blade assembly represents the primary signal of interest, and it is the focus for the development of the WTC suppression technique described in this paper. The suppression of the wind turbine should not significantly suppress precipitation power, especially in the absence of WTC.

The suppression requirements for WTC are difficult to quantify as a single number, given the dynamic and variable nature of WTC. Any level of suppression is desirable, as long as the signal of interest is not negatively impacted. Here, to evaluate the performance of the suppression technique, the spectral moments (see Equations 46-49) are considered before and after filtering, and the estimated wind turbine signature and the filtered spectrogram are discussed.

In general, as the wind turbine's yaw angle with respect to the radar's observation angle approaches 90 degrees or 270 degrees (i.e., the radial is parallel to the plane of rotation), the blade flash becomes more impulsive and lower in magnitude. For such cases, the tower and nacelle's contribution to the overall RCS can be an order of magnitude higher than the rotating assembly. Conversely, as the turbine's relative yaw angle approaches zero degrees or 180 degrees, the broader blade surface is observed by the radar and is contained in a narrow range of near-zero Doppler velocities with a more sinusoidal signature. When the plane of rotation is nearly perpendicular to the radar's radial, the rotating RCS dominates. This

trend has been noted in CSU-CHILL observations (of which a subset are presented in this work) and confirmed by the simulation results presented in [11].

Recall that, assuming cyclostationarity in rotation with all other state variables fixed, the wind turbine's signature can be completely defined using observations from one complete rotation period. Given the cyclostationary nature of the wind turbine over short observation periods, prior observations from the recent past provide a good representation of the current wind turbine state if the rotation angle of the wind turbine under observation can be estimated. Assuming a constant RPM ($\omega_t$), the change in rotation angle ($\Delta\theta$) can be directly related to the elapsed time by $\Delta\theta = \omega_t t$. Given the rotational symmetry of the wind turbine's blades, a blade-pass period may also be used (with little loss of fidelity) to reduce the observation time-lags required. From the definition of a cyclostationary process, a blade-pass period of observations is required to characterize the wind turbine signature if rotational symmetry is assumed. (If rotational symmetry of the turbine is not a valid assumption, a full rotation period is required.)

Leveraging the ESD correlation characteristics of these three scatterer classes, a spectral suppression technique that directly operates on a time series of observations can be considered. Precipitation is modeled as a constant spectra over the observation periods. Although ground clutter also has a constant spectra, a ground clutter filter is available to remove zero-velocity clutter components. To suppress wind turbine clutter, the periodic correlation and cyclostationary properties of the observed wind turbines provide a means to estimate, and ultimately suppress, the rotating blade signature. The filtering technique operate on the spectrograms in decibels (which enables the inverse filter to be implemented as a subtraction). This has the added benefit of converting multiplicative coherency "noise" into additive noise.

5.2.1. Seasonal Moving Average. A cyclic linear filter, also called a "seasonal moving average (SMA) filter," can be used to demonstrate the effectiveness of leveraging the

cyclostationary characteristics of the wind turbine for suppressing the turbine's signature. Prior observations of the wind turbine (in the same operating state) are used as the suppression filter's basis function. Broadly speaking, the spectra of noise, precipitation, ground clutter, and wind turbines can be modeled by a combination of periodic, constant, and white noise components. Assuming a single wind turbine, prior observations at the turbine's rotation period are used to represent the periodic and constant components which correspond to the cyclostationary and stationary processes, respectively.

For observation periods that include one or more blade-pass periods, the wind turbine observation itself can be used under two assumptions: 1) The wind turbine's state is constant during the observation window (with the exception of rotation angle), and 2) all other signal sources are either WSS or transient with a duration less than the SMA filter's period. The cyclic behavior of the turbine provides a highly correlated representation of the turbine's own signature [1]. For a wind turbine-only observation meeting these assumptions, the turbine's spectrogram ($S$) from a time-lag equal to the rotation period, $\widehat{T}_r$, can be directly used to suppress the wind turbine's spectral contribution by

$$S_f[t] = \frac{S[t]}{S[t - \widehat{T}_r]}, \tag{68a}$$

where $S_f$ is the filter result. Using a logarithmic representation for the spectrogram (in units of decibels), this is implemented as

$$10 \log_{10} \left( S_f[t] \right) = 10 \log_{10} \left( S[t] \right) - 10 \log_{10} \left( S[t - \widehat{T}_r] \right). \tag{68b}$$

Equation 68b implements the SMA filter with a time-lag of one rotation period.

Consider the spectrogram of a wind turbine with precipitation included in Figure 5.6A. Characterization of the spectra of precipitation shows that it is well represented by a constant magnitude spectra with additive noise [1]. If the mean Doppler velocity and spectral width

remain constant for the rotation period, an SMA filter model can remove the mean precipitation spectra. Figure 5.6C shows the SMA filter output for wind turbine observations with embedded precipitation. The SMA filter relies on prior observations that are representative of the current observation (i.e., highly correlated and, in this case, equally scaled). The filter basis used in the SMA is shown in Figure 5.6B, which is the same spectrogram as Figure 5.6A but delayed 2.698 seconds (the estimated full rotation period for the wind turbine).

The SMA residual in Figure 5.6C reinforces the idea that ground clutter and precipitation can be modeled as a mean Doppler shape with stochastic noise. The wind turbine can be similarly modeled for a known cyclic period. The level of stochastic variation is a function of the intrinsic variability in the ESD observations, with additional variation due to nonzero time-lags between observations used in the filter (i.e., the target decorrelation). The wide-sense cyclostationary assumption used is only an approximation, and its validity is on the order of seconds to tens of seconds for the cases considered here.

Although this technique produces good results for specific, well-controlled cases, there are shortcomings with it as applied here. One of the main drawbacks of the SMA is that it also filters precipitation (the signal of interest) and can add power to the residual spectra. The wind turbine period must also be estimated exactly, and only a single period can be used, which limits its application to multiple wind turbines in a single volume. The SMA is a simple filtering technique that illustrates a powerful concept, that the cyclostationary behavior of the wind turbine can be leveraged to successfully mitigate WTC. This is the basis for the suppression technique developed next.

5.2.2. Observation-Based Adaptive Filter for WTC. The SMA filter demonstrates that the cyclostationary characteristics of the spectra RCS provide a good basis for estimating and suppressing the wind turbine signature. Here, variations on the filter design are considered to mitigate the unwanted characteristics of the SMA and improve the robustness of the technique for weather radar applications. Echo power should not be added to

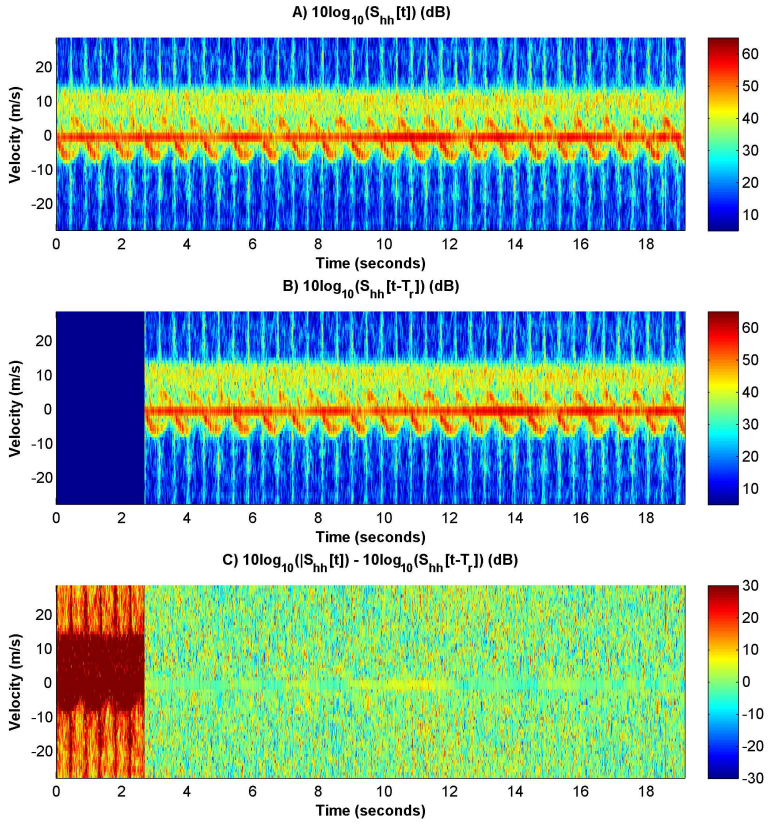


FIGURE 5.6. CSU-CHILL observations of a wind turbine with embedded precipitation on June 26, 2014, 23:07 UTC, at a range of 63.0 km. The wind turbine's average rotation period is estimated to be 2.698 seconds for the observation period considered. Graph A shows the spectrogram including ground clutter, precipitation, and a wind turbine. Graph B is the filter basis used in the SMA. Graph C shows the residual ESD after applying the full-rotation period moving-average whitening filter from Equation 68b.

the result (suppression should only remove the power); therefore, all negative values in the filter basis are set to zero to ensure that power is only subtracted. Using a range of time-lags to construct the filter, wind turbine signatures with different periods can be suppressed. To retain slow-varying (stationary) spectral signatures, such as noise power, ground clutter, or the precipitation echo, an estimate of the mean power at each Doppler velocity can be made using a window of observations.

Using prior observations from the spectrogram $S$, the filter can be constructed to suppress the WTC for each ESD of interest ($S_x$). To synthesize the spectrogram $S$, overlapping samples are considered to maximize the probability of having spectral estimates for any given

turbine state. (Consider a rotation rate of 30 RPM and a sample period of one millisecond. this gives a 0.18-degree rotation between samples. Decorrelation of the wind turbine blade's RCS is on the order of tenths of a degree rotation or less [12].)

The ground clutter and precipitation spectra can be modeled as a constant spectra, with any variation treated as noise. To minimize any suppression of these targets, the WSS spectral RCS ($\bar{S}$) is estimated and removed prior to estimation of the WTC spectra by

$$S_x^{(dB)} = S^{(dB)} - \bar{S}^{(dB)}. \tag{69}$$

The SMA used a single ESD observation time-lagged by the estimated wind turbine rotation period. This requires a temporally localized estimate of the wind turbine's period and is subject to errors if the turbine's state changes or if multiple turbines occupy the same observation volume. A window of ESD observations can be used to create a "dictionary" following

$$D = \left[S_x^{(dB)}[t - T_1], \cdots, S_x^{(dB)}[t - T_2]\right]. \tag{70}$$

An affine fit of each ESD in the dictionary to $S_x$ is evaluated, and the one with the minimum mean-squared error is then selected as the best estimate to use for suppression, following

$$i = \arg\min_i \left\| S_x^{(dB)} - (a[i]D[i] + b[i]) \right\|_2^2. \tag{71a}$$

The estimate for the wind turbine spectra is therefore

$$S_t^{(dB)} = a[i]D[i] + b[i]. \tag{71b}$$

Again, the filter should not add energy back into the spectra; it should only remove it. The estimate of $S_t^{(dB)}$ is subject to the constraint that all spectral bins are nonnegative. This is implemented by setting all spectral bins with negative power to zero. With the estimated

turbine spectra, the filtered observation is given by

$$S_f^{(dB)} = S_x^{(dB)} - S_t^{(dB)}. \tag{72}$$

Multiple observations from $D$ can be used to synthesize the wind turbine spectra to minimize the residual. This also enables multiple wind turbine signatures within a volume to be suppressed simultaneously. The number of spectra may be limited to $K$ samples to prevent over-fitting. After each iteration, the dictionary is similarly modified to subtract the selected ESD from the dictionary's elements before evaluating the next iteration. The dictionary update is performed by

$$D_k = D_{k-1} - S_t^{(dB)}[k-1], \tag{73a}$$

and each stage's estimate of the incremental wind turbine signature contribution (i.e., $S_t^{(dB)}[k-1]$) is still constrained to be nonnegative. After $K$ elements from $D$ are fit, the total wind turbine signature is given as

$$S_t^{(dB)} = \sum_{k=0}^{K-1} S_t^{(dB)}[k]. \tag{73b}$$

The filtered ESD, with the wind turbine's signature suppressed but ground clutter and precipitation unaffected, is

$$S_f^{(dB)} = S_x^{(dB)} - S_t^{(dB)} + \bar{S}^{(dB)} = S^{(dB)} - S_t^{(dB)}. \tag{74}$$

Here, the dictionary used for filtering is a delayed window of prior observations. Ideally, the delay should be sufficiently spaced to ensure independent IQ samples are used for the estimation of the $S_x$ as well as sufficient time to enable independent microphysical observations (typically, microphysical decorrelations are observed on the order of tenths of a second [17]). The dictionary window length should also be set to ensure that a representative observation

of the signature to be suppressed is included in the dictionary (this is typically the rotation period).

The filter technique can also be implemented and applied to sub-bands of the Doppler spectra, which may improve filtering performance with mixtures of targets. Temporal and spectral averaging may also improve the performance of the filter. (Similarly, the data window applied prior to the discrete Fourier transform may influence suppression performance.)

## 5.3. Results and Discussion

The WTC suppression technique will be demonstrated using fixed-pointing observations from the CSU-CHILL S-band radar. The observation spectrogram is constructed from overlapping windows, shifted by a single IQ sample. A window length of $N = 64$ is used; therefore, adjacent ESD have 63/64 or 98.4% of samples in common. This overlap provides the maximum chance for realizing the time-frequency wind turbine features in successive realizations of the rotation period. The dictionary used for estimating the wind turbine signature is a selection of recent observations. For these cases, it is a time-lagged window that is 0.5 seconds prior to the observation $S_x$ and extends to include a full rotation period of past observations. (The length of the dictionary is determined from prior estimates of the wind turbine's full rotation period.)

To estimate the filtered spectrogram, pre- and post-processing of the observation spectrogram is performed to improve the temporal consistency of the results. Given that oversampling is used, filter lengths that are relatively small with respect to the window size are chosen. The data-processing steps to produce the turbine's spectra ($S_t$) from the observed spectra $S$ are

(1) $S^{(dB)}$ is smoothed with a Gaussian kernel, which is 3 Doppler bins by 32 temporal bins.

(2) $S^{(dB)}$ is subdivided into 4 Doppler bin-wide sub-pulses with a 50% overlap (for a total of 32 sub-pulses). The dictionary is fit with $K = 2$.

(3) The turbine signature estimates from the 32 sub-pulses are averaged where they overlap to produce a complete spectrogram for $S_t^{(dB)}$.

(4) The $S_t^{(dB)}$ spectrogram is de-noised using principal component analysis. The principle components containing 60% of the spectrogram's energy are used to reconstruct a "low-noise" version of $S_t^{(dB)}$.

(5) The low-noise $S_t^{(dB)}$ is smoothed using the same Gaussian filter kernel that was used on $S^{(dB)}$.

A variety of wind turbine observations are considered next. For all suppression cases, a quantitative evaluation of the suppression performance is necessary. The suppression ratio performance is dependent on the clutter-to-signal power ratios, the spectral widths of the clutter and the target, and the Doppler spectrum overlap of the clutter and the target. Suppression of WTC in both clear-air and collocated with precipitation is considered.

5.3.1. Wind Turbine Only Combined with Rain Only. Using independent observations of precipitation only and a wind turbine in clear-air conditions, "synthetic observations" are constructed to evaluate the performance with a "ground truth." Coherent summation of the IQ time series for the two cases (one of precipitation (rain) and the other of a wind turbine) is used with varying degrees of attenuation to synthesize six cases to be considered. This allows for an evaluation of the suppression techniques with known underlying processes. The combined spectrograms are shown in Figure 5.7 for the following combinations:

a) precipitation only (rain)

b) precipitation plus a wind turbine

c) precipitation that is attenuated 10 dB plus a wind turbine

d) precipitation that is attenuated 20 dB plus a wind turbine

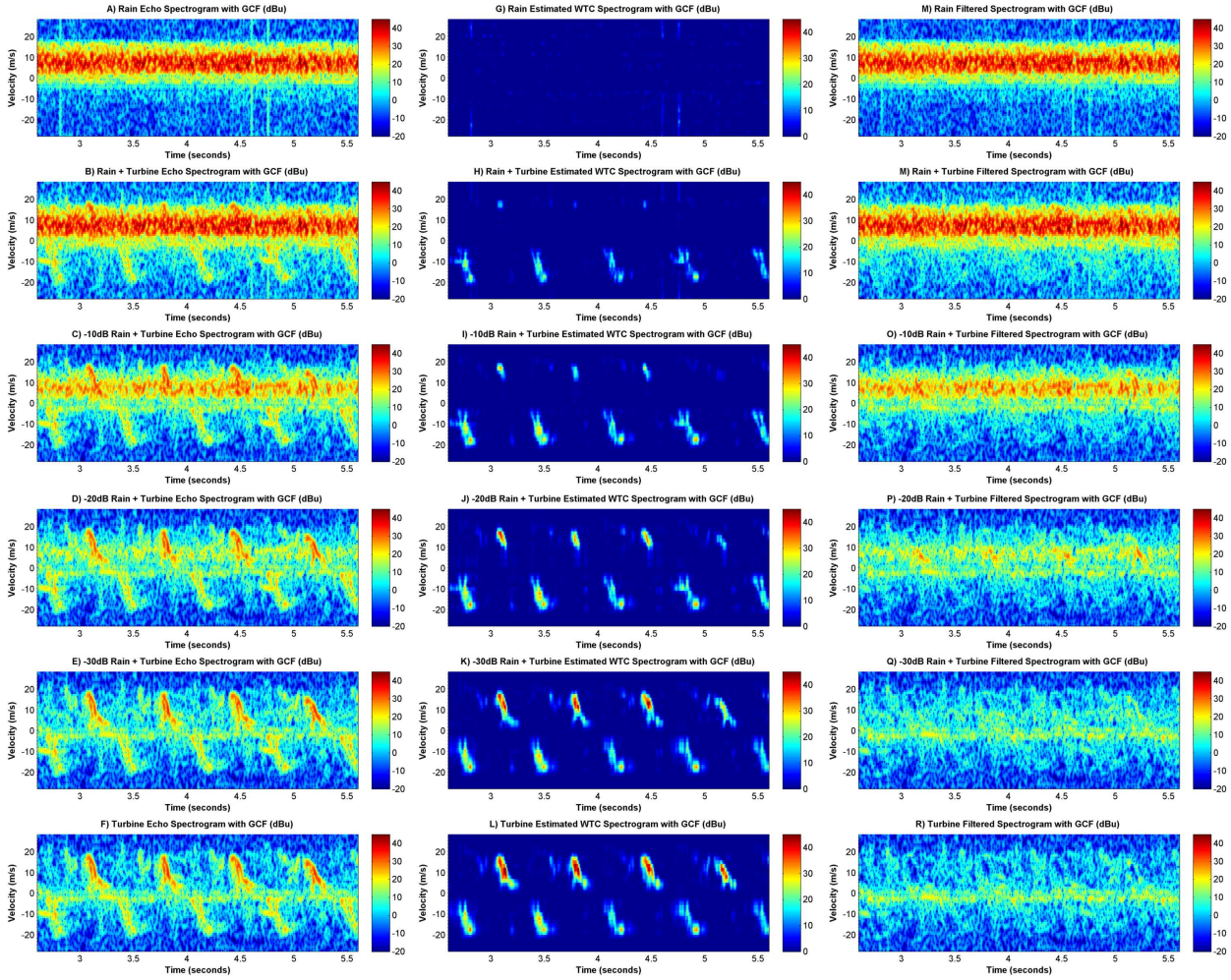


FIGURE 5.7. Each row represents a different coherent combination of precipitation and a wind turbine. The original spectrograms are shown in the left column. The estimated wind turbine signatures are in the center column. The right column contains the filtered spectrograms with the wind turbine signatures suppressed.

e) precipitation that is attenuated 30 dB plus a wind turbine

f) a wind turbine only (no rain)

Cases A and F represent the original observations, which are coherently combined to form cases B through E. The precipitation echo power is varied by 30 dB to synthesize different signal-to-clutter ratios.

Using the observation-based adaptive filter described in Section 5, with the specific implementation details from Section 4.5, the wind turbine's spectrogram has been estimated for

each of the six cases, and these are shown in Figures 5.7G-5.7L. For the case of precipitation only, as expected the estimate of the wind turbine signature in Figure 5.7G shows almost no signal. For cases with a mixture of WTC and rain, the Doppler bins where the signal-to-clutter ratio is high show very little of the spectra identified as wind turbine signature. This is observed in Figures 5.7H through 5.7K, as the precipitation power is varied by 30 dB in total power. As the wind turbine clutter-to-precipitation power ratio increases, the estimate of the wind turbine signature approaches that of the wind turbine only in Figure 5.7L.

The filtered spectrograms, with the estimated WTC suppressed, are shown in the right column of Figure 5.7. The filtered spectrogram is the result of subtracting the estimated wind turbine signature (the middle column of Figure 5.7) from the original observation spectrograms (the left column of Figure 5.7) following Equation 74. As with the estimated wind turbine signatures, the Doppler spectral bins that contain both wind turbine and precipitation signatures may retain some residual wind turbine spectra (consider Figure 5.7P as an example), but the out-of-band WTC signal is significantly attenuated.

For weather radar applications, the radar spectral moments are the typical desired output from the radar signal processor and, ultimately, provide a concise metric by which to evaluate the WTC suppression. The radar moments are estimated from the appropriate spectrograms using Equations 46-49. Moments for the observed spectrogram (Figures 5.8A, 5.8C, and 5.8E) and the filtered spectrogram (Figures 5.8B, 5.8D, and 5.8F) are presented for all six cases.

In the absence of noise, ground clutter, and wind turbine bias, the 10 dB attenuation steps in precipitation should result in equivalent steps in the estimated power moments. Similarly, without these biases, the velocity and spectrum width for the precipitation should remain constant. The original reflectivity (Figure 5.8A) and filtered reflectivity (5.8B) shows that the estimated power has a slight bias effect due to the WTC in the "-20dB Rain + Turbine" case and is dominated by the WTC in the "-30dB Rain + Turbine" case. For reflectivity,

the impact of the suppression of the wind turbine signature is most readily observed for the "-20dB Rain + Turbine," "-30dB Rain + Turbine," and "Turbine" cases where the signal-to-clutter ratio is low. Some suppression is observed in the "-10dB Rain + Turbine" for the peak power excursions, but this is only suppressed by a few decibels due to the significant precipitation echo power.

The spectral moments for the "Rain + Turbine" case are similar to the "Rain" case, indicating that the precipitation's signal power is high with respect to the WTC. Similarly, the moments for "-30dB Rain + Turbine" and "Turbine" are alike due to the dominance of the WTC. Although the wind turbine's signature was significantly attenuated in all cases, the residual power will act to bias the spectral moment estimates. For all observations containing the wind turbine signature, the mean Doppler velocity and spectrum width are improved by suppressing the wind turbine's signature. Even for cases where some residual wind turbine signature remains in the Doppler bins occupied by precipitation, the reflectivity-weighting effect results in a similar estimate for the velocity and spectrum width moments. In the absence of a suitably strong alternative scatterer, the reflectivity-weighting of the wind turbine can still dominate the estimates of the radar moments. This is most easily observed in the "Turbine" velocity and spectrum width moments.

5.3.2. Wind Turbine Coincident with Rain. The observed echo spectrogram of a wind turbine with precipitation in the same observation volume is shown in Figure 5.9 with and without GCF. Considering both GCF states provides a more detailed characterization of the suppression method and enables us to evaluate the bias of the stationary wind turbine components and ground clutter. The wind turbine's average rotation period is estimated to be 2.698 seconds, and this duration is used as the window length for samples in the suppression dictionary. The suppression filter starts processing observations after 3.20 seconds have passed (the dictionary window is delayed 0.5 seconds). Figures 5.9C and 5.9D show the estimated wind turbine signature with and without GCF, respectively. As shown, the estimated

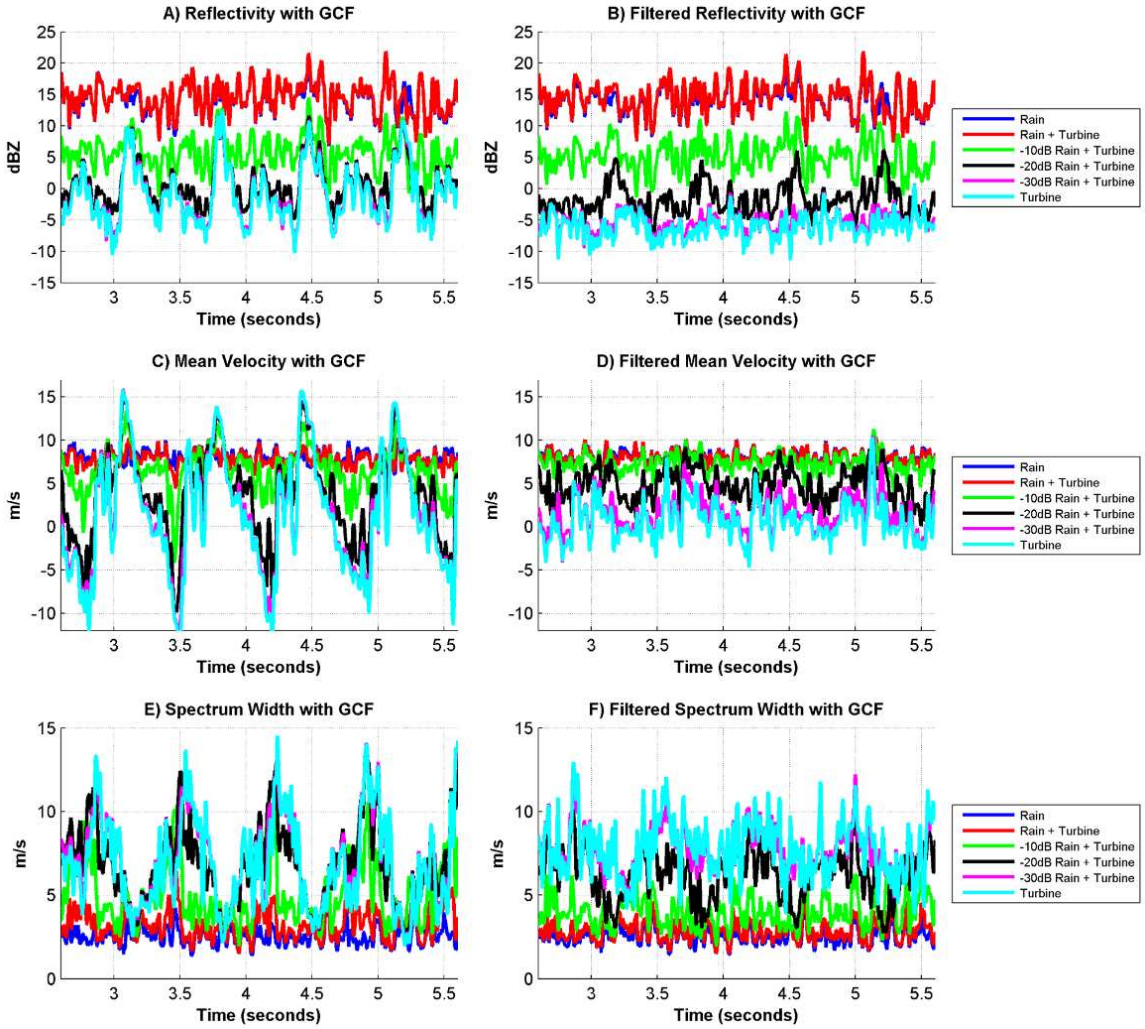


FIGURE 5.8. The observation spectrograms (Figures 5.7A-5.7F) are used to estimate the radar moments (reflectivity, radial mean Doppler velocity, and Doppler spectrum width) in Graphs A, C, and E, respectively. The radar moments after suppressing the wind turbine's signature are shown in Graphs B, D, and F (from Figures 5.7M-5.7R). A comparison of the before-and-after WTC suppression cases shows a clear improvement in the radar moments due to suppression of the WTC for all cases where WTC is present. Notably, the suppression method has a negligible impact on the precipitation power.

wind turbine signatures are similar regardless of the GCF state. The filtered spectrograms, with the wind turbine signature suppressed, are shown in Figure 5.9E without GCF and in Figure 5.9F with GCF.

Additionally, consider that the wind turbine acts on precipitation within the volume, as well as in radar volumes located downwind from the turbine [58]. This can broaden the

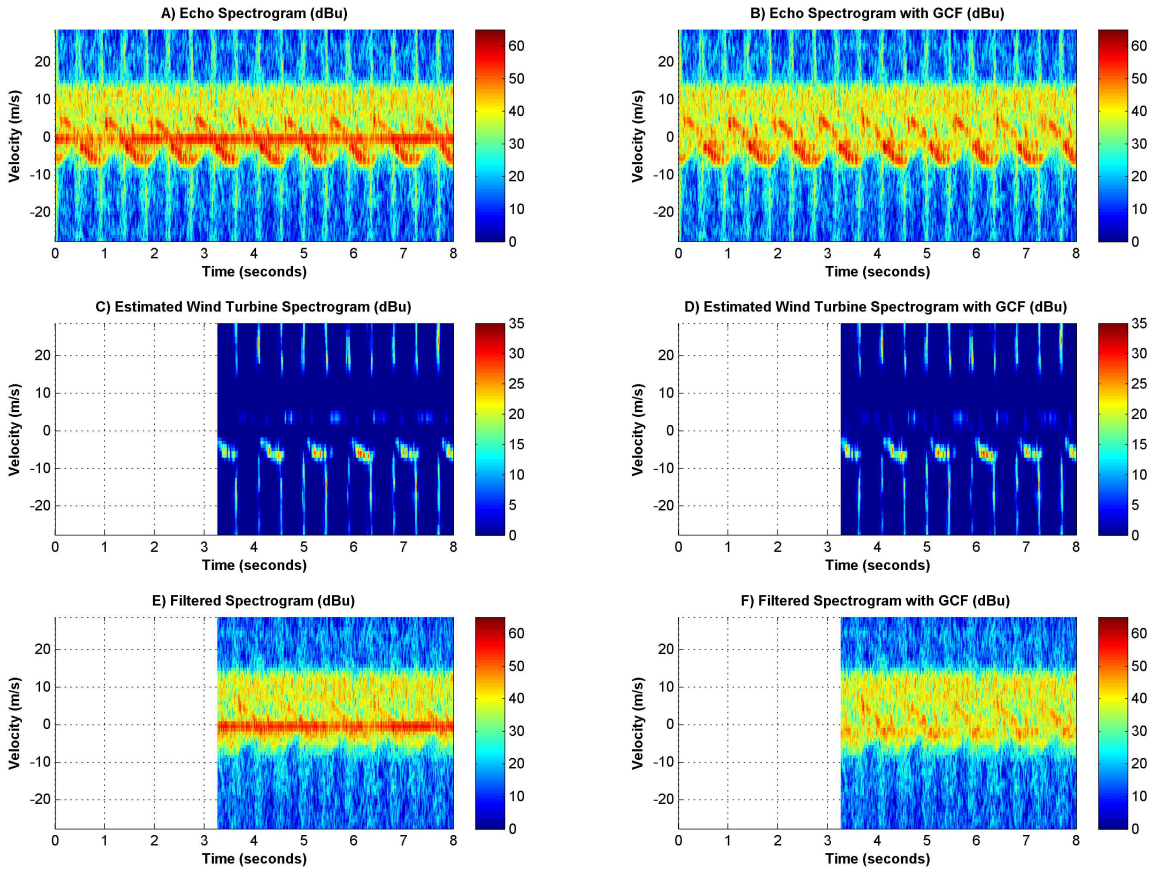


FIGURE 5.9. Observations of collocated precipitation and wind turbine on June 26, 2014, 23:07 UTC, 63.0 km from the CSU-CHILL radar. Graphs A, C, and E are without GCF, and Graphs B, D, and F are with GCF. The original spectrograms are shown in Graphs A and B. The estimated wind turbine signatures are shown in Graphs C and D. The filtered spectrograms, with the turbine signature suppressed, are shown in Graphs E and F.

precipitation's spectra and modulate the velocity of the precipitation over time. The wind turbine's influence can violate the WSS of the precipitation spectra and, in effect, result in precipitation having a periodic signature similar to that of a wind turbine.

To evaluate the overall suppression of the wind turbine signature, and any impact the suppression technique has on the precipitation power, histograms of the estimated wind turbine signature in Figures 5.9C and 5.9D are presented in Figures 5.10A and 5.10B, respectively. First, consider Figure 5.10B. For Doppler velocity bins that are almost exclusively composed of the wind turbine and noise (i.e., $\bar{v} < -5$ m/s and $\bar{v} > -15$ m/s), the suppression of the wind turbine signature exceeds 25 dB. The histograms also highlight that the occurrence of

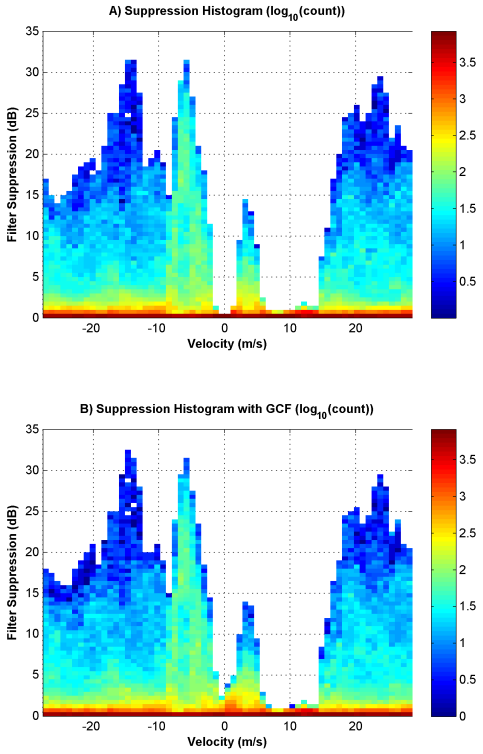


FIGURE 5.10. Histograms of the estimated wind turbine signatures from Figures 5.9C and 5.9D. The observation volume contains a mixture of rain and multiple wind turbine signatures. The precipitation spectra is primarily contained within the 5 to 15 m/s Doppler velocity bins. Graph A considers the estimate of the wind turbine signature including ground clutter. Graph B shows the same observations but instead with GCF enabled.

these large-magnitude contamination events is infrequent. These high-magnitude RCSs are largely due to the specular "flash" that occurs when the blade surface is parallel to the radar's observation plane. The histograms in Figure 5.10 also highlight a larger concentration of the wind turbine power in the Doppler region between $\pm 10$ m/s, which is suggested as containing one of at least two separate wind turbines in the observation volume. The histogram with GCF shows a similar distribution as the histogram without GCF with one notable exception: the near-zero Doppler velocity bins exhibit some degree of suppression with GCF enabled. When the zero-Doppler signature is suppressed, the nonzero, low-velocity scatterers are not obscured by the ground clutter (which can happen due to the spectral broadening effect of the window function). As such, their signature is more easily discriminated for suppression.

Inspection of Figures 5.9 and 5.10 suggests that two wind turbine signatures are observed within the same volume. One of the signatures exhibits the characteristics of a turbine at a lower yaw angle relative to the radar, with its RCS primarily constrained to $|v| < 10$ m/s. Also, the observed rotating RCS is sinusoidal. The other wind turbine signature shows features that are typically associated with relative yaw angles where the blades are rotating in a plane that is closer to parallel with the observation radial. Such a turbine signature is characterized by large Doppler excursions (and possibly Doppler aliasing) and a relatively low, impulsive, dynamic RCS.

A review of Figure 5.9B shows that the wind turbine and precipitation spectra overlap for Doppler velocities greater than zero. Ideally, no suppression of precipitation occurs. The histogram results indicate that, within a spectral bin, up to 2 dB of precipitation power may be sporadically suppressed. The overall impact of this on the radar moments is considered in Figure 5.11. For all moments, with and without GCF, the filtered moments show lower variability during the observation period in which WTC suppression is performed (i.e., from 3.2 to 8 seconds). A clear biasing effect from the ground clutter is noticed in all moments. With GCF and wind turbine suppression, the precipitation's reflectivity is approximately 25 dBZ, which is indicative of light rain. The peak reflectivity of the combined wind turbine and precipitation exceeds 35 dBZ without WTC suppression. Without GCF, the ground clutter has a mean reflectivity of approximately 30 dBZ. The mean velocity estimates still show a residual periodic behavior, but overall, the estimates more closely approximate the precipitation's centroid. The wind turbine's signature is suppressed by 8-10 dB when GCF is enabled. (Less suppression is realized without GCF because the ground clutter dominates the observed reflectivity.)

5.3.3. Wind Turbine with Light Precipitation. Now consider observations of weak-echo precipitation and a wind turbine. The precipitation is observed with a low signal-to-noise ratio (and very low signal-to-clutter ratio), and there is also an indication that it is

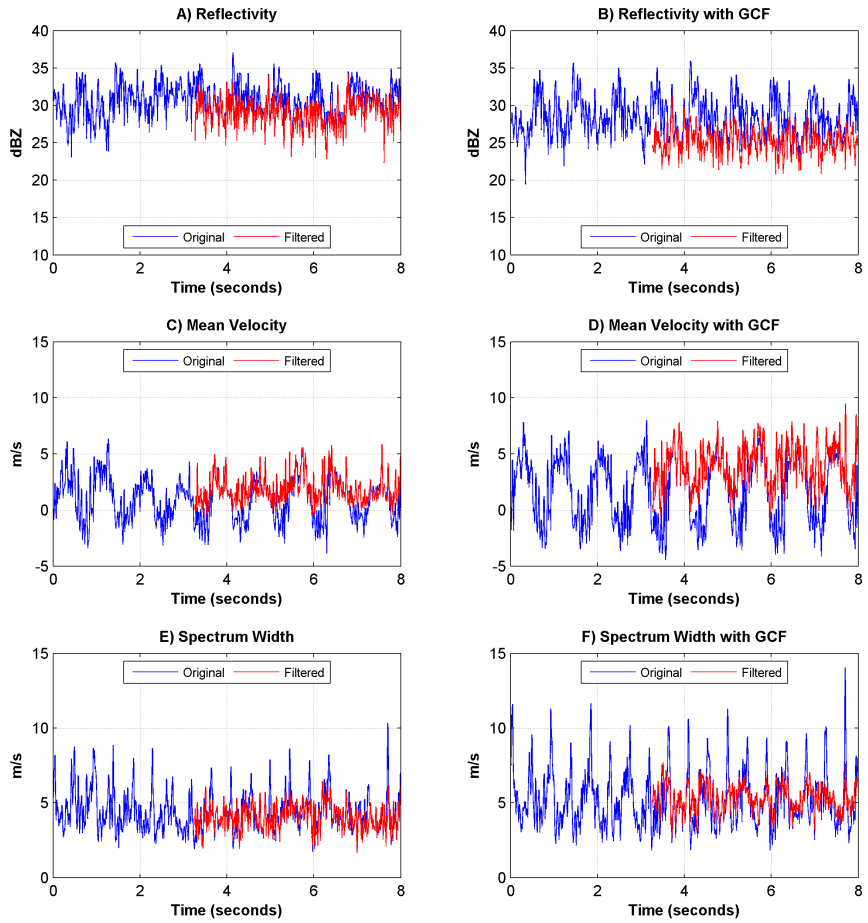


FIGURE 5.11. Spectral radar moment estimates before and after WTC suppression. The moments are estimated from the spectrograms in Figure 5.9. Graphs A, C, and E include ground clutter. Graphs B, D, and F have GCF enabled.

modulated by the wind turbine's blades. Note, this is the same case shown in Figure 5.5 to estimate the rotation period and cyclostationary signature. The average rotation period was estimated to be 4.069 seconds, and therefore, the WTC filter begins for observations after 4.57 seconds (again, allowing for a 0.5-second window delay).

Figure 5.12 shows the spectrograms, with and without GCF, for the observation, wind turbine signature, and filtered result. By comparing Figures 5.12A and 5.12B, it is clear that the ground clutter dominates the overall observed echo power. The wind turbine's signature is primarily a result of an impulsive specular reflection from the blades. Six blade flashes are observed during the full rotation period (three from the leading edge of the blade and

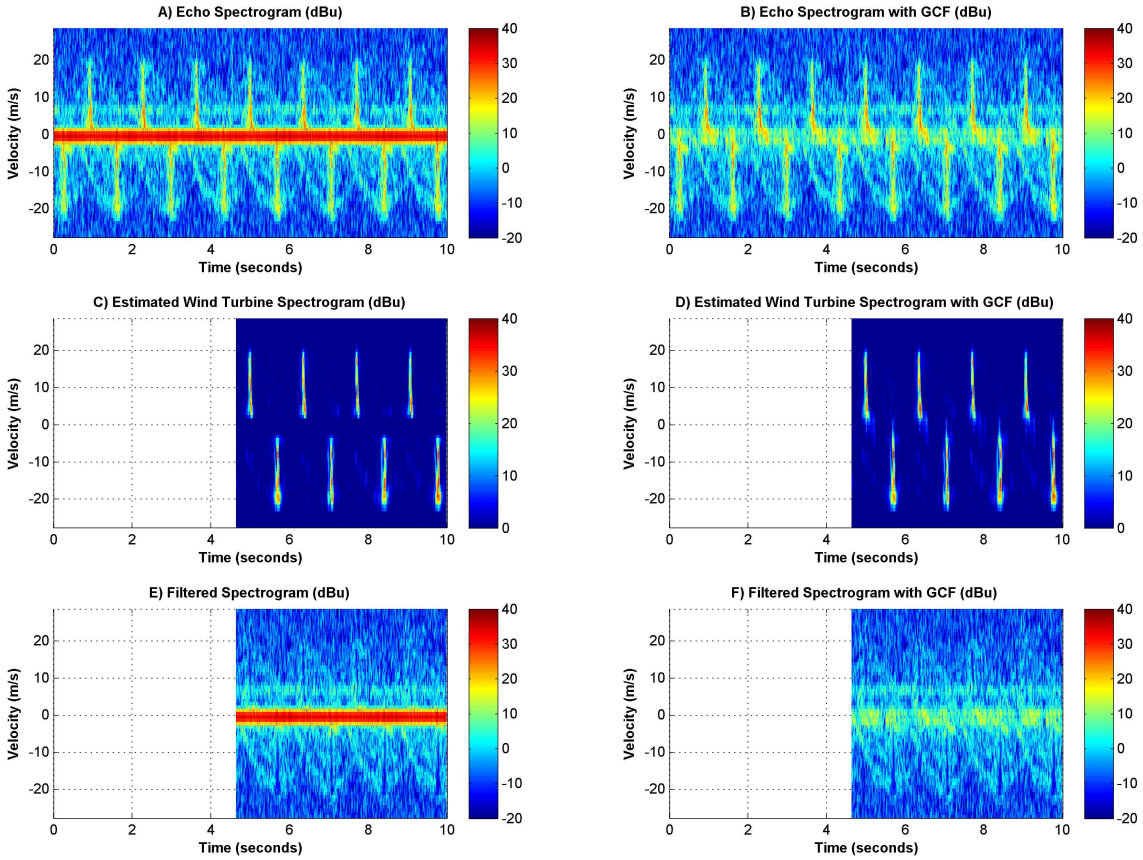


FIGURE 5.12. CSU-CHILL observations of a wind turbine with light precipitation on March 7, 2014, 23:37 UTC, at a range of 62.55 km and an azimuth of 344.54 degrees. Graphs A, C, and E are with ground clutter included, and Graphs B, D, and F have ground clutter filtering enabled. The observed spectrograms are shown in Graphs A and B, the wind turbine signature in Graphs C and D, and the filtered spectrograms in Graphs E and F.

three from the trailing edge of the blade, with an opposite velocity sign). The leading edge of the blade provides a larger, smoother surface and, thus, is typically associated with the higher observed RCS. In this case, the spectrograms indicate that the leading edge of the wind turbine blades is associated with the positive Doppler velocities.

A weak echo is observed that is indicative of precipitation at Doppler velocities around 7 m/s. There is also an indication that the precipitation is impacted by the rotating turbine and is spread through the Doppler spectrum following the wind turbine blades. This may also be a combination of precipitation and scattering from the wind turbine blade tip.

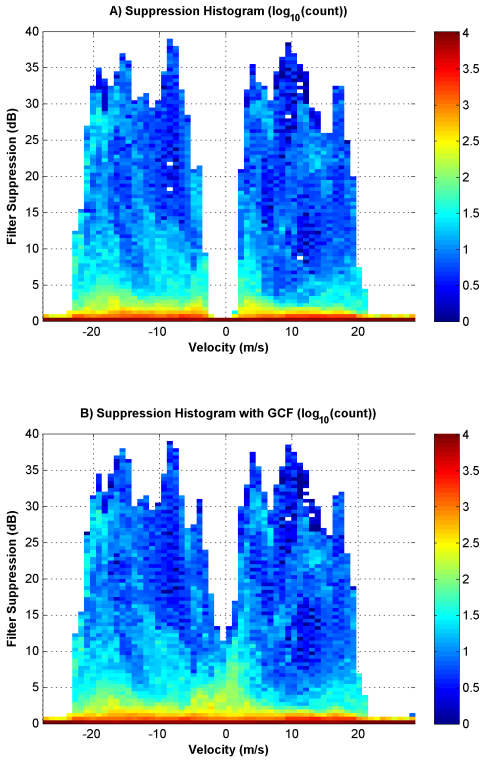


FIGURE 5.13. Histograms of the wind turbine signature, and therefore suppression, for observations from Figure 5.12. Graphs A and B show with and without GCF, respectively.

Figure 5.13 shows histograms of the wind turbine signature, which, subsequently, is also the histogram of the wind turbine suppression. The wind turbine signature occupies the Doppler spectrum from approximately -22 m/s to 22 m/s, and the peak suppression is greater than 35 dB. Without the suppression of ground clutter, the Doppler range around zero ($\pm 2$ m/s) shows no wind turbine signature. By enabling GCF, the same Doppler bins indicate 10 dB or more of spectra power that can be attributed to the wind turbine's periodic signature.

Again, evaluation of the radar spectral moments provides a metric for measuring the utility of the wind turbine suppression technique. The spectral moments are presented in Figure 5.14 before and after suppression, with and without GCF, using the spectrograms in Figure 5.13. The ground clutter contribution is more than 15 dB of the observed echo power and significantly biases all observations. After suppressing the WTC, the mean velocity, with

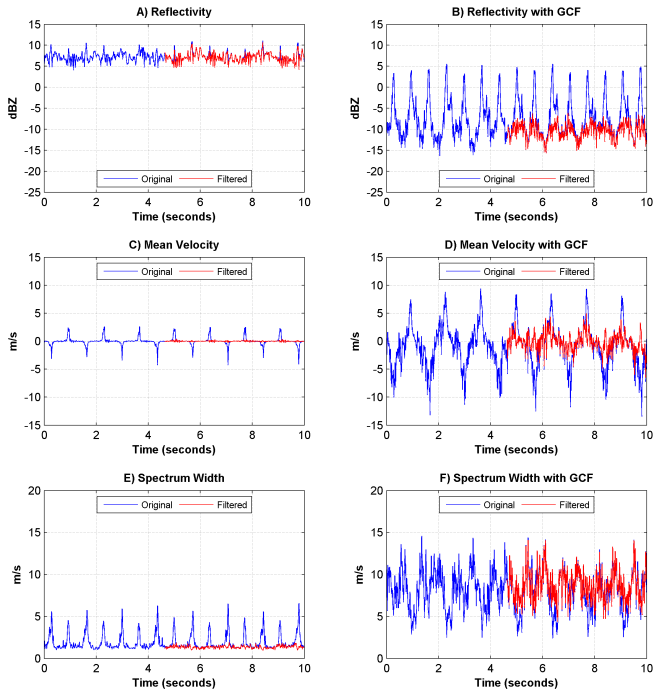


FIGURE 5.14. The spectral radar moment estimates of reflectivity, mean Doppler velocity, and spectrum width before and after filtering WTC. The moments are considered with and without GCF in the left and right columns, respectively.

ground clutter included, is approximately zero, and the spectrum width is nearly constant. With GCF, the approximate filtered reflectivity is -10 dBZ and shows the wind turbine signature suppressed by 10-15 dB during the blade flashes. The mean Doppler velocity and spectrum width variation is reduced but still shows a residual trend that tracks the wind turbine due to the absence of another significant scattering source.

CHAPTER 6

# Wind Turbine Characterization with State Telemetry

The geometry of a wind turbine determines its scattering characteristics (i.e., its radar cross-section, or RCS), and therefore, the turbine's RCS is deterministic. Numerical simulations of wind turbines have been considered by numerous sources, but the electrical size of a turbine has limited direct solutions to fully resolved models due to computational complexity [6, 9, 54, 11]. Despite this, by simplifying assumptions for the physics, it has been demonstrated that a turbine's RCS can be calculated and represents at least the first-order scattering behavior [6, 11]. The wind turbine's signature has also been shown to be deterministic in comparison of observations of commercial-scale turbines and simulation results in [6], and through evaluating the cyclostationarity properties and cyclic correlation of spectral observations in [1]. Given that the turbine's signature is deterministic, this suggests that with prior observations of its signature for a turbine's operating state, the turbine's signature can be suppressed in radar observations of the same state. This leads to the core motivation for this work: With state telemetry from a wind turbine, can the wind turbine's radar signature be suppressed?

In general, the operating state of a wind turbine is not made available for use outside the controller, but exceptions can be found in turbines that have been instrumented for research purposes [59]. For fixed-pointing observations of wind turbines, the state of the turbine can be estimated using information about its structure [7]. For scanning radar systems, sustained, long-duration observations are not feasible, and therefore, other techniques for determining the turbine's state must be considered. For example, consider the relationship

between the observed radar signature and the turbine's state. What state variables are most critical to estimating the signature, and what is the signature's sensitivity to variation (or error) in these variables? Scale model investigations provide some insight into the scattering characteristics of a wind turbine, but the electrical size, inertia forces, and dynamic effects of the wind are not represented [9, 12].

Section 6.1 details the experimental setup for radar observations a utility-scale wind turbine with high-data-rate state telemetry time-synchronized to the radar. A geometric model for the wind turbine signature is presented in Section 6.2 and used to relate the radar's observations and the turbine's state. In Section 6.3, observations and characteristics of the wind turbine signature from multiple operating states are discussed in detail. With the characterization results and turbine model, techniques for suppressing the turbine signature utilizing the turbine's telemetry are demonstrated for both fixed-pointing and scanning cases in Section 6.4.

## 6.1. Description of the Experiment

The NREL CART3, located at the NWTC was observed using the CSU X-band radar systems during November and December of 2015. The CART3 provides 400 Hertz telemetry and is GPS-synchronized, providing an ideal opportunity for direct comparison of radar observations with the turbine's state. Relevant specifications for the CSU X-band radar's deployment and observatiosn of the CART3 are included in Table 6.1.

To evaluate the relationship between the observed turbine radar signature and the turbine's state telemetry, observations from December 15, 2015, UTC, will be considered. For this day, fixed-pointing observations were made, with each followed by a 3-degrees-per-second scan of the turbine covering $\pm 6$ degrees in azimuth with respect to the CART3's direction.

TABLE 6.1. Specifications of the CSU X-band radar relevant to observations of the CART3 at the NREL NWTC. The ranges, azimuth, and yaw are estimated using Google Earth as well as radar observations.

| | |
|---|---|
| Nominal Frequency | 9.45 GHz |
| Antenna Beamwidth | 1.4 degrees |
| TX Peak Power | 15 kW |
| Pulse Repetition Frequency | 3 kHz |
| Pulse Duration | 250 microseconds |
| Range Sampling | $\leq$ 12 meters |
| Unambiguous Velocity | $\pm$ 23.81 m/s |
| Range to Nacelle | 935 meters |
| Beamwidth at Nacelle | 22.8 meters |
| Radar Azimuth to Turbine | 83 degrees |
| Turbine Yaw to Radar | 263 degrees |

The in-phase and quadrature (IQ) data was recorded for these observations to enable post-processing of the data. Histograms of the radar's observed cardinal yaw angles and rotation rate for this day are shown in Figure 6.1. A cardinal yaw angle of 263 degrees is directed along the radar's observation radial. Radar-relative yaw angles are primarily of interest, as these determine the observed radar signature. Positive-value, relative yaw angles are pointed to the north and west side of the radar (up to a yaw of 180 degrees). For the observations available on this day, while the CART3 was in its "operating" mode (i.e., not in standby, start-up, or shutdown mode), the blades' pitch is constant at 3.69 degrees. (Note: A 90-degree pitch is with the blade's leading edge pointing into the wind and is the blade pitch while in the standby state.)

To analyze the wind turbine's signature, spectral methods are used on a single polarization. From the IQ time series ($x$), the spectrogram is calculated as follows:

$$S[t,k] = \frac{1}{N}\left|\sum_{n=0}^{N-1} x[t+n]w[n]e^{-j2\pi kn/N}\right|^2. \tag{75}$$

Here, a Gaussian data window ($w$) of 64 samples is selected for analysis. The spectra differ by four IQ observations (i.e., 60/64 samples are common between sequential spectra). At

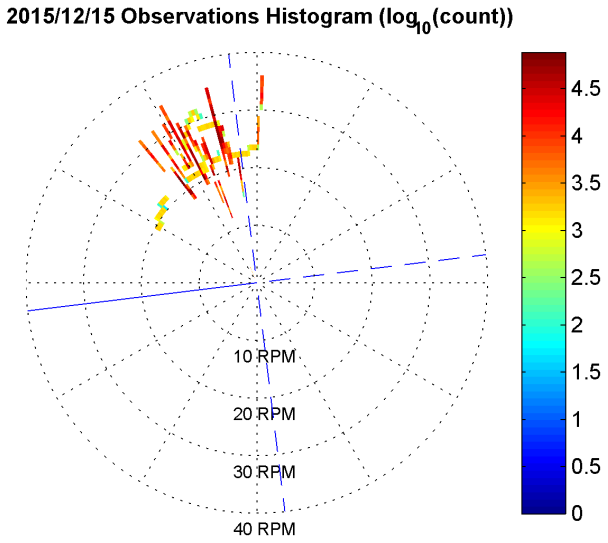


FIGURE 6.1. A histogram (showing a logarithmic count of all observations) of the CART3's cardinal yaw direction and rotation rate for all December 15, 2015, UTC, radar observations. The solid blue line shows the direction of the CSU radar, and the dashed blue lines are 90, 180, and 270 degrees relative to that radial.

the CART3's maximum speed of 37 RPM, this sample period represents a rotation of 0.30, degrees whereas the window covers a total rotation of 4.74 degrees.

The CART3 and X-band radar observations are both synchronized to the global positioning system for a common time source. To effectively compare the telemetry from the CART3 with the observations from the radar, the alignment and synchronization of both systems' clocks must be verified. As a means to evaluate the time alignment, rotation rate estimates and the turbine's reported rotation rate are shown in Figure 6.2 for a period where the blades were decelerating. The radar-based rotation rate estimate is derived from the time differences between peak zero-Doppler power observations for each blade (i.e., nominally 120 degrees of rotation), following $\Delta\theta/\Delta t$. Similarly, the rotation rate is estimated using the times between zero-crossings of the turbine blades' reported positions. The results show very good agreement between the two estimates and the actual reported speed during the observation period. The temporal alignment has also been confirmed by verifying

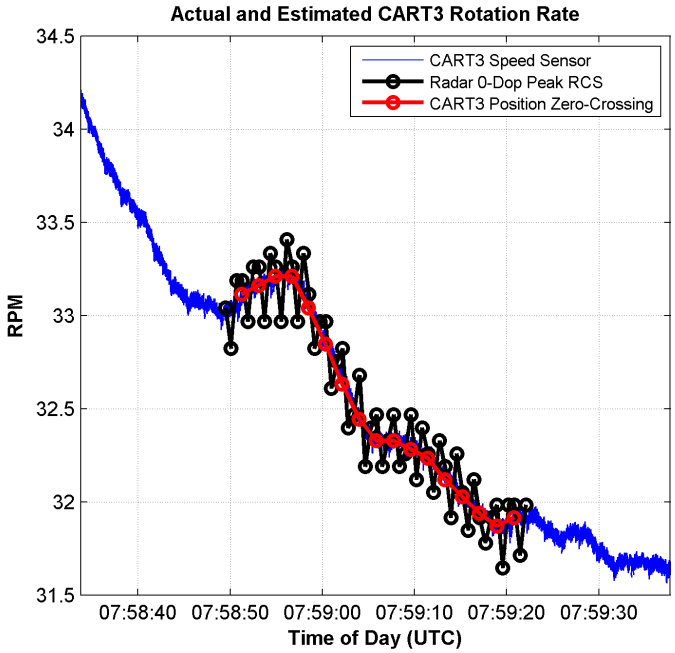


FIGURE 6.2. Validation of the temporal alignment of observations using the estimated rotation rate from radar observations and the CART3's telemetry.

that the selected time-offset between the system clocks yields the minimum variance of all the spectral observations at a fixed state (the results have been omitted for brevity). After comparing the radar observations and CART3 telemetry, the observations are expected to be synchronized to better than a millisecond.

## 6.2. TURBINE MODEL

Consider a point on the turbine's blade. A model for the position and velocity of this point can be derived through Euler coordinate transformations. All of the coordinate transformations act on the coordinate system located at the blades' center of rotation (the turbine's hub). The point's position can be determined for any yaw ($\phi$), blade tilt ($\alpha$), cone angle ($\beta$), and absolute rotation angle ($\theta$) following

$$\mathbf{p} = \begin{bmatrix} p_x & p_y & p_z \end{bmatrix}^T = R_\phi R_\alpha R_\theta R_\beta \begin{bmatrix} 0 & 0 & r \end{bmatrix}^T, \tag{76}$$

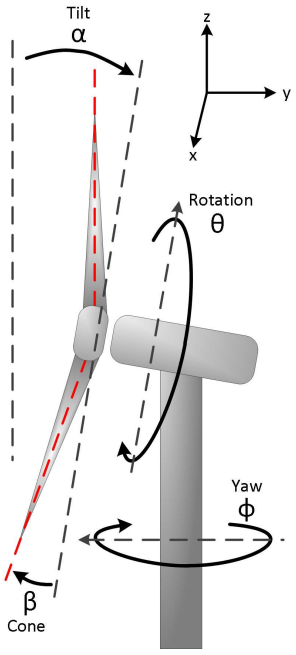


FIGURE 6.3. Angles and directions of movement for the wind turbine model. In some instances, the yaw angle is referenced to North. For the purposes of estimating the radar signature, the radar-relative yaw angle is of interested. The radar-relative yaw angle is zero when the nacelle and hub are directed at the radar and the radar-relative yaw angle is ±90 degrees when the radar's direction of propagation is parallel to the blade's plane of rotation. Note the direction of increasing rotation and yaw angles.

where $^T$ is the matrix transpose and $R$ the Euler rotation matrices for four parameters applied to a point at radius $r$. The blade's rotation angle starts at top-dead-center (i.e., $\theta = 0$ is along the the z-axis). The angles and sign conventions are illustrated in Figure 6.3.

The radar observer is located on the negative y-axis. The Euler rotation matrices for each variable are presented next, and each accounts for its rotation sign convention. The yaw angle increases clockwise about the z-axis:

$$R_\phi = \begin{bmatrix} \cos(-\phi) & -\sin(-\phi) & 0 \\ \sin(-\phi) & \cos(-\phi) & 0 \\ 0 & 0 & 1 \end{bmatrix} = \begin{bmatrix} \cos\phi & \sin\phi & 0 \\ -\sin\phi & \cos\phi & 0 \\ 0 & 0 & 1 \end{bmatrix}. \tag{77a}$$

The blade tilts clockwise about the x-axis:

$$R_\alpha = \begin{bmatrix} 1 & 0 & 0 \\ 0 & \cos(-\alpha) & -\sin(-\alpha) \\ 0 & \sin(-\alpha) & \cos(-\alpha) \end{bmatrix} = \begin{bmatrix} 1 & 0 & 0 \\ 0 & \cos\alpha & \sin\alpha \\ 0 & -\sin\alpha & \cos\alpha \end{bmatrix}. \tag{77b}$$

The rotation angle increases in a counter-clockwise direction about the y-axis:

$$R_\theta = \begin{bmatrix} \cos\theta & 0 & \sin\theta \\ 0 & 1 & 0 \\ -\sin\theta & 0 & \cos\theta \end{bmatrix}. \tag{77c}$$

The cone angle is accounted for by a counter-clockwise rotation about the x-axis:

$$R_\beta = \begin{bmatrix} 1 & 0 & 0 \\ 0 & \cos\beta & -\sin\beta \\ 0 & \sin\beta & \cos\beta \end{bmatrix}. \tag{77d}$$

After the associated rotation transforms are applied, the position of the blade's scattering point (referenced to the hub) is

$$\mathbf{p} = \tilde{r} \begin{bmatrix} \cos\phi\sin\theta\cos\beta - \sin\phi\cos\alpha\sin\beta + \sin\phi\sin\alpha\cos\theta\cos\beta \\ -\sin\phi\sin\theta\cos\beta - \cos\phi\cos\alpha\sin\beta + \cos\phi\sin\alpha\cos\theta\cos\beta \\ \sin\alpha\sin\beta + \cos\alpha\cos\theta\cos\beta \end{bmatrix}, \tag{78}$$

where $\tilde{r}$ is the radius to the scattering point being modeled. If this point on the blade represents the blade's scattering phase center and if we consider far-field radar observations with the radial parallel to the negative y-axis, the radial distance (with the origin at the

center of rotation) is

$$p_r = p_y = -\tilde{r}\left[\sin\phi\sin\theta\cos\beta + \cos\phi\cos\alpha\sin\beta - \cos\phi\sin\alpha\cos\theta\cos\beta\right]. \tag{79}$$

Note: the sign convection is that negative distances are closer to the radar.

The change in the radial position as a function of the rotation angle (and for a fixed radius $\tilde{r}$) can be determined from the derivative of the position with respect to $\theta$:

$$\frac{\partial p_r}{\partial\theta} = -\tilde{r}\cos\beta\left[\sin\phi\cos\theta + \cos\phi\sin\alpha\sin\theta\right]. \tag{80}$$

The radial velocity, again assuming $\tilde{r}$ is constant in $\theta$, is a function of the change in rotation with respect to time: $\frac{\partial\theta}{\partial t}$ or $\dot{\theta}$. The observed radial velocity for the point is then

$$v_r = \frac{\partial p_r}{\partial\theta}\frac{\partial\theta}{\partial t} = -\dot{\theta}\tilde{r}\cos\beta\left[\sin\phi\cos\theta + \cos\phi\sin\alpha\sin\theta\right], \tag{81}$$

which follows the radar's velocity convention, with negative velocities moving toward the radar.

The radar's elevation angle with respect to the turbine ($\psi$) can also be accounted for, giving

$$\begin{aligned} p_r = &-\tilde{r}\cos(\psi)\left[\sin\phi\sin\theta\cos\beta + \cos\phi\cos\alpha\sin\beta - \cos\phi\sin\alpha\cos\theta\cos\beta\right] \\ &+\tilde{r}\sin(\psi)\left[\sin\alpha\sin\beta + \cos\alpha\cos\theta\cos\beta\right] \end{aligned} \tag{82}$$

and

$$v_r = -\dot{\theta}\tilde{r}\cos\beta\left[\cos\psi\left(\sin\phi\cos\theta + \cos\phi\sin\alpha\sin\theta\right) + \sin\psi\cos\alpha\sin\theta\right]. \tag{83}$$

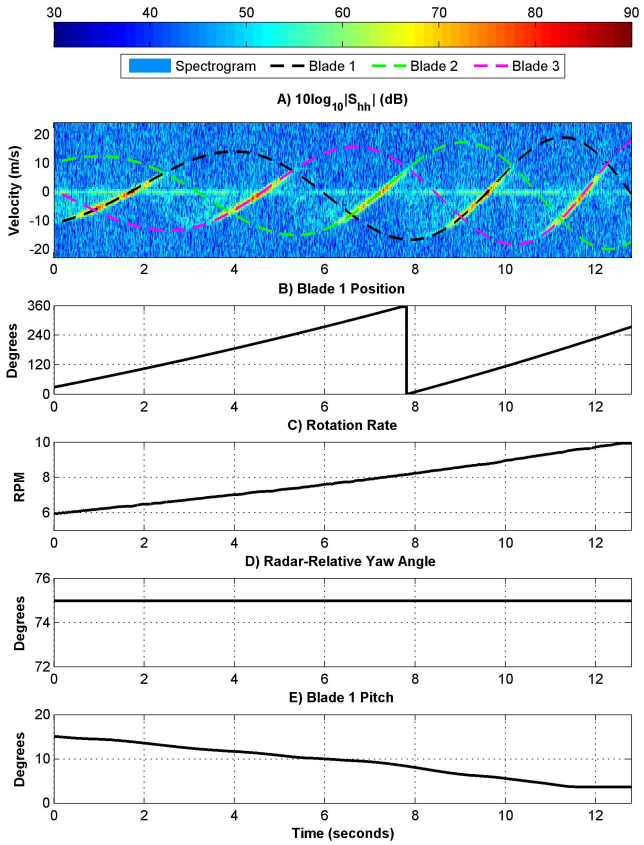


FIGURE 6.4. Velocity model estimates overlaid on radar observations during a ramp-up event for the CART3. The black dashed line is the blade-tip path of Blade 1. Similarly, the green line represents Blade 2, and the magenta dashed line is for Blade 3.

The CART3 has steel blades with no cone angle (i.e., $\beta = 0$), and the tilt angle is 3.77 degrees [59]. The yaw, rotation angle, and rotation rate can be directly applied from the CART3's state telemetry. The mean elevation angle for the CSU X-band radar's observations of the CART3 is approximately 1.3 degrees. To demonstrate and compare the model of the CART3 blade tips' velocities to the radar signature observations, consider Figure 6.4. Note, the radius $\tilde{r}$ used here is the radius to the CART3's blade tip (20 meters).

The CART3 presents an ideal case for the application of this model given its relatively short steel blades. For larger wind turbine systems with composite blades, gravity and wind-loading forces exacerbate the effects of the dynamic bending moments along the blade's length. The geometry of the blades is a complex, dynamic system [60]. Blade flex due to

gravity can be modeled by introducing a rotation angle dependence to $\beta$ (or $\alpha$). Blade flex due to wind loading can be added (potentially with a loose dependence on the rotation rate), and stochastic vibration can also be included here. In reality, $\tilde{r}$ is dependent on $\alpha$, $\beta$, $\phi$, and $\theta$, as the phase center's position on the blade changes due to shifts in the illuminated surface. The time derivative of $\tilde{r}$ may be non-trivial and is a function of the blade's geometry as well as the relative position of the turbine with respect to the radar. The distance to the phase center may also have an additional modulation term that is a result of a non-singular volume. (Even if the blade rotates by $\frac{d\theta}{dt}$, the observed phase center may have an apparent rotation of $\theta'$, where $\frac{d\theta'}{dt} \neq \frac{d\theta}{dt}$, as a result of the changing aspect of the radar wave's projection on the moving blade.)

In Figure 6.4, the blade tip's physical radius was used but may not be the actual location of the scattering phase center observed by the radar. The scatterer's radius ($\tilde{r}$) can be estimated from radar observations. For the CART3, the estimates are shown in Figure 6.5 for all available yaw and RPM combinations where observations are available over the complete range of rotation angles (i.e., from 0 to 360 degrees). The scatterer's radius is estimated for each yaw/RPM state combination by determining the radius that maximizes the total spectral power within the model's selected region. From this, an effective radius of the blade's scattering point is estimated to be $\tilde{r} = 18.3$ meters, which will be used for modeling the CART3's signature for the remainder of this work.

Note, this model only estimates the "tip halo" velocity. Additional constraints may be required to adequately capture the blade "flash" and echoes from the blade surface at lower velocities. In addition, the instantaneous velocity observed may require a range of velocities (i.e., a spectral width) to account for any spectral broadening or variation in the velocity

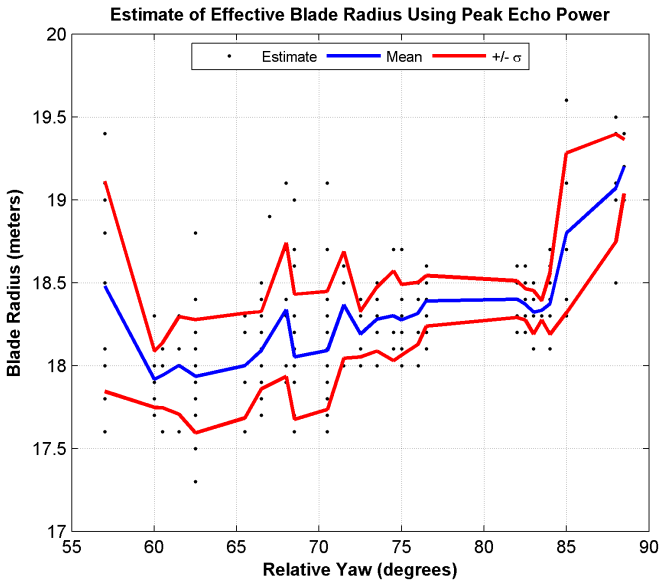


FIGURE 6.5. Estimates of the effective blade radius using full 360-degree rotations for all available yaw and rotation rate states. The mean and standard deviation of the radius estimates are shown for yaw angle states where more than one estimate of the radius is available.

during the radar's observation window. These considerations will be discussed in more detail in subsequent sections as it relates to the observations of the CART3.

## 6.3. Observations of the CART3's Radar Signature

The wind turbine's RCS can be characterized with a high degree of accuracy for a given state. The difficulties in wind turbine characterization are the time-varying and ambiguous state of the turbine from the point of view of a radar observer. A single turbine, multiple turbines, or partial wind turbines may exist in a range-volume cell, depending on the wind farm's and radar's configuration. Within a full wind turbine rotation period, it is expected that six "flashes" will be observed: three flashes from the blades at the top position and three from the blades at the bottom position. If Doppler aliasing does not occur, the blade flashes from the top and bottom of the rotation will have similar velocity magnitudes but opposing velocity signs [6, 12, 11, 1].

In this section, X-band radar observations, in the form of spectrograms, are directly related to the CART3's state (as reported by the turbine's telemetry). The primary state parameters of interest are the turbine's rotation angle, rotation rate, and the radar-relative yaw angle. As noted earlier, the blade pitch for each blade is also reported but typically found to be fixed for the controller configuration used except during ramp-up and ramp-down from an idle state.

6.3.1. Temporal Correlation vs. Rotation Angle Correlation. In [1], the characterization of wind turbines without state telemetry demonstrated that for short periods of time, the wind turbine's signature was well represented as a cyclostationary process, and the spectral observations of the turbine are periodically correlated. Without state telemetry, time was used as the independent variable for characterization and analysis. Time was a proxy for the rotation angle under the cyclostationary assumption. With state telemetry, this assumption is not required, and the cyclostationary properties of the wind turbine's signature can be independently validated. The wind turbine's RCS (and thus the echo power) is expected to be cyclostationary with the rotation angle. The temporal analysis assumes that the wind turbine's state is constant (except for the rotation angle), allowing time ($t$) and the rotation to be interchanged:

$$\theta = \dot{\theta} t. \tag{84}$$

For a time-varying rotation rate, the process remains cyclostationary with respect to the turbine's rotation angle but will no longer be cyclostationary with respect to time. The relationship between time and the rotation angle is used for comparisons between spectra ($S$). Note: For the estimation of the spectra, time remains the independent variable. This is done to simplify estimation of the spectra (where $t$ is uniformly sampled), as well as to

promote cross-comparisons during the analysis (e.g., a common "velocity" axis). The discrete Fourier transform used to generate the spectra could use $\theta$ instead of $t$, giving a normalized, pseudo-"velocity" axis across different rotation rates (see Equation 84).

Here, the cyclostationarity of the wind turbine with respect to time is verified under near-constant operating states. The cyclostationarity of the turbine's signature will also be considered with respect to the absolute rotation angle (i.e., the variable time represents with all states constant except the rotation angle). The temporal correlation is compared to the rotation correlation structure for the CART3 given a constant yaw and blade pitch. A 0.5-degree bin is used for estimation of the rotation angle correlation. The dual-polarization signature correlation structures are also evaluated (following [1]).

The first case shown in Figure 6.6 considers observations for 34 seconds, at a yaw of 70.8 degrees relative to the radar, a constant blade pitch of 3.7 degrees, and a near-constant rotation rate of 20.18 RPM with a standard deviation of 0.06 RPM. A comparison of the temporal correlation of the spectrograms to the correlation of the spectrograms with respect to the change in rotation angles shows good agreement in the overall structure. The correlation of the rotation angles demonstrates higher peak correlations at multiples of the blade-pass period. The correlation at one blade-pass period (approximately 1 second) is similar to that of the correlation at 120 degrees of rotation. This is a result of the slow variation in rotation rate (and therefore, the relationship $\theta = \dot{\theta}t$ holds for short time-lags). As the time-lag increases slightly, even small errors in the estimate of the rotation angle from time (which is really what the correlation is implementing) are noticed (see Figure 6.6C). The decorrelation rate of the wind turbine blade's spectral signature as a function of rotation angle (and the observation window) is less than 1.5 degrees at 20 RPM (see Figure 6.7).

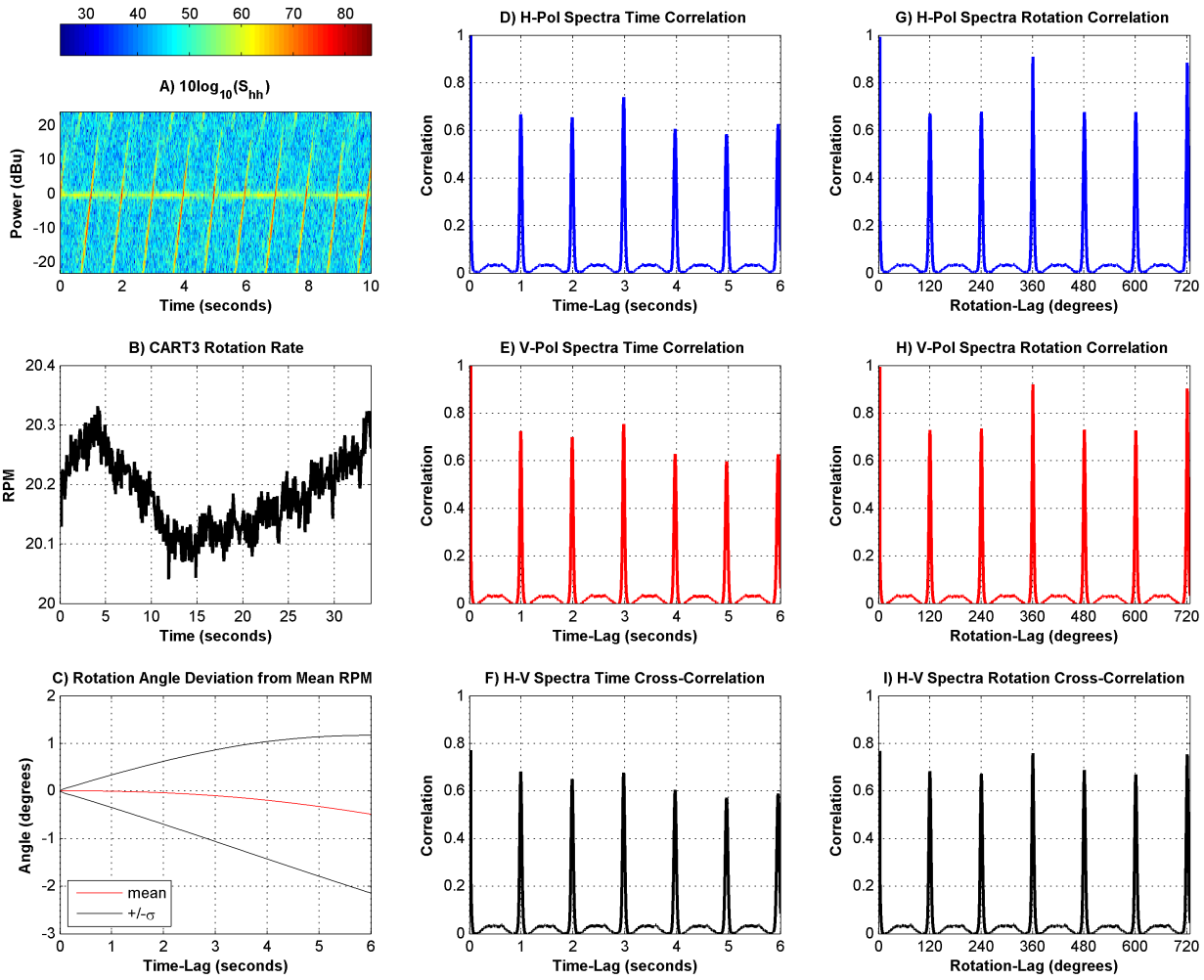


FIGURE 6.6. Correlation of the CART3's radar signature as a function of time and rotation. For this observation period, the CART3's yaw angle is fixed, and the rotation rate is near constant, with a mean of 20.18 RPM (Graph B).

Now consider the correlation structure of the CART3's radar signatures during a ramp in rotation rate, as presented in Figure 6.8. Again, a 34-second observation period is used. Here, the rotation rate of the turbine changes from approximately 25 RPM to 21 RPM over 30 seconds and then remains nearly constant until the observation ends. For this case, the CART3's yaw angle was constant at 84 degrees with respect to the radar. The ramp in rotation rate results in the time-to-rotation angle relationship no longer being constant, and, as a result, the temporal correlation is very poor. When considering the correlation in rotation angle, the structure shows the expected periodic characteristic in 120-degree

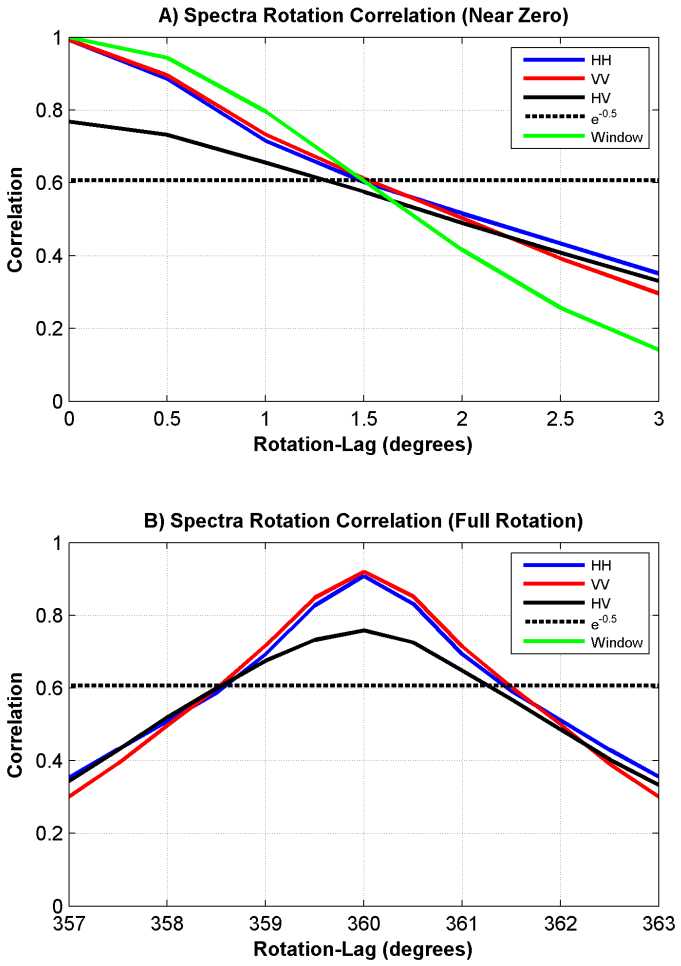


FIGURE 6.7. The correlation of the CART3's radar signature as a function of the rotation angle using the same observations from Figure 6.6. The rotation decorrelation ($r_{xx} = e^{-0.5}$) is illustrated by the horizontal dashed line. The green line represents the artificial correlation introduced by the data's window.

intervals, with very high correlation at multiples of a full rotation. The rotation correlation, even with "small" variations in rotation rate, remains very high and is similar to that for a fixed rotation rate as shown in Figure 6.6.

6.3.2. VARIATION WITH YAW AND ROTATION RATE. To further evaluate the relationship between the observed spectral signature of the wind turbine and its state, observations are considered here across three state parameters: rotation angle, rotation rate, and radar-relative yaw. (Blade pitch is constant for this data set and is therefore not evaluated here).

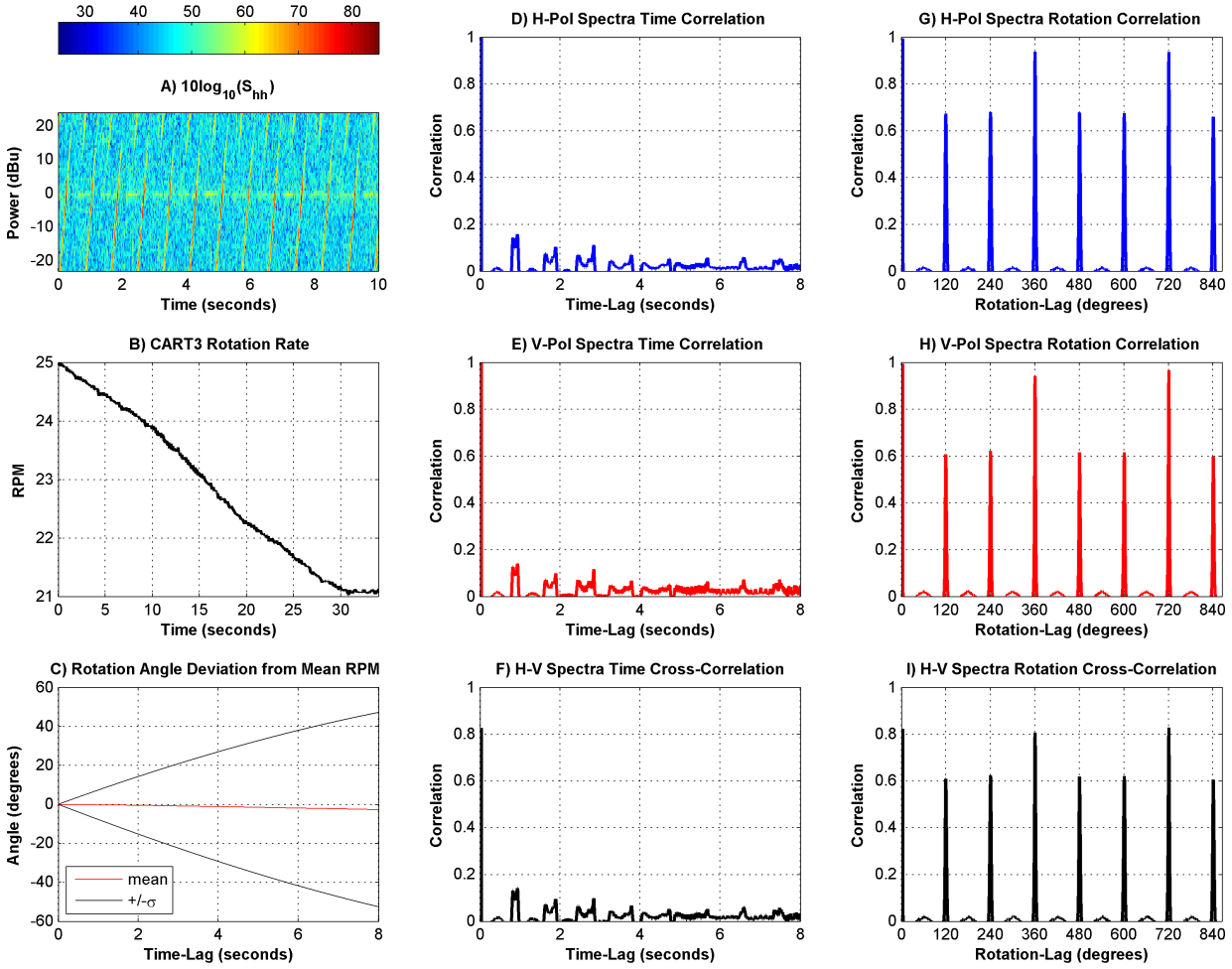


FIGURE 6.8. Temporal and rotation correlation of the CART3's radar signature during a rotation rate ramp event. The rotation angle is no longer related to time by a constant, and the error in correlation when using time as the independent variable is apparent.

Figure 6.9 shows the mean spectral signature, as a function of rotation angle, for six rotation rates at a fixed yaw angle. Similarly, Figure 6.10 shows the mean spectral signature for six yaw angles at a fixed rotation rate. The mean spectral signatures presented are the geometric mean of the spectral echo power at the given state (or the arithmetic mean of the power in decibels). Using all available observations from December 15, 2015, that match the specified state (yaw, rotation rate, rotation angle), the mean spectra is estimated. These spectrograms are examples of "dictionaries" that will be used for analysis (and suppression) of the wind turbine's signature.

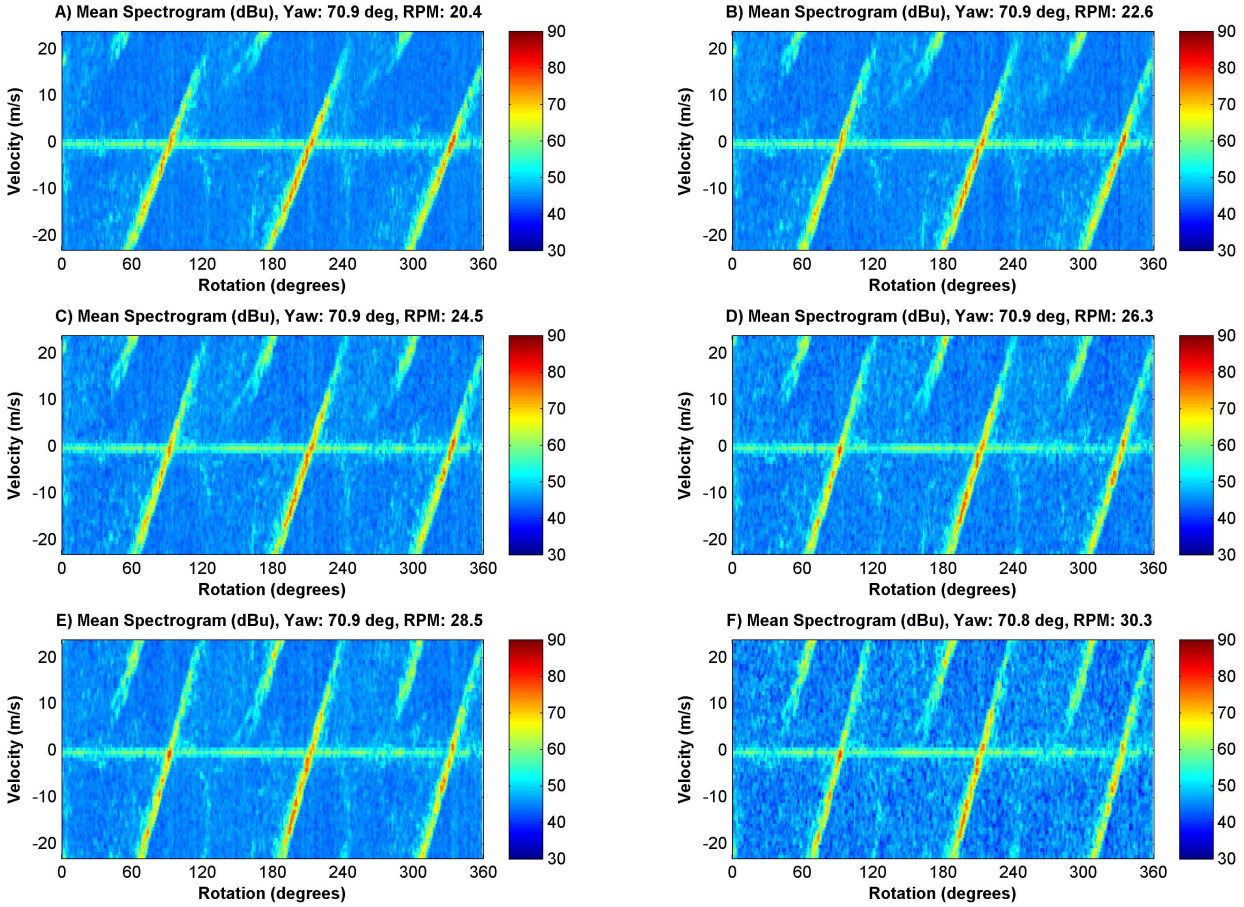


FIGURE 6.9. Dictionaries (the mean spectrograms as a function of the rotation angle) for six rotation rates. All observations are for relative yaw angles between 70 and 71 degrees. Graphs A through F represent rotation rates in two RPM steps from $\dot{\theta} = 20$ RPM to $\dot{\theta} = 30$ RPM, with each averaged over $[\dot{\theta}, \dot{\theta} + 1]$. The mean yaw and RPM for each dictionary are shown in each graph's title.

Figures 6.9 and 6.10 show representative radar observations of the CART3 for various states. Overall, for these yaw angles and rotation rates considered, the general signature is very similar for all cases. Closer inspection shows that as the rotation rate increases (or as the relative yaw angle approaches 90 degrees), the observed peak velocities increase (and more of the turbine's signature is aliased in the Doppler velocity). Note that the number of samples available for each state varies, and as such, the "texture" of each dictionary may vary. For the cases in Figures 6.10C and 6.10D, these states do not have a complete set of observations for all rotation angles.

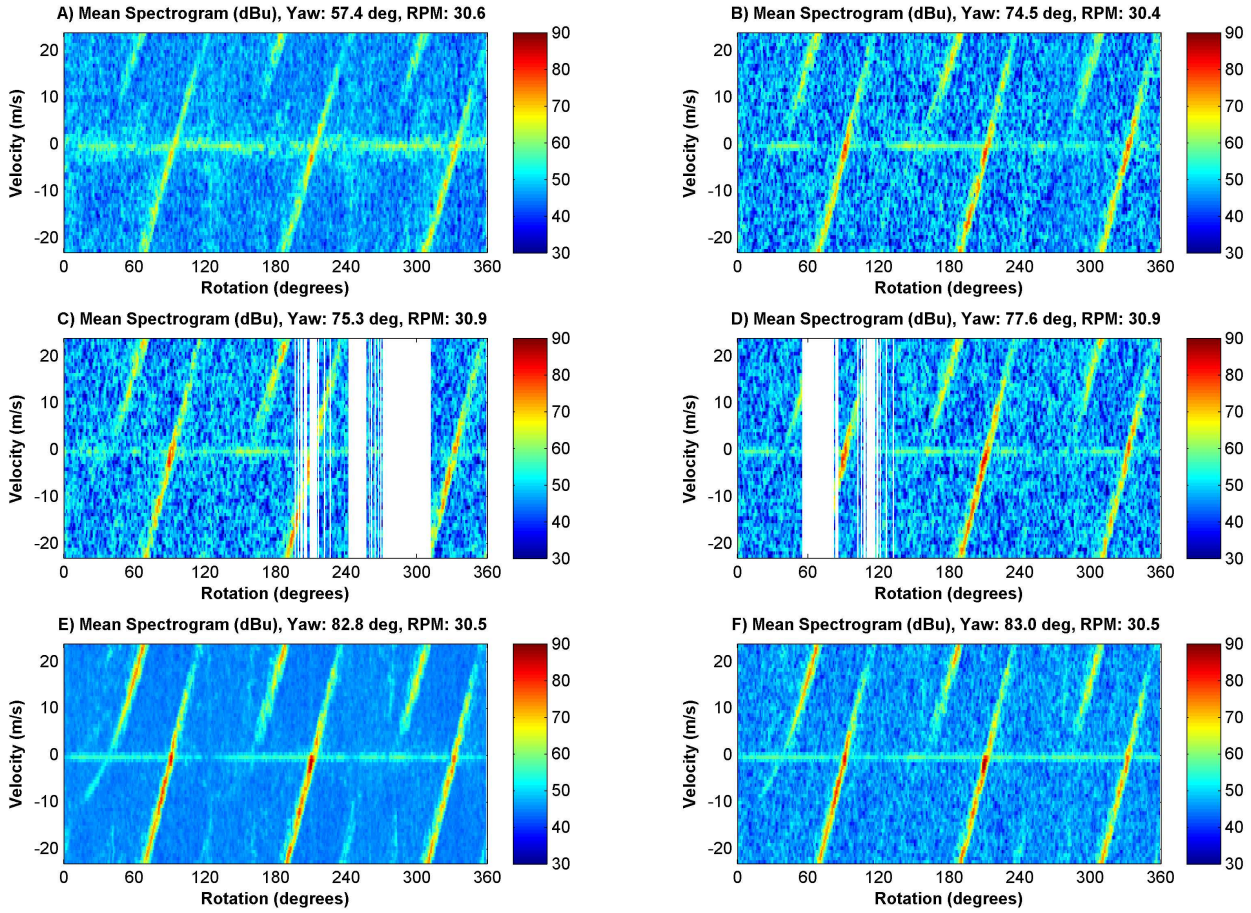


FIGURE 6.10. Dictionaries for six yaw angles with rotation rates between 30 and 31 degrees. Graphs A through F represent relative yaw angles of $\phi = 57.5, 74.5, 75.5, 77.5, 82.5,$ and $83.5$ degrees, with all states considering observations of $\phi \pm 0.5$ degrees. The mean yaw and RPM for each dictionary are shown in each graph's title.

The turbine's blade signature is observed at zero-Doppler velocity when the blade's scattering surface is parallel to the radar's observation radial. If the data is well aligned and the windowed data for estimation of the spectra is at a near-constant state, the zero-Doppler signature and rotation angle should be the same for all rotation rates. Figure 6.11 presents the zero-Doppler signature, as a function of the rotation angle and yaw angle, using all available rotation rates. The rotation angle at which the peak zero-Doppler RCS is observed changes as a function of the relative yaw angle. This is due to the geometry of the wind turbine and the radar's location. It is also likely to be influenced by the fact that the wind turbine's

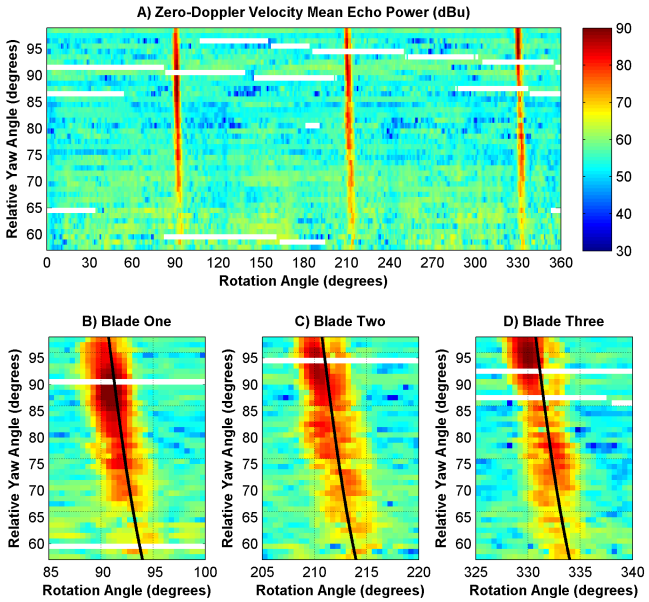


FIGURE 6.11. The mean zero-Doppler echo power as a function of rotation angle, averaged over all rotation rates. Graphs B, C, and D are the same color scale but zoomed in around each blade's signature to highlight the effect of the yaw angle on the rotation angle of the zero-Doppler velocity's specular reflection. The black lines represent the zero-Doppler velocity contours estimated by the turbine model in Equation 83.

blade is a volume with a complex curved surface. (The point at which the blade scatters will necessarily be a function of this curved surface, which may present itself in different ways as a function of yaw and rotation.) A closer examination of the effect of the yaw angle is presented in Figures 6.11B, 6.11C, and 6.11D, for Blade 1, 2, and 3, respectively. The absolute rotation angle that presents a specular surface (in the zero-Doppler velocity space) changes as a function of the yaw angle for each blade. The zero-Doppler contours from the model introduced in Section 6.2 are included as solid black lines and show good agreement with the observed trends of the zero-Doppler echos.

Next, in Figure 6.12, consider the variation in the spectra for a fixed rotation angle of $\theta = 75.25 \pm 0.25$ degrees. Changes in rotation rate are shown at constant relative yaw angles of $\phi = 82$ and $\phi = 68$ degrees in Figures 6.12A and 6.12C, respectively. Similarly, fixed rotation rates of $\dot{\theta} = 25$ and $\dot{\theta} = 22$ RPM, as a function of the relative yaw angle, are

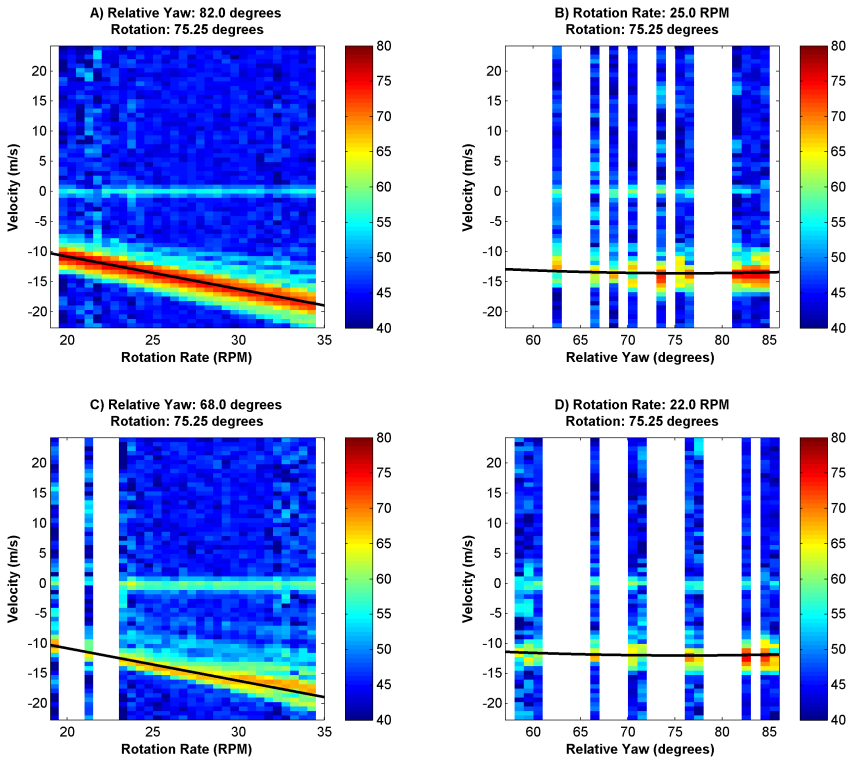


FIGURE 6.12. The variation of the spectral signature is evaluated at a fixed rotation angle as a function of the relative yaw angle (with two fixed rotation rates) and as a function of the rotation rate (with two fixed yaw angles). The black lines are the model's estimated velocity for the observed turbine state.

presented in Figures 6.12B and 6.12D, respectively. The modeled blade Doppler velocities are included in all figures as solid black lines. Again, the model shows good agreement with the observations. In Figures 6.12A and 6.12B, some spectral echo power is observed for Doppler velocities between the modeled velocity and zero-Doppler velocity. This is likely due to the fact that the turbine blade is a continuous surface, extending from the turbine's hub to the blade tip, and the surface scatters the radar's signal along its length (although with a varying RCS). The majority of the echo power is observed to be localized to the blade tip's velocity (with some spectral width).

From Figure 6.12, as the rotation rate and yaw angle change, the turbine's velocity signature is effectively scaled. Using the radial velocity model from Equation 81, consider the effect that rotation rate and yaw angle have on the velocity for a constant rotation

angle. Using the ratio of velocity at two different states, denoted with subscripts 0 and 1, and assuming that $\alpha = 0$ and $\beta$ are constant, the relationship between the yaw, rotation rate, and velocity for the two states is

$$\frac{v_1}{v_0} = \frac{\dot{\theta}_1 \tilde{r}_1 \sin\phi_1}{\dot{\theta}_0 \tilde{r}_0 \sin\phi_0}. \tag{85}$$

If the movement of the scattering point (i.e., the scattering phase center) along the turbine's surface is negligible, then $\tilde{r}_0 = \tilde{r}_1$. It is apparent that for the same velocity to be observed in both states, a change in the ratio of the sines of the relative yaw angles is inversely proportional to a change in the ratio of the rotation rates:

$$\frac{\sin\phi_0}{\sin\phi_1} = \frac{\dot{\theta}_1}{\dot{\theta}_0}. \tag{86}$$

Using dictionaries of radar observations of the CART3, the relationship from Equation 86 can be evaluated. The CART3 dictionaries are generated with 0.5-degree steps in the yaw angle, 0.5-degree steps in the rotation angle, and 0.5-RPM steps in the rotation rate. All of the available fixed-pointing observations from December 15, 2015, are used to generate the dictionaries, and the states for which full dictionaries are available for analysis are shown in Figure 6.13.

The correlation of the dictionaries (with the dictionaries' means subtracted) is presented in Figure 6.14. Figure 6.14A shows the effect of changes in the relative yaw angle on the correlation of the spectra. Similarly, 6.14B highlights how changes in the rotation rate affect the spectral signature. The translation of the RCS due to yaw changes (recall Figure 6.11) affect the correlation, but the velocity scaling (due to changes in the yaw or rotation rate) is expected to be more significant (see Figure 6.9). Figure 6.14C compares the correlation of the dictionaries as a function of changes in the yaw and rotation rate. The black line

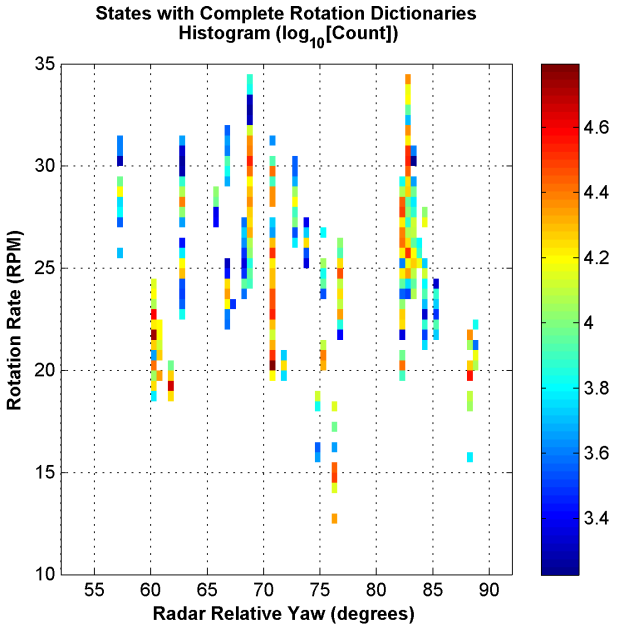


FIGURE 6.13. States with fully represented dictionaries from December 15, 2015. The histogram represents the total number of spectral observations of that state.

represents a "constant velocity" relationship, and the correlation of the dictionaries matches the trend given by Equation 86.

6.3.3. RADAR SPECTRAL MOMENTS. Given a spectra $S$, the total echo power, radial mean Doppler velocity, and spectrum width can be estimated [17]. These three spectral moments can be used to characterize the CART3's radar signature. For the estimation of these moments, three different thresholds for the spectral power are considered to "isolate" the turbine's signature. Note, that the velocity and spectrum width spectral estimators are sensitive to noise and Doppler velocity aliasing. The results of the spectral moment estimation for the three power thresholds are shown in Figure 6.15. As expected, the variations of the mean velocity and spectrum width estimates are reduced as the power threshold increases. Effects from the velocity aliasing are readily observed. Rotation angles where the mean Doppler velocity is near zero generally correspond to the rotation angles where there is no significant echo power from the wind turbine blades and the observation is dominated

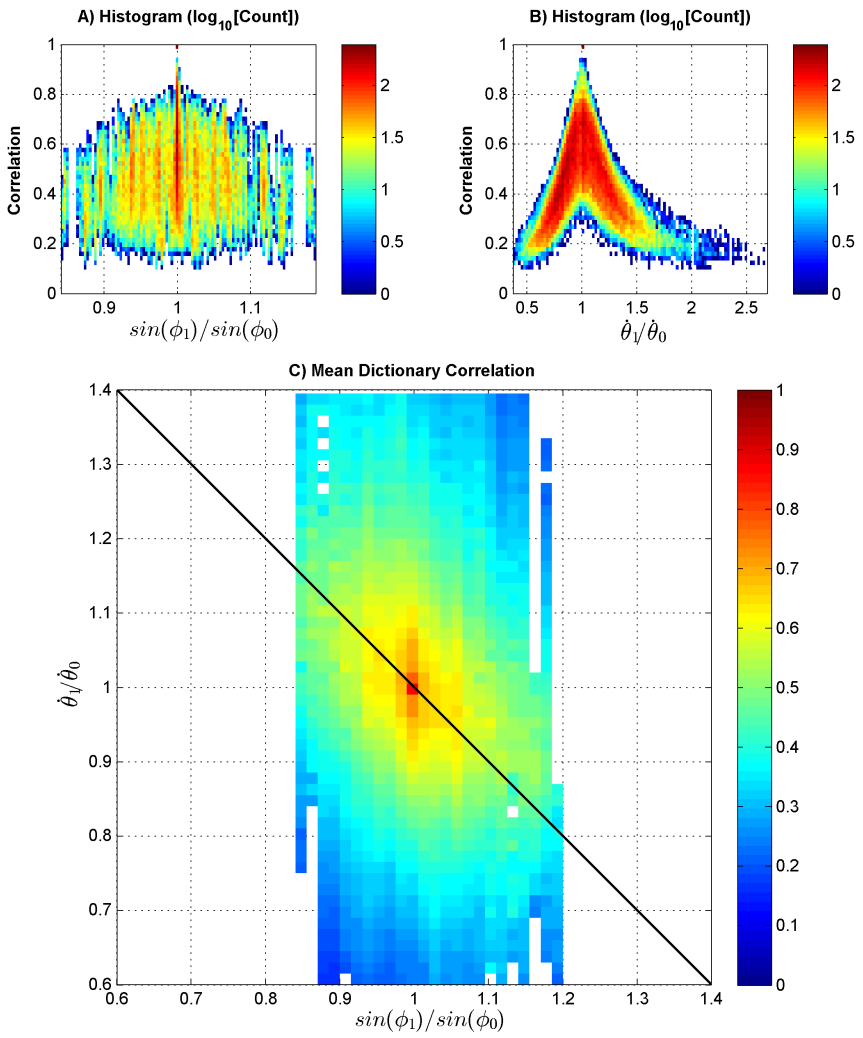


FIGURE 6.14. Graph A shows a histogram of correlations of all available dictionaries as a function of the ratio of the sines of the relative yaw angles. Similarly, Graph B shows a histogram of correlations for the ratio of rotation rates. Graph C presents the mean correlation from all comparisons as a function of both the ratio of yaw angles and the ratio of rotation rates. The solid black line represents a constant tip velocity following Equation 86. All correlations are performed with the dictionaries' means subtracted.

by stationary scatterers (such as ground clutter). The spectrum widths for rotation angles where the blade's echo is largest are typically within 2 m/s (see Figure 6.15I). Doppler aliasing and/or weaker echoes from the turbine blade can result in more significant spectrum width estimates that exceed 10 m/s (see Figures 6.15C and 6.15F). Note the three-blade symmetry (i.e., 120-degree rotation) in all moments.

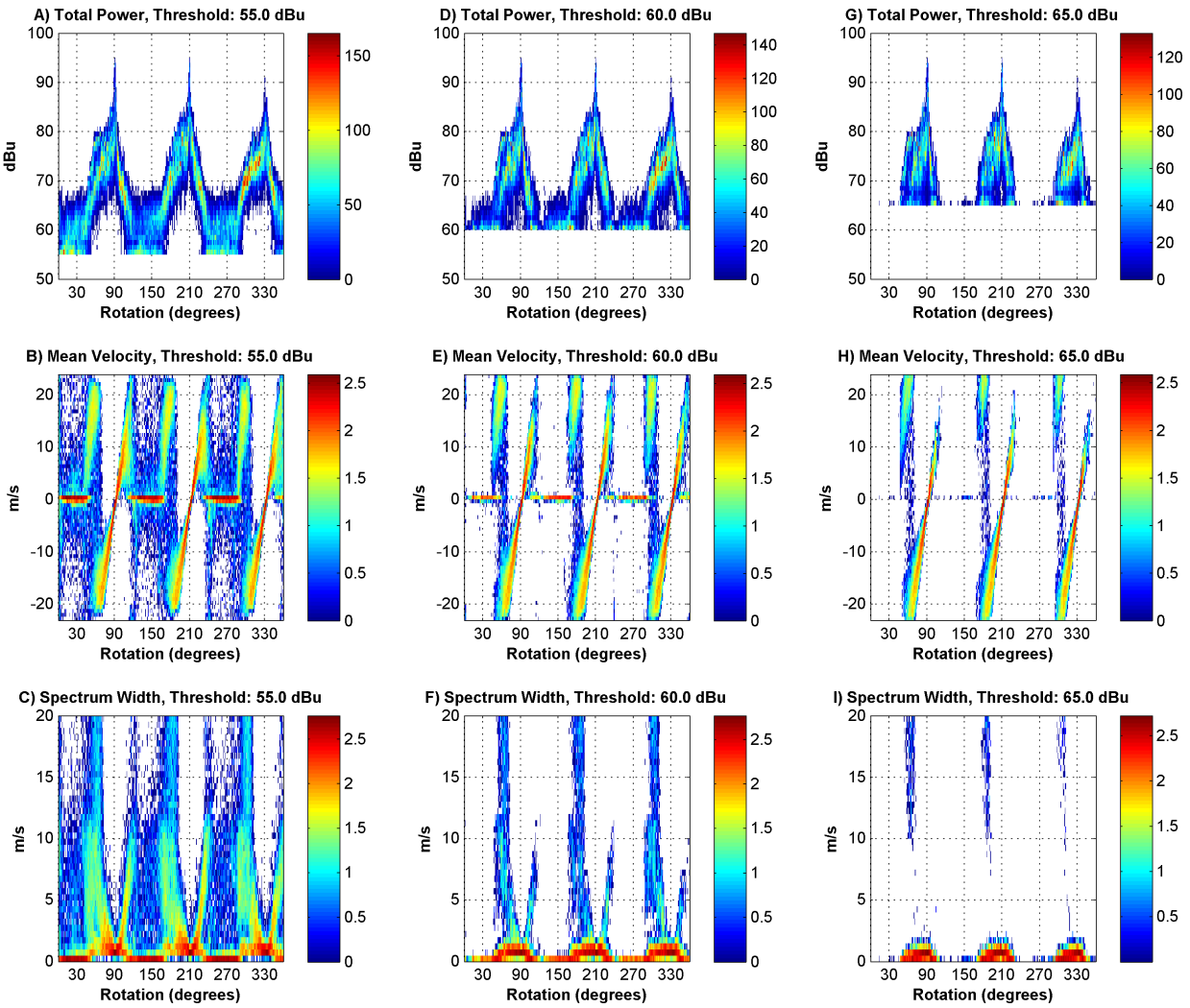


FIGURE 6.15. Histograms of the spectral moment estimates of the power (top row), mean velocity (middle row), and spectrum width (bottom row). The histograms (each shown as the logarithm of the number of occurrences) are presented as a function of the turbine's rotation angle and are estimated for all of the complete dictionaries. Three thresholds for the spectral power are used prior to estimation of the moments (and each set of moments is in a column for the various thresholds).

6.3.4. ISOLATING THE TURBINE SIGNATURE IN ALIASED OBSERVATIONS. The maximum blade-tip velocity of the CART3 (at the rated speed of 37 RPM) is 77.5 m/s. This peak velocity may be observed with either a positive or negative sign, and it exceeds the unambiguous velocity of the CSU X-band radar (and, in fact, for most precipitation radar). The overall effect on the observed wind turbine signature is that the signature may be aliased

in the Doppler spectra (and possibly overlapping itself). This aliasing further complicates effective suppression of the wind turbine's signature when simultaneously observed with other scatterers (such as precipitation or ground clutter).

In Figure 6.16, the rotational RCS turbine model is considered as a means to select and isolate the turbine's signature. With the model's mean blade velocity ($\hat{v}_x$, where $x$ is the blade number), additional constraints on the spectrum width ($\hat{\sigma_v}$), and estimates of the background spectral noise power, the wind turbine's signature can be more effectively isolated. For this case, the turbine's yaw angle relative to the radar is 60 degrees, and its rotation rate is 21 RPM. The turbine signature is selected with $\hat{v}_x \pm \hat{\sigma_v}$, where $\hat{\sigma_v} = \pm 5$ m/s and the region from $\hat{v}_x$ to 0 m/s is also retained (because the rest of the blade is moving within this spectral range). A spectrum width of $\hat{\sigma_v} = 5$ m/s was selected for this case as a compromise based on the observed spectrum widths for the regions with peak RCS in Figure 6.15. For the observation geometry of this case, to further isolate the wind turbine from other scattering signatures, constraints were placed on the absolute rotation angle of each blade for which echo power was expected. For Blade 1 (black line), only rotation angles from 0 to 140 degrees are kept. For Blade 2 (green line), it is 240 to 20 degrees (wrapping at 360 degrees), and Blade 3 (magenta line) is 120 to 260 degrees of rotation. This was done to help mitigate aliased spectra for rotation angles where significant echo power is not expected (note that these constraints are observation geometry-dependent). The noise power is estimated as the median power (in dB) of all the spectral bins to be 46.07 dB. Similarly, the median ground clutter power is 59.73 dB (applied to the zero-Doppler velocity). For areas where the spectral powers do not exceed these respective limits, the spectra are discarded. To further reduce spectral estimation "noise," if either neighboring velocity bin within a spectra is omitted using the noise or ground clutter power thresholds, the bin is also ignored.

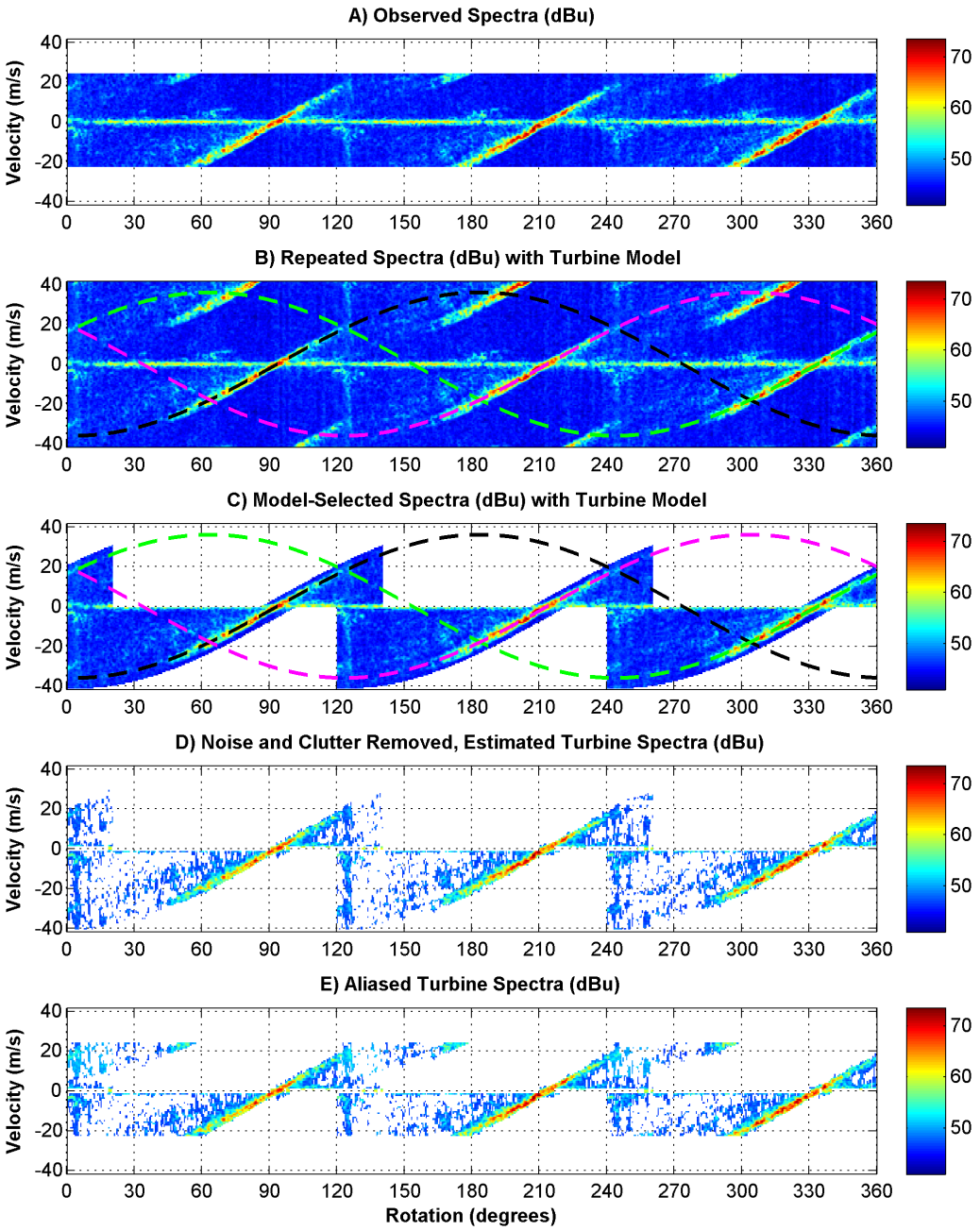


FIGURE 6.16. The spectral velocity is "unwrapped", and the turbine model (Section 6.2) is used to select the wind turbine's signature.

In Figure 6.16, the blades' "flash" signature is faintly observed. The reduced echo power of the flash is likely attributed to being observed outside of the antenna's -6 dB mainlobe. (The antenna's pointing angle is likely not centered on the turbine's hub, and the antenna's beamwidth does not encompass the entire swept area of the turbine.) Although the CART3's

physical structure is not exactly the same, the spectral shape exhibits similar characteristics (namely, the blade tips' "halo") as those observed in observations of other commercial turbines, numerical simulations, and scale model observations [6, 9]. As mentioned, the lack of a significant RCS blade flash in these signatures is attributed to the observation geometry (i.e., it is not in the antenna's mainlobe) rather than the turbine's structure.

The spectral moments presented in Figure 6.15 did not compensate for aliasing, and the only censoring performed to help isolate the wind turbine's signature was a threshold on the spectral echo power. Now, using the turbine signature selection technique described here, the spectral moments were recalculated after de-aliasing (i.e., velocity unwrapping) and isolating the wind turbine signature using the turbine model based on its telemetry and the observation geometry. The moment estimates in Figure 6.17 still censored using the noise power and ground clutter power as before. Comparing Figures 6.15 and 6.17 shows overall narrower distributions of the spectral moments for all dictionaries. Some discontinuity in the moments (as a function of the rotation angle) is apparent due to the turbine signature isolation technique. For areas of high spectrum width ($\sigma_v > 20$), the blade flash is present, or the observation does not contain any significant echo feature (i.e., it is effectively noise, as shown in Figure 6.16). As the blade's observed RCS increases and becomes significant, the spectrum width decreases, and the mean velocity closely matches the expected velocity ranges for the blades. Again, note the three-blade symmetry in all moment estimates.

## 6.4. Suppressing the Wind Turbine Signature via State Telemetry

Evaluation of the X-band radar observations using the CART3's telemetry has demonstrated that the wind turbine's radar signature is deterministic for a given state. Errors in the estimated RCS for a given state may still exist in spectral observations but are largely

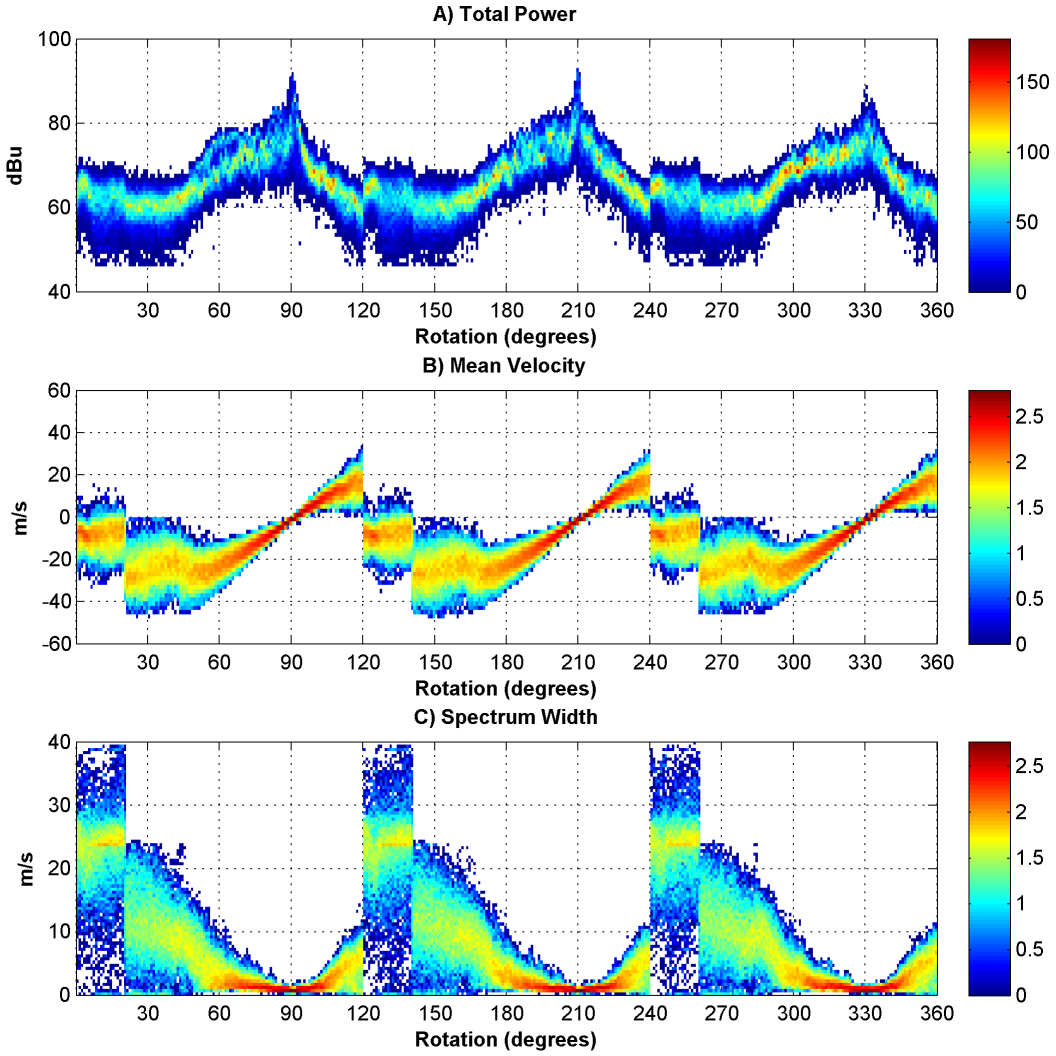


FIGURE 6.17. Histograms of spectral moments estimated from the dictionaries after the velocity is unwrapped and the CART3's signature is isolated, leveraging the state telemetry and observation geometry. Compare the results to Figure 6.15, where only spectral power thresholds are used. Each histogram is presented as the logarithm of the number of occurrences.

due to unknown or uncompensated for state variables, which may include gravity and wind-induced bending (i.e., blade flex) and turbine motion. Again, the CART3 has relatively short steel blades, which, when compared to longer, composite blades on larger turbines, are less subject to deformation from dynamic forces during operation.

Next, two techniques, which leverage the turbine's state telemetry, are considered to suppress the wind turbine's radar signature. The first uses prior spectral observations in

the form of a dictionary. The second technique relies on a simplified scattering model of the turbine (see Section 6.3). Both of these techniques were evaluated for the fixed-pointing observation mode as well as a scanning mode. For the fixed-pointing mode of operation, the characterization of the CART3 and the turbine observations to be suppressed are from the same radar observation volume. For the scanning radar cases, the turbine's signature may not be contained in the volume under observation, or the magnitude of the observed signature may be modified by the antenna's pattern.

6.4.1. Using a Dictionary of Prior Observations for Suppression. Suppression of a wind turbine's signature in an observation spectra ($S_x$) can be achieved using an inverse filter. With the wind turbine's state telemetry, the filter basis can be selected from prior observations of the same state (i.e., a dictionary). With the appropriate dictionary spectra ($S_D$), the filtered spectra ($S_f$), with the wind turbine suppressed, is

$$S_f = \frac{S_x}{S_D} = \frac{S_s + S_D}{S_D} = \frac{S_s}{S_D} + 1, \tag{87}$$

where $S_s$ is the signal's spectra. (The signal may be any signature that is not a wind turbine or noise.) Note that here, the dictionaries' spectra include both clutter and noise spectral power ($S_D = S_c + S_n$). The resulting spectra, $S_f$, closely represents an SNR. The inverse filter, in logarithmic units, is a simple subtraction:

$$S_f^{(dB)} = 10 \log_{10} \left( \frac{S_x}{S_D} \right) = S_x^{(dB)} - S_D^{(dB)}. \tag{88}$$

If the propagation channel and turbine are unchanged, no additional scaling or modification to the dictionary is required before being used as $S_D$.

Consider Figure 6.18C, a 9.5-second, fixed-pointing observation of the CART3 while its state is nearly constant (except for the rotation angle). The dictionary (the mean of the

spectral power observations in decibels) for the same rotation rate and yaw angle, as a function of the rotation angle, is shown in Figure 6.18A. Similarly, the standard deviation of the spectral observation used to create the dictionary (in decibels) is included in Figure 6.18B. The low standard deviations where the turbine's signature has the highest power highlight the consistency of the RCS observations. Compare these areas to those dominated by noise and represented by higher standard deviations in the spectral observations. Using the telemetry from the CART3, the dictionary is directly referenced to suppress the turbine's signature. The resulting inverse-filtered spectrogram is presented in Figure 6.18D. Again, recall that the result of the inverse filter is an SNR-like result. The filtered spectrogram shows a near 0 dB residual power, indicating excellent suppression of the wind turbine signature for this case.

In Figure 6.19B, the radar is scanned in azimuth at 3 degrees per second. The radar's elevation is held constant at the same used for fixed-pointing observations (1.3 degrees). No precipitation was present during the observation, and the CART3's state was nearly constant. The dictionary used for suppression is derived from fixed-pointing observations (Figure 6.19A) and is representative of the same CART3 states during the scan. Because the radar is scanning, the antenna's beamwidth acts as a "window" for the observed volume, and therefore, only $\pm 2$ degrees in azimuth around the CART3's azimuth (see Figure 6.19C) use the dictionary for suppression. The remaining observations are suppressed by the noise power estimated from the dictionary. The noise power is estimated by the median of the logarithmic power of all spectral bins to be 44.34 dB. Figure 6.19D shows the filter results after suppression of the wind turbine signature and the dictionary-estimated noise power. Note that, in reality, the noise power is azimuth-dependent. The wind turbine's signature is almost completely suppressed. A slight feature that resembles a residual signature of the

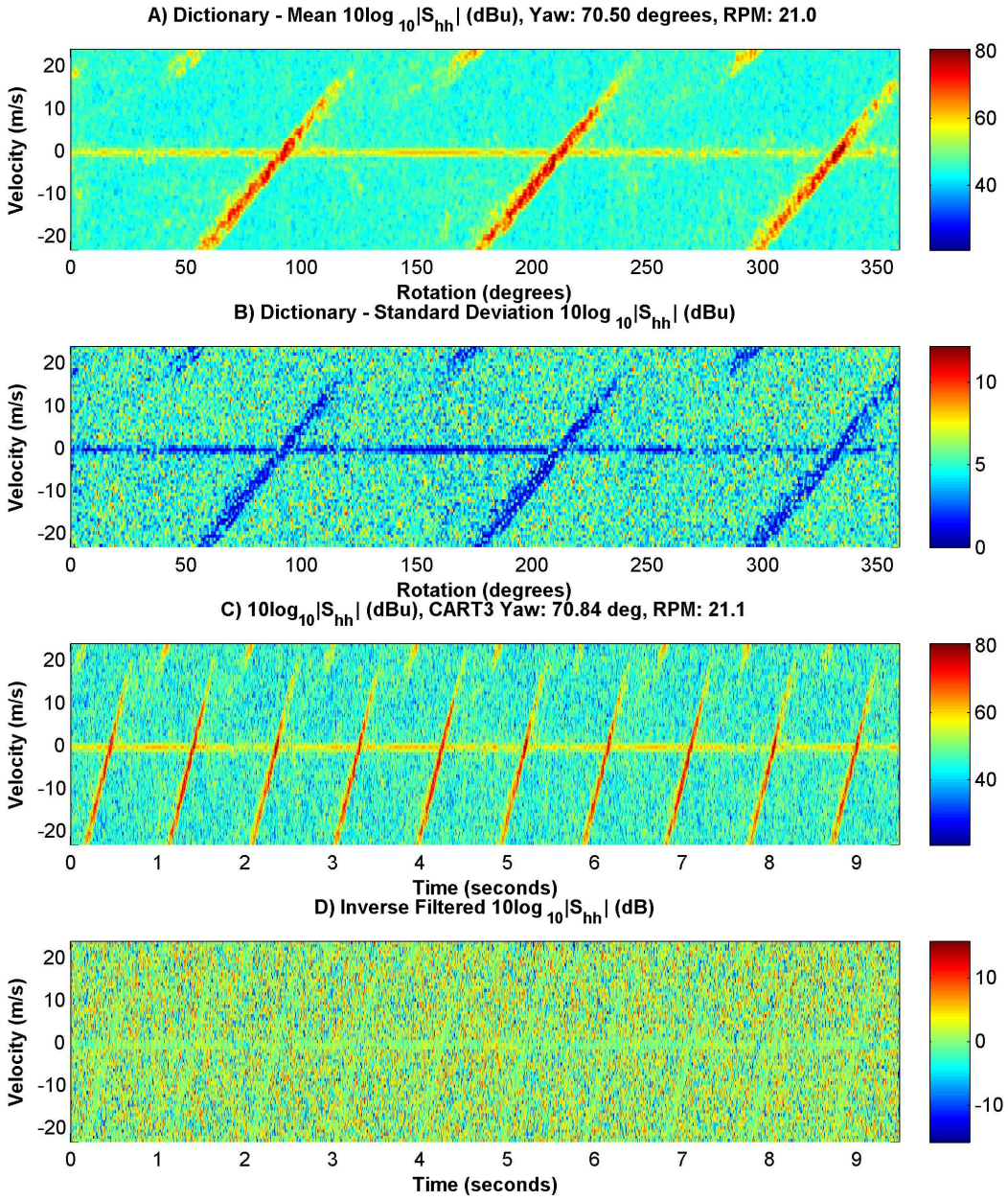


FIGURE 6.18. Fixed-pointing observations of the CART3 in a near constant state (except for rotation) is shown in Graph C. The dictionary used as the inverse filter basis is presented in Graph A. The CART3's relative yaw angle to the radar is 70.84 degrees, and the rotation rate is 21.1 RPM. The standard deviation of the observations used to estimate the dictionary is shown in Graph B. Graph D is the spectrogram after applying the inverse filter.

wind turbine is seen between 4.5 and 5 seconds. This is an artifact of the change in noise power, and the residual SNR for this is less than 0 dB (indicating it has been suppressed).

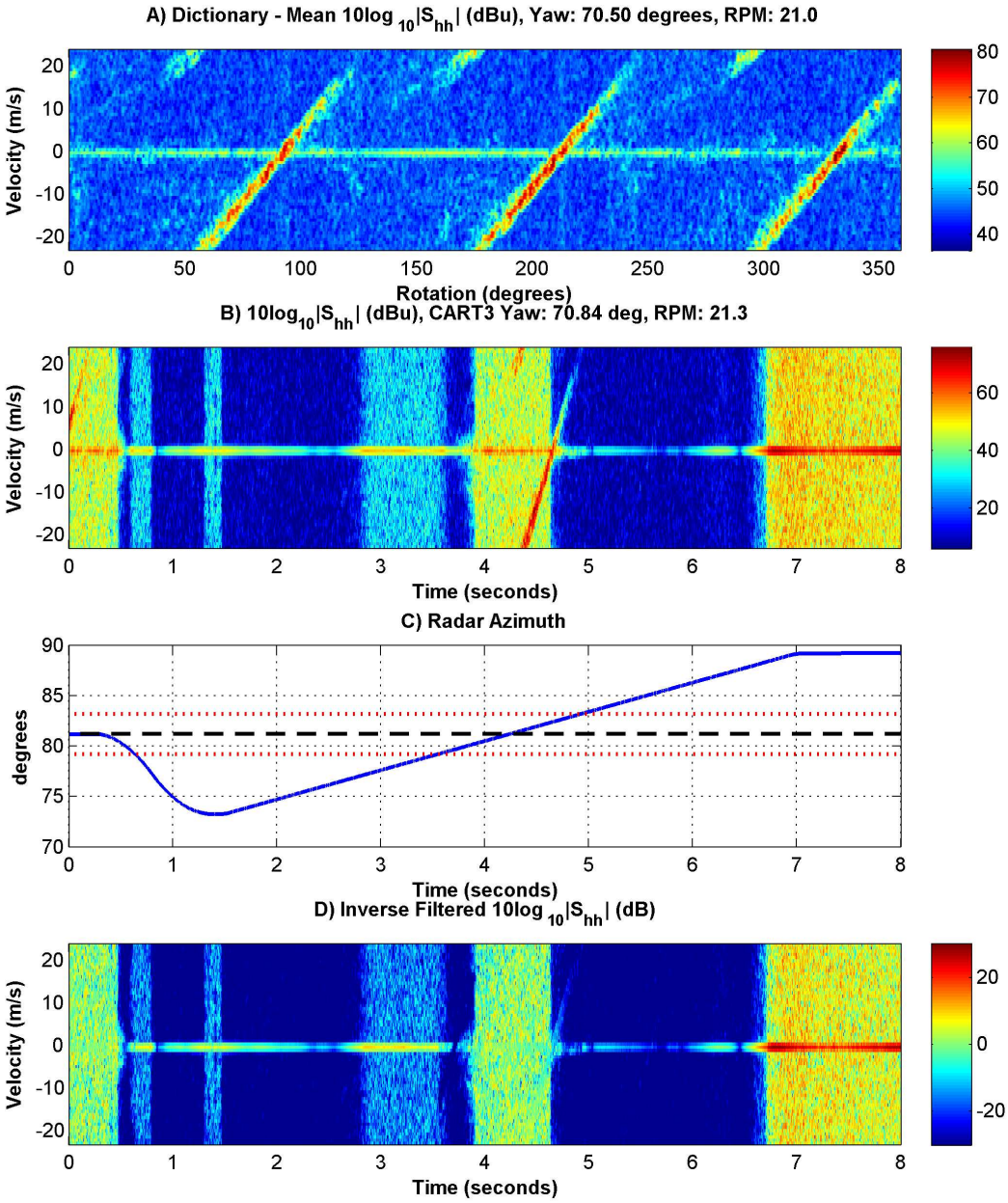


FIGURE 6.19. A 3-degree-per-second scan in azimuth of the CART3 turbine. The CART3's signature is suppressed using a dictionary derived from fixed-pointing observations of the same state. The only compensation for the suppression process is that the dictionary is applied for azimuths within 2 degrees of the CART3's direction. Otherwise, the observation is suppressed by the dictionary's noise power.

Figure 6.20B shows a 3-degree-per-second scanning case with snow in the observation volume. The effects of a mismatched dictionary are considered here. During the scan, the CART3 operated at a relative yaw angle of 98.7 degrees and rotation rate of 32.1 RPM. No

dictionary was available at this state, but a nearby state was available, with a relative yaw of $83 \pm 1$ degrees and RPM of $32 \pm 0.5$ (Figure 6.20A). This state was selected following the relationship presented in Equation 86. To compensate for the difference in state, 1.0 degrees was added to the CART3's rotation angle for the scanning observations prior to lookup in the dictionary. This adjustment is approximated using Equation 83 and Figure 6.11. The noise power was estimated to be 44.84 dBu. For this case, only azimuths within $\pm 1$ degree of the CART3's direction are suppressed with the dictionary. The rest of the observations are normalized by the dictionary's noise power. The filtered result is shown in Figure 6.20D. The effects of the mismatch between the CART3's signature at the two states (the scan and the dictionary) can be noticed when considering the near-zero Doppler velocity region around 0.5 seconds and 4.2 seconds. The effects of applying the dictionary to observations where the CART3 is not within the antenna's mainlobe are also observed in the filter result, from 4.5 to 5 seconds. Overall, even with this mismatched dictionary, the CART3's signature is significantly suppressed, with little adverse impact on the filtered spectrogram.

To evaluate the suppression in more detail, spectral moment estimates before and after filtering are shown in Figure 6.21. The powers in 6.21B are presented as a ratio (SNR-like) because of the inverse filter's structure. The estimated noise power from the dictionary was used to normalize the before-filtering power (blue) and the spectral power from Figure 6.20D for the after-filter result (red). The change in noise power during the scan is apparent in all spectral moments (as the noise floor results in an increase in the reflectivity-weighting for the velocity and spectrum width estimates). The CART3's signature is suppressed by 15 dB or more, and both the velocity's and spectrum width's biases are reduced.

6.4.2. Using a Turbine Model for Suppression. The wind turbine model developed in Section 6.2 is considered here to enable suppression of the turbine's signature. With

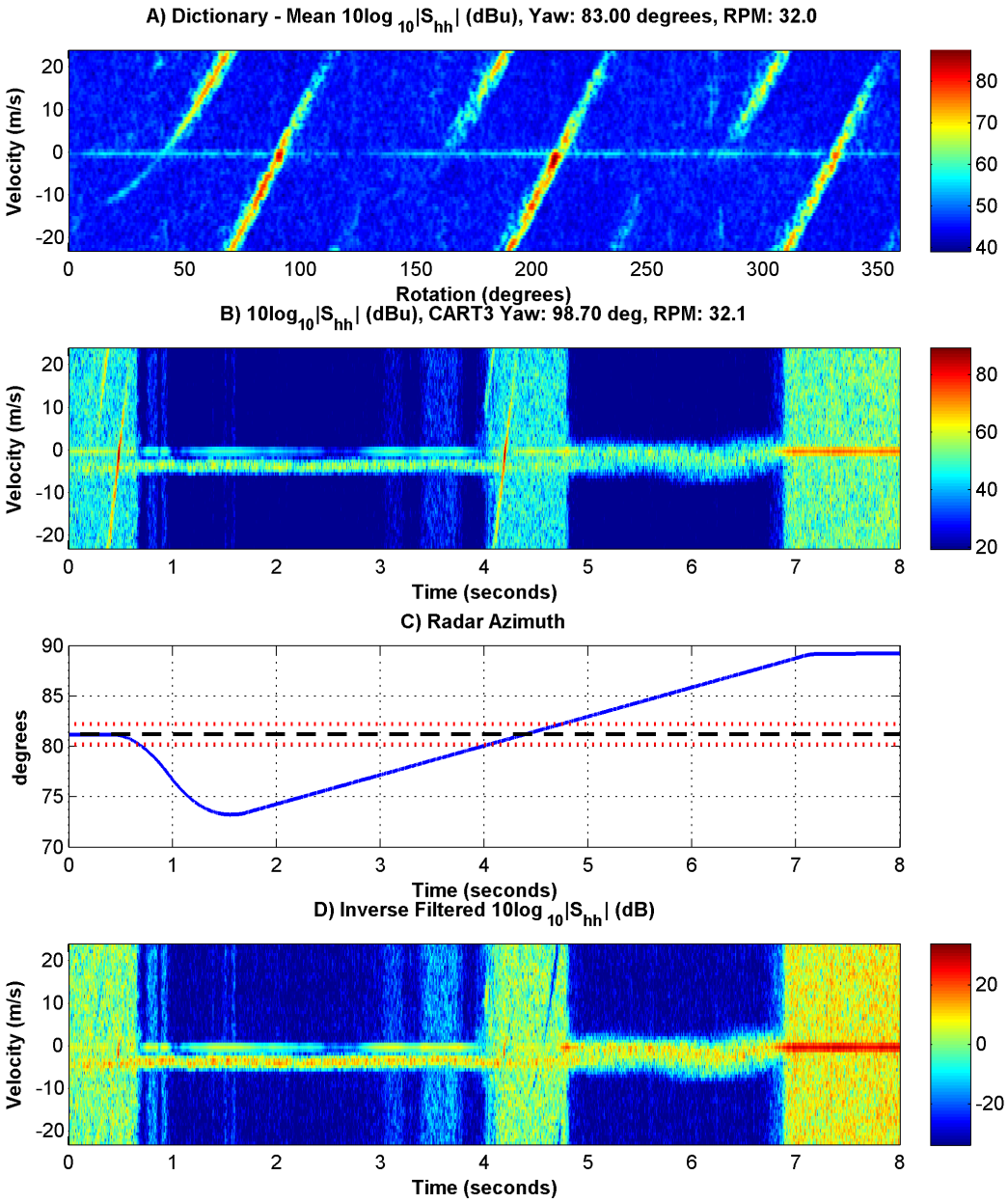


FIGURE 6.20. A scanned observation of the CART3 with precipitation (snow). The dictionary used for suppression is from a nearby state that exhibits similar velocity ranges. The azimuths within 1 degree of the CART3's direction are suppressed by the dictionary, while the rest are suppressed by the dictionary's noise power.

the CART3's state telemetry, a dynamic "notch" filter can be constructed. The rotation limits for isolating the turbine's signature are similar to those discussed in Section 6.3.4, but the spectra between the blade's velocity and zero-Doppler velocity are not considered

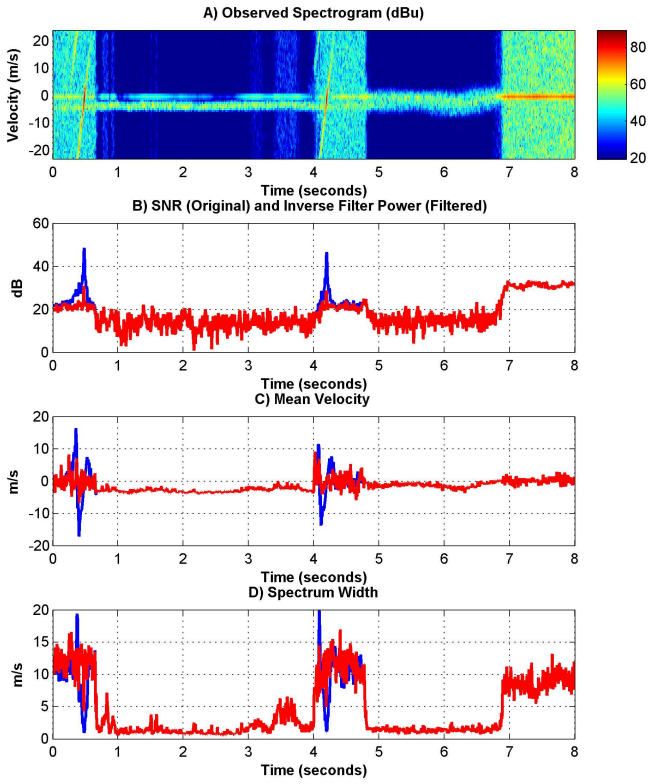


FIGURE 6.21. The before (blue) and after (red) spectral moment estimates for the observations and filter results presented in Figure 6.20.

as turbine echo. Only the spectral observations within $\hat{\sigma_v} = \pm 7.5$ m/s around the modeled velocity are retained (with constraints on the rotation angle). Again, this region of interest is selected to mitigate the wind turbine's signature within the radar observations without significantly impacting other scatter signatures. Any spectral signature detected as being a wind turbine is replaced with the noise floor estimate, and in this way, it effectively acts as a notch filter.

For this technique, an estimate of the noise floor is necessary. From the previous scanning cases in Figures 6.19 and 6.20, the noise power is shown to be azimuth-dependent and may vary by more than an order of magnitude. To implement spectra-by-spectra noise estimation, an exponential power distribution for noise is assumed, as well as that a substantial portion of a given spectra is noise-only. The mean ($\mu_y$) for an exponential distribution with value $y$

at percentile $P$ can be estimated as

$$\mu_y = \frac{-y}{\ln\left(1 - P(\mathbf{y} \leq y)\right)}. \tag{89}$$

Estimates of noise power using the fifth to $30^{\text{th}}$ percentiles of the spectra's power (in 5% steps) are averaged to give the final estimate for the spectra's noise power.

Using the turbine model and the CART3's state telemetry, the filter procedure is evaluated here for two fixed-pointing cases. The first case, in Figure 6.22, considers a rotation rate ramp-up event. The original spectra from Figure 6.22A are dealiased (in this case, velocity aliasing is not observed) and selected according to the modeled velocity and rotation angles to isolate the wind turbine signature shown in Figure 6.22B. The turbine's signature is then aliased back to the radar's available unambiguous velocity to produce Figure 6.22C. The areas where power is shown represent the areas to be notch-filtered and replaced by the estimated noise power. After filtering, the resulting spectrogram is shown in Figure 6.22D. Here, it is easily seen that almost all of the rotating turbine signature is suppressed to the noise level.

The same filter procedure was performed on another fixed-pointing observation, as shown in Figure 6.23. This case shows evidence of velocity aliasing but, again, demonstrates excellent suppression of the CART3's rotating signature. This is the same observation that was considered for suppression using a dictionary in Figure 6.18. Comparing the dictionary and model suppression demonstrates similar results between the two methods (with the exception of the zero-Doppler velocity ground clutter). Slightly better performance is observed when suppressing the turbine using the dictionary, but this is primarily due to a minor overestimate of noise power coupled with the model's conservative identification of the spectral bins to associate with the turbine's signature.

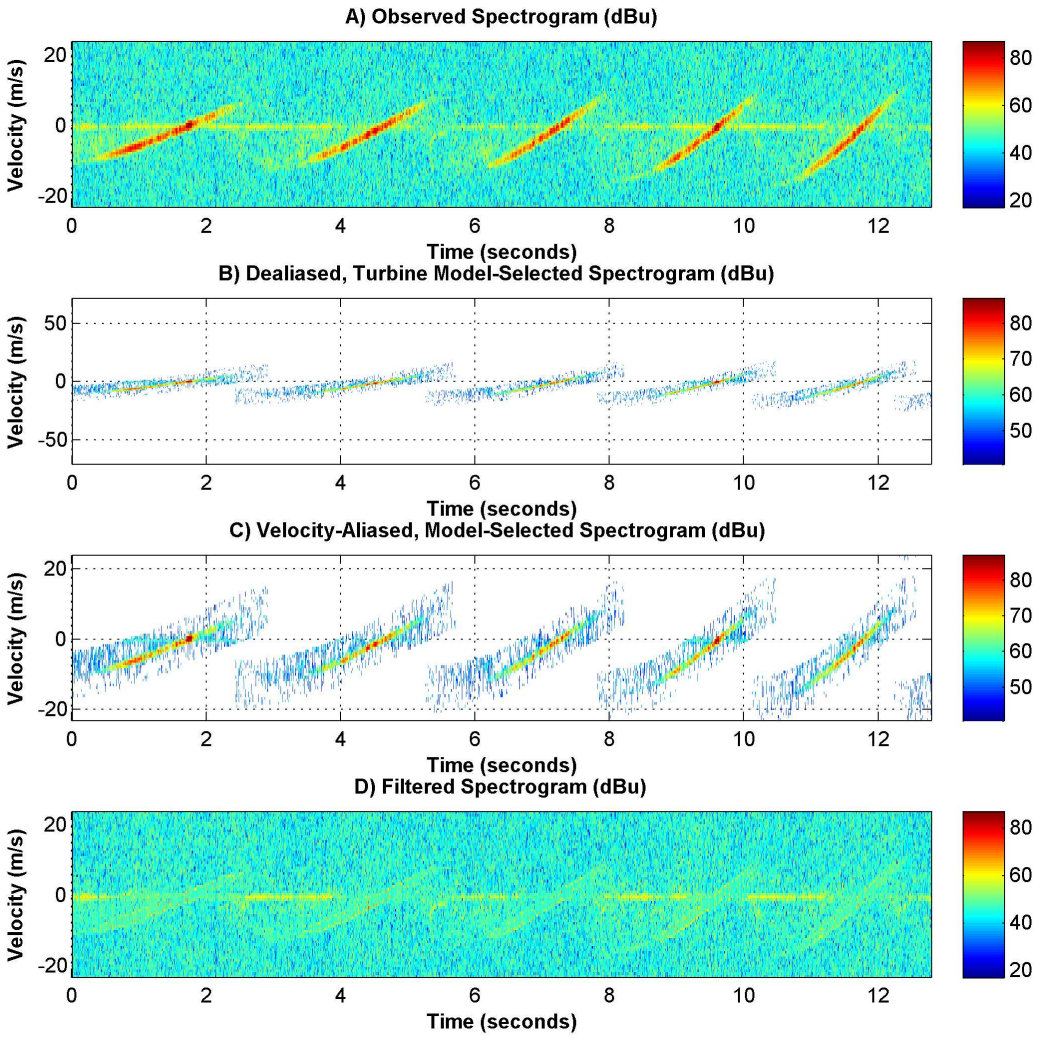


FIGURE 6.22. The wind turbine signature is modeled using the CART3's telemetry to selectively identify and notch-filter the signature in a fixed-pointing observation. The observation shows a rotation rate ramp-up event.

Now consider the scanning observation with snow from Figure 6.20. The turbine model is used instead of a dictionary to select and suppress the CART3's signature, as shown in Figure 6.24. As with the dictionary suppression, observations at azimuths within $\pm 1$ degree of the CART3's direction were filtered (see Figures 6.24A and 6.24D). The same procedure used in the fixed-pointing cases for selecting the spectral bins to be filtered is used here. Again, the noise power is estimated spectra by spectra using the exponential power distribution model from Equation 89. Figure 6.24E shows the residual echo power (in dBu, not dB as

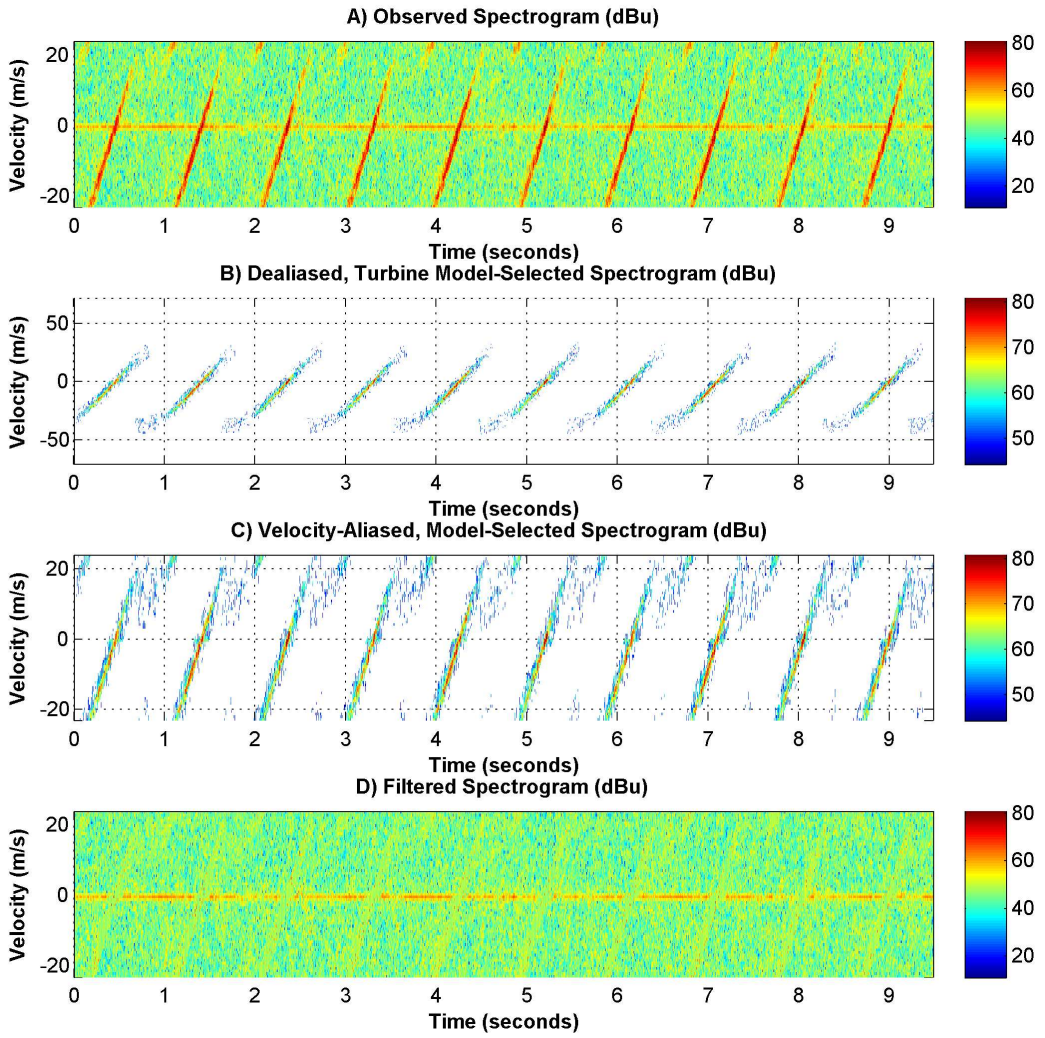


FIGURE 6.23. Again, the wind turbine signature is modeled using the CART3's telemetry, and the signature is filtered for an observation of the CART3 operating at a constant state (except for rotation). This is the same observation considered for suppression via a dictionary in Figure 6.18.

with the dictionary case) after notch-filtering via the wind turbine model with the CART3's telemetry. The turbine's signature is not apparent in these observations except as areas that appear to have slightly elevated (or spatially consistent) noise power. Very little of the precipitation's echo power is lost to the filter.

Figure 6.25 shows the spectral moment estimates before and after suppressing the CART3's signature using the turbine model for the scanning case with precipitation considered in Figure 6.24. By using the model to suppress the wind turbine signature, more than 20 dB of

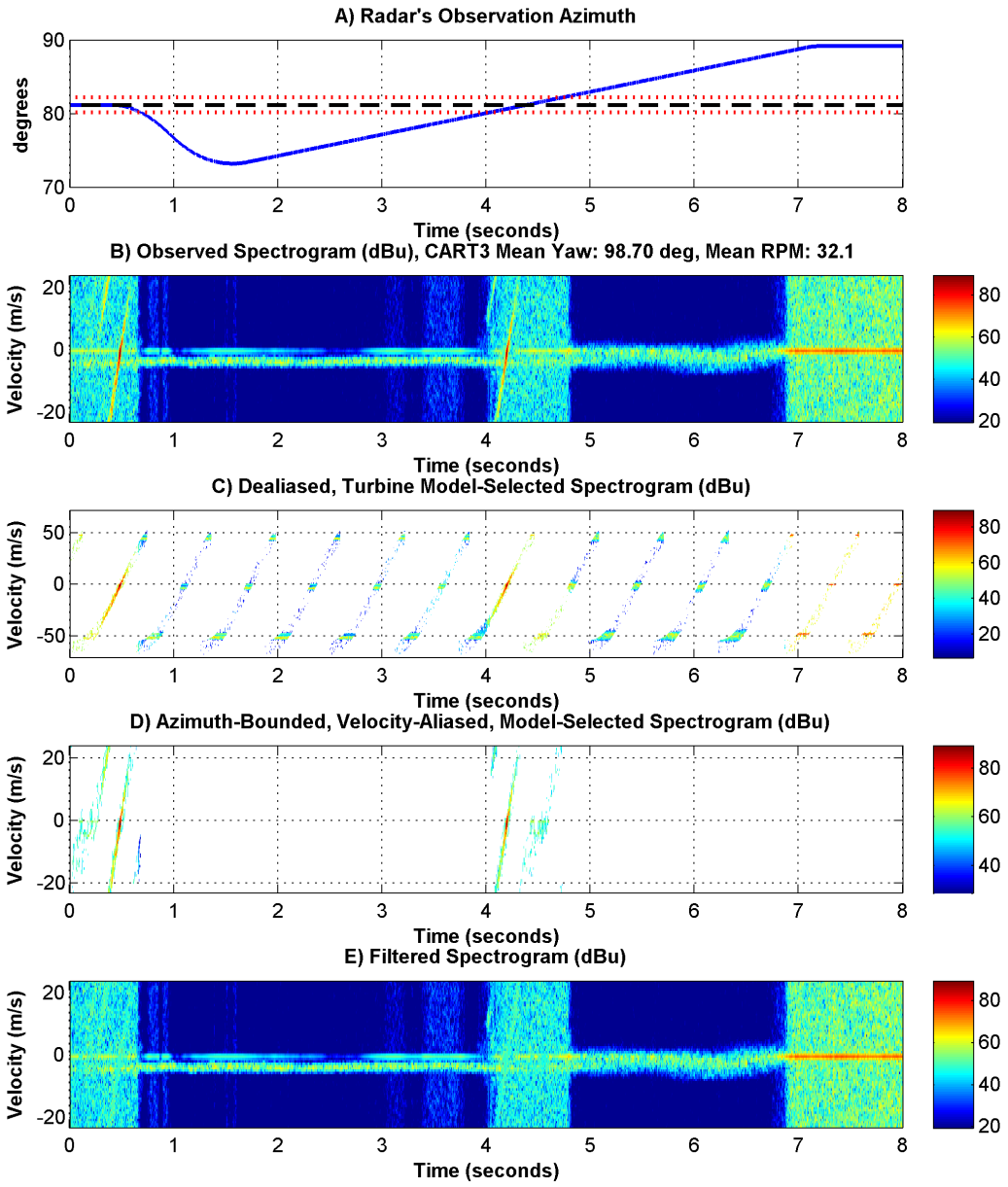


FIGURE 6.24. A scanning observation of the CART3 turbine coincident with snow is shown in Graph B. Graph A shows the radar's observation azimuth during the scan. This is the same scanning case presented in Figure 6.20 for suppression via a dictionary, but instead, here the turbine signature is filtered using the wind turbine model. Graphs C and D highlight the selection of the CART3's signature in the observations. Graph E is the filtered spectrogram with the turbine signature suppressed using the notch-filter for spectral bins selected as the turbine from Graph D.

the peak echo power is suppressed, and again, the biases in velocity and spectrum width due to the turbine's signature are significantly reduced. Compare these results to those

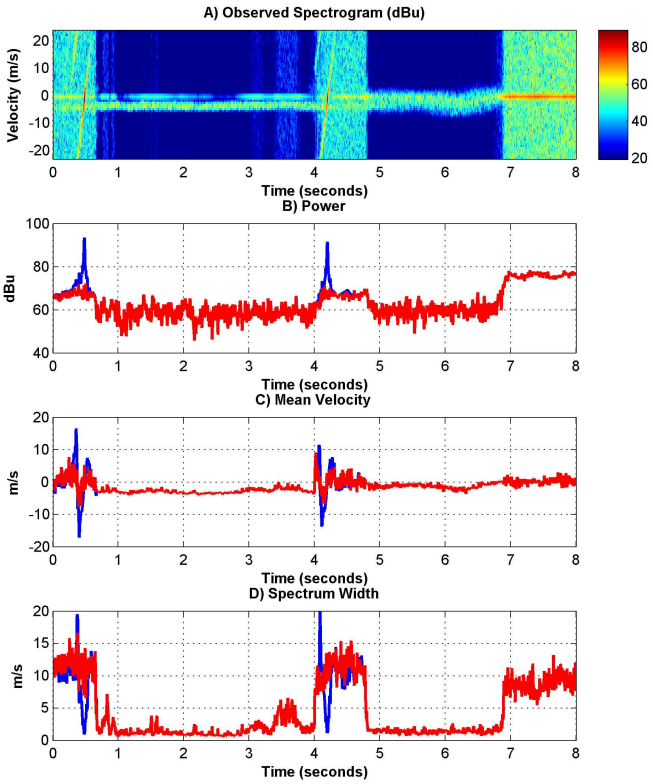


FIGURE 6.25. Before (blue) and after (red) spectral moment estimates using the turbine model and the CART3's telementry to suppress the rotating turbine signature whose spectrograms are shown in Figure 6.24.

from the suppression using the (mismatched) dictionary in Figure 6.21, both shows similar characteristics in the post-suppression moment estimates.

CHAPTER 7

# Summary

Prior wind turbine radar signature characterization efforts have typically fallen into two general categories: simulation or observation. WTC mitigation techniques can include using weather radar moments, advanced signal processing techniques, or changes to wind turbine designs and materials. To date, no single solution has yet to mitigate the wind turbine signature in all operating conditions, and research continues to further advance methods to address radar interference resulting from the increasing size and number of wind turbines.

This dissertation has advanced the understanding of the characteristics of the wind turbine signature in the context of weather radar applications. The wind turbine signature was demonstrated to be cyclostationary using commercial wind turbines. These characteristics of the wind turbine were exploited, which enabled WTC suppression of more than 15 dB relying only on the cyclostationarity of the turbine. With the addition of wind turbine state telemetry, suppression of the WTC is demonstrated to be greater than 25 dB for both fixed-pointing and scanning observations.

The scattering theory and radar-specific background that either directly or indirectly informed the analysis throughout this work was presented in this dissertation. Wind turbines most significantly impact radar systems when specular reflections are observed. The estimation of Doppler velocity for a point scatterer was used to highlight the premise behind using spectral characterization for wind turbines along with possible sources of error in velocity estimation. Radar observations and simulations were used in this work to demonstrate the fundamental concept of a wind turbine's "blade flash" and tip "halo" that is observed in radar spectra and meteorological parameters.

Two dual-polarization Doppler weather radars were used in this work for observing wind turbines and other scatterers of interest. The CSU-CHILL radar was instrumental in the characterization of ground clutter, precipitation, and wind turbines. The portable X-band radar enabled targeted observations of the CART3 turbine at the NREL. To evaluate the impact of turbines on radar systems, the weather radar moments typically used for the characterization of the microphyical structure of precipitation were considered. Although spectral representations were the primary focus of the characterization and suppression effort, the adverse effects of turbines are apparent in the radar moments. These moments provided a concise metric for evaluating suppression techniques and are ultimately the product consumed by most radar operators and algorithms.

A turbine's characteristics define its radar signature. The three-blade wind turbine structure and basic operation was considered in this work. Tower-mounted, horizontal rotation axis, three-blade wind turbines were considered exclusively, but this discussion and the analytical techniques presented are relevant to other wind turbine designs. Wind turbine characterization with the CSU-CHILL radar focused on the Ponnequin Wind Farm, which contains two models of wind turbines: the Vestas V47/660 and the NEG Micon NM48/750. The operating characteristics are different between the two, providing a heterogeneous mix of wind turbines. The impact of the wind farm's layout, as well as the prevailing wind velocity distributions, provides some insight into the probability of the turbines' operating states. This was further validated using measurements from the CART3 to bound the time constants and conditional distributions for state changes within a given time period.

The observation of wind turbines may be complicated by a multitude of factors. Understanding the possible sources of variation allows for an enhanced evaluation of radar observations. These sources of variation in observations include multi-path scattering, object-shadowing, and range- and antenna-windowing.

A consistent framework was used to compare radar observations of precipitation, ground clutter, and wind turbines. The selection of the data window can influence the correlation behavior. Considerations for the data window selection were presented with examples. A 64-sample window was typically selected, with either a Gaussian or rectangular shape, for the spectral analysis presented.

Using fixed-pointing radar observations, a temporal characterization of ground clutter, precipitation, and wind turbines was presented. Ground clutter shows a high correlation for time-lags on the order of seconds and beyond. Ground clutter exists in a very narrow spectral range but can have quite large magnitudes. This large-magnitude spectral response acts to significantly bias the correlation of observations. The spectral correlation of precipitation shows a similar correlation structure as a constant-plus-noise source.

For all observations of wind turbines, a clear cyclic behavior was observed. When the wind turbine is viewed perpendicular to its axis of rotation, the maximum Doppler velocities (the blade-tip velocities) are observed, which may exceed 80 m/s. As the turbine's radar-relative yaw angle approaches this limit, $\phi = \pm 90^{\circ}$, the turbine interference becomes more impulsive, resulting in blade "flashes." As the radar-relative yaw angle increases from 0 to $\pm 90$ degrees(or 180 to $\pm 90$ degrees), the RCS of the blades decreases and observed Doppler velocity increases. (The echo from the blade decreases and is spread over a larger range of Doppler velocities, both leading to reduced power spectral density.) The reduced blade RCS, coupled with the shorter integrated time during which the blade RCS is observed, lowers the

overall magnitude of the wind turbine's dynamic RCS contamination. For these cases, the tower and nacelle RCS dominates, which can be suppressed using available ground clutter filter algorithms. As the turbine's yaw angle approaches those where the hub is parallel to the radial ($\phi = 0°$ or $\phi = 180°$), the wind turbine blade RCS increases and may exceed that of the tower and nacelle. In addition, for low yaw angles, the blade's RCS is observed for long durations, and the integrated echo power can be multiple orders of magnitude larger than that of off-axis yaw angles. These wind turbine characteristics have been noted in radar observations, and corroborated with numerical simulations.

For the wind turbine observations presented for the Ponnequin Wind Farm and the CART3, the wind turbine's state typically shows time-constants on the order of seconds to tens of seconds. With these observations as a guide, the wind turbine's signature can remain correlated for time-lags on the order of 10 seconds or longer. In light, variable winds, the yaw and speed variability may increase as the control system attempts to extract the most energy. For high-speed winds, the turbine's structural vibrations typically increase due to wind-loading. The correlation analysis of the wind turbines shows that the 120-degree symmetry assumption is not perfect, and some asymmetry between different blades is observed. Additionally, the positive velocity-to-negative velocity blade flashes are not necessarily separated by a rotation of 60 degrees as a result of the blade structure's leading and trailing surfaces having a non-trivial angular separation.

Observations demonstrated that the wind turbines can distort the spectral characteristics of precipitation (with the wind turbine physically acting on the precipitation) and modify the local microphysical properties of it. The turbine's wake vortex is dynamic and much different than the conditions without a wind turbine. If the wind turbine's RCS is suppressed, the impact it has on downstream atmospheric conditions remains. It is also noted that the wind

turbine exhibits a cross-polar scattering signature that is significant, while rain typically has a LDR signature that is negligible (below the radar's observation limit).

The characterization results demonstrate that precipitation's Doppler spectrum changes slowly with time, while the turbine's Doppler signature changes relatively fast and in a cyclic manner. Current ground clutter-filtering methods adequately suppress a wind turbine's stationary echo power. Therefore, the rotating component of a wind turbine generates the signature to be suppressed. Results show that the short-time (on the order of seconds) mean Doppler spectrum for a range-volume cell enables a good estimate of the statistically stationary spectral power resulting from noise, ground clutter, and precipitation.

Suppression techniques, that directly operates on a radar volume containing WTC, were also presented in this work. A suppression method operating on a single range cell is desirable so that no loss of spatial resolution is incurred. For fixed-pointing observations, to suppress the rotating component of WTC, the periodic-correlation and cyclostationary properties of the observed wind turbines are used. This cyclic feature enables algorithms to adaptively detect and estimate a wind turbine's echo contribution in the presence of other echo sources. The prior observations of the rotating wind turbine are representative of its signature at intervals of a full rotation period. For the suppression of ground clutter, a ground clutter filter is still available to remove zero-velocity clutter components. By leveraging the cyclostationary nature of the turbine and the statistically stationary characteristics of precipitation, a temporal filtering technique was shown to demonstrate good performance in the presence of both transient targets or precipitation.

Characterization of the radar signature of the DOE NREL CART3 utility scale wind turbine was presented using the CART3's state telemetry. With a common clock between the two systems, the observations and telemetry can be directly related to provide deterministic

estimates of the radar signature for a given turbine state. With the state telemetry, the cyclostationarity of the wind turbine signature was verified using the rotation angle as the independent variable, and, for all state variables constant except the rotation angle, it is confirmed that rotation and time may be interchanged with little error.

Full characterization of the wind turbine's signature was performed over a subset of states to generate a-priori spectral signature dictionaries, which enable suppression of the wind turbine's signature. Using a simple point-scattering model with additional constraints on the turbine's and observation's geometry, the turbine's state telemetry provided a direct relation to the observed spectral signature. This model and telemetry enabled an adaptive "notch-filter" to be implemented on spectral radar observations. This technique is similar to that used for ground clutter filters (which assume a velocity of zero and narrow spectrum width).

Using the dictionary-based and model-based approaches to mitigate the wind turbine signature, suppression of the CART3's signature was demonstrated in both fixed-pointing and scanning observations. From a review of the spectral moments that considered observations coincident with precipitation (snow), the wind turbine's echo power was suppressed by over 20 dB, and the biasing effect of the turbine on velocity and spectrum width was significantly reduced.

Without prior observations, a model of the wind turbine can be used to selectively notch-filter Doppler velocities associated with its signature. If the turbine was previously observed at its operating state, those prior observations can be directly used to suppress its signature. Both of these techniques are complementary, with a common goal of suppressing the wind turbine signature in radar observations. These results demonstrate that with the addition of

state telemetry from a wind turbine, significant suppression of the turbine's radar signature is possible.

## 7.1. Future Work

Suggestions for continued research in the area of characterizing wind turbine signatures and mitigating radar clutter are:

- Enhancing parameter estimation of the WTC state from radar observations, including the detection and estimation of multiple wind turbines with different rotation periods
- Continuing to develop an observation-driven, adaptive filter for the suppression of periodic Doppler signatures
- Integrating the dual-polarization dependent features into the suppression algorithm for better separation from precipitation
- Conducting a more extensive observation campaign of a wind turbine with detailed state telemetry

# Bibliography

[1] R. M. Beauchamp and V. Chandrasekar, "Dual-Polarization Radar Characteristics of Wind Turbines With Ground Clutter and Precipitation," *IEEE Transactions on Geoscience and Remote Sensing*, vol. 54, no. 8, pp. 4833–4846, 2016.

[2] "The Effect of Windmill Farms On Military Readiness, Report to Congressional Defense Committees," tech. rep., 2006.

[3] D. de la Vega, J. C. G. Matthews, L. Norin, and I. Angulo, "Mitigation Techniques to Reduce the Impact of Wind Turbines on Radar Services," *Energies*, vol. 6, pp. 2859–2873, 2013.

[4] Global Wind Energy Council, "Global Wind Report - Annual Market Update 2014," tech. rep., 2014.

[5] L. Y. Pao and K. E. Johnson, "A tutorial on the dynamics and control of wind turbines and wind farms," in *American Control Conference, 2009. ACC '09.*, pp. 2076–2089, 2009.

[6] K. C. Hill, G. Zelinski, T. Van, and C. Vogel, "Computational Electromagnetics ( CEM ) Prediction of a Windmill," in *2007 EMCC Annual Meeting*, 2007.

[7] A. Buterbaugh, B. M. Kent, K. C. Hill, G. Zelinski, R. Hawley, L. Cravens, T. Van, C. Vogel, and T. Coveyou, "Dynamic Radar Cross Section and Radar Doppler Measurements of Commercial General Electric Windmill Power Turbines part 2: Predicted and Measured Doppler Signatures," in *Proc. 2007 AMTA Symposium*, 2007.

[8] B. M. Kent, K. C. Hill, A. Buterbaugh, G. Zelinski, R. Hawley, L. Cravens, Tri-van, C. Vogel, and T. Coveyou, "Dynamic Radar Cross Section and Radar Doppler Measurements of Commercial General Electric Windmill Power Turbines Part 1 : Predicted

and Measured Radar Signatures," *IEEE Antennas and Propagation Magazine*, vol. 50, no. 2, pp. 211–219, 2008.

[9] A. Naqvi, S. T. Yang, and H. Ling, "Investigation of doppler features from wind turbine scattering," *IEEE Antennas and Wireless Propagation Letters*, vol. 9, no. 1583, pp. 485–488, 2010.

[10] B. Gallardo-Hernando, F. Pérez-Martínez, and F. Aguado-Encabo, "Wind Turbine Clutter," in *Radar Technology* (G. Kouemou, ed.), InTech, 2010.

[11] L. R. Danoon and A. K. Brown, "Modeling Methodology for Computing the Radar Cross Section and Doppler Signature of Wind Farms," *IEEE Transactions on Antennas and Propagation*, vol. 61, pp. 5166–5174, Oct. 2013.

[12] F. Kong, Y. Zhang, and R. D. Palmer, "Wind Turbine Radar Interference Studies by Polarimetric Measurements of a Scaled Model," *IEEE TRANSACTIONS ON AEROSPACE AND ELECTRONIC SYSTEMS*, vol. 49, no. 3, pp. 1589–1600, 2013.

[13] B. Gallardo, F. Pérez, and F. Aguado, "Characterization Approach of Wind Turbine Clutter in the Spanish Weather Radar Network," in *THE FIFTH EUROPEAN CONFERENCE ON RADAR IN METEOROLOGY AND HYDROLOGY*, no. 1, 2008.

[14] B. M. Isom, R. D. Palmer, G. S. Secrest, R. D. Rhoton, D. Saxion, T. L. Allmon, J. Reed, T. Crum, and R. Vogt, "Detailed Observations of Wind Turbine Clutter with Scanning Weather Radars," *Journal of Atmospheric and Oceanic Technology*, vol. 26, pp. 894–910, May 2009.

[15] M. Douet, "Stealth Wind Turbines Avoid Radar Interference in France." Scientific American, September 2014. http://www.scientificamerican.com/article/stealth-wind-turbines-avoid-radar-interference-in-france/.

[16] F. Uysal, I. Selesnick, and B. M. Isom, "Mitigation of Wind Turbine Clutter for Weather Radar by Signal Separation," *IEEE Transactions on Geoscience and Remote Sensing*, pp. 1–10, 2016.

[17] V. N. Bringi and V. Chandrasekar, *Polarimetric Doppler Weather Radar: Principles and applications*. Cambridge University Press, first ed., 2001.

[18] M. Kavinsky, "Wind Farm Interference Showing Up on Doppler Radar." website visited June 23, 2016. http://www.weather.gov/mkx/windfarm.

[19] USGS, "windFarm — USGS Energy Resources Program." website visited June 23, 2016, June 2016. http://eerscmap.usgs.gov/windfarm/.

[20] NOAA, "NOAA Next Generation Radar (NEXRAD) Level II Base Data." website, updated March 16, 2015. https://catalog.data.gov/dataset/noaa-next-generation-radar-nexrad-level-ii-base-data.

[21] E. O'Grady, "E.ON completes world's largest wind farm in Texas — Reuters." website visited June 23, 2016, October 1 2009. http://www.reuters.com/article/wind-texas-idUSN3023624320091001.

[22] "California clean energy tour - alta wind energy center." website. http://www.energy.ca.gov/tour/alta/.

[23] L. Rashid and A. Brown, "Partial treatment of wind turbine blades with radar absorbing materials (RAM) for RCS reduction," in *Antennas and Propagation (EuCAP), 2010 Proceedings of the Fourth European Conference on*, 2010.

[24] J. Pinto, J. Matthews, and C. Sarno, "Radar signature reduction of wind turbines through the application of stealth technology," in *2009 3rd European Conference on Antennas and Propagation*, pp. 3886–3890, 2009.

[25] M. Douet, G. De Clercq, and J. Baird, "France builds stealth wind turbines to avoid radar interference." website, September 5 2014. http://uk.reuters.com/article/2014/09/05/us-windfarm-renewables-radar-idUKKBN0H013C20140905.

[26] M. Zarin, "Vestas proud to install 1st large-scale wind farm using stealth blade technology. Big technological step but other options also available.." website, accessed June 30, 2016, September 6 2014. https://www.vestas.com/ /media/9626c36b446e423284ffd0628ada2af5.ashx.

[27] A. D. Siggia and R. E. Passarelli, "Gaussian model adaptive processing (GMAP) for improved ground clutter cancellation and moment calculation," in *ERAD*, pp. 67–73, 2004.

[28] C. M. Nguyen and V. Chandrasekar, "Gaussian Model Adaptive Processing in Time Domain (GMAP-TD) for Weather Radars," *Journal of Atmospheric and Oceanic Technology*, vol. 30, pp. 2571–2584, Nov. 2013.

[29] K. Hood, S. Torres, and R. Palmer, "Automatic Detection of Wind Turbine Clutter for Weather Radars," *Journal of Atmospheric and Oceanic Technology*, vol. 27, pp. 1868–1880, Nov. 2010.

[30] A. R. Naqvi, *Investigation of Doppler Features Resulting from Wind Turbine Scattering.* PhD thesis, University of Texas at Austin, 2010.

[31] F. Uysal, U. Pillai, I. Selesnick, and B. Himed, "Signal decomposition for wind turbine clutter mitigation," in *2014 IEEE Radar Conference*, vol. 2, pp. 0060–0063, Ieee, May 2014.

[32] W. L. Stutzman and G. A. Thiele, *Antenna theory and design.* John Wiley & Sons, Inc., 2nd ed., 1998.

[33] G. Sinclair, "The Transmission and Reception of Elliptically Polarized Waves," *Proceedings of the IRE*, vol. 38, pp. 148–151, 1950.

[34] J. R. Probert-Jones, "The radar equation in meteorology," *Quarterly Journal of the Royal Meteorological Society*, vol. 88, no. 378, pp. 485–495, 1962.

[35] P. Z. Peebles Jr., *Radar Principles*. John Wiley & Sons, Inc., 1998.

[36] J. W. Taylor and G. Brunins, "Design of a New Airport Surveillance Radar (ASR-9).," in *Proceedings of the IEEE*, vol. 73, pp. 284–289, 1985.

[37] M. E. Weber, "FAA Surveillance Radar Data as a Complement to the WSR-88D Network," in *Ninth Conference on Aviation, Range, and Aerospace Meteorology*, 2000.

[38] J. George, V. Chandrasekar, and D. Brunkow, "CSU-CHILL Radar." website. http://www.chill.colostate.edu/wiki/images/4/4b/Brochure_web.pdf.

[39] D. N. Moisseev and V. Chandrasekar, "Polarimetric Spectral Filter for Adaptive Clutter and Noise Suppression," *Journal of Atmospheric and Oceanic Technology*, vol. 26, pp. 215–228, Feb. 2009.

[40] F. Harris, "On the use of windows for harmonic analysis with the discrete Fourier transform," *Proceedings of the IEEE*, vol. 66, no. 1, pp. 51–83, 1978.

[41] "The world's 10 biggest wind turbines." website, January 2 2014. http://www.power-technology.com/features/featurethe-worlds-biggest-wind-turbines-4154395/.

[42] M. Ragheb and A. M. Ragheb, "Wind Turbines Theory - The Betz Equation and Optimal Rotor Tip Speed Ratio," *Fundamental and Advanced Topics in Wind Power*, vol. 1, no. 1, 2011.

[43] I. Standard, "Wind turbines - Part 1: Design requirements," tech. rep., 2005.

[44] R. V. Rooij, "Terminology , Reference Systems and Convections," Tech. Rep. October, 2001.

[45] M. H. Hansen, "Improved modal dynamics of wind turbines to avoid stall-induced vibrations," *Wind Energy*, vol. 6, no. August 2002, pp. 179–195, 2003.

[46] S. Krenk, M. N. Svendsen, and J. Hø gsberg, "Resonant Vibration Control of Three-Bladed Wind Turbine Rotors," *AIAA Journal*, vol. 50, no. 1, pp. 148–161, 2012.

[47] J. Meyers and C. Meneveau, "Optimal turbine spacing in fully developed wind farm boundary layers," *Wind Energy*, vol. 15, no. April 2011, pp. 305–317, 2012.

[48] "Ponnequin Wind Farm." website. http://www.xcelenergy.com/Company/Operations/Power_Generation_Stations/Ponnequin_Wind_Farm.

[49] Vestas Wind Systems A/S, "V47-660 kW." Brochure. http://www.creswindfarm.gr/site1/Articles/V47_US.pdf.

[50] NEG Micon A/S, "NM48/750." Brochure. http://www.creswindfarm.gr/site1/Articles/nm48_750_gb.pdf.

[51] "The Wind Power: Wind Energy Market Intellegence." website. http://www.thewindpower.net/.

[52] M. Kostrzewa, D. Fink, J. Renquist, E. Rasbach, T. MacDonald, and N. Davis, "Anemometer Loan Program: HEREFORD - 12/30/2009 to 4/28/2011." website. http://projects-web.engr.colostate.edu/ALP/ALP_76_Hereford.htm.

[53] "Turbines at the NWTC." website, access June 27, 2016. http://wind.nrel.gov/turbines.html.

[54] N. Whitelonis, S.-t. Yang, and H. Ling, "Application of Near-Field to Far-Field Transformation to Doppler Features From Wind Turbine Scattering," *IEEE TRANSACTIONS ON ANTENNAS AND PROPAGATION*, vol. 60, no. 3, pp. 1660–1665, 2012.

[55] W. A. Gardner, A. Napolitano, and L. Paura, "Cyclostationarity: Half a century of research," *Signal Processing*, vol. 86, no. 4, pp. 639–697, 2006.

[56] S. Starosielec and D. Hägele, "Discrete-time windows with minimal RMS bandwidth for given RMS temporal width," *Signal Processing*, vol. 102, pp. 240–246, 2014.

[57] A. Papoulis and S. U. Pillai, *Probability, Random Variables, and Stochastic Processes*. McGraw-Hill Higher Education, 2002.

[58] B. D. Hirth, J. L. Schroeder, W. S. Gunter, and J. G. Guynes, "Measuring a utility-scale turbine wake using the ttuka mobile research radars," *Journal of Atmospheric and Oceanic Technology*, vol. 29, no. 6, pp. 765–771, 2012.

[59] E. Bossanyi, A. Wright, and P. Fleming, "Controller Field Tests on the NREL CART2 Turbine," Tech. Rep. December, 2010.

[60] L. Wang, X. Liu, N. Renevier, M. Stables, and G. M. Hall, "Nonlinear aeroelastic modelling for wind turbine blades based on blade element momentum theory and geometrically exact beam theory," *Energy*, vol. 76, pp. 487–501, 2014.